



Microgravity Materials Science Conference 2000

Edited by

*Narayanan Ramachandran
Universities Space Research Association
Huntsville AL*

*Nancy Bennett
Universities Space Research Association
Huntsville AL*

*Dannah McCauley
University of Alabama in Huntsville
Huntsville AL*

*Karen Murphy
Morgan Research Corporation
Marshall Space Flight Center
Huntsville AL*

*Samantha Poindexter
Universities Space Research Association
Huntsville AL*

Proceedings of a conference sponsored by the
Microgravity Research Division, NASA Headquarters
and held at Huntsville, Alabama, June 6-8, 2000

The NASA STI Program Office...in Profile

Since its founding, NASA has been dedicated to the advancement of aeronautics and space science. The NASA Scientific and Technical Information (STI) Program Office plays a key part in helping NASA maintain this important role.

The NASA STI Program Office is operated by Langley Research Center, the lead center for NASA's scientific and technical information. The NASA STI Program Office provides access to the NASA STI Database, the largest collection of aeronautical and space science STI in the world. The Program Office is also NASA's institutional mechanism for disseminating the results of its research and development activities. These results are published by NASA in the NASA STI Report Series, which includes the following report types:

- **TECHNICAL PUBLICATION.** Reports of completed research or a major significant phase of research that present the results of NASA programs and include extensive data or theoretical analysis. Includes compilations of significant scientific and technical data and information deemed to be of continuing reference value. NASA's counterpart of peer-reviewed formal professional papers but has less stringent limitations on manuscript length and extent of graphic presentations.
- **TECHNICAL MEMORANDUM.** Scientific and technical findings that are preliminary or of specialized interest, e.g., quick release reports, working papers, and bibliographies that contain minimal annotation. Does not contain extensive analysis.
- **CONTRACTOR REPORT.** Scientific and technical findings by NASA-sponsored contractors and grantees.

- **CONFERENCE PUBLICATION.** Collected papers from scientific and technical conferences, symposia, seminars, or other meetings sponsored or cosponsored by NASA.
- **SPECIAL PUBLICATION.** Scientific, technical, or historical information from NASA programs, projects, and mission, often concerned with subjects having substantial public interest.
- **TECHNICAL TRANSLATION.** English-language translations of foreign scientific and technical material pertinent to NASA's mission.

Specialized services that complement the STI Program Office's diverse offerings include creating custom thesauri, building customized databases, organizing and publishing research results...even providing videos.

For more information about the NASA STI Program Office, see the following:

- Access the NASA STI Program Home Page at <http://www.sti.nasa.gov>
- E-mail your question via the Internet to help@sti.nasa.gov
- Fax your question to the NASA Access Help Desk at (301) 621-0134
- Telephone the NASA Access Help Desk at (301) 621-0390
- Write to:
NASA Access Help Desk
NASA Center for AeroSpace Information
7121 Standard Drive
Hanover, MD 21076-1320
(301)621-0390

Available from:

NASA Center for AeroSpace Information
7121 Standard Drive
Hanover, MD 21076-1320
(301) 621-0390

National Technical Information Service
5285 Port Royal Road
Springfield, VA 22161
(703) 487-4650

Microgravity

Von Braun Center, Huntsville, Alabama



June 6 - 8, 2000

Organized by
Microgravity Materials Science Discipline Working Group

Sponsored by
Microgravity Research Division, NASA Headquarters, Washington, D. C.

Hosted by
NASA Marshall Space Flight Center, Huntsville, Alabama

Conference

Materials Science

Foreword

The 2000 Microgravity Materials Science Conference was held June 6-8 at the Von Braun Center, Huntsville, Alabama. It was organized by the Microgravity Materials Science Discipline Working Group, sponsored by the Microgravity Research Division (MRD) at NASA Headquarters, and hosted by NASA Marshall Space Flight Center and the Alliance for Microgravity Materials Science and Applications (AMMSA). It was the fourth NASA conference of this type in the microgravity materials science discipline. The microgravity science program sponsored approximately two hundred investigations, all of whom made oral or poster presentations at this conference. In addition, posters and exhibits covering NASA microgravity facilities, Advanced Technology Development projects sponsored by the NASA Microgravity Research Division at NASA Headquarters, and commercial interests were exhibited. The purpose of the conference was to inform the materials science community of research opportunities in reduced gravity and to highlight the spring 2001 release of the NASA Research Announcement (NRA) to solicit proposals for future investigations. It also served to review the current research and activities in materials science, to discuss the envisioned long-term goals, and to highlight new crosscutting research areas of particular interest to MRD. The conference was aimed at materials science researchers from academia, industry, and government. A workshop on In Situ Resource Utilization (ISRU) was held in conjunction with the conference with the goal of evaluating and prioritizing processing issues in Lunar and Martian-type environments. The workshop participation included invited speakers and investigators currently funded in the material science program under the Human Exploration and Development of Space (HEDS) initiative. The conference featured a plenary session every day with an invited speaker that was followed by three parallel breakout sessions in sub-disciplines. Attendance was close to three hundred and fifty people. Posters were available for viewing during the conference and a dedicated poster session was held on the second day. Nanotechnology, Radiation shielding materials, Space Station science opportunities, Biomaterials research and Outreach and Educational aspects of the program were featured in the plenary talks. This volume, the first to be released on CD-Rom for materials science, is comprised of the research reports submitted by the Principal Investigators at the conference.

Table of Contents

Research Reports: Section I	1
Reza Abbaschian - <i>In Situ</i> Monitoring of Crystal Growth Using MEPHISTO	1
Reza Abbaschian - Morphological Stability of Faceted Interfaces	21
J. Iwan D. Alexander - Vibrations and G-jitter: Transport Disturbances Due to Residual Acceleration During Low Gravity Directional Solidification and Diffusion Experiments	22
Jens Alkemper - The Evolution of Dendrite Morphology During Isothermal Coarsening	24
M. C. Altan - Microgravity Impregnation of Fiber Preforms	27
Timothy J. Anderson - An Electrochemical Method for Measuring Convection and Diffusion in Liquid Metals	33
J. B. Andrews - Wetting Characteristics of Immiscibles	39
J. B. Andrews - Coupled Growth in Hypermonotectics	45
Robert E. Apfel - Foaming of Thermoplastic Polymers in a Dynamic Decompression and Cooling Process	52
Michael J. Aziz * - Terrestrial Measurements of Diffusivities in Refractory Melts by Pulsed Melting of Thin Films ..	57
R. Michael Banish - Self-Diffusion in Liquid Elements	63
R. Michael Banish - Thermophysical Property Measurements of Te-Based II-VI Semiconductor Compounds	70
R.J. Bayuzick - Investigation of the Relationship Between Undercooling and Solidification Velocity	76
C. Beckermann - Equiaxed Dendritic Solidification Experiment (EDSE)	82
C. Beckermann - Dendritic Alloy Solidification Experiment (DASE)	86
A. Benard - Experimental and Numerical Investigation of Solidification Processes with Convection	92
George B. Benedek - Kinetic Evolution of Stable and Metastable States in Protein Solutions	98
Jerry Bernholc - Theoretical Investigations of the Mechanical and Electrical Properties of Carbon Nanotubes	103
J. F. Brady - Dispersion Microstructure and Rheology in Ceramics Processing	109
Kenneth Brezinsky - Combustion Synthesis of Materials in Microgravity	113
Peggy Cebe - Study of Development of Polymer Structure in Microgravity Using Ellipsometry	116
Soyoung Stephen Cha - Three-Dimensional Velocity Field Characterization in a Bridgman Apparatus: Technique Development and Analysis	121
A.A. Chernov - Differential Phase-Shifting Interferometry Studies of the Onset of Morphological Instability of Stepped Interfaces Growing from Solution	127
Michael J. Cima - Forces During Manufacture and Assembly of Microscale Discrete Electronic Components	133
Reid F. Cooper - Dynamic Reduction of Multicomponent, Transition-Metal-Cation-Bearing Ceramic Melts and Their Internal Crystalline Nucleation	135
T.H. Courtney - Sedimentation and Macrosegregation in Quiescent Melting and Liquid Phase Sintering	141
F.A. Cucinotta - Integration of the QMSFRG Database into the HZETRN Code	149
Jonathan A. Dantzig - Adaptive-Grid Methods for Phase Field Models of Microstructure Development	150
Jonathan A. Dantzig - Phase Field Modeling of Microstructure Development in Microgravity	157
Delbert E. Day - Kinetics of Nucleation and Crystal Growth in Glass Forming Melts in Microgravity	158
Kenneth A. Debelak - Recovery of Minerals in Martian Soils Via Supercritical Fluid Extraction	164
J.J. Derby - First Principles Calculations of Molten II-VI Compounds and Their Solidification Behavior	170
J.J. Derby - Theoretical Analysis of 3-D, Transient Convection and Segregation in Microgravity Bridgman Crystal Growth	172
J.J. Derby - Atomistic Simulations of Cadmium Telluride: Toward Understanding the Benefits of Microgravity Crystal Growth	174

*Dr. Frans Spaepen is the Co-Principal Investigator on this project.

N. Dietz - Real-Time Optical Monitoring of Flow Kinetics and Gas Phase Reactions Under High-Pressure OMCVD Conditions	176
E.L. Dreizin - High Temperature Phases and Phase Equilibria in Reactive Molten Metal-Based Systems	182
P. Ducheyne - Reactions and Surface Transformations of a Bioactive Material in a Simulated Microgravity Environment: an Experimental and Numerical Study	188
M. Dudley - Combined Synchrotron White Beam X-ray Topography and High Resolution Triple Axis X-ray Diffraction Characterization and Analysis of Crystals Grown in Microgravity and Ground-Based Environments	194
Prabir K. Dutta - Fundamental Studies of Crystal Growth of Microporous Materials	199
M.S. El-Shall - Nucleation and Polymerization Experiments in the Vapor Phase	204
Edwin C. Ethridge - Mechanisms for the Crystallization of ZBLAN	210
J.W. Evans - Exploiting the Temperature Dependence of Magnetic Susceptibility to Control Convection in Fundamental Studies of Solidification Phenomena	213
Alexandre I. Fedoseyev - Investigation of Vibrational Control of Convective Flows of the Bridgman Crystal Growth Technique	216
R.S. Feigelson - Investigation of the Crystal Growth of Dielectric Materials by the Bridgman Technique Using Vibrational Control	222
M.C. Flemings - The role of convection and growth competition in phase selection in microgravity: Controlled Convection in the Containerless Processing of Steel Alloys	228
Andrienne C. Friedli - Thermal Stability and Conductivity Properties of Monomeric and Polymeric Oxanorbornenes	234
Randall M. German - Gravitational Effects on Distortion in Sintering	239
Donald C. Gillies - Use of Computed Tomography for Characterizing Materials Grown Terrestrially and in Microgravity	244
M.E. Glicksman - Follow-on Research Activities for the Rensselaer Isothermal-Dendritic Growth Experiment (RIDGE) ...	246
M.E. Glicksman - The Isothermal Dendritic Growth Experiment (IDGE)	253
M.E. Glicksman - Evolution of Local Microstructures: Spatial Instabilities of Coarsening Clusters	259
A.M. Gokhale - Effect of Gravity on the Evolution of Spatial Arrangement of Features in Microstructures: A Quantitative Approach	267
A.R. Greenberg - Influence of Solutocapillary Convection on Macrovoid Defect Formation in Polymeric Membranes ...	273
R.N. Grugel - Utilizing Controlled Vibrations in a Microgravity Environment to Understand and Promote Microstructural Homogeneity During Floating-Zone Crystal Growth	279
R.N. Grugel - Solidification Processing of Immiscible Liquids in the Presence of Applied Ultrasonic Energy	282
P. K. Gupta - Inter- Diffusion in the Presence of Free Convection	283
Research Reports: Section II	288
N.J. Halas - The Effect of Microgravity on the Growth of Silica Nanostructures	288
D.A. Hammer - Polymersomes: Tough, Giant Vesicles Made from Diblock Copolymers	293
L. Heilbronn - Radiation Transmission Properties of in-Situ Materials	295
W.H. Hofmeister - Formation of $Y_xNd_{1-x}Ba_2Cu_3O_{7-\delta}$ ($0 \leq x \leq 0.7$) Superconductors from an Undercooled Melt Via Aero-Acoustic Levitation	301
M.D. Hollingsworth - Tailor-Made Impurity Control of Elastic Versus Plastic Domain Switching in Ferroelastic Inclusion Compounds	308
George M. Homsy - Solid State Electrochemical Oxygen Conversion for Martian and Lunar Environments	310
A.J. Hunt - Porosity and Variations in Microgravity Aerogel Nanostructures: II. New Laser Speckle Characterization Methods	316
Kenneth A. Jackson - Growth of Rod Eutectics	322

Kenneth A. Jackson - Non-Equilibrium Phase Transformations	323
David R. Johnson - Experimental and Numerical Investigations of Growth Morphologies of Peritectic Reactions ...	325
W.L. Johnson - Physical Properties and Processing of Undercooled Metallic Glass Forming Melts	332
David L. Kaplan - Hierarchical Assembly of Collagen	334
Alain Karma - Phase-Field Simulations of Equiaxed Dendritic Growth at Low Undercooling: Confronting Theory and Experiment	340
Alain Karma - Role of Dynamic Nucleation at Moving Boundaries in Phase and Microstructure Selection	345
M. Kassemi - Effect of Marangoni Convection Generated by Voids on Segregation During Low-G and 1-G Solidification	346
K.F. Kelton - Studies of Nucleation, Growth, Specific Heat, and Viscosity of Undercooled Melts of Quasicrystals and Polytetrahedral-Phase-Forming Alloys	353
K.J. Klabunde - Nanocrystal Superlattices: Synthesis and Properties	359
M.B. Koss - The Transient Dendritic Solidification Experiment (TDSE)	360
S. Kou - Experiments to Observe Marangoni Convection in Simulated Weld Pools and Its Effect on the Weld Pool Shape	366
Shankar Krishnan - Structure-Property Correlation and Phase Transitions in Group IV and III-V Liquids	372
David J. Larson, Jr. - Defects Numerically Decreased	374
Sandor L. Lehoczy - Growth of Solid Solution Single Crystals	375
J.A. Lewis - Phase Behavior of Asymmetric Binary Colloid Mixtures: Influence on Colloidal Processing of Ceramics	377
Ben Q. Li - A Comparative Modeling Study of Magnetic and Electrostatic Levitation in Microgravity	382
Ben Q. Li - Study of Magnetic Damping Effect on Convection and Solidification Under G-jitter Conditions	388
S. Lowry - Influence of Natural Convection and Thermal Radiation on Multi-Component Transport and Chemistry in MOCVD Reactors	394
Nancy Ma - Models of Mass Transport During Microgravity Crystal Growth of Alloyed Semiconductors in A Magnetic Field	401
A. MacKnight - Carbon Nanotubes Growth and Containerless Directional Crystallization (CDC) in Microgravity for Electromechanical Actuation Applications	407
Jules J. Magda - Novel Microstructures for Polymer-Liquid Crystal Composite Materials	409
L.W. Mason - CO ₂ Acquisition Membrane (CAM) Project	411
D.H. Matthiesen - Diffusion Processes in Molten Semiconductors	413
R.H. Maurer - Development of a Neutron Spectrometer to Assess Biological Radiation Damage Behind Spacecraft Materials	419
Jimmy W. Mays - Controlled Synthesis of Nanoparticles Using Block Copolymers: Nanoreactors in Microgravity Conditions	422
Dr. Konstantin Mazuruk - Effects of Traveling Magnetic Field on Dynamics of Solidification	423
G.B. McFadden - Convective and Morphological Instabilities During Crystal Growth	430
G.B. McFadden - A Phase-Field/Fluid Motion Model of Solidification: Investigation of Flow Effects During Directional Solidification and Dendritic Growth	435
C.M. Megaridis - Microgravity Investigation of Dynamic Oxygen Adsorption in Molten Solder Jetting Technology	440
J. Miller - Radiation Transport Properties of Potential <i>In Situ</i> -Developed Regolith-Epoxy Materials for Martian Habitats	446
A.S. Myerson - Statistical Studies of Heterogeneous and Homogeneous Nucleation	447
Robert J. Naumann - Reduction of Convection in Closed Tube Vapor Growth Experiments	449
A.G. Ostrogorsky - Space- and Ground-based Crystal Growth Using a Baffle (CGB)	451

J.H. Perepezko - Analysis of Containerless Solidification Microstructures in Undercooled Melts and Composite Systems	458
L.S. Pinsky - Development of a Space Radiation Monte-Carlo Computer Simulation Based on the FLUKA and ROOT Codes	465
D.R. Poirier - Comparison of Structure and Segregation in Alloys Directionally Solidified in Terrestrial and Microgravity Environments	471
John A. Pojman - Frontal Polymerization in Microgravity: Bubble Behavior and Convection on the KC-135 Aircraft	477
Research Reports: Section III	483
Miriam H. Rafailovich - Microgravity Processing of Polymer Thin Films	483
Liya L. Regel - Improved Crystal Quality by Detached Solidification in Microgravity	487
Won-Kyu Rhim - Measurements of Thermophysical Properties of Molten Silicon and Germanium	493
E.E. Rice - Carbon-Based Reduction of Lunar Regolith (CRLR)	499
G.S. Rohrer - Shape Change Kinetics of Faceted Crystals	505
P.D. Ronney - Extinction and Instability Mechanisms of Polymerization Fronts	510
T.P. Russell - Capillary Waves at Interfaces: the Role of Gravity and Electric Fields	516
A. Sacco, Jr. - Particle-Fluid Dynamics Under Variable Gravity Conditions	517
S.S. Sadhal - Non-Intrusive Measurement of Thermophysical Properties of Liquids by Electrostatic-Acoustic Hybrid Levitation	519
Donald R. Sadoway - From Oxygen Generation to Metals Production: in Situ Resource Utilization by Molten Oxide Electrolysis	525
Robert Schaefer - Thermophysical Properties of High Temperature Liquid Metals and Alloys	531
Robert F. Sekerka - Lattice Boltzmann Computations of Binary Diffusion in Liquids under Stochastic Microgravity	533
A.J. Sievers - Influence of Processing on the Dynamical Properties of Glassy Networks	539
Jogender Singh: Gravitational Effects on the Weld Pool Geometry During Gas Tungsten Arc and Laser Welding ..	543
N.B. Singh - Flight Experiment to Study Double-Diffusive Instabilities in Silver-Doped Lead Bromide Crystals	548
K.R. Sridhar - The Effect of Doping on the Ion Conductivity and Bi-axial Flexural Strength of YSZ Solid Oxide Electrolyzers	551
D.M. Stefanescu - Particle Engulfment and Pushing by Solidifying Interfaces	556
Ching-Hua Su - Structural Fluctuations and Thermophysical Properties of Molten II-VI Compounds	562
Ching-Hua Su - Crystal Growth of ZnSe and Related Ternary Compound Semiconductors by Vapor Transport	568
F.R. Szofran - Reduction of Defects in Germanium-Silicon	573
Daniel R. Talham - The Features of Self-Assembling Organic Bilayers Important to the Formation of Anisotropic Inorganic Materials in Microgravity Conditions	580
Padetha Tin - Interfacial Energy Determination of Succinonitrile and Succinonitrile-Acetone Alloy Using Surface Light Scattering Spectrometer	585
R. Trivedi - Interface Pattern Selection in Directional Solidification	586
R. Trivedi - Dynamical Selection of Three-Dimensional Pattern in Directional Solidification	593
James D. Trolinger - SHIVA: (Spaceflight Holography Investigation in a Virtual Apparatus)	599
M. Tsapatsis - Growth Studies of Silicalite-1 Crystals and Thin Films	608
P.W. Voorhees - Coarsening in Solid-Liquid Mixtures	614
John S. Walker - Modelling the Effects of Magnetic Fields in Crystal Growth	619
Richard Weber - Process-Property-Structure Relationships in Complex Oxide Melts	624
Richard Weber - Microgravity Studies of Liquid-Liquid Phase Transitions in Undercooled Alumina-Yttria Melts ..	630
J.B. Whitehead, Jr. - Polymer Dispersions: A Ground-Based Feasibility Study for Microgravity	637

William R. Wilcox - Residual Gas Effects on Detached Solidification in Microgravity	638
William R. Wilcox - Use of Microgravity to Control the Microstructure of Eutectics	643
J.W. Wilson - Improved Spacecraft Materials for Radiation Protection Shield Materials Optimization and Testing	648
A.F. Witt - Identification and Control of Gravity Related Defect Formation During Melt Growth of Electro-optic Single Crystals: Sillenites, Bismuth silicate ($\text{Bi}_{12}\text{SiO}_{20}$)	656
N. Zabaras - On the Control of the Effects of Gravity on Solidification Microstructures Using Optimally Designed Boundary Heat Fluxes and Electromagnetic Fields	658
C. Zeitlin - Measurement of Charged Particle Interactions in Spacecraft and Planetary Habitat Shielding Materials	664
M.Ittu Zugrav - Ground Based Experiments in Support of Microgravity Research Results - Vapor Growth of Organic Nonlinear Optical Thin Film	666
 Appendix A: Author Index	 672
Appendix B: Acronyms and Abbreviations	676
Appendix C: Contributor Address List	683

MICROGRAVITY PROCESSING OF POLYMER THIN FILMS

Miriam H. Rafailovich

SUNY-Stony Brook

PREAMBLE

The official starting date for funding the period corresponding to this proposal (submitted for the NRA-99-HEDS-02 announcement) has not yet been established. The initial proposal involved studying the combined effects of micro-gravity and surface interactions on stabilization of thin films. The initial proposal was scaled back to include only ground based experiments during this funding period. Hence we chose to concentrate on obtaining a fundamental understanding of the effects of surface interactions on the polymer thin film dewetting. The effects of gravity can be decoupled from those of the surface interactions by using films that are thin enough, so that the gravitational influence is negligible in comparison to the surface interaction. Since the funding period has not officially begun, we describe in this report some preliminary experiments that are in progress which should help us establish the direction of the funded research that is expected to commence this summer.

I. Introduction

Polymeric materials are often reinforced with inorganic fillers in order to enhance such properties as mechanical toughness, thermal degradation, and UV and other radiation stability. Even though a great deal of research has been done on the bulk materials, little is known about the effects of fillers on the stability of thin films. In the past our group has done extensive research on dewetting of polymer bilayers near inorganic planar interfaces¹⁻³. We would like to extend our knowledge of interfacial properties to the study of fillers where the interfaces are more complex. The main questions we then wish to answer are:

- (1) What is the effect of the filler on polymer chain dynamics and hence film viscosity?
- (2) Can we control film stability by varying the interaction at the interface between the polymer matrix and the filler?

II. Experimental Procedure

Alkane thiol functionalized gold particles were synthesized using a novel one phase method described in reference 1. The mean diameter of the particles, as determined by TEM was 8.5nm. The Au was introduced into the polymer films by mixing a fixed weight percentage in the toluene/polymer solution used for spin casting.

A film, 250Å thick, of monodisperse polymethylmethacrylate (PMMA) of $M_w=125K$ was spun cast from toluene solution onto a native oxide covered Si wafer. Two other thin films (260Å thick) of monodisperse polystyrene ($M_w=127K$), one containing gold particles and the other without gold were

floated onto different section of the substrate. The sample was then annealed at 165°C in a vacuum of 10^{-3} Torr for various times. The diameter of the dewetting holes in the PS layer was recorded as a function of time using an optical microscope.

III. Results and Discussion

PS and PMMA are highly immiscible polymers. When bilayer films of the two polymer are prepared, they dewet each other upon annealing due to the large interfacial tension (approximately 2 dyne/cm) between the polymers⁵.

Figure 1 shows a typical sample after annealing for 10 hours. From the figure we can clearly see that the film with the gold particles dewets much faster than the film without the particles. In figure 2 we plot the diameter of the holes as a function of annealing time. From the figure we can see that the dewetting velocity increases monotonically with Au concentration. Similar results were also obtained for free standing PS films.

In a previous publication⁴ we have shown that the dewetting velocity was a good indicator of the film viscosity when the viscosity was lower than that of the substrate. We were able to show that the dewetting velocity had the same scaling ($V \sim Mw^{-3.4}$) as the viscosity when the molecular weight of the film was high enough for the melt to be entangled. Hence from these results we can conclude that the filler are in some way changing the viscosity of the film.

We can at this point only speculate on the mechanism. If the particles are non interacting then their presence serves only to disturb the entangled network of the blend. Decreasing the entanglement density would increase the viscosity. If the particles interacted favorably with the matrix then the viscosity would be increased.

IV. Future Work

In order to prove our model we must:

- (1) Determine the dependence of the dewetting velocity on the molecular weight of the PS film. If the scaling deviates from that observed in reference 4 then the chain dynamics are no longer determined by the reptation model. Determination of the exact scaling relationship will enable us to derive a model for the dynamics in the presence of obstacles.
- (2) Vary the functional groups on the Au particles in order to determine the effect of the interactions between the particles and the matrix. As described in reference 1, it is fairly straightforward to attach different functional groups to the thiol chains.

REFERENCES

1. Novel One-Phase Synthesis of Thiol-Functionalized Gold, Palladium, and Iridium Phase Segregation in Polymer Thin Films: Elucidations by X-ray and Scanning Force Microscopy, H. Ade, D.A. Winesett, A.P. Smith, S. Qu, S. Ge, J. Sokolov, and M.H. Rafailovich, *Europhys. Lett*, 45, 526 (1999).
2. Phase Segregation in Polymer Thin Films: Elucidations by X-ray and Scanning Force Microscopy, H. Ade, D.A. Winesett, A.P. Smith, S. Qu, S. Ge, J. Sokolov, and M.H. Rafailovich, *Europhys. Lett*, 45, 526 (1999).

3. Bulk and Surface Characterization of a Dewetting Thin Film Polymer Bilayer, S. Anders, T. Stammeler, H. Ade, D. Slep, J. Sokolov, M. Rafailovich, J. Stohr, *Appl. Phys. Lett.* 73, 3775 (1998).
4. Dewetting dynamics at a polymer-polymer interface, S. Qu, C.J. Clarke, Y. Liu, M.H. Rafailovich, J. Sokolov, K.C. Phelan, and G. Krausch, *Macromolecules*, 30, 3640-3645 (1997).
5. Compatibilizing A/B blends with AB diblock copolymers: effect of copolymer molecular weight, R. Israels, D. Jasnow, A. Balasz, L. Guo, J. Sokolov, M.H. Rafailovich, and G. Krausch, *J. Chem. Phys.* 102, 8149 (1995).

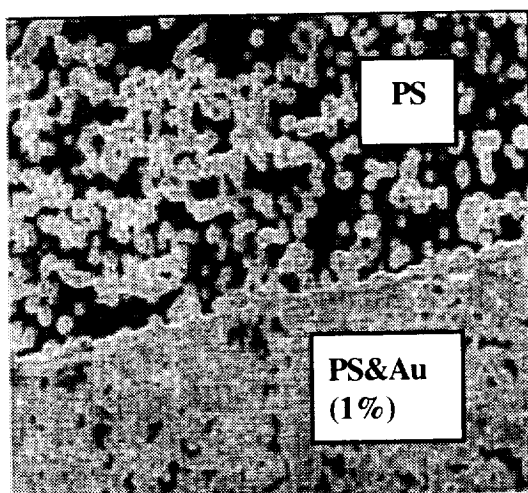


Figure 1. Optical microscope view of the PS overlayer on the PMMA substrate after annealing for 10 hrs. at 165°C.

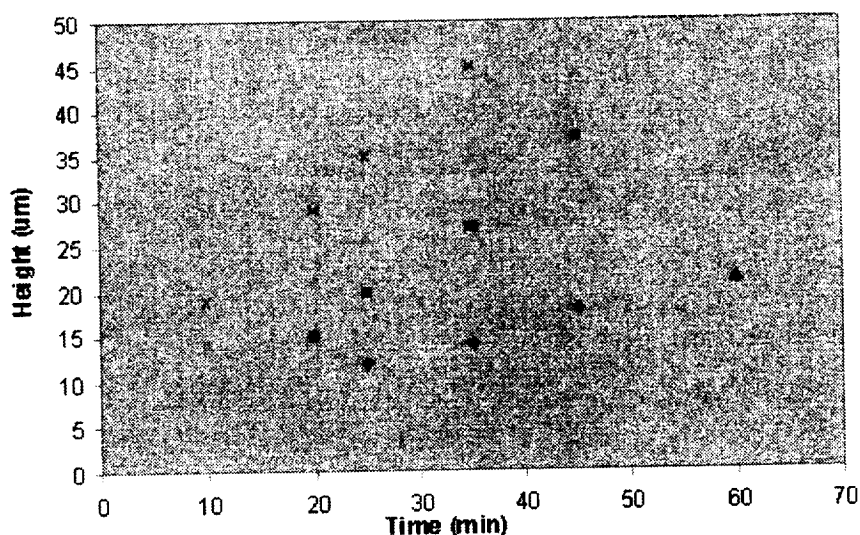


Figure 2. Diameter vs time of the dewetting holes in the PS films shown in Figure 1.

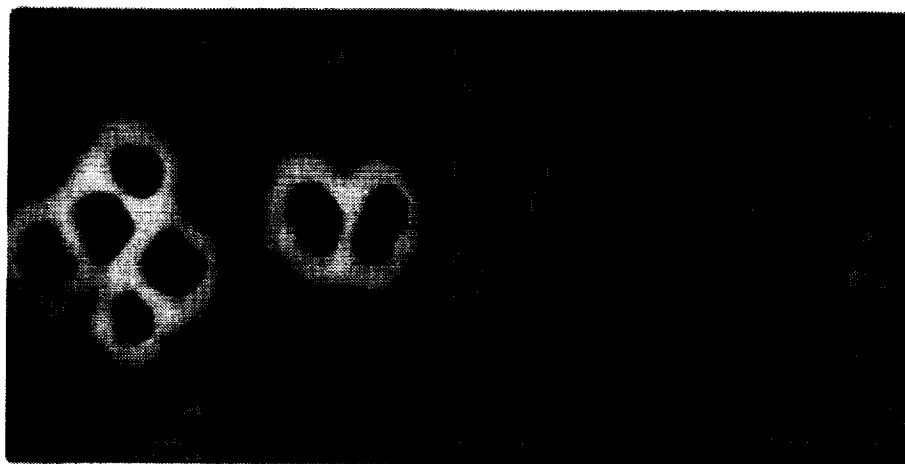


Figure 3. AFM topography and friction micrograph of the sample in Figure 1 after only 0.5 hour anneal. From the friction scan one can see that each hole is nucleated around an Au particle cluster. The scale on the figures is 5 microns.

IMPROVED CRYSTAL QUALITY BY DETACHED SOLIDIFICATION IN MICROGRAVITY

Liya L. Regel, William R. Wilcox, Yazhen Wang and Craig Burkhard

Clarkson University, Potsdam, NY 13699-5814

“Detached solidification” is the term we use to describe the situation where the growing solid is not in intimate contact with the ampoule wall. Detachment has very often been observed in microgravity experiments [1], including full detachment in which the growth interface nowhere contacts the ampoule wall. The flight experiments have been explained by the Moving Meniscus Model [2-8; see reference 9], in which a liquid meniscus is between the periphery of the growth interface and the ampoule wall. As freezing proceeds down the ampoule, the liquid meniscus is forced to move along the wall. The melt itself remains in contact with the ampoule wall while there is a gap between the solid and the wall. This gap is filled with a gas which was dissolved in the melt and segregated out by the growing solid. This is equivalent to a gas bubble surrounding (or partially surrounding) the periphery of the growth interface.

Our long term goals are:

- To develop a complete understanding of all of the phenomena of detached solidification.
- To make it possible to achieve detached solidification reproducibly.
- To increase crystallographic perfection through detached solidification.

The objectives of the current grant are to:

- Further develop our theoretical model in order to provide understanding and guidance for achievement of detached solidification in microgravity experiments.
- Develop a low-melting, transparent system that can be used to observe detached solidification as it occurs, along with convection in the melt.
- Observe bubble formation and interaction with the freezing interface.
- Attempt to achieve detached solidification on earth.

We summarized and correlated the observations of detached solidification in microgravity [1]. Additional numerical solutions of the Moving Meniscus Model showed that in order for steady-state detached solidification to occur in a sealed ampoule under zero gravity, it is necessary for the growth angle to exceed a critical value (all other operating parameters held constant), the contact angle for the melt on the ampoule wall to exceed a critical value, and the melt-gas surface tension to be below a critical value [5]. These critical values depend on the material properties and the other growth parameters. For InSb under the conditions assumed, the sum of the growth angle and the contact angle must exceed approximately 130° , which is significantly less than required if both ends of the ampoule are open. Calculations were also performed for freezing of water, as illustrated in Figure 1. The influence on detachment of freezing rate, gas pressure above the melt, temperature of the hot zone, and gas solubility are similar to these for InSb. That means that, under

proper conditions, it should be possible to achieve steady-state detachment of non-semiconductor materials such as water under zero gravity. A simple analytical solution was obtained using a material balance with the Moving Meniscus Model. It replicates many of the predictions obtained numerically.

Coatings were developed for the interior of Pyrex ampoules that greatly increased the contact angle for water beyond anything reported in the literature. These have proven useful in the detached experiments described below.

A large number of vertical Bridgman experiments were performed on water containing dissolved gases and different coatings on the ampoule wall. We can reproducibly produce large numbers of voids on the ampoule wall, although full detachment has not yet been achieved. The most interesting observation is the formation of vertical periodic gas tubes around the wall, as illustrated in Figures 2 and 3. The formation and growth of gas bubbles and tubes was favored by a large contact angle of water on the ampoule wall. There was an optimal range of freezing rates and an optimal range for temperature difference between the heater and refrigerated bath. Increasing the concentration of dissolved gas yielded larger gas bubbles and tubes. Longer gas tubes were produced when the ampoule was not rotated. For given conditions the gas tube spacing was approximately inversely proportional to the freezing rate, as shown in Figure 4. Flow visualization studies showed that the convection patterns near the freezing interface, as illustrated in Figure 5, are the reverse of those observed experimentally and theoretically in systems that do not display a maximum in liquid density near the freezing temperature. A rough polyfluoro coating caused by mixing in solid particles resulted in a contact angle for water of approximately 170° , resulting in nearly complete detachment (*e.g.*, Figure 6).

Naphthalene was zone refined for use in detachment experiments. Periodic gas tubes often formed around the ampoule wall identical to those observed in ice (Figure 7). Gas tubes and occasional bubbles often nucleated at the wall when the solid audibly popped away from the ampoule wall.

We will continue our quest to achieve detached solidification on earth with transparent low-melting systems. We will determine the influence of operating conditions on bubble formation and propagation at the ampoule wall. We will further develop the Moving Meniscus Model to elucidate the nature of the bifurcation of solutions observed in both the numerical and simplified analytical solutions.

REFERENCES

1. L.L. Regel and W.R. Wilcox, "Detached Solidification in Microgravity: A Review," *Microgravity Sci. Technol.* **14**, 152-166 (1999).
2. D.I. Popov, L.L. Regel and W.R. Wilcox, "Detached Solidification: 1. Steady-State Results at Zero Gravity," *J. Mat. Synth. & Proc.* **5**, 283-297 (1997).
3. D.I. Popov, L.L. Regel and W.R. Wilcox, "Detached Solidification: 2. Stability," *J. Mat. Synth. & Proc.* **5**, 299-311 (1997).
4. D.I. Popov, L.L. Regel and W.R. Wilcox, "Detached Solidification: 3. Influence of Acceleration and Heat Transfer," *J. Mat. Synth. & Proc.* **5**, 313-336 (1997).
5. Y. Wang, L.L. Regel and W.R. Wilcox, "Influence of Contact Angle, Growth Angle and Melt Surface Tension on Detached Solidification of InSb," *J. Crystal Growth* **209**, 175-180 (2000).

6. L.L. Regel and W.R. Wilcox, "Detached Solidification," Proceedings of the First Pan Pacific Basin Workshop on Microgravity Sciences, J. Jap. Soc. Microgravity Appl. 15 (1998) 460-465.
7. L.L. Regel and W.R. Wilcox, "Improved Crystal Quality by Detached Solidification in Microgravity," Proceedings of the 1998 Microgravity Materials Science Conference, compiled by D.C. Gillies and D.E. McCauley, NASA/CP-1999-209092, Marshall Space Flight Center, pp 533-540 (1999).
8. L.L. Regel, W.R. Wilcox, Y. Wang, D. Popov and C. Burkhard, "Experimental and Theoretical Modeling of Detached Solidification," American Conference on Crystal Growth and Epitaxy, Tucson (August 1999).
9. Liya L. Regel and W.R. Wilcox, "Residual Gas Effects on Detailed Solidification in Microgravity," Proceedings of the 2000 NASA Microgravity Materials Science Conference, N. Bennett, D. McCauley, K. Murphy, S. Poindexter, and N. Ramachandran, compilers, in press (2001)

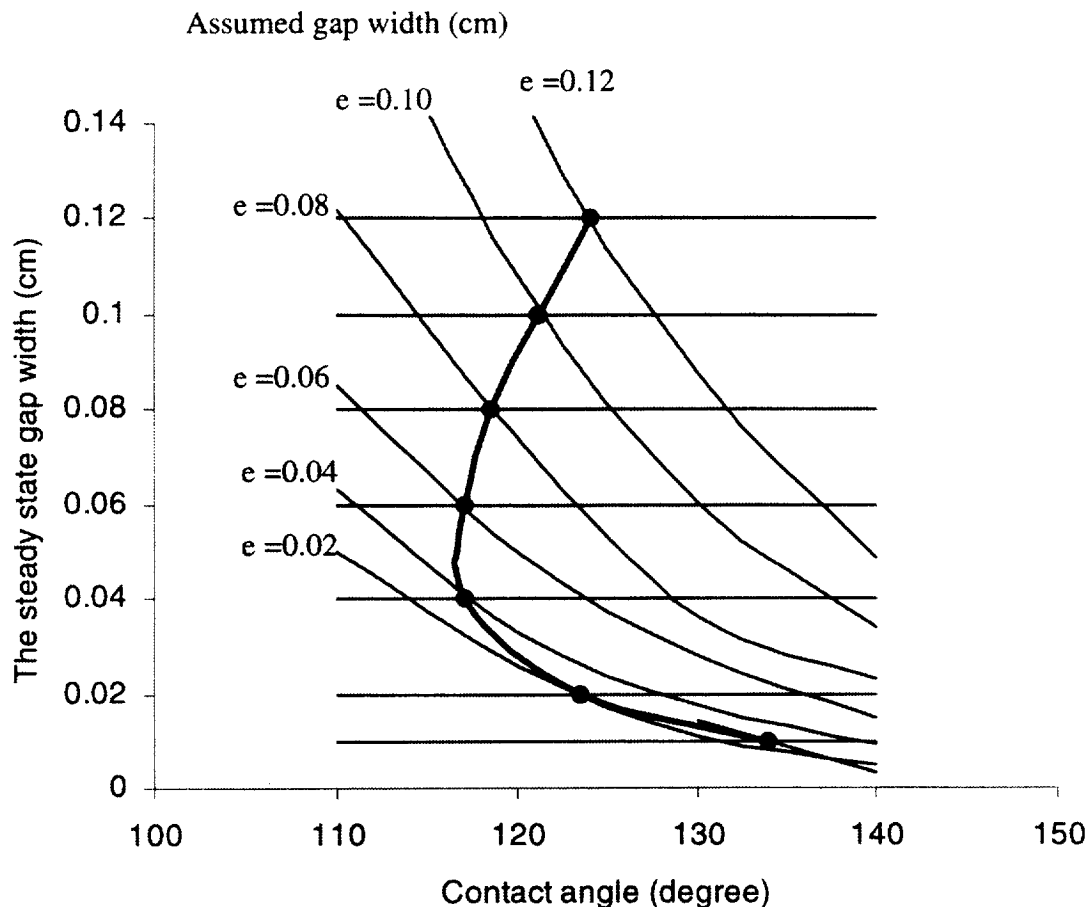


Figure 1. The dependence on the contact angle of the water on the ampoule wall of the computed steady state gap width using the Moving Meniscus Model [2-5]. The light curves are for assumed gap widths. The dark curve represents the solution, and connects points for which the calculated gap width equals the assumed gap width.



Figure 2. Periodic growth of gas tubes on the ampoule wall during freezing of water. The water was saturated with air at 1 atm and the ampoule was coated with Teflon. 20mm/hr freezing rate, -20°C cold bath temperature, 40°C heater temperature, no ampoule rotation.



Figure 3. Cross section of ice sample with gas tubes on the wall. The water was saturated with air at 1 atm and the ampoule was coated with Teflon. 20mm/hr freezing rate, -20°C cold bath temperature, 40°C heater temperature, and no ampoule rotation. Composite of two photographs taken after ampoule removal.

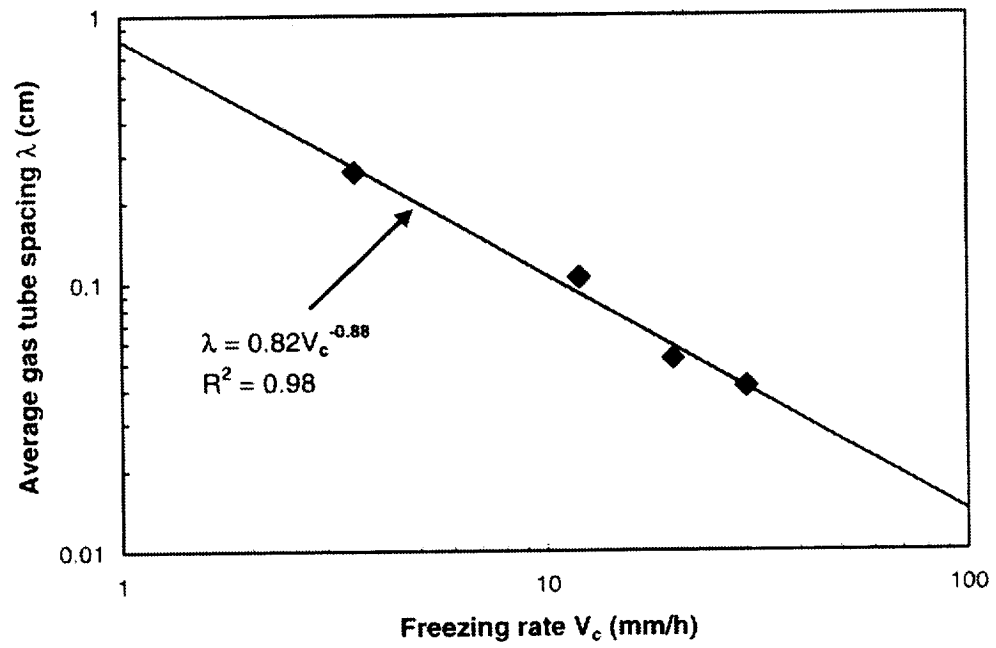


Figure 4. Average spacing of gas tubes versus ice freezing rate.

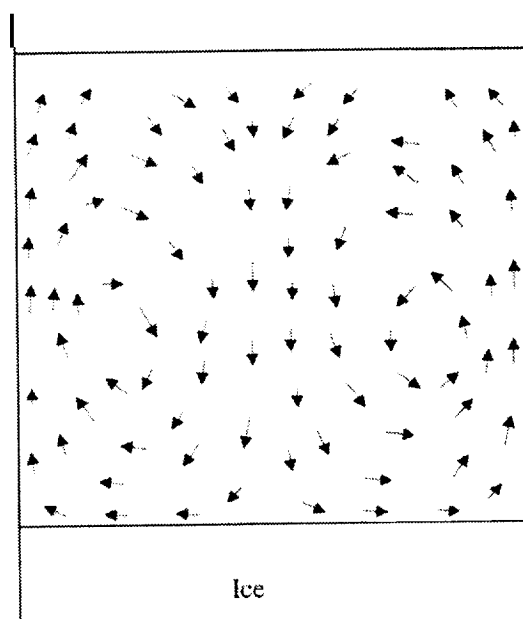


Figure 5. Convection in water with a nearly planar freezing interface.



Figure 6. Nearly complete detachment of ice caused by coating with a fluorinated polymer with powder dispersed in it. Composite of several photographs taken with ampoule in place. 12 mm/hr freezing rate.

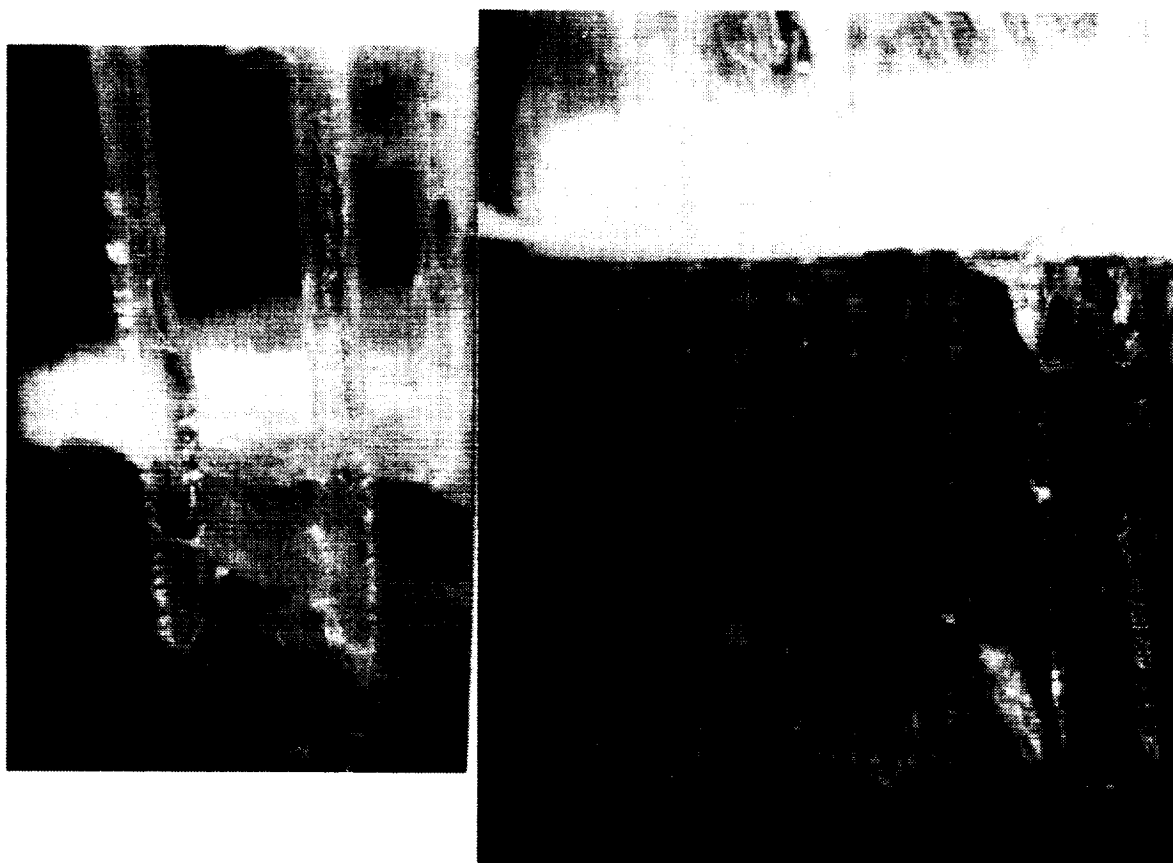


Figure 7. Gas tubes formed at the ampoule wall during zone refining of naphthalene.

MEASUREMENTS OF THERMOPHYSICAL PROPERTIES OF MOLTEN SILICON AND GERMANIUM

Won-Kyu Rhim

Jet Propulsion Laboratory, California Institute of Technology
4800 Oak Grove Drive, Pasadena, CA 91109

The objective of this ground base program is to measure thermophysical properties of molten/undercooled silicon, germanium, and Si-Ge alloys using a high temperature electrostatic levitator and in clearly assessing the need of the microgravity environment to achieve the objective with higher degrees of accuracy. Silicon and germanium are two of the most important semiconductors for industrial applications: silicon is unsurpassed as a microelectronics material, occupying more than 95% of the electronics market. Si-Ge alloy is attracting keen interest for advanced electronic and optoelectronic applications in view of its variable band gap and lattice parameter depending upon its composition. Accurate thermophysical properties of these materials are very much needed in the semiconductor industry for the growth of large high quality crystals.

Over the past ten years, there have been several organized efforts both in the United States and Japan on measuring accurate thermophysical properties of molten silicon using various techniques. However, the reported thermophysical properties have failed to show a converging trend. The gravity field could have directly or indirectly affected the property measurements. Molten silicon and germanium are highly reactive with most crucibles. When certain containers were used in a measurement process, the measured properties of the melt showed strong dependence on the container materials. If chemical reactions took place during property measurements, one could not have avoided the effects of contamination to the experimental results. Also, a certain physical property can affect the final results. For example, the conventional oscillating cup method for viscosity measurements relies on the wetting property of a melt with crucible. If the wetting property is such that a physical slip takes place at the interface, the resulting viscosity would be erroneous. Containerless approach alleviates sample contamination problems by isolating melts from containers. However, levitation experiments conducted in the strong gravitational field suffered from other kinds of problems which are physical in nature. Sample levitation on the ground base is achieved by applying a strong levitation force to sample against the gravity. Strong levitation forces tend to generate internal flows as well as vibrational and rotational instabilities on a drop. These undesirable instabilities can contribute to increased uncertainties in measurement results. Molten silicon and germanium have viscosity in the range of 1 mPa·s. Transport properties of such low viscosity liquids can be readily affected by the external perturbation forces. These problems, however, may be greatly reduced by conducting experiments in the low-g environment where the perturbation forces originating from the sample levitation can be reduced by several orders of magnitude.

Until NASA finds it appropriate to redesignate this program as a flight definition program, this research project will be devoted to conducting the following ground based experiments:

- (i) Investigation of the effect of low pressure hydrogen gas to reduce surface oxides and to produce deeply undercooled states of molten germanium. If successful, measurements of all the Thermophysical properties of undercooled germanium will be attempted. The properties that will be measured include:
 - Density
 - Thermal expansion coefficient
 - Surface tension
 - Viscosity
 - Specific Heat/Hemispherical total emissivity
 - Electrical conductivity
 - Thermal Conductivity
- (ii) To measure thermophysical properties of Si-Ge alloys of varied composition. Thermophysical properties that will be measured will basically include most of the properties listed in (i). All these properties will be measured as a function of true temperatures. The high temperature electrostatic levitator (HTESL) at JPL and, if necessary, a similar levitation system available at the Marshall Space Flight Center (MSFC) will be used for this work.
- (iii) Measurements of surface tension and viscosity of molten silicon, germanium, and various $\text{Si}_x\text{Ge}_{1-x}$ alloys will be conducted under conditions where the sample rotation is strictly controlled.
- (iv) Develop a high resolution/high speed linear video imaging device that can detect sample size and drop oscillation amplitude with greater accuracy.

I. Progress of the Research

Progress has been made in thermophysical property measurements of molten silicon and germanium using the high temperature electrostatic levitator (HTESL) at JPL [1, 2]. In molten silicon, the density, the ratio between the specific heat and the hemispherical total emissivity, the surface tension, and the viscosity have been measured [3]. These results are unique in themselves since no other techniques would have been able to produce such results that spanned a temperature range that included 300K of undercooled state.

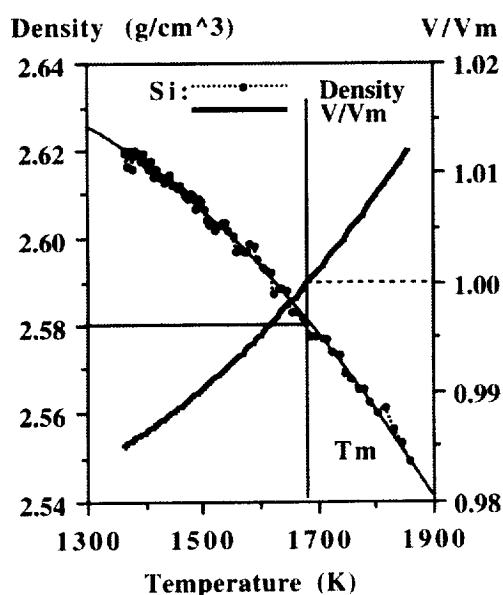


Figure 1. Density of molten silicon.

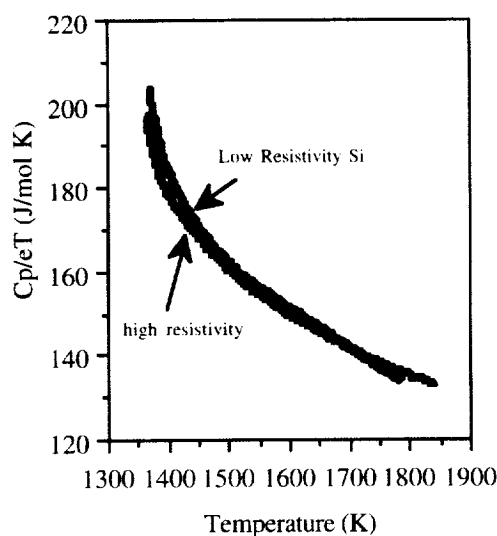


Figure 2. C_p/ϵ_T vs. temperature of molten Si.

The earlier observations of quadratic nature [3, 4] of liquid silicon density was confirmed, showing that a certain short range orders is taking place as the liquid undercooled. Figure 1 shows our recent density data on a high purity silicon showing such a quadratic behavior. Also shown in the figure is the volume changes that were normalized with respect to the sample volume at the melting temperature. The nonlinear behavior of specific heat has also been observed (see the Figure 2). Again, the formation of short range order must be related to such behavior. When we used the literature value $C_p(T_m) = 25.61 \text{ J/mol/K}$, the hemispherical total emissivity that could be determined from Figure 2 was $\epsilon_T = 0.183$, again showing a good agreement with our previous result $\epsilon_T = 0.18$ [3].

All that was needed to measure the density and the C_p/ϵ_T with reasonable accuracy was the position stability of the drop that could be met rather easily both in molten silicon and in germanium. However, for those properties which require dynamic responses of the drop, a greater care may be required since they are much more susceptible to any vibrational and rotational instabilities of the drop. Surface tension and viscosity are the two properties that belong to this case. Figure 3 and Figure 4 respectively show the surface tension and the viscosity of a pure silicon, and they are compared with the data by Kimura *et al.* [6]. However, during the measurements the sample rotation which set in during the sample heating process could not be controlled. Since the drop resonance frequency depends on the rotation rate according to Busse[7], the reliability of the data as shown in Figure 3 are in doubt. The viscosity data which depended on the decay time constants of freely oscillating drops also showed a wide scatter. Unless the drop oscillated freely in a true sense, the decay time constants extracted from the free decay curves would be affected by the perturbing forces, producing erroneous viscosity data. Such effect will appear greater in lower viscosity liquids. In the case of the HTESL, probably the strongest external perturbation comes from the position controlling electrostatic forces that is needed to keep the drop levitated against the 1-g.

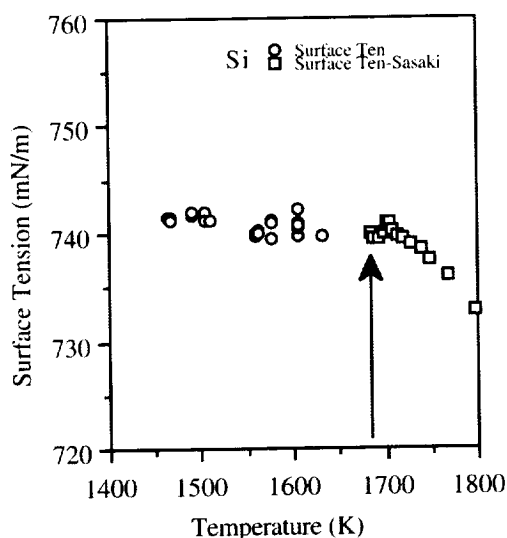


Figure 3. Surface tension of molten silicon.

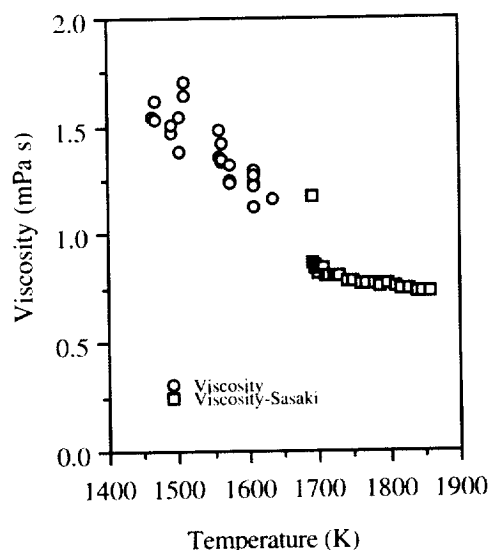


Figure 4. Viscosity of molten silicon.

Pure germanium was melted and the density, the ratio of heat capacity to hemispherical total emissivity, the surface tension, and the viscosity were measured [8]. Although the drop temperature was raised to $\sim 200 \text{ K}$ above the melting temperature, germanium undercooled less than 100 K . Probably it was necessary to dissolve the remaining impurity particles by further superheating the

sample or to reduce oxides by bleeding some hydrogen into the chamber in the future work. Temperature dependence of the electrical resistivity of molten germanium was measured using the newly developed non-contact method for electrical resistivity [9]. This method was based on the fact that electrical conductivity of the rotor in an induction motor was proportional to the torque when all other parameters were kept fixed. From the measured resistivity, the thermal conductivity of germanium was determined using the Wiedemann-Franz-Lorenz relationship.

Figure 5 and Figure 6 respectively show the density and the specific heat of molten germanium. The measured liquid germanium density could be expressed by $\rho_{\text{liq.}} = 5.67 \times 10^{-3} - 0.542 (T - T_m)$ Kg m^{-3} with $T_m = 1211.3$ K, the volume expansion coefficient by $\alpha = 0.9656 \times 10^{-4} \text{ K}^{-1}$, and the hemispherical total emissivity at the melting temperature by $\epsilon_{T,\text{liq.}}(T_m) = 0.17$. Assuming constant $\epsilon_{T,\text{liq.}}(T) = 0.17$ in the relevant liquid temperature range, the constant pressure specific heat was evaluated as a function of temperature.

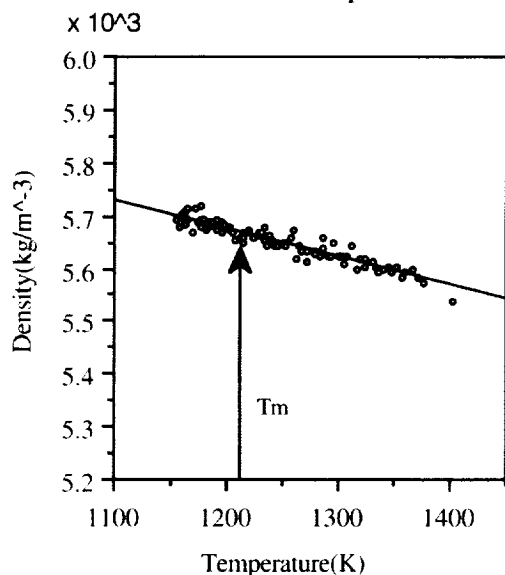


Figure 5. Density of molten Ge vs. temperature.

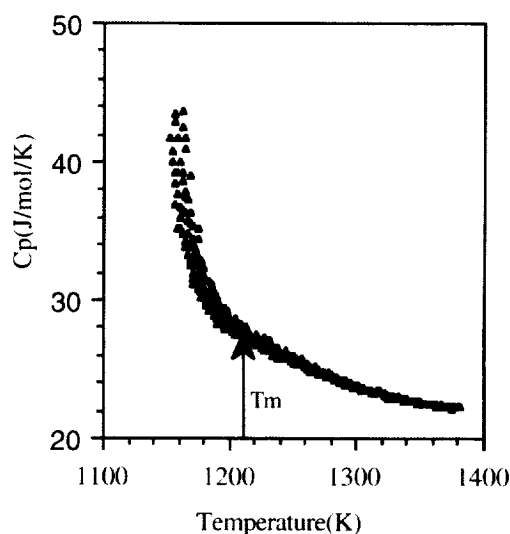


Figure 6. Cp of molten germanium.

Figure 7 and Figure 8 respectively show the surface tension and the viscosity of molten germanium. The surface tension data could be expressed by $\sigma(T) = 583 - 0.08 (T - T_m) \text{ mN m}^{-1}$. These data were obtained giving a greater care on the rotational state of the drop. As a result, these data may be reliable than the silicon data shown in Figure 3. The viscosity data show unacceptably large scatter which were caused by the sample levitation control forces.

Temperature dependence of the electrical resistivity of molten germanium was measured using the newly developed non-contact method [9]. This method was based on the fact that electrical conductivity of the rotor in an induction motor was proportional to the torque when all other parameters remained fixed. From the measured resistivity, the thermal conductivity of germanium was determined using the Wiedemann-Franz-Lorenz relationship. Thermal conductivity is one of the transport properties of liquids which are susceptible to the convective flows in the liquid. Determination of thermal conductivity from the measured electrical conductivity may in fact result in a more accurate thermal conductivity than what can be obtained from the direct measurement in the 1-g environment. Figure 9 shows the electrical resistivity of the molten germanium. The experimental results could be fit by $r_{e,\text{liq.}}(T) = 60 + 1.18 \times 10^{-2} (T - 1211.3) \mu\Omega \cdot \text{cm}$. The thermal conductivity which was determined by the resistivity data according to the Wiedemann-Franz-Lorenz law

is shown in Figure 10, which could be expressed by $\kappa_{\text{liq}}(T) = 49.43 + 2.90 \times 10^{-2}(T - T_m)$ W/m/K. It would be interesting to see the validity of this result when the thermal conductivity of molten germanium is directly measured in the quiescent environment of space.

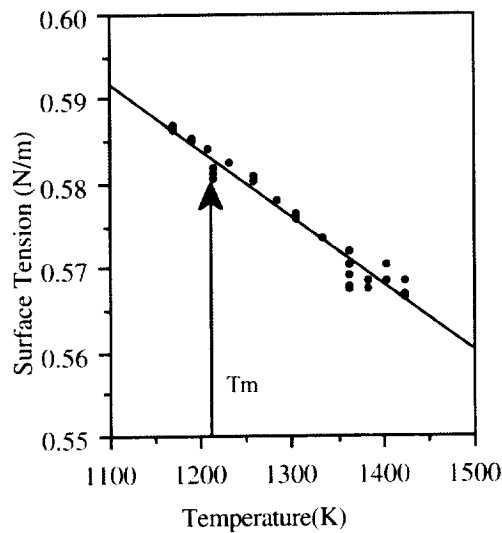


Figure 7. Surface tension of molten Ge.

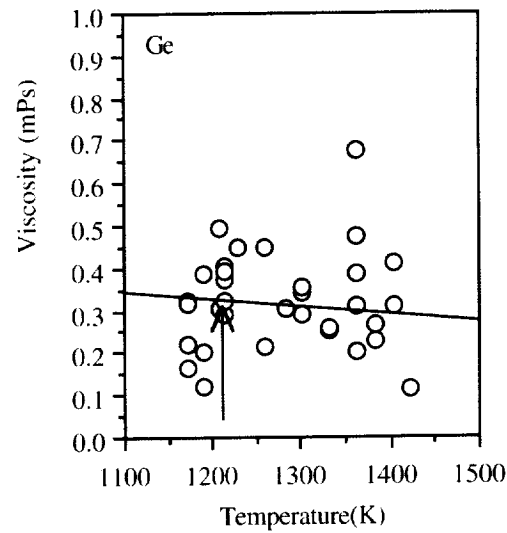


Figure 8. Viscosity of molten germanium.

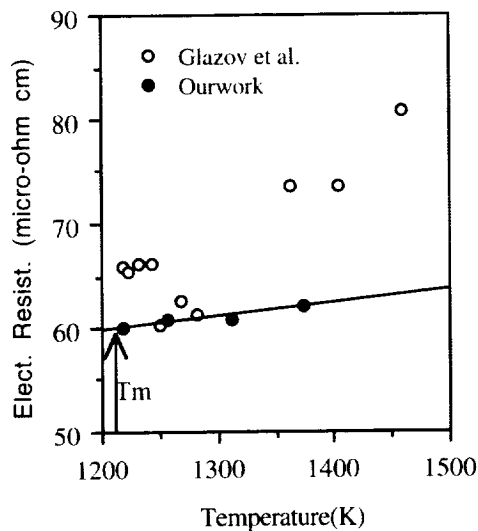


Figure 9. Electrical resistivity of molten Ge.

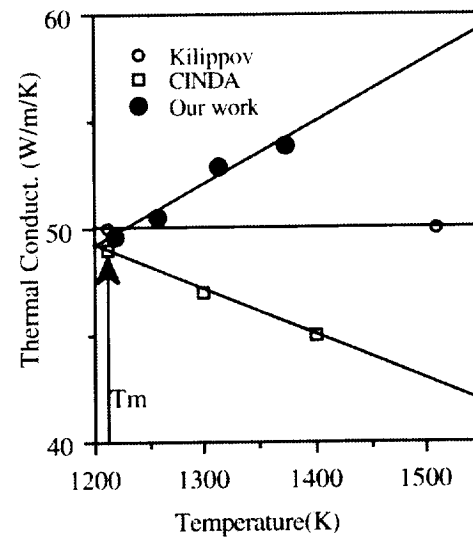


Figure 10. Thermal conductivity of Ge.

II. Gravity Effects

When containerless experiments are conducted in the 1-g environment, all gravity caused effects such as convection, sedimentation and buoyancy still remain in levitated melts. In addition, large forces needed to levitate a sample in the presence of gravity can cause additional flows in the melts. The lower the liquid viscosity is, the more susceptible the measured properties will be to the external perturbations. The most seriously affected by the perturbations will be those transport properties such as diffusion, viscosity, surface tension, and thermal conductivity. Our recent viscosity measurements using HTESL confirmed this.

Shown in Figure 11 and Figure 12 are respectively the viscosity of molten zirconium [2] and several molten Ni-Zr alloys [10]. (As far as we know this zirconium viscosity data is the first and

the only data of its kind, covering undercooled region as much as 300K). In contrast to Figure 4 and Figure 8, the scatter amplitudes are relatively small in comparison. On the basis of these different viscosity data, one can conclude that the HTESL in the 1-g condition can measure the viscosity with better than 100% accuracy only of those liquids which have viscosity much larger than 1 mP-s. Clearly the HTESL failed to measure accurately the viscosity of both molten silicon and molten germanium in 1-g condition. However, such wide scatter on viscosity data may be reduced by orders of magnitude if measurements can be made in the microgravity environment.

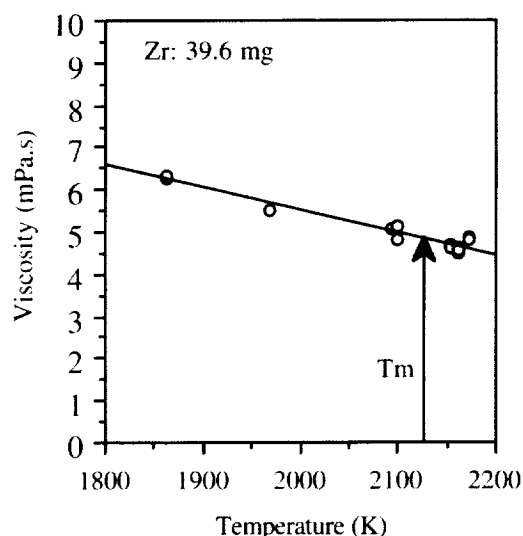


Figure 11. Viscosity of molten zirconium measured by the HTESL at JPL.

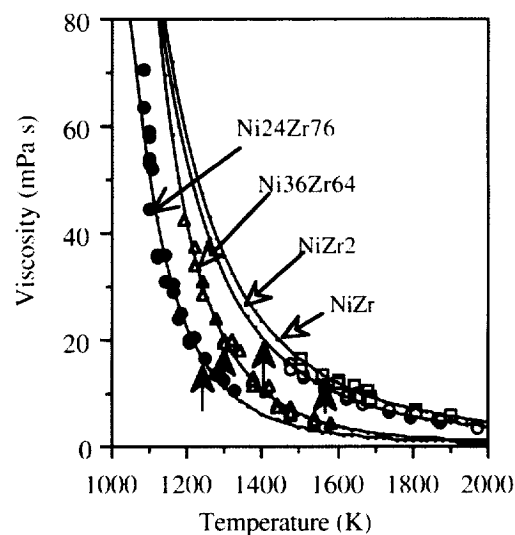


Figure 12. Viscosity of molten Ni-Zr alloys measured by the HTESL at JPL.

REFERENCES

1. W. K. Rhim, S. K. Chung, D. Barber, K. F. Man, Gary Gutt, A. Rulison, R. E. Spjut: *Rev.Sci. Instrum.* 64: 2961, 1993.
2. P-F. Paradis and W. K. Rhim: *J. Mat. Res.* 14, 3713, 1999.
3. W. K. Rhim and K. Ohsaka: *J. Crystal Growth* 208, 313-321, 2000.
4. W. K. Rhim, S. K. Chung, A. J. Rulison, and R. E. Spjut: *Int. J. Thermophysics* 18, 459, 1997.
5. K. Ohsaka, S. K. Chung, W. K. Rhim, and J. C. Holzer: *Appl. Phys. Lett.* 70, 423, 1997.
6. S. Kimura, K. Terashima: *J. Crystal Growth* 180, 323, 1997.
7. F. H. Busse: *J. Fluid Mech.* 142, 1, 1984.
8. W. K. Rhim and T. Ishikawa: *Int. J. Thermophysics* (accepted)
9. W. K. Rhim and T. Ishikawa: *Rev. Sci. Instrum.* 69, 3628-3633, 1998.
10. K. Ohsaka, S. K. Chung, and W. K. Rhim, *Acta Materialia* 46, 4535-4542, 1998.

CARBON-BASED REDUCTION OF LUNAR REGOLITH (CRLR)

E.E. Rice, R.J. Gustafson, and J. Jordan

Orbital Technologies Corporation (ORBITEC™)

INTRODUCTION

ORBITEC is developing a new high-temperature processing technique to produce oxygen and metals from lunar regolith via carbonaceous high-temperature reduction. The utility in this technique overcomes problematic issues inherent in traditional high-temperature processing methods that employ crucible-type containment vessels and hot-walled (i.e., resistance or inductive) furnaces. Crucible containment structures either crack from thermal and mechanical stress and/or react with the molten reaction mix, making it very unlikely that such a material could survive the repeated high-temperature thermal cycling in an economical LOX plant on the Moon. To enable *in situ* production of lunar oxygen, high-temperature reduction of lunar soil can be accomplished using a direct heating source, achieving high oxygen yield and high carbon (or hydrogen, depending on the reducing source) recovery. The direct heating approach uses the lunar regolith as its own insulative container (Figure 1). This approach allows extremely high processing temperatures (>2000 C) while eliminating the difficult requirement of developing a containment vessel that withstands these temperatures, is impervious to prolonged chemical attack, and is capable of thermal cycling. Reduction of regolith using this heating approach will provide NASA with a manageable, practical, and efficient technique for extracting oxygen from indigenous lunar resources for life support and propellant applications. In this effort, ORBITEC intends to demonstrate new techniques for achieving high oxygen yield and high carbon or hydrogen recovery. This will include developing integrated designs for both a production plant and a possible flight experiment on a NASA reduced-gravity aircraft.

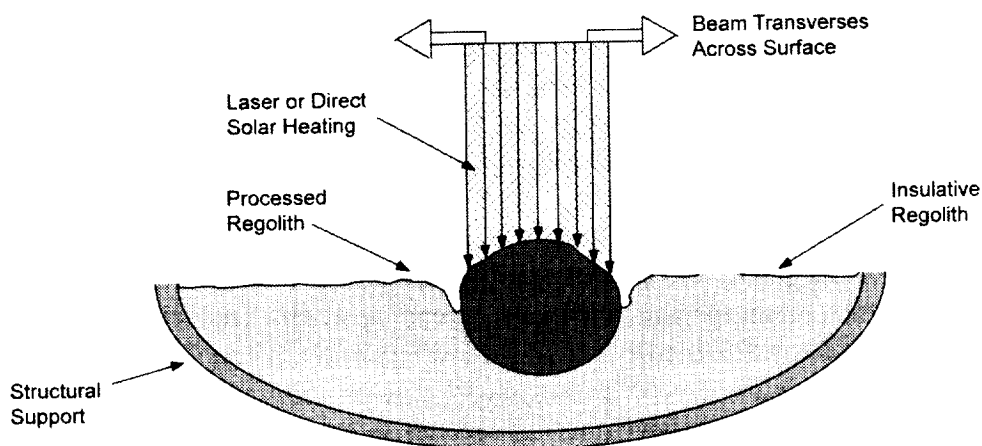


Figure 1. Lunar Regolith serves as an insulative "container."

I. Objectives

The primary objective of this effort is to demonstrate a practical and feasible technique for heating to $>2000^{\circ}\text{C}$ and the reduction of simulant by carbon and hydrogen, with very high recovery of carbon and hydrogen. This effort will look at both carbonaceous and hydrogen gas reduction of lunar simulant, focusing on the first step, in either case, in the overall production of oxygen from metallic oxides. Furthermore, efficient demonstration on the ground will provide the foundation for future flight experiment designs. Demonstration of a flight experiment in 1/6-g on a NASA parabolic aircraft would further substantiate development of a technology demonstration experiment on the Moon.

As part of these overall goals, the CRLR design and development effort is focused on these technical objectives:

1. Design, develop, and fabricate a test chamber in which laser heating of lunar simulant to temperatures greater than $\sim 2000^{\circ}\text{C}$ can be demonstrated
2. Determine temperature profiles, both experimentally and theoretically, within the regolith surrounding the processing zone, including transient and steady state behavior
3. Evaluate the effects of the new heating approach on regolith heating profiles
4. Demonstrate carbonaceous reduction of, at least, the silica, titania, and iron oxide components of lunar simulant using three separate reducing agents, including carbon-based agents and hydrogen gas, heating to temperatures greater than $\sim 2000^{\circ}\text{C}$
5. Develop a preliminary space flight experiment design that incorporates the new heating approach and is capable of acquiring samples from the lunar surface
6. Assess possible low-g processing tests in a 1/6-g environment using a NASA reduced gravity aircraft to study the effect of low-g on the process.

II. Relationship to Microgravity Research

It is envisioned that development of the proposed technique will ultimately lead to a scaled production plant on planetary surfaces, providing an indigenous source of oxygen for propulsion and life support and the production of useful metal and ceramic by products. Before a production plant can be fully realized, several demonstrations of the technology and concept must be made in the lunar environment. These demonstrations would most likely take the form of low-mass, low-power, experiment packages that would be part of an ISRU technology demonstration mission on the Moon that is envisioned by NASA and ORBITEC. However, the design of a space flight experiment package would require knowledge of the system's behavior and performance in the lunar environment. Certain aspects of the Moon's environment could be simulated in the laboratory, such as the temperature extremes and its vacuum-like atmosphere. Simulation of the reduced gravity, however, would require flight-time on a NASA parabolic aircraft. Modeling of the processes also needs to be verified by experiments in 1/6-g.

It is highly desirable to investigate the proposed concept in a 1/6-g environment. It is presently unknown how the 1/6-g gravity will affect the processed regolith. It is also unknown how the transport mechanisms of carbon-based agents or hydrogen (depending on which reducing agent is used) to the hot sample surface will be influenced by 1/6-g. The lower gravity environment may affect the rate at which the reducing agent transports or diffuses into the reactant material. ORBITEC has considered the test environments available and believes that ~ 20 seconds, or more, of 1/6-g is sufficient time to allow for heating of small amounts of lunar simulant material and subsequent reaction with either carbon-based agents or hydrogen gas.

III. Project Status

The ground-based experimental system has been designed, built, tested, and integrated. A functional diagram of the overall experimental system is shown in Figure 2. The experimental system includes an integrated reaction chamber, CO₂ laser equipment, laser beam rastering system, mass spectrometer, internal/external thermocouples, and the control computers. Software has been developed to operate the mass spectrometer, control the laser power, and perform data acquisition on a desktop computer. A 120 W CO₂ laser is used for direct heating for the lunar simulant. The laser system is cooled with a closed-loop water reservoir and the water chiller. The laser beam is reflected off a gold-plated mirror down into the reaction chamber. The position of the mirror can be changed through the computer-controlled laser mirror mount. This laser mirror mount allows full pan and tilt control of the mirror

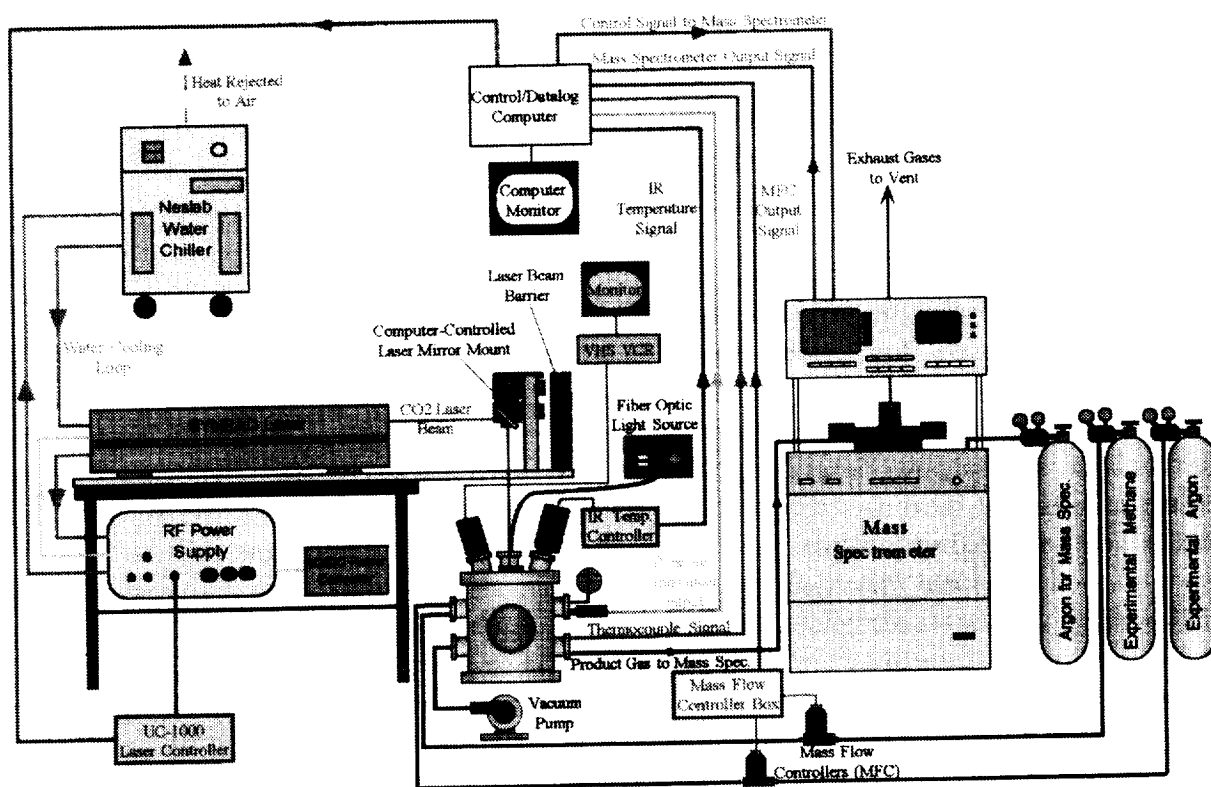


Figure 2. Functional diagram of the CRLR experimental system.

surface. A second computer is used to control the laser beam rastering system. The reflected laser energy enters the reaction chamber and is absorbed by the lunar simulant. The position and velocity of the laser beam on the surface of the simulant can be precisely controlled. A controlled flow of methane gas enters the reaction chamber and rapidly diffuses to the hot, molten simulant found near the laser beam. The methane will crack on the hot surface, allowing the carbon to dissolve into the melt. The carbon reduces the iron and silicon oxides, releasing carbon monoxide. Filtered images from the video camera are recorded during laser processing. Carbon monoxide and other product gases exit the chamber through a mass flow controller. After being sampled by the mass spectrometer, the gases are vented. The mass flow rate and chemical composition of the exhaust gases are calculated and recorded in the control computer for analysis. The software for the control computers allows the operator to select the power output level of the laser, command the position of the laser beam, operate the mass spectrometer, and record the output from the thermocouples, pressure transducer, IR thermometer, mass flow controllers, and the mass spectrometer.

An argon gas injection system was developed to keep the zinc selenide window in the reaction chamber clean during laser processing. In early experiments, a black powder formed on the laser window during reduction experiments. This powder appears to be carbon. Video images taken during the reduction experiments show particulates rising up from the melt. An argon gas flow is positioned near the laser window. The argon flow is intended to keep the window clean by preventing any particulates from accumulating on the window. Large argon flows ($>5,000$ sccm) did keep the window clean during reduction experiments. However, the higher argon flow reduces the sensitivity of the system to the smaller amount of carbon monoxide that is produced. An acrylic tube was then installed inside the processing chamber that extends from the laser window to several inches above the simulant. This tube creates a column of argon gas above the simulant melt that prevents any smoke or particulates from reaching the laser window. The addition of this tube did reduce the required argon flow rate down to $\sim 2,000$ sccm. In an effort to reduce the argon flow rate further, a small electric fan was placed inside the processing chamber. The fan blows gas across the melt and deflects the particulates away from the tube that extends up to the laser window. The fan has allowed the argon flow to be reduced below 1,000 sccm. This allows a higher resolution mass flow sensor to be used to measure the output flow. This improved the accuracy of carbon monoxide level readings. Rastering of the laser beam also allows a larger area of simulant to be processed at one time. This produces higher levels of carbon monoxide in the processing chamber.

Heat transfer models have been developed to predict the temperature gradients in the lunar simulant during laser processing. In addition to predicting the steady-state temperature profile, the model was used to predict the molten regolith bead size that would form as a function of the laser beam power. Several experiments were conducted to verify the results of this model. Lunar simulant was exposed at several different laser power levels for several minutes to establish steady-state conditions. When the laser was turned off, the molten regolith cooled and formed glassy black beads. These solid regolith beads were measured and compared with the results of the model. The experimental bead sizes showed good agreement with those predicted by the model. The experimental results were generally 10% smaller than the sizes predicted by the model. The results of this thermal model were used to select the type and sizing of a thermocouple array that will be used to experimentally measure the temperature of the lunar simulant (non-molten simulant outside the laser beam). Type K thermocouples were installed in the simulant to determine the surface temperature gradients present during laser processing.

Carbothermal reduction of the lunar simulant via laser processing has been demonstrated using two different methods. In the first case, carbon black was mixed directly in the lunar simulant. This mixture was placed inside the reaction chamber and laser heated in a pure argon gas environment. Analysis of the product gas showed the formation of carbon monoxide, indicating carbothermal reduction. The second method places simulant inside the reaction chamber in an argon gas environment. A small flow of methane gas is introduced near the surface of the simulant during laser processing. Analysis of the product gas showed the formation of carbon monoxide gas.

A series of carbothermal reduction experiments were performed using carbon black mixed into JSC-1 simulant. For each experiment, 20 g of carbon black was thoroughly mixed into 100 g of simulant. The simulant was heated with a stationary laser beam at $\sim 50\%$ maximum power. A small amount of carbon monoxide gas was produced in each case. A shiny black melt or dull gray melt was observed in every experiment. There were small pockets of a shiny metallic substance observed inside the melts. This

material is likely iron/silicon, but it has not yet been analyzed. Figure 3 shows a plot of the carbon monoxide flow rates observed during one of these experiments.

CO Flow Rate During Carbothermal Reduction (Carbon Mixed with JSC-1, Laser 50% Power)

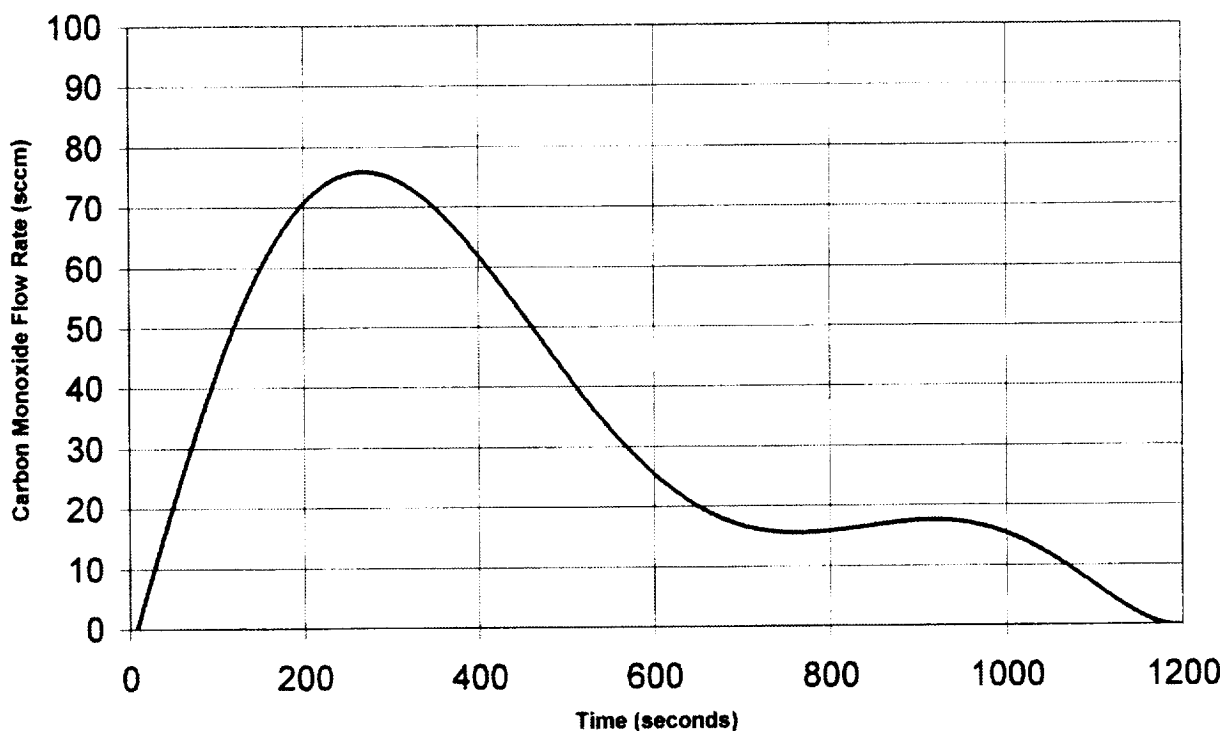


Figure 3. Carbon monoxide production during carbothermal reduction

Figure 4 shows a comparison of simulant that was reduced during the laser heating experiment with simulant that was simply melted in open air. The simulant that was melted in open air has a black, glassy appearance while the simulant that was processed in methane and argon gas has a dull, gray color. The shape of the melt in each case was very different. The simulant that was processed in the methane gas environment formed a pointed cone that appears to be growing towards the laser beam. This process is currently being studied in greater detail.

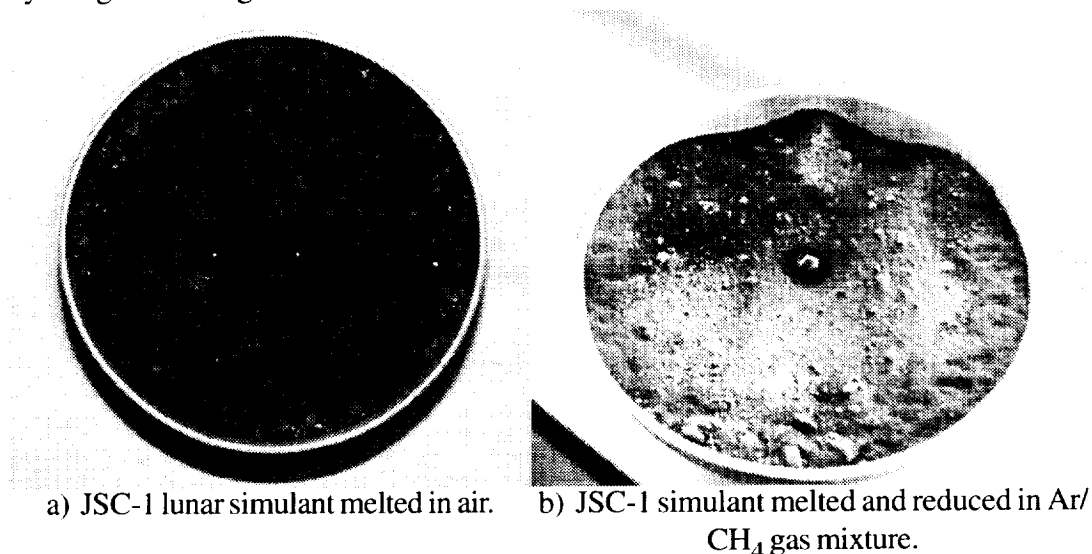


Figure 4. JSC-1 simulant melted in air and reduced in an argon/methane environment.

IV. Project Results to Date

- Developed a computer controlled laser beam rastering system to facilitate processing;
- Developed techniques to maintain a clean laser window during laser processing;
- Developed an experimental system that facilitates laser heating, melting, and processing of lunar simulant and analysis of the reaction products;
- Demonstrated carbothermal reduction of lunar simulant via laser processing in an argon and methane gas environment;
- Demonstrated carbothermal reduction of lunar simulant and carbon black mixture via laser processing in an argon gas environment;
- Developed a heat transfer model within the lunar simulant during laser heating;
- Verified the heat transfer model with experimental temperature measurements;

SHAPE CHANGE KINETICS OF FACETED CRYSTALS

W.W. Mullins and G.S. Rohrer

Department of Materials Science and Engineering
Carnegie Mellon University

When small ceramic particles facet, they reduce the driving force for sintering without necessarily increasing the density of the product. Predictive, quantitative models to relate the processing, structure, and properties of sintered bodies must include an accurate description of this phenomenon. The objective of this project, which is scheduled to begin in the near future, is to determine the minimum energy shapes for small crystallites and to determine the mechanism by which they reach this shape.

We argue that for a fully-faceted dislocation-free particle (of constant volume) to change shape, the required surface steps will not be present. We begin our argument by noting that the nucleation of new steps on a facet at the small chemical potential deviations associated with shape changes of typical small particles is completely negligible. To confirm this, we estimate the magnitude of the chemical potential driving force for shape change and hence for nucleation as that corresponding to a critical nucleus of radius R_c equal some fraction α of the approximate particle radius R . This would also be the approximate critical radius of a pill box nucleus on the facet. The work W of formation of a circular nucleus of radius αR_c and height h is $W = \pi \alpha R_c \gamma h$. For the values $R_c = 10^{-4}$ cm, $\alpha = 0.1$, $\gamma = 1000$ ergs/cm², and $h = 2 \times 10^{-8}$ cm, we find $W = 6.28 \times 10^{-10}$ ergs which is 2.27×10^3 kT at $T = 2000^\circ\text{K}$; this is about two orders of magnitude greater than the value $W = 60$ kT which would make the nucleation rate $\exp[-2.21 \times 10^3]$ slower than that usually regarded as the lowest detectable rate.

It follows that facet motion requires a pre-existing source of steps (of the right sign) on, or adjacent to, the facet. Consider, for example, the facet shown in Figure 1a. Advance or retreat of the facet cannot occur by the motion of preexisting steps. As material is transferred from one facet (or from a continuously curved surface) to another facet, the advancing facet must, at some point, be covered by a partial layer. This intermediate state has a relatively higher energy that is approximately equal to the energy required to form a two-dimensional nucleus with an equivalent radial dimension comparable to the facet size. The equivalent supersaturation generated by particles larger than a few nanometers is insufficient to drive significant nucleation on a facet. The implication of this conclusion is that crystals with facets larger than the limiting size can only reach an equilibrium shape if their bounding singular surfaces are intersected by dislocations with a screw component. It follows that *a fully faceted particle will be immobilized in its initial shape, equilibrium or non-equilibrium, if it contains no dislocations*. The rationale behind this conclusion is articulated in greater detail in reference [1]. If, on the other hand, a facet is intersected by a dislocation with a normal screw component as shown in Figure 1b, then the endless supply of steps permit it to advance at arbitrarily low overpotentials.

Experimental support of our hypothesis can be found in the observations of Lemaire and Bowen [2, 3], who studied pore migration in KCl crystals. They found that small pores (≤ 1 micron) have an erratic

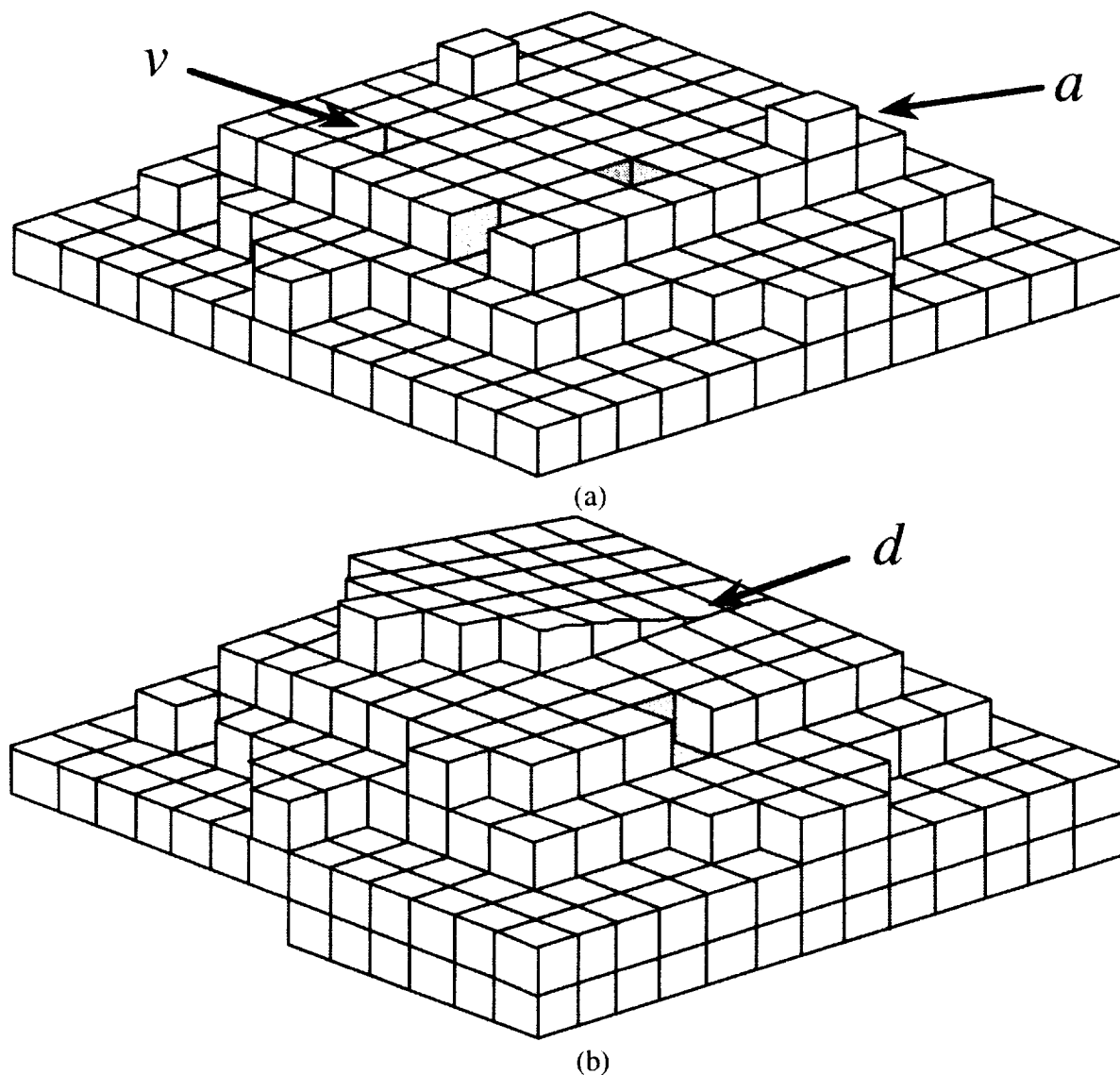


Figure 1. (a) Schematic of a faceted particle. Surface layer vacancies (v) and adatoms (a) will be present on the surface. (b) Schematic of a faceted particle with a screw dislocation (d) emerging on an otherwise flat facet. See text for description.

mobility (including very low values) compared to larger pores which show a steady larger mobility under a comparable thermal gradient driving force. They interpreted the observations in terms of the lower fluctuating probability that small pores intersect a dislocation, consistent with the above hypothesis. Experimental observations reported by Olander *et al.* [4] and Kitayama and Glaeser [5] were interpreted in a similar way.

We should also point out that our hypothesis can be reformulated in terms of coarsening. For a particle to change size while retaining its form, a new layer of atoms must be added to or subtracted from a facet. This also requires the formation of a nucleus of adatoms (for growth) or surface vacancies (for dissolution). The energy barrier for the nucleation of new layers will only exist for particles greater than a critical size, without step sources (dislocations). Thus, the defect density of particles should also strongly influence the rate at which particles coarsen and the distribution of particle sizes that results after a given annealing time increment.

It is possible to test our hypothesis in the following way. A sample will consist of a collection of small (micron-sized) single crystals prepared to have nonequilibrium shapes. For each sample, the particle size, shape, and dislocation density will be statistically determined by microscopic analysis. This sample will then be isothermally annealed (1200 °C to 1600 °C) in a sealed system containing a vapor with a composition that is in quasi-equilibrium with the particles. The microgravity environment is important because it allows the particles to remain dispersed in the vapor so that on all sides, the crystallites are only in contact with their vapor. After the annealing interval, the contents of the containers will be examined so that changes in the particle sizes and shapes can be determined. These experiments will be conducted with variations in composition, temperature, and initial particle characteristics (size, aspect ratio, average dislocation density). For example, examining the evolution of particles whose shapes depart significantly from the equilibrium form will be instructive. The observations from such an experiment will unambiguously verify or refute the hypothesis stated above. If dislocations are not required for the motion of facets, then all of the particles should evolve to the same equilibrium form, regardless of the initial particle shape or dislocation density. If dislocations are required, then the number of particles reaching their equilibrium state should be comparable to the probability that any given crystallite contains an appropriate dislocation which is able to supply growth steps. The remaining particles will be trapped in morphologies related to their initial shapes.

Because our primary goal is to study the approach to equilibrium, not the growth or evaporation process, it is essential that the particles do not lose or gain a significant amount of mass during the course of the experiment. Annealing will take place in a sealed, inert container (for example, Pt) charged with the crystallites and a fixed volume of Ar such that at the annealing temperature, the pressure will be approximately 1 atm. The closed system guarantees that the total mass will be conserved. However, some fraction of each particle will evaporate until the vapor is saturated. Taking 10^3 one micron diameter crystallites/cm³ and considering the equilibrium partial pressure of MgO (5×10^{-9} atm at 1400 °C) and the solid to gas volume expansion factor, one finds that less than 1% of each particle is lost to the vapor. Further, assuming a particle density of 10^3 /cm³, the average separation is large compared to the particle diameter. Therefore, the rate of coarsening (interparticle transport) is expected to be small compared to intraparticle transport by surface diffusion. However, a coarsening experiment where interparticle transport dominates will also be instructive. The key feature for either experiment is to control the conditions in such a way that one transport mechanism or the other dominates.

The key feature of the microgravity experiments is that although there are many crystallites in the sample, the majority of them remain dispersed and their shapes develop independently. Therefore, the conditions for dispersal are worth considering. Taking a particle density of 10^3 /cm³, the average particle separation will be 0.1 cm. Once the particles are dispersed (before heating), they will undergo Brownian motion and it is therefore possible that they will collide. If two crystallites coalesce after the collision, both are effectively removed from consideration in the experiment. The collision probability can be estimated in the following way. The Brownian motion diffusion constant is [6]:

$$D = \frac{kT}{6\pi\eta R} \quad (1)$$

Where η is the viscosity and R is the particle radius. Substituting the appropriate values for our experiment, the diffusion constant for a one micron MgO particle is approximately 5×10^{-7} cm²/sec. Therefore, in 10^2 hours, the root mean squared displacement is 1 cm. Chandrasekhar [6] discussed the probability that particles undergoing random diffusive displacement would collide. This result, together with the assumption that all collisions result in coalescence, leads to the conclusion that after 10^2 hours, 70 % of the crystallites

would remain independent. This figure is likely to be an under estimate; the inequivalence of the Mg and O vacancy formation energy creates a positive surface charge on each particle that would tend to keep them separated. In either case, there are many particles so the experiment would not suffer if 30 % were eliminated. It is also possible that the particles colliding with the wall will adhere to it. This is something that will be determined through ground-based testing. If the particles do stick to the walls, the problem might be remedied by making the annealing vessel significantly larger than the root mean squared displacement or by testing alternate container materials.

While gravity does not directly affect the driving force or transport mechanisms involved in morphological changes, it complicates the experimental investigation of these phenomena. In a one-g field, the particles will always settle to the bottom of the vessel where they will remain in contact with the container wall or each other. In this case, the particles would assume nonequilibrium shapes associated with the growth (or shrinkage) process that occurs during coarsening. Further, particle morphologies will also be strongly influenced by capillary effects at the contact points between the crystallites and, depending on the container, impurities or reaction products. We propose to eliminate these effects by allowing the particles to freely "float" during annealing in a reduced gravity environment.

An extensive ground-based research program is planned in advance of experiments in space to obtain information required to plan the details of the flight experiments. First, we will select a model system for our studies and determine the mass transport rates and mechanisms by measuring the kinetics of grain boundary thermal groove evolution. One can discriminate between surface diffusion and evaporation/condensation mechanisms of morphological evolution by measuring the time dependence of the thermal groove width. For the dominant transport mechanism, the relevant (surface or gas) diffusion coefficient can also be determined.

We will begin by fabricating large grained polycrystalline ceramics of MgO, NiO, and $\text{Mg}_{1-x}\text{Ni}_x\text{O}$ (or other appropriate model materials) using conventional solid state sintering in air. Specimens with flat, parallel surfaces will be produced by lapping and polishing. All grooving will be conducted in an environment as nearly identical as possible to the anticipated space experiments. The sample will be encapsulated in Pt foil and placed in a high purity alumina furnace tube terminated at either end by caps with valves. The system will then be heated and degassed at 1000 °C. After a 30 min residence at 1000 °C, the system will be purged by repeated evacuation/refill cycles with Ar. The final step will be to refill the system with a fixed quantity of Ar (such that the total pressure at the final temperature will be approximately 1 atm), close the system, and heat the furnace to the annealing temperature. Atomic force microscopy will be used to measure the groove geometry at selected time intervals and D_s will be calculated from the time dependence of the groove width. Previously, we used this same technique to measure the surface diffusion coefficient of alumina and the details of this method are described in [7]. This measurement will be repeated at each MgO-NiO composition and at a range of temperatures between 1200 ° and 1600 °C.

The next important step will be to establish methods to make fine particles with consistent sizes and shapes. The most direct way to make one to ten micron diameter single crystal particles is to pulverize a large grained ($\approx 100 \mu\text{m}$) ceramic produced by extended high temperature sintering. Particles of different sizes can be separated using sieves; their sizes and shapes can be characterized using high resolution SEM. Alternate methods for particle preparation will also be explored, if necessary. For example, small (0.1 micron), nearly dislocations-free particles can be formed by burning Mg metal [8]. Another potential alternate method is to precipitate fine powdered hydroxides from an aqueous solution and then calcine the powder to increase the particle size. If the powders are annealed in a

closed system with a mineralizer such as Cl_2 , the rate of growth (and potentially the particle shape) can be influenced.

We also plan to assess and control the dislocation density of the particles. If we assume an initial dislocation density as high as $10^6/\text{cm}^2$, and that the powder particles are formed by brittle fracture, then the total length of dislocation line in a particle with a one micron diameter is approximately 10 nm. In other words, most of the particles are expected to be dislocation free. We intend to form particles with high and low defect densities in the following way. To form low defect particles, a well annealed, coarse grained ceramic will be pulverized to form a powder. The powder will be briefly annealed at 1000°C to remove any surface disorder left over from the pulverizing process. Bright-field TEM imaging of a random sample of the particles will then be used to determine the probability of finding a dislocation in any given particle. To form high defect density powders, a coarse grained ceramic specimen will be plastically deformed in a hot isostatic press (to increase the relative dislocation density by several orders of magnitude) and then pulverized. This material will be subjected to the same TEM analysis to determine the probability of finding a dislocation in any of the particles. From this preparation and analysis, we will have comparable specimens with known and different dislocation contents. By comparing the morphological evolution of powder particles with different sizes from each of these specimens, it will be possible to determine if dislocations play an important role in shape evolution kinetics.

REFERENCES

1. W.W. Mullins and G.S. Rohrer, *J. Amer. Ceram. Soc.* 83 (2000) 214.
2. P. J. Lemaire and H. K. Bowen, *J. Amer. Ceram. Soc.* 65 (1982) 49.
3. P. J. Lemaire and H. K. Bowen, *J. Amer. Ceram. Soc.* 65 (1982) 41.
4. D.R. Olander, A.J. Machiels, M. Balooch, and S.K. Yagnik, *J. Appl. Phys.* 53 (1982) 669.
5. M. Kitayama and A. M. Glaeser, *Key Engineering Materials* 159-160 (1998) 193.
6. S. Chandrasekhar, *Rev. Mod. Phys.* 15 (1943) 1.
7. D.M.Saylor and G.S. Rohrer, *J. Amer. Ceram. Soc.*, 82 (1999) 529.
8. P. Chaudhari and J.W. Matthews, *J. Appl. Phys.* 42 (1971) 3063.

EXTINCTION AND INSTABILITY MECHANISMS OF POLYMERIZATION FRONTS

M. Abid¹, P.D. Ronney^{2*} and E. Meiburg²

¹Department of Aerospace and Mechanical Engineering
University of Southern California; Los Angeles, CA 90089-1453

²Department of Mechanical and Environmental Engineering
University of California at Santa Barbara; Santa Barbara, CA 93106

Recent advances in polymer chemistry have led to the development of monomers and initiation agents providing propagating polymerization fronts driven by the exothermicity of the polymerization reaction and the transport of heat from the polymerized product to the monomer (Pojman *et al.*, 1995; Pojman *et al.*, 1996; Pojman *et al.*, 1997). The use of polymerization processes based on this mode of polymerization has many applications including rapid curing of polymers without external heating, uniform curing of thick samples, solventless preparation of some polymers, and filling/sealing of structures having cavities of arbitrary shape without having to heat the structure externally. One important limitation of this process is that the fronts extinguish when they try to propagate through channels that are too narrow (probably due to conductive heat losses) or too wide (for unknown reasons, which we propose to be convective heat losses driven by buoyancy-induced flow.) Even when extinction does not occur, convective and buoyant instabilities can affect the structure and properties of the resulting polymerized materials as well as the propagation rates of the fronts. The purpose of the proposed study is to determine the mechanisms of extinction and instability and thereby determine means to obtain more useful product material at earth gravity and μg .

Propagating fronts occur in entities A and B exhibiting transformations (*e.g.* due to chemical reaction) of the generic form $A + nB \rightarrow (n+1)B$, where n is a constant. This reaction is said to be *autocatalytic* in B since it is a product of reaction that also catalyzes the reaction. Autocatalytic systems are common in nature, *e.g.* flames. Why can't we infer everything we want to know about polymer fronts based on the extensive literature on other autocatalytic systems such as flames and aqueous chemical fronts? The answer to this lies in the unique properties of polymer fronts, which have a number of similarities and a number of differences from other types of autocatalytic systems based on chemical reactions such as premixed-gas flames and aqueous autocatalytic chemical fronts (Figure 1). One important difference is the dimensionless density difference across the front which affects both buoyancy- and thermal expansion-driven instabilities. Also, for flames, where both heat and chemical species are autocatalysts, the *Lewis number* $\equiv \alpha/D$, where D is the mass diffusivity, is also an important parameter because it leads to *diffusive-thermal instability*. Moreover, in polymer fronts, Le is very high, which has the additional effect that the product (polymer) cannot diffuse upstream nearly as far as thermal energy does.

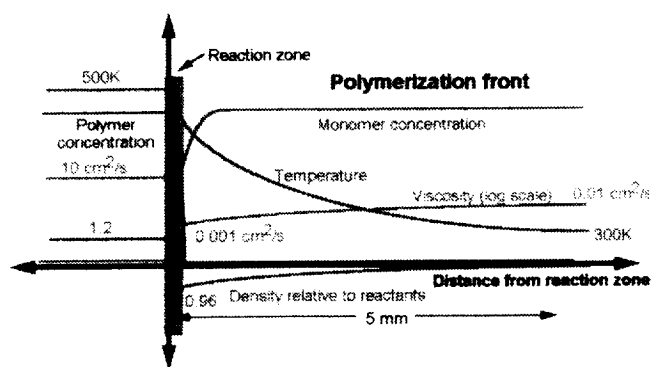
Additionally, the difference between product and reactant viscosity causes the Saffman-Taylor instability when $v_\infty < v_a$. We are conducting experiments in two distinct geometries, specifically Hele-Shaw cells and round tubes (Figure 2), in which to study the extinction and dynamics of

polymer fronts. Both are being studied at both Earth gravity and μg . Our prior experiments in gas combustion in round tubes of varying diameter have demonstrated two distinct extinction limits due to these processes; it will be determined if the same applies to polymer fronts. In addition to μg experiments, in the Hele-Shaw cell varying the angle of the cell relative to the horizontal will be used to assess buoyancy effects – though with limitations because a minimum cell thickness and thus minimum Rayleigh number is required to avoid heat-loss induced quenching. The two methods of assessing buoyancy effects will then be compared. Comparisons to instabilities and extinction mechanisms in flames and aqueous autocatalytic chemical reaction fronts will also be made.

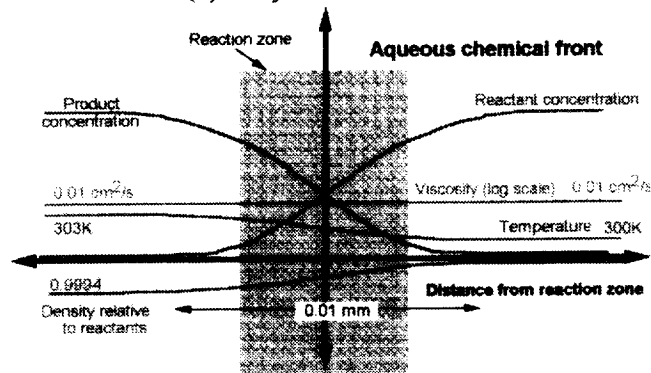
A factor which does not appear to have been controlled in prior experiments is the wall boundary condition. Two types of boundaries are most amenable to experimental interpretation and numerical analysis: isothermal or adiabatic. Isothermal walls are typically obtained by using thin walls (which must be transparent) and immersing the entire apparatus in a rapidly stirred water bath, and are preferred for this investigation. Adiabatic walls are also possible in principle, but would require a thick transparent wall material with very low thermal conductivity compared to the polymer product. Such a material is not readily identified, since the mixtures themselves have fairly low conductivity (typically $1 \text{ W/m}^\circ\text{C}$). Thin walls surrounded by an evacuated region (like a Thermos bottle) are possible, but a simple estimate indicates that radiative transfer, which is not suppressed by the evacuated region, might be significant at the temperatures of interest. Therefore the value of this technique to produce adiabatic walls is uncertain, but will nonetheless be investigated.

Our prior experiments in aqueous autocatalytic chemical reaction fronts in Hele-Shaw cells (Abid *et al.*, 2000) have shown a previously unknown manifestation of the Saffman-Taylor instability due to surface tension effects, even though the reactants and products are completely miscible in each other. We are determining if such surface tension effects exist in polymer fronts as well. A factor not present in the autocatalytic systems (due to the negligible temperature rise), but which may be present in the polymer systems, is flow due to gradients in surface tension driven by temperature gradients along the front, which affects the front thickness. In the round-tube experiment, this is expected to lead to net flow from the tube walls toward the axis (Figure 3), which will cause a compressional strain that will discourage extinction but encourage instabilities. This flow mechanism should be especially important at microgravity, and is proposed to be in the direction opposite that of conventional Marangoni convection due to differences in the mechanisms of surface tension of propagating polymer fronts vs. passive immiscible fronts.

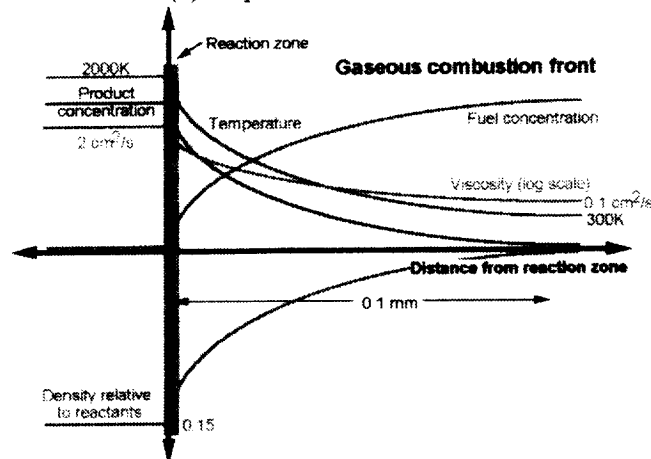
For the purposes of this study, a polymerization reaction is needed that has a liquid reactant and liquid product, produces few bubbles (high monomer boiling point), and is simple and inexpensive to prepare. For these reasons 2-hydroxyethyl methacrylate (HEMA, glycol methacrylate) monomer with ammonium persulfate (AP) initiator in DMSO solvent is being used for the majority of tests. Once the mechanisms of instability and extinction are determined, other polymerization reactions with industrial applications, *e.g.* with solid cross-linked polymer product, will be investigated as well. The viscosity of the product relative to the reactant will be controlled by controlling the polymer chain length, which in turn will be adjusted using varying concentrations of a chain transfer agent (dodecyl mercaptan). Another task of this study is the development of frontal polymerization processes for use in water at ambient pressure. Current polymerization fronts require a high-temperature solvent such as DMSO, or very high pressures to avoid boiling, despite the fact that water at ambient pressure is the most convenient medium and the most important for practical



(a) Polymerization front



(b) Aqueous chemical front



(c) Premixed-gas flame front

Figure 1. Schematic diagrams of propagating fronts.

applications (because of the cost and environmental issues associated with other solvents). High temperatures are needed for polymerization fronts because fronts with peak temperatures less than 100°C have not been identified – at such low temperatures the fronts extinguish. By developing a better understanding of extinction and instability mechanisms in polymer fronts, we hope to establish low-temperature water-based polymerization reactions supporting propagating fronts. In particular, we will determine if acrylic acid can be polymerized in a front in solutions with adiabatic temperatures below 100°C .

The experiments will measure propagation rates and front shapes using direct video, laser-induced fluorescence (LIF) imaging, a technique not previously used in studies of polymerization fronts, along with temperature measurements using thermocouples and laser interferometry, and flow

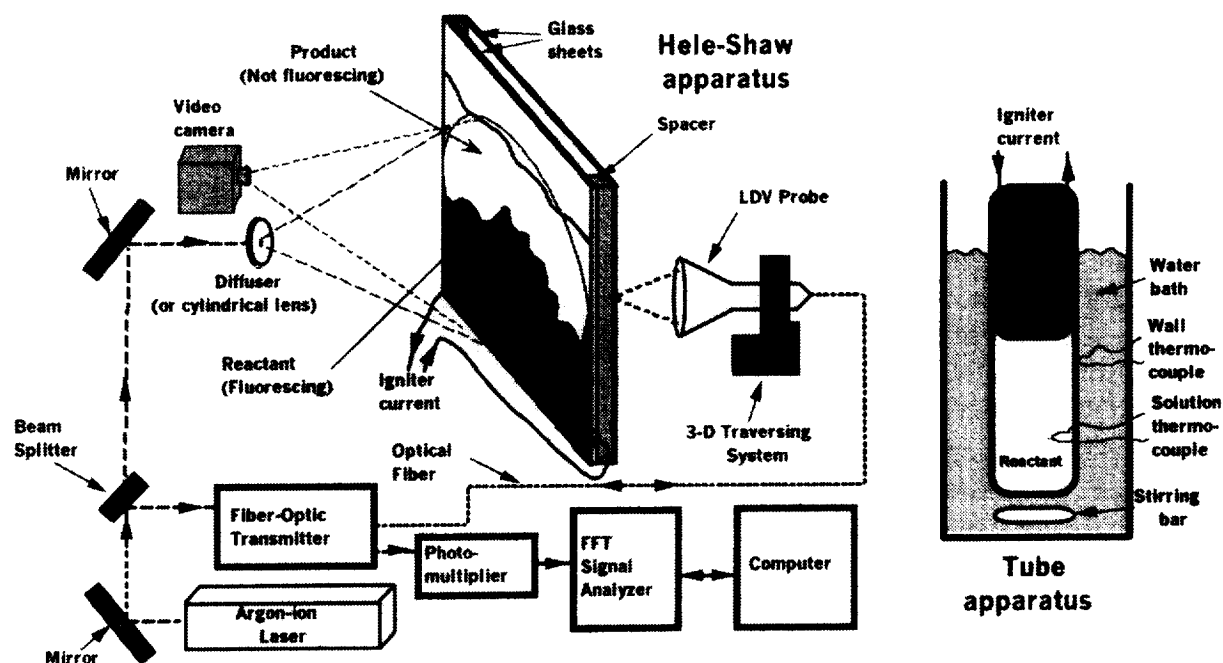


Figure 2. Schematic diagram of experimental apparatuses, shown for upward-propagating fronts in Hele-Shaw cells and downward propagating fronts in tubes. Water bath and all diagnostics shown used for both Hele-Shaw and tube apparatuses. LDV system for 1g tests only. Not shown: Laser shearing interferometer.

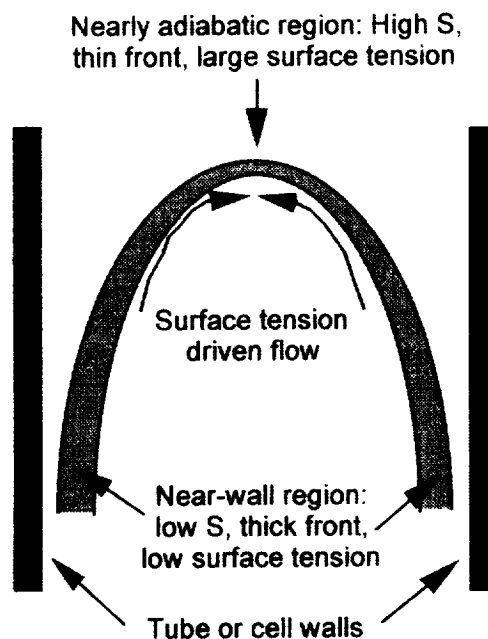


Figure 3. Schematic illustration of proposed effect of surface tension gradients on flow along polymer front (shown propagating upward). Note flow direction is opposite conventional thermocapillary flow.

properties via particle tracking and laser Doppler velocimetry. Consequently, a secondary objective of this work is the development of improved diagnostic techniques for frontal polymerization studies. The polymerized products will be characterized using NMR to determine the conversion efficiency and Gel Permeation Chromatography to measure the product molecular weight distribution.

LIF imaging can be accomplished using a fluorescent indicator that is excited by 488 nm argon-ion laser light formed into a sheet using a cylindrical lens. By using LIF in this way, at one cross-section the actual front shape is obtained rather than simply a path-integrated (and possibly misleading) image. This technique is standard in many fluid mechanics and combustion experiments. We have conducted feasibility tests in polymerization using this imaging technique. Example results are shown in Figure 4. It can be seen that, not surprisingly, the LIF technique provides better front visualization and clearer delineation of front features than direct video. Note that the LIF images show the different fingering modes for both upward- and downward propagating fronts present without the Cab-o-sil viscosity enhancing agent. While conventional fluorescein is not very soluble in DMSO, a fluorescein derivative, BODIPY 493503 from Molecular Probes Inc., Eugene, OR, is soluble in DMSO and is effective at mass fractions of 10 ppm or less. We have found that it will fluoresce in the reactants but not the products, which could either be due to attack by free radicals or thermal decomposition at elevated temperatures. Tests in pure DMSO heated by a resistance wire showed no degradation of fluorescence, thus we believe the suppression of fluorescence in the products (which is permanent) is due to attack by free radicals. For aircraft or space flight experiments, other BODIPY dyes are available that are excited by other laser sources, *e.g.* 630 nm miniature diode lasers. For experiments in Hele-Shaw cells, a diffuser can be used to create a broad beam rather than a planar sheet of light if it is desired to illuminate the entire cell (though in this case the image is integrated across the cell gap.) We will also examine the use of a “caged” fluorescent molecule that is “uncaged” by UV light in order to “tag” a line of molecules, then follow their progress. Since the Schmidt number $Sc \equiv \nu/\Delta$ is very high in polymer fronts, the line will stay thin for a long time (*i.e.* many fluid mechanical time scales) before it starts to smear out. Many of these agents are soluble in DMSO, which is the most practical solvent for the polymer reactions proposed in this study. The PI has demonstrated the use of 8-((4,5-dimethoxy-2-nitrobenzyl) oxy)pyrene-1,3,6-trisulfonic acid, trisodium salt (DMNB-caged HPTS) (also obtained from Molecular Probes) for use in fluid mechanics experiments (Lempert *et al.*, 1995). This may provide a useful alternative to particle tracking or laser Doppler velocimetry.

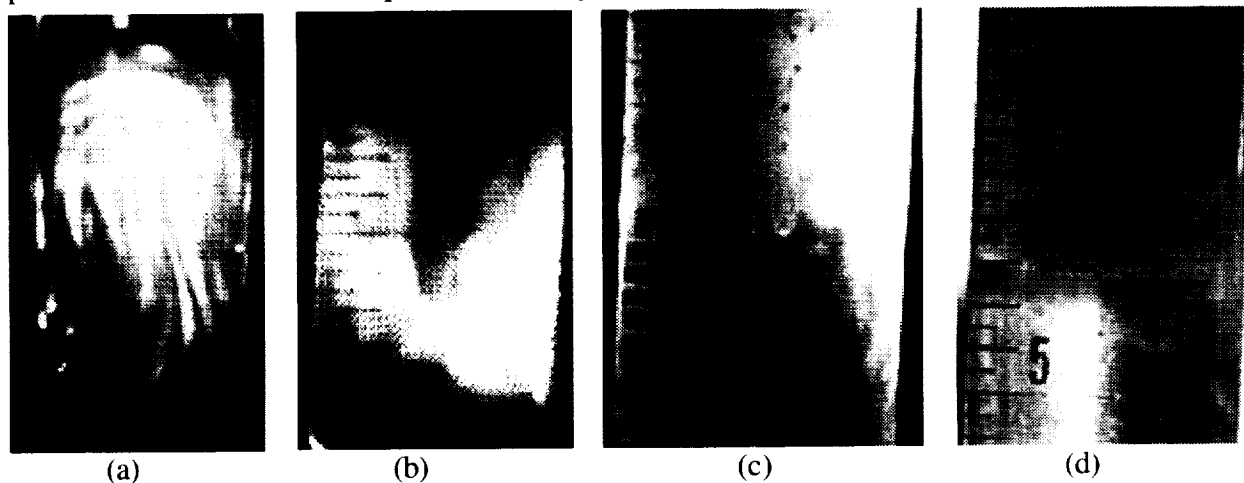


Figure 4. Images of polymerization fronts. (a) LIF image using 20 ppm (by mass) BODIPY 493503 fluorescent indicator (from Molecular Probes Inc., Eugene, OR) illuminated by a sheet of argon-ion laser light 0.5 mm thick, upward propagation, no Cab-o-sil (note thermal plumes rising from turns of igniter wire); (b) LIF image using BODIPY 493503 indicator, downward propagation, no Cab-o-sil (note finger of downward-spreading non-fluorescent products); (c) LIF image using BODIPY 493503 indicator, downward propagation, 0.75 g Cab-o-sil; (d) same as (c) but direct image (not LIF). All images: tube diameter (ϕ) 18 mm, mixture composition 1.5g AP, 15 ml HEMA, 15 ml DMSO.

Microgravity experiments are an indispensable aspect of the proposed study for several reasons. Polymer fronts are very likely subject to quenching by buoyancy-driven mechanisms, and buoyancy also leads to a wide variety of instabilities which may overwhelm effects due to surface tension, viscosity difference, and thermal expansion/contraction. Without microgravity experiments, these effects cannot be isolated (though experiments in tilted Hele-Shaw cells will help, as noted above). The use of thickening agents to decrease buoyant flow at earth gravity are proposed, at the expense of also suppressing surface tension, thermal expansion, and viscosity-difference driven flow. The thickening agents are also chemically active, and have some effect on the properties of the resulting polymers. Microgravity experiments in the KC-135 aircraft are proposed because the time available in drop towers is shown to be too short compared to the characteristic time scales of polymer fronts.

A companion numerical modelling effort will be performed and the results compared to experimental observations. Within this computational work, the emphasis will be on performing high-accuracy, direct numerical simulations for two different classes of problems: first, the initial growth and subsequent non-linear evolution of a variety of relatively simple, well-controlled initial perturbations will be investigated. The initial perturbation typically will consist of a single, wavy disturbance of the frontal shape, as well as its sub- and/or superharmonic wavelengths. These simulations will provide some insight into the evolution of a single-wave perturbation, as well as into the basic mechanisms that govern the interaction of waves of different wavenumbers. Subsequently, the long time evolution of the polymerization front will be simulated for cases in which the initial perturbation consists of a whole bandwidth of wavenumbers, with random amplitudes and phases. These simulations will serve to extract the scaling laws that govern the nonlinear evolution of the front over long time intervals which in turn determine the mean propagation rate of the wrinkled fronts. For both of these classes of problems, the evolution will be documented as a function of the governing dimensionless parameters. A novel aspect of these studies is the inclusion of Korteweg stresses which enable modelling of surface tension-like forces in regions of steep concentration or temperature gradients at the interface between miscible fluids. An understanding of the surface tension of miscible fluids is also relevant to many industrial processes such as solvent-based cleaning. Another important aspect of the modelling study is the inclusion of heat losses to walls, which are anecdotally known to cause extinction of polymer fronts but have not been the subject of systematic evaluation in prior literature.

REFERENCES

1. Abid, M., Liu, J. B., Ronney, P. D. (2000). "Surface Tension and Fingering of Miscible Interfaces," submitted to *Physical Review Letters*.
2. Lempert, W. R., Magee, K., Ronney, P. D., Gee, K. R., Haugland, R. P. (1995). Flow Tagging Velocimetry In Incompressible Flow Using PHoto-Activated Nonintrusive Tracking Of Molecular Motion (PHANTOMM). *Experiments in Fluids* 18, 249.
3. Pojman, J. A. *et al.* (1995). Factors Affecting Propagating Fronts of Addition Polymerization: Velocity, Front Curvature, Temperature Profile, Conversion and Molecular Weight Distribution. *J. Polymer Sci. Part A: Polymer Chem.* 33, 643-52.
4. Pojman, J. A., Hyashenko, V. M., Khan, A. M. (1996). Free-radical frontal polymerization: self-propagating reaction waves. *J. Chem. Soc., Faraday Trans.* 92, 2825.
5. Pojman, J. A., Khan, A. M., Mathias, L. (1997). Frontal Polymerization in Microgravity: Results from the Conquest I Sounding Rocket Flight. *Microgravity Sci. Tech.* 10, 36.

CAPILLARY WAVES AT INTERFACES: THE ROLE OF GRAVITY AND ELECTRIC FIELDS

T. Kerle¹, Z. Lin¹, S. Baker^{1,2}, J. Mays³, and T.P. Russell^{1*}

¹University of Massachusetts at Amherst

²Harvey Mudd College

³University of Alabama at Birmingham

Any interface between a fluid and a gas or two fluids contains capillary waves whose amplitudes are governed by interfacial tension and geometric constraints and whose wavelengths are dictated by the interfacial tension and external fields, *e.g.* electric or gravitational fields. Earlier studies of our group on capillary waves at liquid-air interfaces have shown, that electric fields applied normal to the interface may be used to effectively select and amplify fluctuations of the interface with a characteristic wavelength λ_m . Ultimately a hexagonal array of vertically standing columns is created. Here we extend this study to the more general case of a liquid-liquid interface subjected to an external field.

The objective of this study is to develop a basic understanding of the manner in which capillary waves at interfaces can be manipulated by external fields. This is an essential key for controlling structure formation at these interfaces. Two component polymer systems in an external field may then be used to develop novel morphologies that can be quenched or frozen-in for potential further applications.

We present here a theoretical framework for the early stages of structure formation at liquid-liquid interfaces along with supporting experimental evidence. Both, calculations and experiments, indicate that the lateral structure size can be effectively tuned over many orders of magnitude simply by modifying the interfacial tension.

PARTICLE-FLUID DYNAMICS UNDER VARIABLE GRAVITY CONDITIONS

A.N. Alexandrou¹, R.A. Lemdiasov², N.A. Gatsonis³, A. Sacco, Jr.⁴

^{1,2,3} Worcester Polytechnic Institute

⁴ NorthEastern University

Crystals grown from specially prepared liquid solutions have important industrial applications. The efficiency of these crystals is usually a function of their size. Therefore, during the synthesis of the crystals, it is important to optimize their size, and to control the defect location and concentration. For this reason, crystals have been grown in space in order to take advantage of the reduced gravity. In this paper we discuss the description of macroscopic fluid-crystal dynamics under various microgravity conditions in a 3-D cubic container. The process is modeled using the conservation of mass and momentum equations for the fluid phase and a discrete particle model for the crystals. The settling particles exert a force on the ambient fluid and, therefore, they induce bulk motion. The force on the fluid is applied at the point where the particles reside. Fluid was considered to be Newtonian and no-slip boundary conditions for the fluid were applied on the sides of the cubic container.

In the paper we first discuss the basic physics of the process, through the use of exact analytic solution which are possible for simplified geometries. The exact solutions are obtained for a cylindrical container by assuming that particle settle directly to the bottom with their terminal velocities, particle sedimentation produces a body force, which induces fluid motion. These assumptions were sufficient to obtain (a) steady state solution for fluid velocity, (b) unsteady solution, (c) particular solution for periodic gravity modulations.

The analytical solutions were used in deriving of relations between the parameters of the solid particles and major flow characteristics such as fluid velocity, maximum fluid velocities, the magnitude of vorticity, etc. Fluid flow was investigated under two gravity conditions: (a) constant gravity and (b) variable gravity. For constant gravity we can find steady state fluid velocity and characteristic time, during which the flow develops. We can also take into account that in a real container particles have finite sedimentation time. Therefore, the character of the flow depends on the interplay between the time it takes to reach steady state and sedimentation time. In the low gravity case we have linear dependence of maximum fluid velocity on gravity level, and it does not depend on gravity at high gravity level.

In the case of variable gravity we determined the magnitude of the fluid and particle oscillations. The maximum fluid velocity is found to depend strongly on frequency of gravity oscillations. The analytic solutions were also used to study the effects of the frequency on the fluid oscillations. It is shown that the fluid behavior in the case of low and high frequencies is sufficiently different: fluid velocity tends to a steady state case at low frequencies and it is inversely proportional to the frequency in the case of high frequencies. We also have a $\pi/2$ phase shift between gravity and fluid velocity oscillations in high frequency case. The spread parameter of Gaussian distribution also affects significantly the fluid velocity:

the higher this parameter is, the lower fluid velocity is. It is also shown that the top and bottom of the container affect significantly the fluid flow: the higher the cylinder is, the more close velocity distribution in the finite container to the one in the infinite container.

The analytic solutions were used in order to obtain several estimates for fluid and particle motion in the 3-D cubic container. Processes of particle sedimentation and fluid motion in the container are qualitatively described with use of these estimates. These results can be used to explain and to justify results that were obtained numerically. Estimates obtained in these analytical solutions have the same scale as the values obtained numerically. Generally speaking we can use analytical formulae for predicting the fluid behavior under parameters, for which we do not have numerical results. Under some choice of parameters (especially in the low gravity conditions) numerical calculations can take weeks or months of run-time. Analytically, the most basic characteristics of the flow can be estimated almost instantly.

The solution to the conservation of mass and momentum equations along with the constitutive relations was obtained using a Mixed Galerkin Finite Element discretization with twenty seven-noded brick elements. The resulting non-linear system of equations was solved using a Newton-Raphson iteration procedure. Due to the three dimensional nature of the problem, in order to save on storage requirements, the Jacobian of the Newton-Raphson procedure was saved using an element-by-element storage, and solved by an iterative method based on the modification of the BiConjugate Gradient Stabilized Method. To speed up convergence, the Jacobian matrix was preconditioned using Jacobi preconditioning. The independent unknowns in this problem are the three velocity components and pressure. In this work two distinct cases are considered: (a) randomly distributed particles in the fluid, and (b) a Gaussian distribution of particles with highest concentration in the center of the cube. The problem was solved for different gravity levels. Furthermore, a case of variable gravity (g -gitters) was considered.

NON-INTRUSIVE MEASUREMENT OF THERMOPHYSICAL PROPERTIES OF LIQUIDS BY ELECTROSTATIC-ACOUSTIC HYBRID LEVITATION

S.S. Sadhal* and K. Ohsaka

Aerospace & Mechanical Engineering
University of Southern California
Los Angeles, CA 90089-1453

ABSTRACT

Ground-based experimental and analytical studies to rigorously validate existing techniques and to develop new approaches for measuring the thermophysical properties of liquids in a containerless environment are being carried out. The important application here is towards understanding the thermal behavior of liquids in undercooled states that can be achieved in microgravity or other containerless environments. The measurement of properties in such a state is particularly difficult because any physical intrusion can lead to instantaneous solidification, thus destroying the undercooled state. The focus of the effort here will be on the rigorous evaluation of the effects of the levitation fields on the liquid samples under scrutiny. Such effects induce equilibrium drop shape deformation, uncontrolled rotation, significant internal flows, and dynamic shape instability. We are also aiming to develop measurement techniques that can be employed while maintaining minimal disturbance levels to the liquid samples. As such, electrostatic and acoustic levitation has shown considerable promise, and this technique will mature to a point of high accuracy.

The focus of the measurements will be on density, surface tension, viscosity, and thermal diffusivity of levitated liquid drops. For the thermal property measurement, the methods consist of applying a thermal stimulus to a levitated liquid sample and measuring the response from which the thermophysical properties can be inferred. Viscosity and surface tension measurements will be carried out by observing the response of initially deformed drops (acoustically and electrostatically) to more spherical shapes upon relaxation of the deforming force fields. By using the hybrid levitation approach we plan to quantitatively evaluate the effects of surface charge on the measurement of surface tension and viscosity, the influence of thermocapillary flows on the shape oscillation dynamics and frequencies, and the impact of oscillation mode coupling on the measurement of thermophysical properties.

Considerable analytical work will be directly tied in with the measurements because much of the experimentation will be conducted in 1-g where the disturbances from the acoustic and electrostatic fields will need to be accounted for. Therefore, the thermal and the fluid phenomena associated with the local heating of acoustically and electrostatically levitated drops need to be thoroughly understood. In addition, the thermal and flow measurement techniques that have been established in prior studies need to be refined to make them sufficiently non-intrusive and applicable to undercooled liquids.

I. Introduction

Recent microgravity flight experiments using electromagnetically levitated molten metals have demonstrated the feasibility of measuring the thermophysical properties of highly undercooled melts [1]. With Earth-based investigations in the same area using electrostatically levitated and laser-heated metals and semiconductors, deep undercooling has also been achieved and the feasibility of the measurement surface tension, viscosity, specific heat, density, and electrical conductivity has been demonstrated [2-6].

The research we describe here relates to the theoretical and experimental developments to validate novel non-contacting techniques for the measurement of these thermophysical parameters at 1-g with an emphasis on high viscosity melts. The fundamental motivation is to use recently- developed containerless experimentation methods to determine these properties of levitated undercooled molten materials for use both at 1-g and in reduced gravity. The advantage of levitation over, say, a free fall is the spatial stability of the sample for a sufficiently long time to carry out the measurement of its characteristics. The issue we are particularly concerned with is accuracy of the measurement of the properties of levitated samples and how we deal with highly viscous melts. For the next year, we plan to carry out research on two specific but related topics involving the measurement of the thermophysical properties of levitated droplets. The first one will involve the measurement of surface tension and viscosity by elongating drops with electrostatic and/or acoustic fields and following the ensuing shape restoration when the force fields are relaxed. The second topic deals with thermocapillary flow measurements in flattened disk-like drops, as shown in Figure 1. The flattening is achieved by the acoustic field that is applied for levitation.

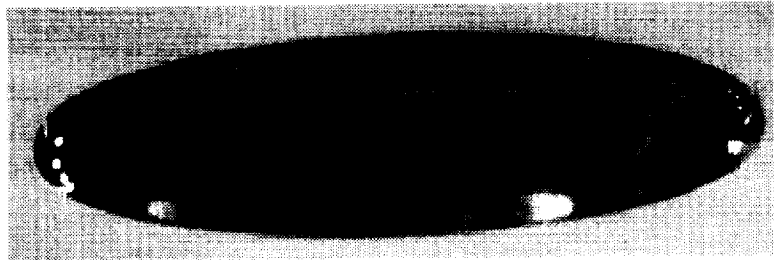


Figure 1: A disk-shaped ultrasonically levitated drop of glycerol. The aspect ratio can be continuously varied by adjusting the acoustic pressure level. The central portion can be made very thin ($< 1 \mu\text{m}$) for viscous liquids. The central dimple observed in the photograph is removed for lower acoustic pressure, and the opposed drop surfaces can be made more parallel. The drop side dimension is 4.5 mm.

II. Experimental Approach

An existing apparatus that allows the combined ultrasonic and electrostatic levitation capability is schematically described in Figure 2. The levitation capability at 1-g can be provided by each device alone, or using a combination of both capabilities at the same time [7]. In a prior implementation, we have levitated charged drops using an electric field, and introduced a rotational capability by using the ultrasonic field [8]. Variations on this theme will be obtained by introducing a number of ultrasonic or lower frequency devices to combine the levitation and rotational capabilities along different axes.

A. Relaxation of Elongated or Flattened Drops

In some applications involving deeply undercooled melts of metal alloys we face very high values for the viscosity. The same situation is, of course, applicable to the processing of glassy and polymeric materials. The currently practiced technique of using the resonant frequency and decay rate of shape oscillations

tions is not applicable because the drops are overdamped. The other method to measure the viscosity of a drop involves the acoustic flattening of the drop to a disk-like shape, followed by a sudden release of the acoustic stresses. We will rotate a levitated drop up to its bifurcation point. The acoustic torque will be subsequently terminated or reversed in order to initiate the shape relaxation back to the equilibrium shape. Tracer particles will be suspended in the transparent test droplets in order to measure the relative motion of the relaxing drop, and a high speed video recording system (2,000 fps with 240 by 240 pixels images) will be used to measure the drop shape. Typical drop size will be between 2 and 5 mm spherical diameter, and rotation rates will be no greater than 30 rps. The time history of the shape recovery of the overdamped drop will provide the means to determine the viscosity. Figure 3 is a composite of photographs taken during such shape relaxation for a levitated 4-mm diameter glycerol drop. Theoretical analyses of the two different processes will be developed.

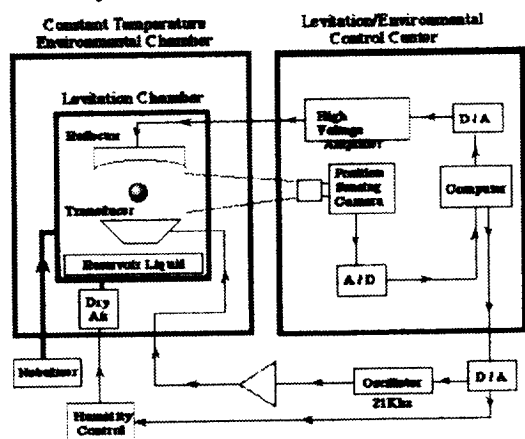


Figure 2: Schematic description of an existing version of the electrostatic-ultrasonic hybrid levitator.

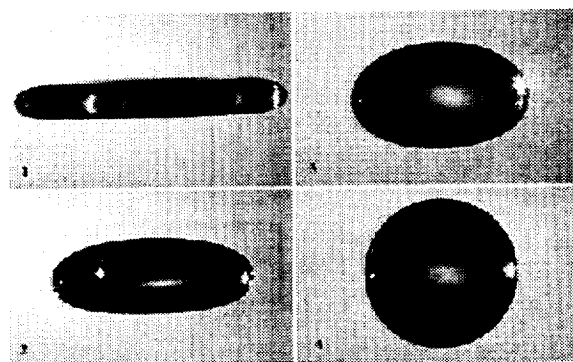


Figure 3: Relaxation of a drastically flattened drop back to the spherical shape after termination of the acoustic radiation force.

B. Measurement of the Thermal Diffusivity of a Disk-Shaped Levitated Viscous Drop

Using a high-viscosity liquid ($\mu > 10$ poise) and an ultrasonic levitator, a drop can be stably held in a very thin disk-like shape for a substantial amount of time without the onset of shape instability, *i.e.* the shape will remain stationary for a long time. The central area of the drop will be shaped by the acoustic field into a dimple or very nearly flat if so desired. The thickness of this central region can be adjusted through an increase or decrease in the acoustic pressure. We shall measure the thermal diffusivity of the thin liquid sheet by implementing pulse heating from one side and thermal detection on the other. We are undertaking an experimental study of the fluid flow and heat transport across the thin liquid membrane at the center of a flattened levitated drop. The experiments will also be conducted with pulsed heating. From a measurement standpoint, this has the advantage that the transient heat input signal is very precise and the response corresponding to the pulse frequency can also be precisely measured. The analysis to correlate the response with the thermal properties and geometrical parameters will need to be carried out. Therefore, the preliminary analysis discussed above will be extended to include pulsed heating. The measurement of the thermal diffusivity of all materials has been a very active area of research in the past 15 years. Unfortunately, very few experimental methods have yet been developed and validated for the remote measurement of that parameter for levitated liquid [9-12]. We shall apply the approach described earlier, using levitated disk-shape liquid droplets, to implement and modify existing transient methods based on laser flash and other photoacoustic effects [13-15]. The thermal diffusivity measurement experiments will be carried out using the apparatus schematically described in Figure 4. The drop

is levitated and flattened by a standing wave established between the piezoelectric transducer with a transparent quartz radiating plate and the window of a high-speed radiant detector. The beam of a pulsed 100W Nd-Yag laser is directed towards the lower center face of the drop. The radiant detector at the other side of the drop is triggered by the laser, and records the time dependence of the radiant energy from the upper face after each pulse. The thickness of the central part of the drop can be adjusted in steps and the heat signature time transients are recorded for each step. This relative measurement will eliminate the need for the absolute calibration of the laser pulse absorbed energy because the incident power will be kept constant, only the thickness of the liquid film will be changed. A numerical model will be developed to calculate the thermal diffusivity.

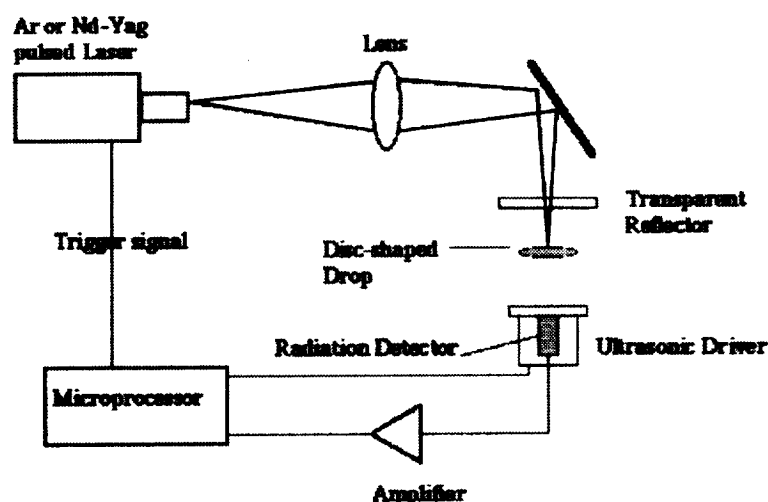


Figure 4. Schematic description of the apparatus design for the implementation of the laser flash method for the measurement of the thermal diffusivity of disk-shaped levitated drops. A laser pulse deposits energy on the upper side of the drop, and the thermal response is monitored on the other side by a radiation detector or thermal imager. The amplified thermal signature is processed by the microprocessor that also controls the acoustic pressure level to change the drop central area thickness.

III. Analysis

There will be a significant amount of analytical work closely tied to the experimentation. In particular, with regard to obtaining the precise values of the thermophysical properties, we will need to carry out detailed analysis and modeling of the fluid mechanics and thermal transport in the levitated liquid samples. The specific tasks will focus on the theoretically duplicating the experimental conditions so that the measurements can be interpreted in terms of the physical properties being sought.

A. Relaxation of Elongated or Flattened Drops

For the type of problems being posed in this investigation (non-spherical drops), perturbation-type analysis will be of limited value. Therefore, numerical techniques will be used. A finite-difference model is presently being developed to obtain the relaxation histories of initially stretched drops. The stretching of a levitated drop can take place by either an electrostatic field or a centrifugal force field brought about by acoustically-driven rotation. By switching off or lowering the intensity of the field providing the stretching, the drop will tend towards a more spherical shape. The evolution of this shape can be predicted, and since this history depends on the surface tension and viscosity, it will be used to infer these properties by comparing with experiments.

The numerical techniques used in the literature for calculating transient flows involving free surfaces adopt either Eulerian, or Lagrangian approaches to the fluid motion. In the Eulerian approach, the flow is considered with respect to a stationary numerical mesh. The Lagrangian approach assumes that the mesh moves together with the fluid so that fluid inside any cell of the mesh always remains inside that cell. Thus, the mass of a cell remains constant in time and, if fluid is incompressible, the same is true for the volume. The main advantage of the Lagrangian approach is the ease to deal with free surfaces and interfaces, and in particular, to take surface tension into account.

B. Thermocapillary Flows and Diffusive Transport

As discussed earlier, large drops levitated in a gravity field can take on the shape of a nearly flat disk. The measurement of its thermal diffusivity will be conducted by heating the center of the disk with a laser, and thermographically measuring the temperature history of the other side of the disk. While it is a reasonable approximation to assume that all of the laser energy is deposited on the surface of the drop, provisions will be made to obtain predictions independent of the radiative absorptivity, transmittivity and reflectivity. The modeling will take place in several stages. Initially, a simple conduction model will be developed, based on pure conduction in a large disk, and lumped convection in the surrounding gas region. Subsequent refinements will be made to accommodate the finite disk size, followed by fully-coupled convective transport in the gas. A rigorous evaluation of the limits of the conduction model will also be included.

While we can mitigate gravity effects by reducing the drop to a thin horizontal region, the thermocapillary effects will be present. A great deal of work has been carried out on single drops and bubbles with aspect ratio of $O(1)$, especially for low Marangoni number [16-31]. More complex situations, such as a fluid particle near a flat surface, have also been successfully treated [32-41]. For the present situation, the analysis will first be carried out for $Ma \ll 1$. That is, with conduction-dominated results, the thermal driving force will be calculated and a first correction to obtain the flow field will be obtained. For $Ma = O(1)$ and higher, we will resort to numerical methods.

REFERENCES

1. M.B. Robinson, Final Report, *Proceedings of the Microgravity Science Laboratory (MSL-1)*, One-Year Science Review Meeting, Space Flight Center, Huntsville, AL, Aug. 25-26 (1998).
2. W.K. Rhim, S.K. Chung, E.H. Trinh, and D.D. Elleman, *Mat. Res. Soc. Symp. Proc.* 87:329-337, 1987.
3. W.K. Rhim and T. Ishikawa, *Rev. Sci. Instrum.* 69:3628-, 1998.
4. K. Ohsaka, S.K. Chung, and W.K. Rhim, *Acta Mater.* 46: 4535-, 1998.
5. S.K. Chung, D.B. Thiessen, and W.K. Rhim., *Rev. Sci. Instrum.* 68:2597-, 1997.
6. A.J. Rulison and W.K. Rhim, *Metall. Mater. Trans. B* 26:503-, 1995.
7. E.H. Trinh, R.G. Holt, and D.B. Thiessen, *Phys. Fluids* 8:43-, 1996.
8. S.K. Chung and E.H. Trinh., *J. Crystal Growth* 194:384-397, 1998.
9. F. Shen and J. Khodadadi, *ASME J. Heat Transfer*, 120:777-, 1998.
10. F. Shen and J. Khodadadi, *Heat Transfer in Microgravity Systems -1993* (Eds.: S.S. Sadhal and A. Hashemi), *Proc. 29th National Heat Transfer Conference*, Atlanta, August 1993}, volume HTD-235, pages 33-42. American Society of Mechanical Engineers, 1993.
11. Y.W. Kim and C.S. Park, *Int. J. Thermophysics* 17:1125-, 1996.
12. J. Murphy and Y. Bayazitoglu, *Numerical Heat Transfer A* 22:109, 1992.

13. P.K. Wong, P.C.W. Fung, and H.L. Tam, *J. Appl. Phys.* 84:6623—, 1998.
14. S.B. Peralta, I.A. Vitkin, K. Ghandi, A. Mandelis, W. Sadowski, and E. Walker, *Photoacoustic and Photothermal Phenomena II.*, pp. 211, Springer, Berlin, 1990.
15. M. Hangyo, S. Nakashima, Y. Oohara, and S. Kimura, *J. Appl. Phys.* 63:295—, 1988.
16. R. Balasubramaniam and A.T. Chai, *J. Colloid Interface Sci.* 119:531—538, 1987.
17. R. Balasubramaniam and J.E. Lavery, *Numerical Heat Transfer A* 16:175—187, 1989.
18. K.D. Barton and R.S. Subramanian, *J. Colloid Interface Sci.* 133:211—222, 1989.
19. Y.K. Bratukhin., *Izv. Akad. Nauk SSSR Mekh. Zhidk. Gaza* 10(5):833—837, 1975.
20. L. Dill, *J. Colloid Interface Sci.* 46:533—540, 1991.
21. M. Hahnel, V. Delitzsch, and H. Eckelmann, *Phys. Fluids A*, 1:1460—1466, 1989.
22. H.S. Kim and R.S. Subramanian, *J. Colloid Interface Sci.* 130:112—129, 1989.
23. H.S. Kim and R.S. Subramanian, *J. Colloid Interface Sci.* 127:417—428, 1989.
24. R.M. Merritt, D.S. Morton, and R.S. Subramanian, *J. Colloid Interface Sci.* 155:200—209, 1993.
25. R.M. Merritt and R.S. Subramanian, *J. Colloid Interface Sci.* 125:333—339, 1988.
26. M. Nallani and R.S. Subramanian, *J. Colloid Interface Sci.* 157:24—31, 1993.
27. D.L.R. Oliver and K.J. De Witt, *Int. J. Heat Mass Transfer* 31:1534—1537, 1988.
28. R.S. Subramanian., *AIChE J.* 27:646—654, 1981.
29. R.S. Subramanian., *Adv. Space Res.* 3:145—153, 1983.
30. R.L. Thompson, *Marangoni Bubble Motion in Zero Gravity*, PhD thesis, University of Toledo, Toledo, Ohio, 1979.
31. N.O. Young, J.S. Goldstein, and M.J. Block, *J. Fluid Mech.* 6:350-356, 1959.
32. K.D. Barton and R.S. Subramanian, *J. Colloid Interface Sci.* 137:170-182, 1990.
33. K.D. Barton and R.S. Subramanian., *J. Colloid Interface Sci* 141:146-156, 1991.
34. Y.S. Kao and D.B.R. Kenning, *J. Fluid Mech.* 53:715-735, 1972.
35. B.K. Larkin, *AIChE J.* 16(1):101-107, 1970.
36. D.M. Mattox, H.D. Smith, W.R. Wilcox, and R.S. Subramanian, *J. Amer. Ceramic Soc.* 65:437-442, 1982.
37. R.M. Merritt and R.S. Subramanian, *J. Colloid Interface Sci.* 131:514-525, 1989.
38. M. Meyyappan and R.S. Subramanian, *J. Colloid Interface Sci.* 115(1):206-219, 1987.
39. M. Meyyappan, W.R. Wilcox, and R.S. Subramanian, *J. Colloid Interface Sci.* 83:199-208, 1981.
40. S.S. Sadhal, *J. Colloid Interface Sci.* 95:283—286, 1983.
41. S.S. Sadhal, P.S. Ayyaswamy, and J.N. Chung, *Transport Phenomena with Drops and Bubbles*, Springer-Verlag, New York, 1997.

FROM OXYGEN GENERATION TO METALS PRODUCTION: IN SITU RESOURCE UTILIZATION BY MOLTEN OXIDE ELECTROLYSIS

Donald R. Sadoway

Massachusetts Institute of Technology

ABSTRACT

The proposed work is in the area of Extraterrestrial Processes and Technology Development, specifically *In Situ* Resource Utilization (ISRU), and seeks to explore the use of molten oxide electrolysis for the generation of oxygen and the production of metals from natural resources found on the Moon/Mars. For the exploration of other bodies in the solar system, electrochemical processing is arguably the most versatile technology for conversion of local resources into usable commodities: by electrolysis one can produce (1) breathable oxygen, (2) silicon for the fabrication of solar cells, (3) various reactive metals for use as electrodes in advanced storage batteries, and (4) structural metals such as steel and aluminum. To date there has been no sustained effort to develop a process, in part due to the inadequacy of the database. The present study will identify chemistries capable of sustaining molten oxide electrolysis in the cited applications and will examine the behavior of laboratory-scale cells designed to generate oxygen and produce metal.

The basic research will include the study of the underlying high-temperature physical chemistry of oxide melts representative of lunar regolith and of Martian soil. To move beyond empirical approaches to process development, the thermodynamic and transport properties of oxide melts will be studied to help set the limits of composition and temperature for the processing trials that will follow. Process efficiency will be investigated in laboratory-scale electrolysis cells. For optimization, the kinetics of the relevant processes at the cathode and the anode will be studied by a.c. voltammetry and electrochemical impedance spectroscopy. The goal of this investigation is to deliver a working prototype cell that can use lunar regolith and Martian soil to produce breathable oxygen along with metal by-product. Additionally, the results of this work can be generalized to permit adaptation to accommodate different feedstock chemistries, such as those that will be encountered on other bodies in the solar system.

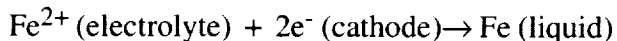
The expected results of the proposed research are (1) the identification of appropriate electrolyte chemistries; (2) the selection of candidate anode and cathode materials compatible with electrolytes named above; and (3) performance data from laboratory-scale cells producing oxygen and metal. This information will enable assessment of the technical viability of molten oxide electrolysis for *in situ* resource utilization on the Moon and Mars. In parallel, there may be commercial applications here on earth, specifically, new "green" technologies for extraction of metals and for treatment of hazardous waste, *e.g.*, fixing heavy metals.

I. Background

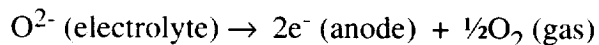
There is plenty of oxygen on the Moon to sustain life — indeed, the lunar surface is over 60% oxygen [1]. Martian soil is about 45% oxygen [2]. However, all of this is chemically bound to other elements in the form of very stable compounds. Molten oxide electrolysis is potentially the basis of a technology for exploiting local resources in order to produce breathable oxygen along with a host of valuable by-products such as silicon for use in solar cells, reactive metals for use in advanced storage batteries, and steel and aluminum for use in construction [3]. No special reagents need to be transported from earth in order to employ the technology. The only process input that needs to be furnished on site is electric power, and this, presumably, can be generated photovoltaically or by nuclear fission. Research conducted at MIT in the laboratory of the Principal Investigator has shown that molten oxide electrolysis has potential for treating certain forms of hazardous waste produced by the metals and chemicals industries while generating oxygen gas as the by-product [4]. For this reason the process is judged to be adaptable to different feedstocks, an attribute making it attractive for use with the resources available on the Moon or Mars.

Molten oxide electrolysis is an extreme form of molten salt electrolysis, a technology that has been producing tonnage metal for over 100 years; aluminum, magnesium, lithium, sodium, and the rare-earth metals are all produced in this manner. What sets molten oxide electrolysis apart is its ability to produce **oxygen gas** at the anode. *No contemporary electrolytic technology can do this*. Indeed, in the light of the push to reduce greenhouse gas emissions in the metals industry one of the greatest challenges for the aluminum industry is the replacement of the consumable carbon anode (which produces CO₂) with a nonconsumable anode, which would produce oxygen [5]. So molten oxide electrolysis then both avoids the use of molten halide electrolytes and enables the production of oxygen gas.

Figure 1 shows how iron and oxygen might be produced by the proposed technology [4]. The reactor depicted is an electrolytic cell, which decomposes iron oxide by the action of electric current passing between two electrodes. The electrolyte in this case is a multicomponent solution consisting of iron oxide and other oxides, such as silica, alumina, magnesia, and calcia. All of these oxides are highly abundant in the lunar regolith [1] and Martian soil [2]. The cathode is a pool of molten iron at the bottom of the cell. At the interface of liquid metal and electrolyte, the electrochemical reduction of iron occurs according to the following reaction:



The origin of the Fe²⁺ is the iron oxide feed, which has dissolved in the molten oxide electrolyte and dissociated to form Fe²⁺ cations and O²⁻ anions. The liquid iron produced is instantly incorporated into the metal pool without the need for mass transport to another site within the cell. Thus, as the reaction proceeds, the depth of the iron pool increases. The solid member forming the floor of the cell and also acting as current collector must be made of a material that is chemically inert in contact with molten iron and also is a good electronic conductor. At the top of the cell is the anode, which acts as the current feeder. The anode must be chemically inert with respect to both oxygen gas and the molten oxide electrolyte. Evolution of oxygen occurs according to the following reaction:



The source of O²⁻ is the iron oxide feed which has dissolved and dissociated in the molten oxide

electrolyte. The anode functions as an electron sink, and the product oxygen gas evolves as bubbles on the surface of the anode and floats to the surface of the melt. Candidate anode materials include electronically conducting oxide and metals protected by an oxide film on the surface [6]. The sidewall consists of electrolyte frozen against a shell made of refractory brick. This is the electrolytic equivalent of skull melting, and is precisely the condition in a modern Hall cell producing tonnage aluminum. Feed consisting of iron oxide is added to the cell from the top. The process is continuous. Periodically, metal is removed from the cell by siphoning.

At 1800 K, the standard free energy of formation of FeO is 159 kJ/mol [7] which via the Nernst equation gives a standard decomposition potential of 0.825 V. In practice, molten salt electrolysis cells operate at about 2 to 2½ times theoretical voltage in order to surmount kinetic barriers and in order to supply adequate energy to keep the electrolyte molten by Joule heating [8], so we can expect the cell in Figure 1 to operate at about 2 V. The value of the current will be governed by the thermal balance of the cell: the current must exceed a minimum level in order to generate adequate Joule heat to keep the electrolyte molten. Given the thermal and electrical properties of molten salts, it turns out that the threshold of thermal sustainability is 1 kA. In one hour, such a cell would produce 1.04 kg iron and 0.30 kg oxygen or 0.23 standard cubic meters oxygen. Current densities in molten salt cells are in the vicinity of 1 A/cm². This means that the anode would be on the order of 30 cm in diameter, immersed in the electrolyte to a depth of 1 cm. This translates into a rather compact device with a small footprint. The oxygen produced at the anode bubbles through the electrolyte and rises to the top of the cell for collection. Molten iron needs to be periodically harvested, and this is typically done by siphon. All that is required to keep the oxygen coming is iron oxide (about 1.4 kg/hr) and electric power (2 kVA).

Recent measurements made in the laboratory of the Principal Investigator have begun to define the range of electrolyte composition suitable for sustaining electrolysis [9,10]. Specifically, we have found that electronic conduction is related to the average valence of dissolved iron; melts of mixed valence (Fe²⁺ and Fe³⁺) provide electronic pathways thanks to valence shifting. The control of total FeO content and melt basicity (ratio of CaO + MgO to SiO₂) is the key to successful management of the electrical properties of these melts. This points to the need for more work on the characterization of the electrical properties of these melts as a function of composition, temperature, and partial pressure of oxygen. Also, there are formidable materials problems associated with the principal elements of the electrolytic cell, i.e., the anode, cathode, and cell wall. In previous work directed at identifying a carbon-free anode for use in the electrolytic production of aluminum, the Principal Investigator has developed a methodology for materials selection [11,12].

II. Electrical Conductivity Measurements

The variation in electrical conductivity with temperature and composition will be measured for multicomponent oxide melts consisting of SiO₂ - Al₂O₃ - MgO - CaO into which FeO and TiO₂ are dissolved. There are no reports in the literature of electrical conductivity measurements in this system. A small body of literature exists, however, on the electrical properties of iron silicate slags [13-15]. Results in these studies indicate that the ferrites display a propensity for electronic conduction. To sustain faradaic processes requires that electronic conduction be kept to a minimum. There is evidence that the conduction mechanism in such melts can be altered by control of the chemical composition. In addition to the approaches described above, the addition of network forming silicates represses electronic conduction [13]. Furthermore, measurements taken recently in the

laboratory of the Principal Investigator on titanium bearing oxide melts indicate again that the mode of electrical conduction can be controlled by tailoring the chemistry of the supporting electrolyte [16]. As NASA confronts the need to exploit *in situ* resources on other bodies in the solar system, a generalizable set of electrolyte design criteria would prove to be of value: hence, the interest in learning to control the electrical properties of melts containing various transition-metal oxides.

The variation in electrical conductivity of oxide melts representative of lunar regolith and Martian soil will be measured by electrochemical impedance spectroscopy (EIS) using a new technique invented by the Principal Investigator and co-workers [9, 17, 18]. Attention will be paid to the SiO_2 - Al_2O_3 - MgO - CaO system with varying amounts of FeO and TiO_2 . Data will be fitted to a quasi-chemical solution model to determine how to optimize the ionic conductivity of the melts.

III. Kinetic Studies of Electrode Processes

To optimize the throughput of a reactor it is necessary to know the values of the relevant kinetic parameters. In an electrochemical reactor, this includes the rate constants of the reactions at each electrode. Cathodic and anodic processes will be studied by a.c. voltammetry and EIS. In a.c. voltammetry one imposes on the working electrode a voltage of the form, $E_{\text{dc}} + \Delta E \sin \omega t$, and monitors the a.c. component of the current response, I_{ac} [19]. The plot of I_{ac} vs E_{dc} reveals not only the identities of the species undergoing electrochemical conversion, but also their relative concentrations and valences in the melt.

IV. Electrolysis Trials

The viability of molten oxide electrolysis for oxygen generation and for metal production (silicon, iron, and aluminum) will be tested in bench-scale experiments consisting of galvano-static electrolysis of candidate melts. The anode gas will be sampled and analyzed in real time by gas chromatography to confirm oxygen evolution and to detect the presence of impurities. The cathodic metal product will also be subjected to chemical analysis [20, 21]. The newly acquired data in parts (a) and (b) will influence the choice of composition of the electrolyte and cell operating parameters, *e.g.*, temperature, current density, concentration of electroactive species. Effectiveness will be judged on the basis of the chemical analyses of cell products, both metal and gas. The measured values of cell operating parameters along with a mass balance will permit an accurate calculation of the cell's productivity. This will permit the determination of the size of cell necessary to meet the oxygen requirements a space colony.

V. Construction of Prototype Electrolytic Cell

On the basis of the results from parts (a) through (c) a prototype electrolytic cell capable of producing oxygen from lunar regolith and Martian soil will be designed, constructed, and tested at the bench scale. Performance characteristics will be measured.

REFERENCES

1. L. Haskin and P. Warren, "Lunar Chemistry," in Lunar Sourcebook, Chapter 8, G.H. Heiken, D.T. Vaniman, and B.M. French, editors, Cambridge University Press, Cambridge, 1991, pp. 357-474.

2. R. Reider, T. Economou, H. Wänke, A. Turkevich, J. Crisp, J. Brückner, G. Dreibus, and H.Y. McSween, Jr., "The Chemical Composition of Martian Soil and Rocks Returned by the Mobile Alpha Proton X-ray Spectrometer: Preliminary Results from the X-ray Mode," *Science*, 278, 1771-1774 (1997).
3. D.R. Sadoway, "New Opportunities for Metals Extraction and Waste Treatment by Electrochemical Processing in Molten Salts," *J. Mater. Res.*, 10 (3), 487-492 (1995).
4. D.R. Sadoway, "New Opportunities for Waste Treatment by Electrochemical Processing in Molten Salts," in *Metals and Materials Waste Reduction, Recovery and Remediation*, K.C. Liddell, R.G. Bautista, and R.J. Orth, editors, TMS, Warrendale, PA, 1994, pp. 73-76.
5. *Inert Anode Roadmap: A Framework for Technology Development*, The Aluminum Association, Washington, DC, February, 1998.
6. D.R. Sadoway, inventor, Massachusetts Institute of Technology, assignee, "Electrolytic Production of Metals Using Consumable Anodes," U.S. patent no. 5,185,068, February 9, 1993.
7. M.W. Chase, Jr., C.A. Davies, J.R. Downey, Jr., D.J. Frurip, R.A. McDonald, and A.N. Syverud, *JANAF Thermochemical Tables*, 3rd edition, part II, American Institute of Physics, Inc., New York, 1986.
8. N. Jarrett, "Aluminum Smelting: Past, Present, and Future Challenges," in *Tutorial Lectures in Electrochemical Engineering and Technology*, R.A. Alkire and T. Beck, editors, American Institute of Chemical Engineers, New York, 1981, pp. 27-38.
9. S.L. Schiefelbein and D.R. Sadoway, "A High-accuracy, Calibration-free Technique for Measuring the Electrical Conductivity of Molten Oxides," *Metall. Materials Trans. B*, 28 B, 1141-1149 (1997)
10. A.C. Ducret and D.R. Sadoway, "Measurements of Electrical Conductivity and Transference Number of Melts in the FeO - CaO - MgO - SiO₂ System," in preparation for submission to *Metall. Materials Trans. B*.
11. D.R. Sadoway, "A Materials Systems Approach to Selection and Testing of Nonconsumable Anodes for the Hall Cell," *Light Metals 1990*, C.A. Bickert, editor, TMS, Warrendale PA, 1990, pp. 403-407.
12. J.N. Hryn and D.R. Sadoway, "Cell Testing of Metal Anodes for Aluminum Electrolysis," *Light Metals 1993*, S.K. Das, editor, TMS, Warrendale PA, 1993, pp. 475-483.
13. M.T. Simnad, G. Derge, and I. George, *J. Metals*, 6 (1954), 1954.
14. K.C. Mills, *ISIJ International*, 33, 148-155 (1993).
15. K.C. Mills and B.J. Keene, *Internat. Mater. Rev.*, 32, 1-37 (1987).
16. N.A. Fried and D.R. Sadoway, "Electrical Conductivity Measurements of Binary Solutions of Molten TiO₂ - BaO," in preparation for submission to *Metall. Materials Trans. B*.
17. S.L. Schiefelbein, N.A. Fried, K.G. Rhoads, and D.R. Sadoway, "A high-accuracy, calibration-free technique for measuring the electrical conductivity of liquids," *Rev. Sci. Instrum.*, 69 (9), 3308-3313 (1998).
18. D.R. Sadoway, K.G. Rhoads, N.A. Fried, and S.L. Schiefelbein, inventors, Massachusetts Institute of Technology, assignee, "High Accuracy Calibration-free Electrical Parameter Measurements using Differential Measurement with respect to Immersion Depth," U.S. patent no. 5,489,849, February 6, 1996.
19. A.J. Bard and L.R. Faulkner, *Electrochemical Methods*, Wiley, New York, 1980, Chapter 9.
20. H. Zhu and D.R. Sadoway, "The Electrode Kinetics of Perfluorocarbon (PFC) Generation," *Light Metals, 1999*, C.E. Eckert, editor, TMS, Warrendale, PA, 1999, pp. 241-246.
21. S.S. Nissen and D.R. Sadoway, "Perfluorocarbon (PFC) Generation in Laboratory-Scale Aluminum Reduction Cells," *Light Metals, 1997*, R. Huglen, editor, TMS, Warrendale, PA, 1997, pp. 159-164.

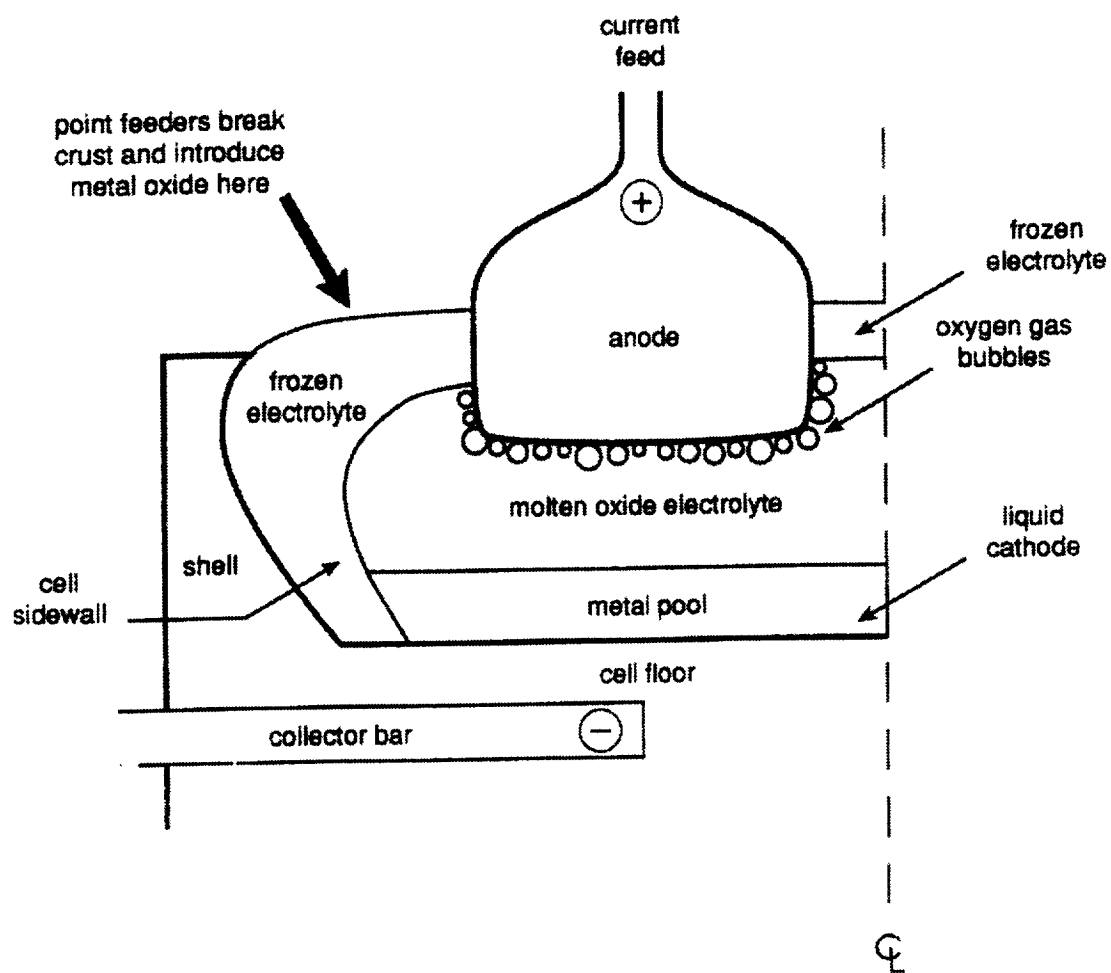


Figure 1. Schematic of cell for production of oxygen by molten oxide electrolysis.

THERMOPHYSICAL PROPERTIES OF HIGH TEMPERATURE LIQUID METALS AND ALLOYS

Robert Schaefer¹, Shankar Krishnan², and Konstantinos Boboridis¹

¹National Institute of Standards and Technology, Gaithersburg, MD

²Containerless Research, Inc., Evanston, IL

The objective of this research is to extend, for the first time, the laser polarimetry technique for measuring the normal spectral emissivity to the microsecond time regime. This will enable accurate determination of true temperature of liquid specimens at high temperatures in rapid pulse heating experiments. In addition to the measurement of other experimental quantities, the technique will yield data on selected thermophysical properties with unsurpassed accuracy that can be used in support of microgravity materials science research. The properties measured include enthalpy, specific heat capacity, heat of fusion, and electrical resistivity up to and above the melting point of selected refractory metals and alloys. The key accomplishment of this research is that the laser polarimeter system has been applied to microsecond pulse heating studies and absolute true temperature measurements have been obtained to provide the basis for accurate thermophysical property measurements in the liquid state.

Thermophysical property values for liquid metals and alloys are needed in modeling solidification, casting design, crystal growth and in welding designs. A number of these processes (and related experiments) are currently being practiced in the reduced gravity environment of space. The present research supports these efforts by aiming to provide thermophysical measurements methodology and thermophysical data of unsurpassed accuracy on standard materials, pure elements and alloys of importance to NASA's microgravity mission.

Several years ago, the National Institute of Standards and Technology and Containerless Research, Inc. began a NASA-sponsored joint effort to integrate the laser polarimeter and the millisecond pulse-heating system to conduct research with the objective of validating and establishing the accuracy of the laser polarimetry method and obtaining accurate emissivity data on selected metals. An initial three-year National Research Announcement (NRA) program resulted in the validation of the laser polarimetric technique and the determination of the spectral emissivity and thermophysical properties on a number of materials at temperatures up to and including the melting point [1-4]. Three years ago, we began the current NRA program aimed at extending the operating range of this system for the measurement of spectral emissivities and true temperature into the liquid state by integration of a microsecond pulse-heating and pyrometry system with an ultra-high speed laser polarimeter system. These studies have advanced significantly in the last three years leading to the complete development and validation of a new ultra-high speed laser polarimeter system for the measurement of normal spectral emissivity of liquid materials with microsecond time resolution, allowing determination of true temperature and thermophysical properties in the liquid state during microsecond pulse-heating.

The microsecond pulse heating system was modified to accommodate a new chamber, new electrical and electronic systems to control the pulse heating and provisions to accommodate the ultra-high speed polarimeter system. A single wavelength pyrometer was used to measure the radiance temperature of the specimen at an effective wavelength of 652 nm, which is close to the laser polarimeter's operating wavelength of 677 nm. In addition, the voltage drop across a known specimen length (with the aid of voltage probes) and the current through the specimen are also recorded precisely. Preliminary studies were conducted in the past year leading to the first precise results of the normal spectral emissivity, true temperature, enthalpy, heat capacity and electrical resistivity of liquid niobium at temperatures up to 500 K above the melting point. Preliminary results for liquid niobium in the 2800-3300K temperature range for the emissivity, enthalpy, resistivity and heat capacity were presented at the previous conference [5]. New results will be presented on pure Nb, Ti, and Nb-Ti alloys.

In addition, the methods of calibration of the polarimeter, the experimental techniques employed for pulse-heating and methods of data analysis will be presented and discussed. Calibration techniques for polarimetry and pyrometry, error analysis, and uncertainties of the results will be provided.

In summary, this NRA project has resulted in a successful demonstration of the application of high-speed laser polarimetry to microsecond pulse-heated materials leading to absolute true temperature measurements on liquid materials at temperatures above the melting point. This has led to significant reduction in uncertainties of various thermophysical properties of liquid materials including heat capacity, electrical resistivity and enthalpy. The results from the present work serve as a point of reference for future ground-based and flight-based experiments that involve either the measurement of thermophysical property data or the use of these data in the design and implementation of future materials science experiments in microgravity.

REFERENCES

1. A. Cezairliyan, S. Krishnan, and J. L. McClure, *Int. J. Thermophys.*, 17, 1455 (1996) .
2. A. Cezairliyan, S. Krishnan, J. L. McClure and D. Basak, *Int. J. Thermophys.*, 19, 1267 (1998).
3. S. Krishnan and D. Basak, *Int. J. Thermophysics*, 20, 1811 (1998).
4. D. Basak, W. J. Boettinger, D. Josell, S. R. Coriell, J. L. McClure, S. Krishnan and A. Cezairliyan, *Acta Met.*, 47, 3147 (1999).
5. S. Krishnan and K. Boboridis, *Rev. Sci. Instrum.*, Submitted for publication, 2000.

LATTICE BOLTZMANN COMPUTATIONS OF BINARY DIFFUSION IN LIQUIDS UNDER STOCHASTIC MICROGRAVITY

Robert F. Sekerka

Physics and Mathematics, Carnegie Mellon University
Pittsburgh, PA 15213

ABSTRACT

The broad objective of this research is to further develop the Lattice Boltzmann (LB) model in binary liquids as a computational tool in order to better understand convective diffusion in stochastic microgravity. We focus on binary liquid alloy diffusion couples and seek to estimate the accuracy of, or make corrections to, binary liquid diffusivities measured in microgravity. We hypothesize that the Lattice Boltzmann model might be superior to computational fluid dynamics for computation of diffusion and fluid flow in binary liquids under the influence of *stochastic* microgravity because the LB model is intrinsically statistical and therefore more compatible with stochastic forces. The ultimate objective is to provide powerful computational methods to analyze the effects of stochastic microgravity on various space experiments that involve convective diffusion in liquids. The methodology requires reformulation of the LB model for binary fluids to account for non-solenoidal flows for species of different mass and for incompressible fluids whose density is a function of composition. Finite Difference Lattice Boltzmann models are used in order to allow the space lattice to be decoupled from the velocity discretization. Such models will first be used to explore the effect of periodic g-jitter on measured diffusivities in microgravity. Then the effect of stochastic g-jitter will be studied.

I. Introduction

We hypothesize that the Lattice Boltzmann (LB) model might be superior to computational fluid dynamics (CFD) for computation of diffusion and fluid flow in binary liquids under the influence of *stochastic* microgravity. We make this conjecture because the LB model, which is based on a distribution function, is intrinsically statistical and therefore more compatible with stochastic forces. The ultimate objective of this research is to further develop the Lattice Boltzmann model in binary liquids as a computational tool to better understand convective diffusion in stochastic microgravity. We approach this problem by focusing on binary liquid alloy diffusion couples. In particular, we shall seek to estimate the accuracy of, or make corrections to, binary liquid diffusivities measured in microgravity. The binary liquid diffusion couple will serve as a prototype problem for other experiments that have been or will be conducted in microgravity, for example, solidification (crystal growth) from binary melts. Thus, this research is likely to result in powerful computational methods to analyze the effects of stochastic microgravity on various space experiments that involve convective diffusion in liquids.

It is well known that diffusivities in binary liquids are difficult if not impossible to measure accurately on Earth because of solute transport due to buoyancy driven fluid convection. Consequently, diffusivities

that have been measured in microgravity have resulted in dramatic differences from measurements on Earth [1-7]. Nevertheless, there is still some convection in the microgravity environment, and this can affect measured diffusivities. Recent measurements by Smith [7] for alloys of Pb-Au, Pb-Ag, Pb-Sb, Sb-In and In-Sb result in considerable differences of the measured diffusivity D on temperature T : Arrhenius on Earth, proportional to T^2 in microgravity with g -jitter, and proportional to T in microgravity with g -jitter damped by means of an isolation platform. In order to understand these and other measurements, it is necessary to model the influence of residual convection on diffusion in microgravity.

In our previous research [8,9] supported by NASA, we have shown that non-solenoidal flows caused by density changes during transient diffusion are present in even strictly zero gravity and can be comparable at short times to buoyancy-driven flows in microgravity. This has also been confirmed in numerical computations by Bune *et al.* [10] who refer to it as “stealth convection.” Thus, the results of using computational fluid dynamics codes based on the Oberbeck-Boussinesq (OB) approximation [11] are unreliable at short times for transient diffusion in microgravity because the OB approximation includes the assumption of solenoidal flows. Since there are still residual accelerations (equivalently residual gravity) in the microgravity environment [12-18], there are buoyancy driven flows that can affect measured diffusivities [19].

We decompose the residual acceleration as $\mathbf{g} = \mathbf{g}_s + \mathbf{g}_j$ where \mathbf{g}_s is a rather steady acceleration, due for example to drag, and \mathbf{g}_j is the so-called g -jitter. The component \mathbf{g}_s varies slowly over a time scale that is large compared to the characteristic time scale of g -jitter but small compared to the period of a space-craft orbit. Such g -jitter can have both deterministic components with some well-defined frequency ω_0 as well as stochastic components that can only be described statistically. A model for g -jitter based on a narrow band noise has been proposed and explored in our previous research supported by NASA [20-23]. It is very difficult to incorporate stochastic accelerations in numerical computations by using CFD. This follows because the use of standard numerical algorithms to solve stochastic differential equations is subject to numerical instabilities and large errors (including apparent convergence to false values), due to the fact that the stochastic terms are not differentiable. The LB model [24-26] is an intrinsically statistical model that can be used to simulate fluid dynamics. For simple problems, it is much less efficient than CFD, but for more complicated problems, such as convective diffusion in binary liquids with stochastic forces, it might well be better.

II. Lattice Boltzmann Model

The Lattice Boltzmann model is based on a distribution function such that $f^\sigma(\mathbf{r}, \mathbf{v}, t) d^3x d^3v$ is the number of particles of type $\sigma = A, B$ which at time t have positions \mathbf{r} in the volume element d^3x about \mathbf{r} and velocities \mathbf{v} in the volume element d^3v about \mathbf{v} . The distribution function is assumed to obey a Boltzmann equation in the relaxation time approximation of the form

$$\left(\frac{\partial}{\partial t} + \mathbf{v} \cdot \nabla_{\mathbf{r}} + \frac{\mathbf{F}^\sigma}{m^\sigma} \cdot \nabla_{\mathbf{v}} \right) f^\sigma(\mathbf{r}, \mathbf{v}, t) = - \frac{1}{\tau^\sigma} [f^\sigma(\mathbf{r}, \mathbf{v}, t) - f_{\text{eq}}^\sigma(\mathbf{r}, \mathbf{v}, t)] \quad (1)$$

where \mathbf{F}^σ is the force on a particle of mass m^σ and τ^σ is a physical relaxation time, comparable to the collision time of fluid particles. The distribution relaxes toward its equilibrium value for a fluid of average local number density

$$n^\sigma(\mathbf{r}, t) = \int f^\sigma(\mathbf{r}, \mathbf{v}, t) d^3v \quad (2)$$

and local velocity

$$\mathbf{u}^\sigma(\mathbf{r}, t) = \frac{1}{n^\sigma(\mathbf{r}, t)} \int \mathbf{v} f^\sigma(\mathbf{r}, \mathbf{v}, t) d^3v \quad (3)$$

In typical LB models, the equilibrium distribution function is taken to be the Maxwell-Boltzmann distribution function

$$f_{\text{eq}}^\sigma(\mathbf{r}, \mathbf{v}, t) = n^\sigma(\mathbf{r}, t) \left(\frac{m^\sigma}{2\pi kT} \right)^{3/2} e^{-(m^\sigma/2 kT)[\mathbf{v} - \mathbf{u}(\mathbf{r}, t)]^2}, \quad (4)$$

where k is Boltzmann's constant.

For a system not too far from equilibrium, we can approximate the force term in Equation (1) by replacing the distribution function by its equilibrium value. The LB model is then completed by discretizing the velocity space [27-31] and solving the resulting equations numerically. To discretize, we replace $f^\sigma(\mathbf{r}, \mathbf{v}, t) d^3v$ for $\mathbf{v} = \mathbf{v}_i$ by $f_{\sigma i}(\mathbf{r}, t)$ and then replace integrals over the velocity by sums over i . Thus the discrete distribution functions obey

$$\left(\frac{\partial}{\partial t} + \mathbf{v}_i \cdot \nabla \right) f_{\sigma i}(\mathbf{r}, t) = - \frac{1}{\tau^\sigma} [f_{\sigma i}(\mathbf{r}, t) - f_{\sigma i}^{\text{eq}}(\mathbf{r}, t)] + \frac{\mathbf{F}^\sigma}{kT} [\mathbf{v}_i - \mathbf{u}(\mathbf{r}, t)] f_{\sigma i}^{\text{eq}}(\mathbf{r}, t) \quad (5)$$

Equation (5) can be solved numerically by a number of techniques. Some LB models are solved by means of "streaming algorithms" [24-26] in which the spatial grid is tied to the time steps by means of an equation of the form $\delta \mathbf{r} = \mathbf{v}_i \delta t$. It is far less restrictive, however, to discretize space over distances that are large compared to the mean free path but small compared to distances over which $n(\mathbf{r}, t)$ and $\mathbf{u}(\mathbf{r}, t)$ vary significantly. This leads to Finite Difference Lattice Boltzmann (FDLB) models [32-33], which we use. To be useful in microgravity, these models must incorporate non-solenoidal flows, which we now discuss.

III. Non-Solenoidal Flows

We can illustrate the importance of non-solenoidal flows quite simply if the density, ρ , is related to the mass fraction of solute, ω , by the equation

$$1/\rho = \bar{V}_1 + (\bar{V}_2 - \bar{V}_1) \omega \quad (6)$$

where \bar{V}_1 and \bar{V}_2 are partial specific volumes, assumed to be constant. Then the continuity equation

$$\frac{D\rho}{Dt} + \rho \nabla \cdot \mathbf{v} = 0 \quad (7)$$

and the convective diffusion equation

$$\rho \frac{D\omega}{Dt} + \nabla \cdot \mathbf{j} = 0 \quad (8)$$

can be combined to yield

$$\nabla \cdot \mathbf{v} = - (\bar{V}_2 - \bar{V}_1) \nabla \cdot \mathbf{j}. \quad (9)$$

From Equation (9) we see that a nonvanishing divergence of diffusive flux, which will always result when ω is changing with time, will demand a nonvanishing barycentric velocity. Integration of Equation (9) yields

$$\mathbf{v} = -(\bar{V}_2 - \bar{V}_1) \mathbf{j} + \nabla \times \mathbf{A} \quad (10)$$

where the vector field \mathbf{A} leads to a solenoidal field that is necessary to satisfy the boundary conditions (such as no slip conditions at the walls of the container). This type of convection, *demanded* by the continuity equation during transient diffusion (as in a diffusion couple), does not require a body force such as gravity [8,9]. It will actually dominate buoyancy driven convection for a phenomenon of characteristic length L whenever $|\mathbf{g}| < \nu D/L^3$ where ν is the kinematic viscosity. For $\nu \sim 10^{-3} \text{ cm}^2/\text{s}$, $D \sim 5 \times 10^{-5} \text{ cm}^2/\text{s}$ and $L \sim 5 \times 10^{-2} \text{ cm}$, one obtains $|\mathbf{g}| < 4 \times 10^{-3} \text{ cm/s}^2$. For transient diffusion one should use $L \sim (Dt)^{1/2}$ which shows that non-solenoidal flows will be especially important at short times. Such non-solenoidal convection has also been studied [34-35] in the analogous situation of heat conduction, in which case the thermal diffusivity κ replaces D . Since κ is typically $10^4 D$, the above estimate would lead to much larger values of $|\mathbf{g}|$ for the same value of L . As mentioned above, such non-solenoidal flow has been studied recently by other researchers and referred to as “stealth convection” [10].

IV. Discussion

We have conducted preliminary simulations based on Equation (5) for ideal solutions and no external forces when both species have the same mass. The resulting interdiffusion profiles agree well with analytical solutions. The challenge is now to incorporate interatomic forces to guarantee Equation (6) as well as local momentum conservation when the masses are different. Although there are several prescriptions [36-40] for handling binary and multicomponent LB models, they have not been tested except for equilibrium. Once we are assured that our model properly describes interdiffusion for no external forces, including non-solenoidal flows, we will proceed to add g-jitter, both deterministic and stochastic.

REFERENCES

1. A.O. Ukanwa, “M558 Radioactive Tracer Diffusion,” in *Proceeding III Space Processing Symposium Skylab Results*, Marshall Space Flight Center, Huntsville, AL, Vol. 1, 425-456 (1974)
2. Y. Malmejac and G. Frohnberg, “Mass Transport by Diffusion,” in *Fluid Sciences and Materials Science in Space*, edited by H.U. Walter (European Space Agency, Springer-Verlag, NY 1987) Chapter V, pp. 159-190
3. S. Van Vaerenberg, J.C. Legros and J.C. Dupin, “First results of Soret coefficient measurement,” *Advances in Space Research* 16 69 (1995)
4. R.W. Smith and X. Zhu, “Diffusion in Liquid Pb-Au Binary System,” *Materials Science Forum* 113 215-216 (1996)
5. L.B. Jalbert, R.M. Banish and F. Rosenberger, “Real time diffusivity measurements in liquids at several temperatures with one sample,” *Physical Review E* 57 1727 (1998)
6. A. Griesche, K.H. Kraatz and G. Frohberg, “A modified shear cell for mass transport measurements in melts,” *Rev. Sci. Instruments* 69 315-316 (1998)
7. R.W. Smith, “The influence of g-jitter on liquid diffusion – the QUELD.MIM/MIR programme,” *Microgravity Science and Technology*, 11 (1999) 78-84
8. P.S. Perera and R.F. Sekerka, “Non solenoidal flow in a liquid diffusion couple,” *Physics of Fluids* 9 376-391 (1997)
9. P.S. Perera, “Liquid Diffusion Couple in a Microgravity Environment,” Doctoral Thesis, Carnegie Mellon University (1997)
10. Andris V. Bune, Donald C. Gillies and Sandor L. Lehoczy, “Double-Diffusive Convection under Microgravity Conditions: Numerical Modeling with and without Oberbeck-Boussinesq Approximation,” *Journal of the Japan Society of Microgravity Application* 15 Supplement II, 235-237 (1999)

11. D.D. Joseph, *Stability of fluid motions II* (Springer-Verlag, Berlin, 1976) Ch. VIII, pp. 1-3
12. H. Hamacher, B. Fitton and J. Kingdon, "The Environment of Earth Orbiting Systems," in *Fluid Sciences and Materials Science in Space*, edited by H.U. Walter (European Space Agency, Springer-Verlag, NY 1987) Chapter I, pp. 1-50
13. V.A. Sarychev, V.V. Sazanov, M. Yu. Belyaev, S.G. Zykov and V.M. Stazhkov, "Microaccelerations on the Board of the Earth's Artificial Satellites," *Hydromechanics and Heat/Mass Transfer in Microgravity*, Reviewed Proc. First Internat. Symposium, Perm-Moscow, Russia 1991 (Gordon and Breach, Amsterdam, 1992) pp. 25-30
14. M.J.B. Rogers and J.I.D. Alexander, "Analysis of Spacelab 3 Residual Acceleration Data," *AIAA Journal of Spacecraft and Rockets* 28 52-59 (1992)
15. M.J.B. Rogers and J.I.D. Alexander, "Residual acceleration data analysis for spacelab missions," *Microgravity Science and Technology* 5 43-49 (1992)
16. R. Wolf, M.J.B. Rogers and J.I.D. Alexander, "A residual acceleration data analysis and management system," *Advances in Space Research* 13 (7)256-(7)265 (1993)
17. M.J.B. Rogers, J.I.D. Alexander and J. Schoess, "Detailed analysis of Honeywell In-Space accelerometer data - STS-32," *Microgravity Science and Technology* 6 28-35 (1993)
18. M.J.B. Rogers, B.P. Matisak and J.I.D. Alexander, "Venting force contributions to acceleration on USML-1," *Microgravity Science and Technology* 7 293-297 (1995)
19. J.I.D. Alexander, J.F. Ramus and F. Rosenberger, "Numerical Simulation of the Convective Contamination of Diffusivity Measurements in Liquids," *Microgravity Science and Technology* 9 158-162 (1996)
20. J. Casademunt, W. Zhang, J. Viñals and R. F. Sekerka, "Stability of a Fluid Surface in a Microgravity Environment," *AIAA Journal* 31 2027-2032 (1993)
21. Wenbin Zhang, Jaume Casademunt and Jorge Viñals, "Study of the parametric oscillator driven by narrow-band noise to model the response of a fluid surface to time-dependent accelerations," *Physics of Fluids A* 5 3147-3161 (1993)
22. F. Drolet and J. Viñals, "Onset of oscillating instabilities under stochastic modulation," *Physical Review E* 56 2649 (1997)
23. J.R. Thomson, J. Casademunt and J. Viñals, "Cavity flow induced by a fluctuating acceleration field," *Physics of Fluids A* 7 292 (1995)
24. Shiyi Chen and Gary D. Doolen, "Lattice Boltzmann Methods for Fluid Flows," *Annual Review of Fluid Mechanics* 30 (1998) 329-364
25. D.H. Rothman and S. Zaleski, *Lattice-Gas Cellular Automata, Simple Models of Complex Hydrodynamics*, Cambridge University Press, Cambridge 1997
26. B. Chopard and M. Droz, *Cellular Automata Modeling of Physical Systems*, Cambridge University Press, Cambridge (1998)
27. G.R. McNamara and G. Zanetti, "Use of the Boltzmann equation to simulate lattice-gas automata," *Physical Review Letters* 61 (1988) 2332
28. F.J. Higuera and J Jimenez, "Boltzmann approach to lattice gas simulations," *Europhysics Letters* 9 (1989) 663
29. S. Succi, R. Benzi and F.J. Higuera, "The lattice-Boltzmann equation - a new tool for computational fluid dynamics," *Physica C* 47 (1991) 219
30. R. Benzi, S. Succi and M. Vergassola, "The Lattice Boltzmann Equation: Theory and Applications," *Physics Reports* 222 (1992) 145
31. Y.H.Qian, D.D'Humières and P.Lallemand, "Lattice BGK models for Navier Stokes Equations," *Europhysics Letters* 17 (1992) 479

32. N. Cao, S. Chen, S. Jin and D. Martinez, "Physical symmetry and lattice symmetry in the lattice Boltzmann method," *Physical Review E* 55 (1997) R21
33. X. He and L.S. Luo, "A priori derivation of the lattice Boltzmann equation," *Physical Review E* 55 (1997) R6333
34. V. V. Pukhnachov, "Model of convective motion under low gravity," in *Proceedings of the VIIIth European Symposium on Materials and Fluid Sciences in Microgravity*, Brussels, Belgium 12-16 April 1992 (ESASP), pp. 157-160
35. V. V. Pukhnachov, "Mathematical model of natural convection under low gravity," *IMA Preprint Series* #796, University of Minnesota, Minneapolis, MN (May 1991)
36. E. Orlandini, M.R. Swift and J.M. Yeomans, "Lattice Boltzmann Model of Binary Fluid Mixtures," *Europhysics Letters* 32 (1995) 463
37. X. Shang and G. Doolen, "Multicomponent Lattice-Boltzmann Model with Interparticle Interactions," *J. Statistical Physics* 81 (1995) 379
38. M.R. Swift, E. Orlandini, W.R. Osborn and J.M. Yeomans, "Lattice Boltzmann simulations of liquid-gas and binary fluid systems," *Physical Review E* 54 (1996) 5041-5052
39. Nicos S. Martys and Hudong Chen, "Simulation of multicomponent fluids in complex three-dimensional geometries by the Lattice Boltzmann method," *Physical Review E* 53 (1996) 743
40. X. Shang and G. Doolen, "Diffusion in a multicomponent lattice Boltzmann equation model," *Phys. Rev. E* 54 (1996) 3614

INFLUENCE OF PROCESSING ON THE DYNAMICAL PROPERTIES OF GLASSY NETWORKS

N.I. Agladze and A.J. Sievers

Laboratory of Atomic and Solid State Physics and Center for Radiophysics and Space Research,
Cornell University
Ithaca, NY 14853-2501

Low temperature specific heat measurements on glasses reveal a linear temperature dependence [1] quite different from that found for crystals. The introduction of two level systems (TLS's) [2,3], in which the low lying dynamics of amorphous materials is characterized by atoms or groups of atoms tunneling, has enjoyed outstanding success in explaining this and other observations, with an admittedly parameterized model. Although these materials have been studied for over 20 years with a variety of experimental techniques and theoretical descriptions [4], the source of the TLS's described in these original proposals remains a mystery. Two basic questions remain unanswered: why the density of tunneling states is comparable for all amorphous substances and its microscopic origin? So far all studies have ignored the possibility that the glass production techniques may be obscuring the validity of any such comparisons.

There are a number of indicators that the dynamics of strong and fragile [5] glass formers may appear in the low temperature dynamical properties of the glasses. The high-density amorphous (HDA) phase [6] of ice is known to undergo a first order transition to a low-density amorphous (LDA) phase on warming to about 120 K [7-11]. Recently far infrared absorption measurements have been carried out on bulk amorphous ice produced by a pressure-induced amorphization process, which has the attractive feature that both the low density amorphous (LDA) phase and the high density amorphous (HDA) one [7] can be examined sequentially. The measurements on the low temperature far infrared absorption spectra of the LDA phase demonstrates that it does not display the supposedly universal two level systems (TLS) associated with the amorphous state despite its known amorphous properties [12]. A consistent way to account for the disappearance of TLS in the far infrared absorption data after the HDA sample has been cycled to the LDA, or water II phase [13], is to recognize that the supercooled liquid in this water II phase is a strong liquid in Angell's strong/fragile classification scheme [14]. For such a strong liquid the defects in the rigid disordered network can, in principle, be annealed out. On the other hand, the HDA phase is thought to be extremely fragile and, in this limit, the defects are intrinsic and, in fact, are responsible for the relaxational dynamics producing the fragile behavior. The conclusion is that the presence of such intrinsic defects in the HDA phase gives rise to the TLS. A very general implication about the dynamics of all glasses stems from these unusual experimental results: two level systems universally found in all glasses may be a product of structural defects produced at glass inhomogeneities when the glass is formed. Although they are intrinsic for the fragile glass formers, for the class of strong liquids there is the likelihood that under controlled conditions such defects, and hence the TLS associated with them, may be eliminated.

In addition, it has been found that when SiO_2 is doped with Na_2O or K_2O , which makes the resulting system more fragile, then there is a large increase in the magnitude of the linear term and a slight increase in the size of the cubic term in the specific heat [15]. These findings are consistent with the idea that the resulting system is shifted toward the fragile region where defects are less likely to be annealed out. However, when the linear term specific heat values for a variety of systems of different fragility are compared, the dependence of this linear term on fragility remains unclear with one group reporting that there is a connection [16,17] while another group reports the opposite conclusion [18]. So far all of the studies have ignored the possibility that the glass production techniques may be obscuring the validity of any such comparisons.

Given that the structural network of μ -g produced glasses should be vastly superior to those produced in a 1-g environment and provide a more intrinsic configuration of the glass network then the analysis of the relationship between homogeneity, the strong/fragile classification scheme, structural defects and the low temperature dynamical properties of glasses takes on new meaning. We shall apply the techniques of specific heat, IR absorption, and Raman scattering to characterize the defects in glasses produced in the microgravity environment and compare them with that obtained with ground based experiments using containerless techniques for glass processing.

Microgravity studies of both chalcogenide and silicate glasses have demonstrated that the suppression of convective transport processes in the melt not only increases the probability for glass formation over a wider compositional range but also increases the compositional homogeneity in such microgravity processed glasses by over an order of magnitude when compared to 1-g glasses. In preparing a glass by quenching a liquid, as it is customary in the space experiments, control of nucleation is the key [19]. The heterogeneous nucleation on impurities and on container walls and surfaces is the controllable parameter in this case whereas homogeneous nucleation is an intrinsic process determined by the material itself. In microgravity conditions the buoyancy is absent and the related convection responsible for transport of nucleation centers from the wall into the bulk is removed. In this case homogeneous nucleation determines the critical cooling rate of undercooled melt from which the glass is formed, therefore, the range of glass formation is increased. This is not the only consequence of microgravity processing. Another important result is that the glass turns out to be much more uniform. Even without containerless processing the inhomogeneities caused by heterogeneous nucleation next to the container wall does not penetrate very far into the bulk of the sample. During the D1 mission on board the space shuttle 'Challenger' in 1985, glasses of the binary system $\text{Li}_2\text{O-SiO}_2$ were melted in platinum crucibles [20]. The same heating facility was used to produce reference samples under normal gravity conditions. The electron microprobe composition scans of the microgravity and the reference samples, which are displayed in Figure 1, show that compositional uniformity of the flight sample was more than order of magnitude better than the normal gravity reference one. Deviations from the nominal composition are found only near the container wall for the flight sample, whereas a high degree of scattering is observed for the reference sample both near the wall and in the bulk.

We propose to investigate the dependence of the two level spectrum on defect concentration for a number of glasses with varying fragilities starting with GeO_2 . Such a strong glass former is expected to produce the most dramatic change in the TLS concentration due to μ -g processing. The critical cooling rate for GeO_2 as estimated from homogeneous nucleation theory is slow so the optimum cooling time for this glass is on the order of a few hours. Similar analysis of the other simple glasses indicates that the duration of the cooling stage is long enough to exclude drop tube or parabolic flight possibilities. Different experimental techniques, which are very sensitive to TLS, will be used to

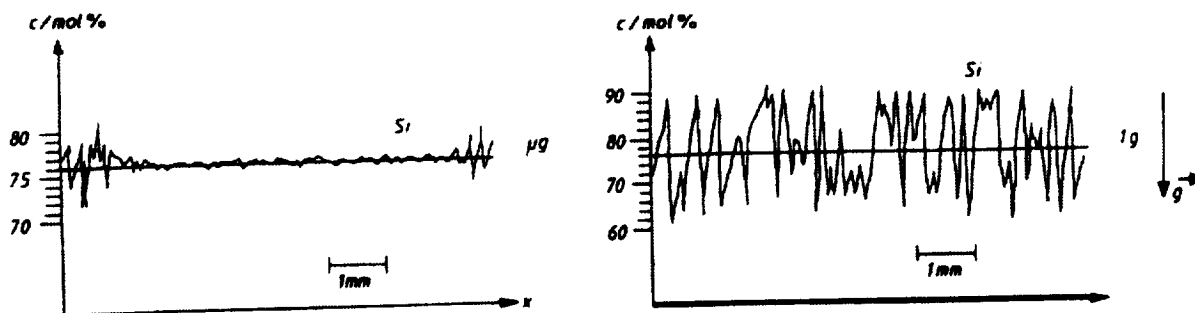


Figure 1. Electron microprobe composition scans of microgravity and normal gravity prepared samples. Glass composition 24%Li₂O, 76%SiO₂. (After Reference [20].)

analyze the low temperature dynamical properties of the glass samples produced in the μ -g and 1-g environments.

Various levitating techniques, due to the absence of contact with the container wall, can also produce more homogeneous glasses. We shall construct a gas film levitation (GFL) furnace for the production of high quality samples. This furnace will be a tubular vertical levitator [21,22] and will produce glass in rod shapes. We propose to use porous graphite membranes on the sides and the bottom for the gas film levitation of the sample. Such glass samples generated in the GFL furnace will provide reproducible glass starting material for the space-based production of glasses as well as eliminating crucible interactions, associated contamination, mechanical stresses and surface defects usually found in glass samples produced at 1-g in a crucible environment [23]. An additional advantage of the GFL technique is its ability to permit a slower cooling of the melt without significant crystallization due to the elimination of heterogeneous nucleation.

This research program will result in the development of new experimental tools for the characterization of glass microstructure and also in a deeper understanding of the general source of excitations in glasses. Since laboratory studies of such excitations in silicate dust grains [24] indicate that they dominate the mm- and submm-wave temperature-dependent properties in the temperature range appropriate to interstellar dust emission, there is added interest in identifying the source of these excitations.

REFERENCES

1. R. C. Zeller and R. O. Pohl, Phys. Rev. B 4, 2029 (1971).
2. P. W. Anderson, B. I. Halperin, and C. M. Varma, Phil. Mag. 25, 1 (1972).
3. W. A. Phillips, J. Low Temp. Phys. 7, 351 (1972).
4. W. A. Phillips, Rep. Progr. Phys. 50, 1657 (1987).
5. C. A. Angell, J. Non-Cryst. Sol. 131-133, 13 (1991).
6. O. Mishima, L. D. Calvert, and E. Whalley, Nature 310, 393 (1984).
7. O. Mishima, L. D. Calvert, and E. Whalley, Nature 314, 76 (1985).
8. G. P. Johari, A. Hallbrucker, and E. Mayer, Nature 330, 552 (1987).
9. A. Hallbrucker, E. Mayer, and G. P. Johari, Phil. Mag. B 60, 179 (1989).
10. G. P. Johari, G. Astl, and E. Mayer, J. Chem. Phys. 92, 809 (1990).
11. D. D. Klug and Y. P. Handa, J. Phys. Chem. 92, 3323 (1988).
12. N. I. Agladze and A. J. Sievers, Phys. Rev. Lett. 80, 4209 (1998).
13. R. J. Speedy, J. Phys. Chem. 96, 2322 (1992).

14. C. A. Angell, *Science* 267, 1924 (1995).
15. W. M. MacDonald, A. C. Anderson, and J. Schroeder, *Phys. Rev. B* 31, 1090 (1985).
16. D.-M. Zhu, *Phys. Rev. B* 54, 6287 (1996).
17. D.-M. Zhu and H. Chen, *J. Non-Cryst. Sol.* 224, 97 (1998).
18. A. P. Sokolov, R. Calemczuk, B. Salce, A. Kisliuk, D. Quitman, and E. Duval, *Phys. Rev. Lett.* 78, 2405 (1997).
19. J. Zarzycki, G. H. Frischat, and D. M. Herlach, in *Fluid Sciences and Materials Science in Space*, edited by H.U. Walter (Springer-Verlag, Berlin, Heidelberg, New York, London, Paris, Tokyo, 1987), p. 599.
20. G. H. Frischat, *J. Non-Cryst. Sol.* 183, 92 (1995).
21. P. Baniel and C. Belouet, *J. Non-Cryst. Sol.* 161, 1 (1993).
22. P. Baniel, A. Lopez, P. Gall, and J. Granier, *J. Non-Cryst. Sol.* 203, 143 (1996).
23. A. Janke and G. H. Frischat, *Glass Sci. & Tech.* 71, 193 (1998).
24. N. I. Agladze, A. J. Sievers, S. A. Jones, J. M. Burlitch, and V. W. Beckwith, *Ap. J.* 462, 1026 (1996).

GRAVITATIONAL EFFECTS ON THE WELD POOL GEOMETRY DURING GAS TUNGSTEN ARC AND LASER WELDING

Nam Hyun Kang, Anil K. Kulkarni*, and Jogender Singh

Materials Science and Engineering, * Mechanical Engineering
The Pennsylvania State University, University Park, PA 16802

INTRODUCTION

A welding process needs more precise understanding of free surface geometry and corresponding shape of the weld pool during melting and solidification. In normal earth gravity, surface tension gradient driven flow has been determined to be the dominant force and gravity driven force has been treated as a minimal factor for a melt convection [1,2]. However, the high pressure at the center of an arc causes the pool center to be depressed and its edges to be risen by the surrounding solid around the weld pool [3]. Authors' preliminary investigation shows that the gravitational force can considerably affect the surface deformation of the liquid metal. The scientific and technological benefits of this investigation are to understand the nature of the gravitational effects on the welding convection flows and the free surface deformation. The long-term goal is to optimize future applications in predicting the geometry of the weld pool in normal Earth gravity and microgravity.

I. Ground-Based Experiments

A new concept of ground based experiments was applied in this investigation to examine the gravitational effects without changing the gravitational acceleration level. Gas tungsten arc welding (GTAW) was conducted with different angles (Ω) between the direction of gravitational vector (\vec{g}) and heat source translation as shown in Figure 1.

An oxygen free copper (Cu) and a pure nickel (Ni) plate were utilized for a bead-on-top experiment. The copper plate had a dimension of 10 cm x 5 cm x 0.22 cm for translational welding and of 5 cm x 5 cm x 0.22 cm for spot welding. The nickel base metal was a 7.5 cm x 2 cm x 0.22 cm. The base metal was moved at a constant speed, and a tungsten (W) electrode of 0.15 cm diameter was stationary. The GTAW was performed with a constant direct current of 140 A and a variable arc voltage of 12 V (\pm 0.5 V).

The copper and nickel welds were etched by diluted ammonium persulphate solution in H₂O and nitric acid: acetic acid (1:1) solution, respectively. The shape of the weld pool was observed using an optical microscope. The surface morphology was examined by a laser profilometer.

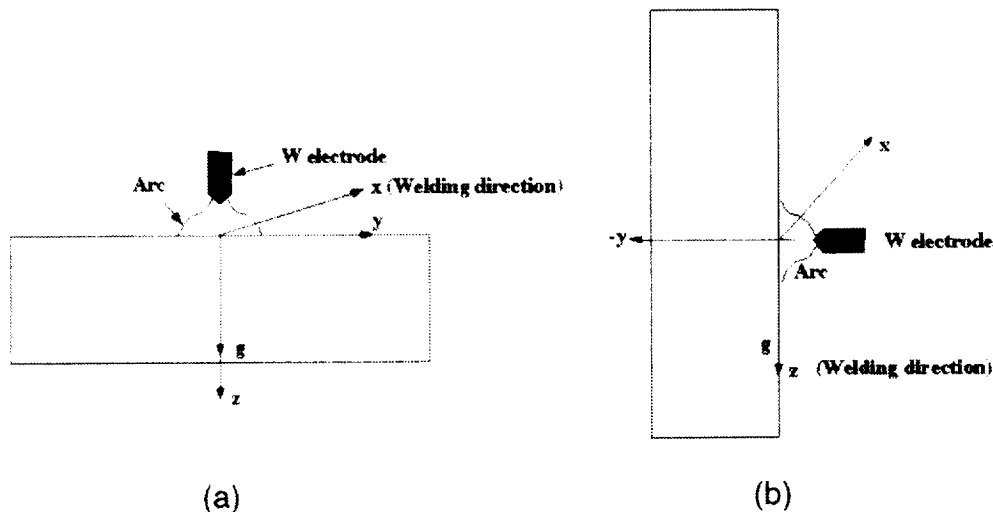


Figure 1. Ground-based experimental setup: (a) welding horizontally perpendicular to gravity ($\Omega=90^\circ$) and (b) welding upward or downward parallel to gravity ($\Omega=0^\circ$).

II. Results

Analysis of Cu and Ni welds demonstrated that the weld-pool geometry was changed considerably by the variation of welding direction with respect to the \vec{g} orientations in the ground-based experiments for both configurations, the translational and spot weld:

- (1) The translational welding experiment results are presented with three \vec{g} orientations, perpendicular, parallel-up, and parallel-down. Depth, width and depth/width ratio of the weld pool was measured as a function of welding speed for Cu and Ni. At 3 mm/sec in Figure 2, the perpendicular welds of Cu and Ni have ~25% deeper penetration compared with the parallel-down welds. The depth of the parallel-up welding is between that of the perpendicular and the parallel-down welds. As the welding speed increases, the depth difference as a function of gravitational orientation decreases. However, the width of the weldments shows no dependence on \vec{g} as indicated in Figure 3. Thus, the weld pool penetration was more sensitive to the gravity than the average width of the weldments. The error bars are based on scatter of measurements. The depth/width ratio of the weld pool in Figure 4 was higher at the perpendicular welding setup ($\Omega=90^\circ$) and lowest at the parallel-down welding condition ($\Omega=0^\circ$).

The possible explanation for the deeper penetration at the perpendicular welding setup lies in the surface depression action by the arc pressure. The dynamic balance between arc pressure, pool gravity and surface tension determines the shape of a weld pool surface [4, 5]. At the highest welding speed for the Cu, the width and the depth showed the reverse trend compared with other speeds.

That is probably because of insufficient heat accumulation to sustain a stable weld pool or an experimental uncertainty.

- (2) The spot weld experiments are presented with two \vec{g} orientations, perpendicular and parallel. Free surface shape after spot weld was measured using a profilometer to explain the effects of surface depression on the penetration. The spot welding was conducted for 15 and 20 seconds at the same condition (~12 V and 140 A) as the translational welding on Cu. The 15 seconds spot weld had a surface depression of ~0.18 mm at the center for both perpendicular and

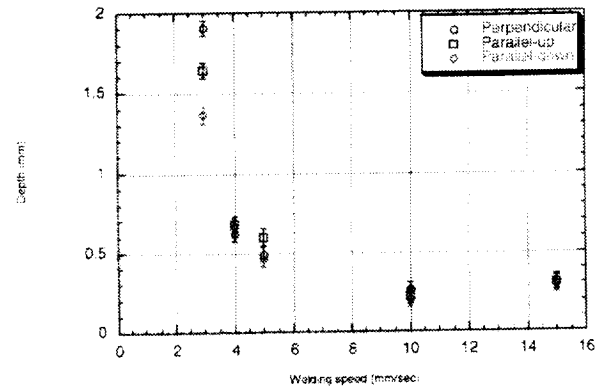
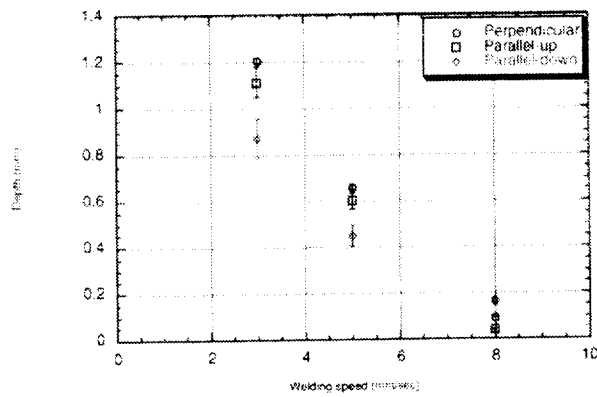


Figure 2. The effect of gravity on weld pool depth of the Cu (left) and the Ni (right).

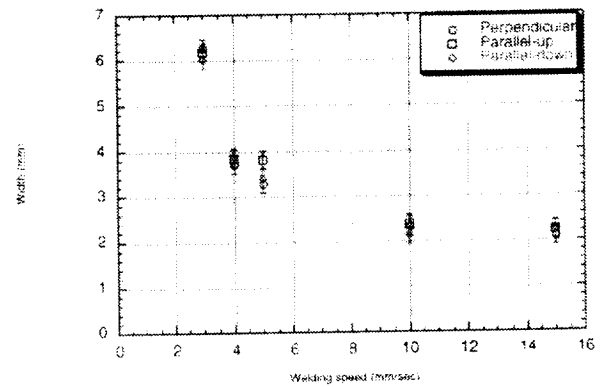
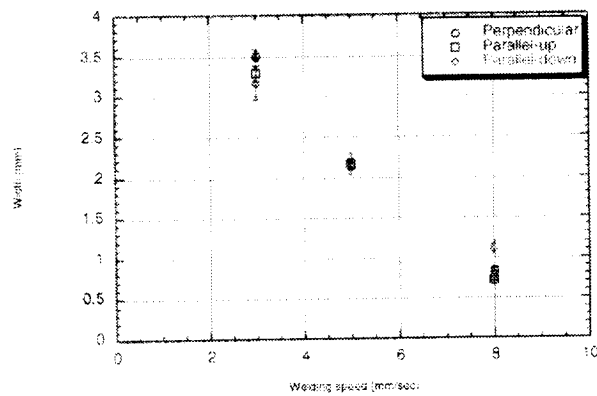


Figure 3. The effect of gravity on weld pool width of the Cu (left) and Ni (right).

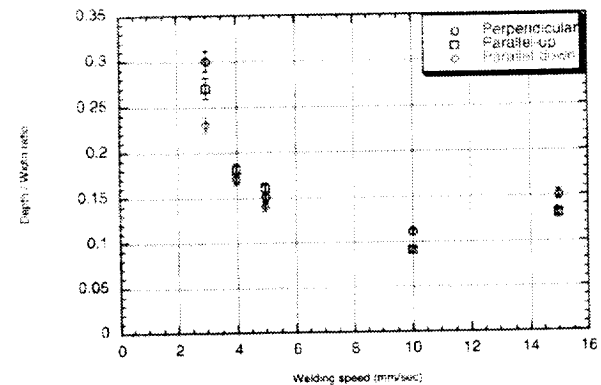
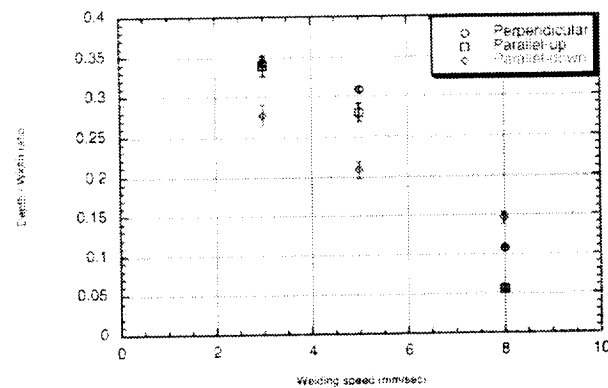


Figure 4. The effect of gravity on weld pool depth/width ratio of the Cu (left) and Ni (right).

parallel welding as shown in Figure 5. Figure 6 indicates a teardrop shape of the free surface deformation for the parallel heat source, whereas symmetrical free surface was observed at the perpendicular source for 20 seconds (Figure 6).

Arc voltage between the W electrode tip and the metal surface was measured in-situ at each welding condition. Both parallel and perpendicular spot welding exhibited similar trend of arc voltage, which indicates similar power input into the work piece. However, a change in the free surface morphology can modify heat distribution on the free surface of the weld pool, influencing the geometry of the weld pool for 20-second welds.

In another set of experiments, the initial arc voltage was increased from 12 V to 13 V by increasing the gap between the W tip and the metal surface. Teardrop shape of the free surface was produced for the parallel heat source at 14 seconds in Figure 7 as opposed to the symmetrical shape seen in Figure 5-top. A larger weld pool created by higher heat input is probably the main cause for more significant gravitational effects on the free surface deformation.

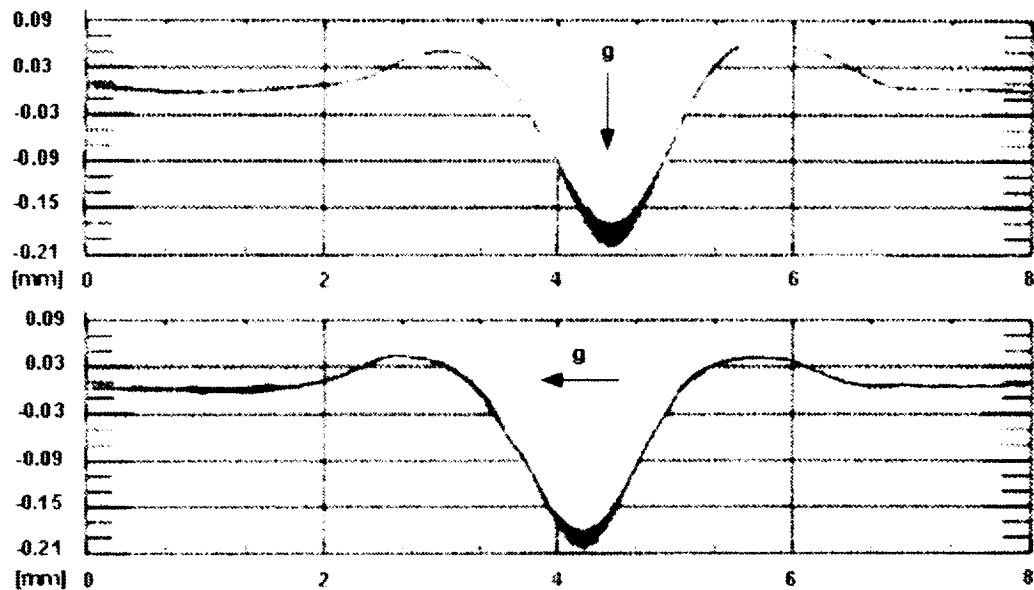


Figure 5. Spot GTAW for 15 seconds: perpendicular (top) and parallel (bottom) heat source. 0.889 mm gap between the W tip and the sample.

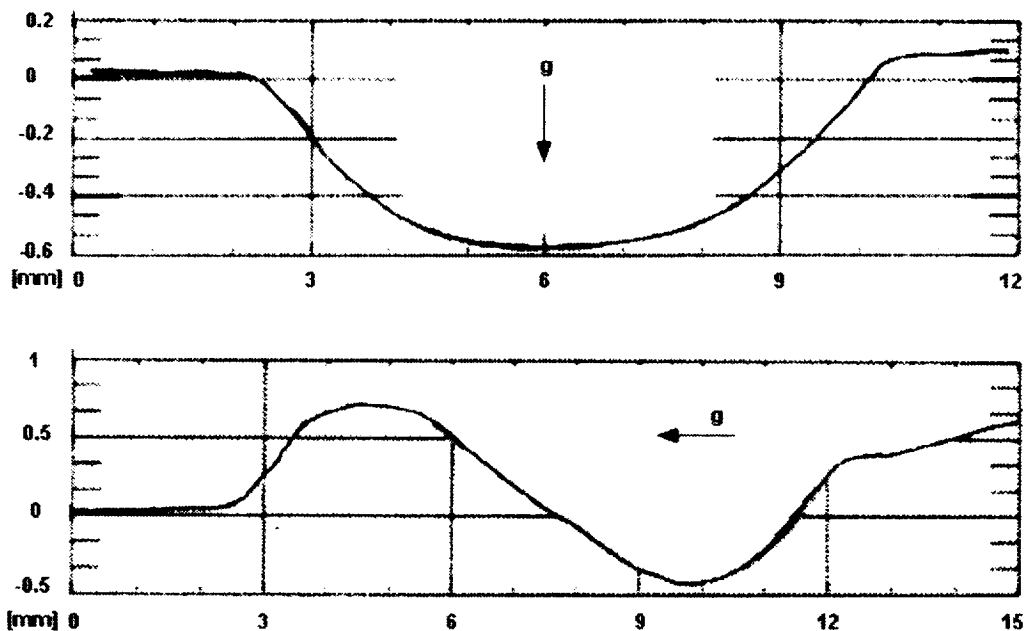


Figure 6. Spot GTAW for 20 seconds: perpendicular (top) and parallel (bottom) heat source. 0.889 mm gap between the W tip and the sample.

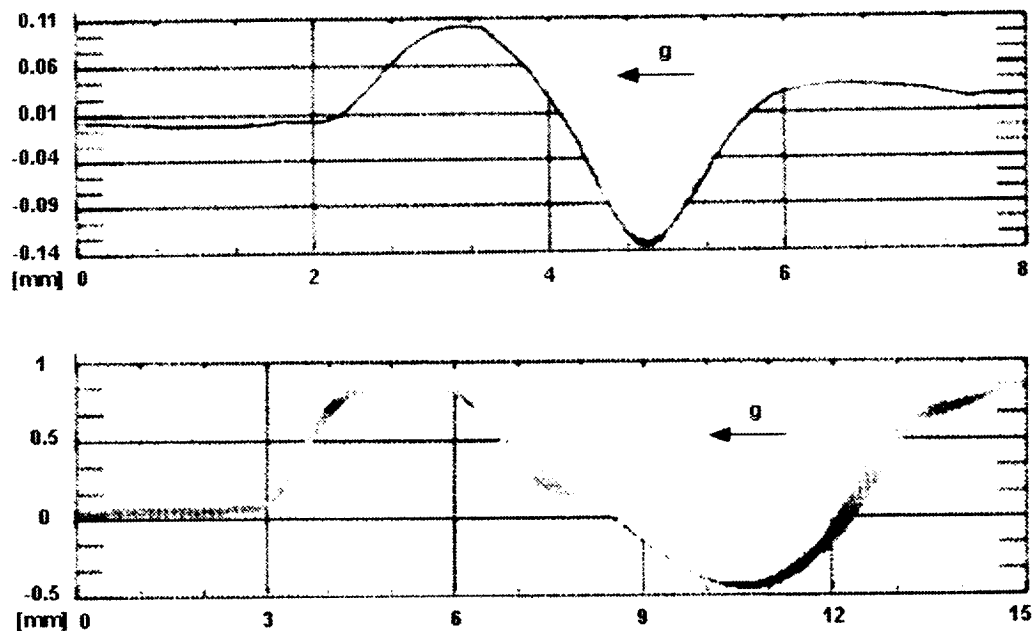


Figure 7. Parallel spot GTAW for 14 seconds (top) and for 18 seconds (bottom).
1.702 mm gap between the W tip and the sample.

III. Summary and Future Plans

The different welding setups (perpendicular, parallel-up, and parallel-down) created different surface morphology. This morphological change of surface deformation had a minimal effect on the weld pool width, but a larger effect on the penetration. However, the change of penetration was not as significant as the authors had expected. That is probably because GTAW usually creates the weld pool of small depth to width ratio. Therefore, it is difficult to detect a significant effect of gravity on the weld pool shape.

For better understanding on gravitational effects, laser welding is underway on the pure Ni and the alloy of 304 stainless steel. For these materials, their thermal properties are different significantly. The gravity may have a more significant effect on the penetration produced by the laser welding. Microstructural and microchemical examinations are being characterized for the above materials to clarify the gravitational effects on the welding process. Mathematical modeling is expected to provide better explanation on the gravitational effects during laser welding.

REFERENCES

1. C. Chan, J. Mazumder, and M. M. Chen, Metallurgical Transactions, 15A, 2175 (1984).
2. S. Kou and D. K. Sun, Metallurgical Transactions, 16A, 203 (1985).
3. M. L. Lin and T. W. Eagar, Welding research supplement, 163s - 169s (June 1985).
4. C. S. Wu and L. Dorn, Journal of Engineering manufacture, vol. 209, 209 - 226 (1995).
5. S. -Y. Lee and S. -J. Na, Welding research supplement, 484s - 497s (November 1997).

FLIGHT EXPERIMENT TO STUDY DOUBLE-DIFFUSIVE INSTABILITIES IN SILVER-DOPED LEAD BROMIDE CRYSTALS

N.B. Singh, J.D. Adam and H. Zhang¹; S.R. Coriell²; W.M.B. Duval³

¹Science and Technology Center, ESSS, Northrop Grumman Corporation
P. O. Box 1521, MS-3D14, Room-A110, Baltimore, MD 21203

²National Institute of Standards and Technology, Gaithersburg, MD 20899

³NASA, Glenn Research Center, Cleveland, OH 44135

OBJECTIVES

The main objective of the present program is to understand thermosolutal convection during crystal growth of PbBr_2 -AgBr alloys. This involves identification of the growth conditions for microgravity experiments delineating the microsegregation, observation of convecto-diffusive instabilities and comparison with theoretical models. The overall objectives can be summarized as follows:

- Observe and study the double diffusive and morphological instabilities in controlled conditions and to compare with theoretically predicted convective and morphological instability curves.
- Study the three-dimensional morphological instabilities and resulting cellular growth that occur near the onset of morphological instability in the bulk samples under purely diffusive conditions.
- Understand the micro-and macro-segregation of silver dopant in lead bromide crystals in microgravity.
- Provide basic data on convective behavior in alloy crystals grown by the commercially important Bridgman crystal growth process.

I. Necessity of Microgravity

Lead bromide doped with silver can be grown under normal gravity conditions; the double diffusive nature of the convection will cause mixing of the molten charge material. This in turn will cause the solute composition in the crystal to constantly increase during growth. In semiconductor devices, where the electronic properties are a function of the crystal composition, this constant compositional variation is undesirable.

During the solidification of doped materials in Bridgman geometry, generation of destabilizing temperature gradients in the melt is unavoidable, resulting in buoyancy-induced convective mixing of the liquid phase. On earth this mixing is generally very intensive and prevention of convection is important in order to minimize micro- and macro-segregation and to obtain homogeneous properties throughout the solidified material. In an actual furnace it is extremely difficult to eliminate the radial temperature gradient completely. Unavoidable gradients may give rise to flows, which lead to lateral segregation in the solidified material. In binary systems, if the solute pile up ahead of the

solidification front were lighter than the solvent, this alone would cause positive density gradient. The net density gradient can have various profiles, depending on the properties of the melt such as thermal conductivity and diffusion coefficient or growth conditions such as growth rate and thermal gradient. Even if the net resulting temperature gradient is stable, convection can occur due to double diffusive character of solute and temperature with different diffusivities. While there have been many observations on earth of this phenomena in thin samples where convection is not important, it is nearly impossible to study three-dimensional instabilities in bulk samples on Earth under purely diffusive conditions. The space experiment on transparent lead bromide-silver bromide alloys would permit a study of the various three dimensional morphologies that occur near the onset of morphological instability. Since the lead bromide-silver bromide system is transparent, experiments in space would allow the direct observation of morphological instability and the resulting cellular growth.

The present experiment on lead bromide-silver bromide alloys permits a study of various three dimensional morphologies that occur near the onset of morphological instability in a bulk crystal grown by solidification technique. Being able to see exactly what is happening during growth in low earth orbit makes this a unique system for microgravity experimentation. The system chosen here has dual advantages: (a) lead bromide is a transparent system almost ideally suitable for direct in situ observations to study solid-liquid interface phenomena and (b) lead bromide holds great promise for technological applications of acousto-optic devices and narrow band ultraviolet filters.

II. Impact on America

The heavy metal halide crystals, which are investigated in this program, are excellent acousto-optic materials. The improvements in the quality of crystals will enable us to use these crystals for defense and commercial applications.

A. Defense Systems

A hyperspectral sensor is a key component within the Office of the Secretary of Defense (OSD) of the US NBC warfare defenses. The NBC objective is to provide US forces with the capability to detect and survive an initial NBC attack. To achieve this goal the OSD envisions an integrated suite of chemical and biological sensors. The acousto-optic tunable filter (AOTF) hyperspectral imaging camera could significantly enhance the performance of this suit of sensors by either taking the spectral signatures of the chemicals/hard targets present on the battlefield or by, for an active probe such as a laser, reducing interfering background signals by narrowing the spectral region being imaged.

B. Commercial Systems

The principal application area of the halides is Bragg cells for acousto-optic signal processing typically found in RF spectrum analyzers, correlation and receivers, for which there is a continuing need to improve resolution and dynamic range while reducing volume and power requirements. It is the anomalous low acoustic velocity and high figure of merit (leading to high efficiency) that allows these objectives to be reached. Another major area of applications is for spectroscopic systems (both imaging and non-imaging), for which the acousto-optic tunable filter (AOTF) is the major device. Typical systems in which this device plays a role include environmental monitoring,

liquid and gas analyzers and communication. The critical material properties for such spectroscopic devices include wide optical transparency range so light from the UV through the far IR can be analyzed. There are important applications throughout this wavelength range. The high figure of merit of materials investigated under this program assures efficient operation.

III. Significant Results

We evaluated the growth of lead bromide system by state feedback system in the existing furnaces. The most challenging aspect of the interface control problem is the lack of a good sensor that can provide the controller with the necessary information about the interface position and the shape. The controller proposed here uses a model based sensor which receives partially measured material temperatures through the shape of the interface (PbBr_2 being an excellent system) or the outside surface temperatures of the ampoule. Using this partial information, and a finite element based model of the thermal dynamics, the model based sensor estimates the unknown temperatures $T(r, z, t)$ inside the ampoule. This measurement technique can be viewed as “a soft sensor” or “an intelligent sensor” since the unknown temperatures are estimated with a thermal model. The interface controller receives both the desired material temperature distribution $T_d(r, z, t)$ and the estimated temperature distribution $T(r, z, t)$. The task of the Interface Controller is to determine the required heating zone temperatures inside the furnace so that a proper set of boundary conditions around the ampoule can be established in order to grow the crystal with a desired interface shape and speed. The controller uses a state-space model of the solidification process by employing a modified finite element technique to the governing conduction equation. This model is used to design a dynamic controller that would set up the required zone temperatures inside the furnace. The solidification experiments with PbBr_2 -AgBr alloys (500 and 5000 ppm) showed double-diffusive instabilities at the solid-liquid interface. When the sample was held stationary, any convection present in the liquid was attributed to the radial heat losses. Systematic observations at the interface showed the development of the depression, which finally ends in interfacial breakdown. When we repeated this experiment with pure lead bromide at speeds of 2.5 cm/day the interface remained flat and did not show any instability. The interface got depressed in the center and then slowly formed the instability. As a function of time, the instability developed with much larger amplitude. When the translation velocity was increased, the interface started breaking down. The flow pattern observed in the PbBr_2 -AgBr system can be described as a “toroidal roll.” A slight asymmetry of the system resulted in the displacement of the node and axis of the rolls from the central axis of the tube. When the toroidal flow persisted for many hours and the tube was moving, the interface was observed to be pinched where the radial inflow converged leading to the line defect. A theoretical calculation was performed to generate the concentration profile for the solute distribution and we are comparing with the experimentally measured values. We measured the diffusion coefficient and thermal conductivities of solid and liquid, which were used in computing stability curves and solute distribution in the crystal.

THE EFFECT OF DOPING ON THE ION CONDUCTIVITY AND BI-AXIAL FLEXURAL STRENGTH OF YSZ SOLID OXIDE ELECTROLYZERS

K.R. Sridhar¹ (PI), W. Chen² (Co-I)

Department of Aerospace and Mechanical Engineering
The University of Arizona, Tucson, AZ 85721-0119
Fax: (520) 621-8191

¹Phone: (520) 621-6111, Email: sridhar@shakti.ame.arizona.edu

²Phone: (520) 621-6114, Email: weinong@u.arizona.edu

RESEARCH OBJECTIVES

Solid oxide electrolyzers generate pure oxygen from oxygen bearing gases such as carbon dioxide, water, and air. Such electrolyzers can generate oxygen from the carbon dioxide rich atmosphere of Mars, and also from the evolved gases obtained from hydrogen or carbon reduction of the lunar regolith. Several studies have shown that oxygen production from Martian atmosphere as a key technology that will reduce the cost of both robotic and human missions with the added advantage of risk reduction.^{1,2} Space exploration missions call for developing better electrolyzer materials that offer superior thermal and mechanical characteristics as well as improved electrical performance. The electrolyte of the electrolyzer is a ceramic solid oxide such as yttria stabilized zirconia (YSZ). In order to develop structurally robust electrolyzers that would withstand the severe vibration and shock loads experienced during the launch and landing phases of the mission, it is essential to understand the damage initiation and consequent failure mechanisms and their relation to material composition and processing parameters.

The objective of this research is to understand and quantify the relation between the mechanical properties of the electrolyte and its microstructure (thus processing parameters and choice of electrolyte compositions) and loading/environmental conditions. In this research program, we will investigate the effects of dopants on both the electrical performance (oxygen conductivity) and the mechanical properties (bi-axial bending strengths under quasi-static and dynamic loading conditions at room and high temperatures) of YSZ in an environment.

I. Relevance to Microgravity Program

All the major studies conducted by NASA in the recent past, such as the 90 day study and the Stafford Committee report, have identified the need for utilizing space resources, *i.e.*, “living off the land,” as an important and necessary part of future exploration of the solar system. Several studies have shown that oxygen production from the Martian atmosphere and from lunar regolith as a key technology that can reduce the cost of both robotic and human missions. The production of oxygen from carbon dioxide and water is of importance for both life support and propellant production. For example, it would be highly desirable to have a closed loop life support system with oxygen reclamation in the transit vehicle to Mars as well as for extended stays aboard the Space Station. This research program addresses the material

issues related to electrochemical systems used for ISRU. The use of local resources is especially important for a long-duration mission, high-cost/long-time transportation, or for settlement missions. The research focus here is on developing superior materials that will ultimately lead to structurally and thermally robust electrolyzers and fuel cells. The improved electrolyzers would process in-situ materials to produce usable consumables for human space exploration in micro and reduced gravity environments.

II. Research Progress

A. Choice of Dopants

Yttria Stabilized Zirconia (8 mole percent doped, 8YSZ) is the most commonly used electrolyte for electrolyzers. The main drawbacks of this electrolyte are its poor structural and thermal properties. In the literature, several dopants are known to strengthen the 8YSZ. For example, 3YSZ may be used as a dopant, it is stronger than 8YSZ even though it is not totally stabilized and partly adopts tetragonal structure at low temperatures [3]. Also, its ionic conductivity is lower than 8YSZ. Aluminum oxide has been the most widely used strengthener of 8YSZ [e.g., 4, 5]. Although alumina is an insulating material, small amounts added as dopant do not significantly affect ionic conductivity of 8YSZ. Titanium oxide plays a similar role [4, 6]. Bismuth and cerium oxides are known as low temperature oxygen conductors and have been used as electrolyte materials [7-8]. Addition of a small amount of those oxides may increase the ionic conductivity of 8YSZ. In this research, we use only small amounts of dopants (from 1 to 3 mol%, except for 3YSZ) to avoid drastic change in the desired 8YSZ properties, particularly changes in coefficient of thermal expansion (CTE). The reason to conserve the CTE characteristics is to match with other components of a cell stack such as electrodes and interconnects that have already been developed with great care.

B. Ion-Conductivity Measurements

To compare the ionic conductivity of the samples with different dopants, a four-probe d.c. conductivity test was used [9], which provides the total conductivity of the samples but does not provide the individual contributions due to ionic and electronic conductivities. A test starts at 500°C and goes up to 1000°C by steps of 50°C, and goes back down by steps of 100°C. At each temperature, the system stabilizes for 0.5 hour. Then, 5 data points are taken every 10 seconds, measuring temperature, voltage across inner electrodes and current in the circuit (see the schematic of the setup shown in Figure 1). For each composition, three different samples were tested.

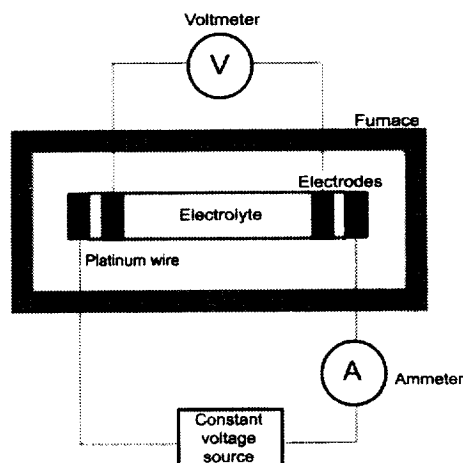


Figure 1. A simple schematic of a four probe d.c. conductivity test.

The conductivity of the material is calculated with the formula:

$$\sigma = \frac{A}{Vl}$$

where σ is the conductivity, I the current in the circuit, A the cross-section of the electrolyte, V the voltage between the two inner electrodes, l the distance between the two inner electrodes. As an example of the results, the ionic conductivity at 1000°C as a function of dopant concentration is shown in Figure 2.

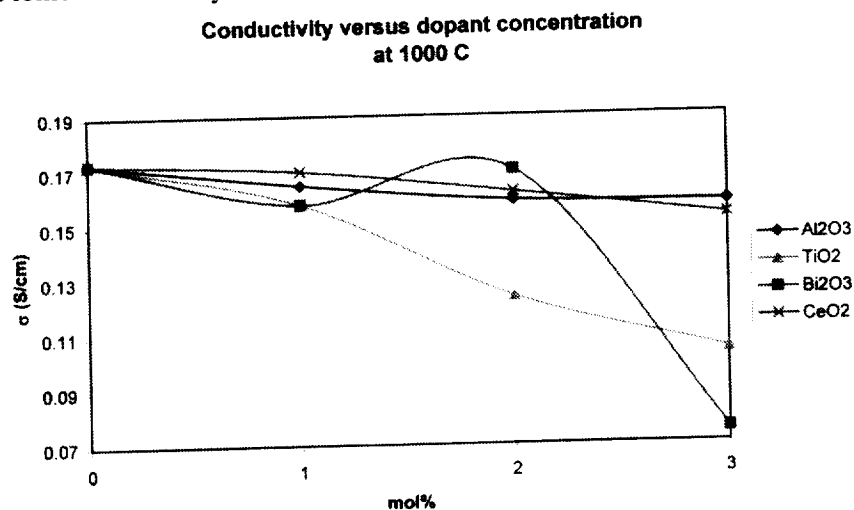


Figure 2 Variation of ionic conductivity versus dopant concentration at 1000°C.

C. Bi-Axial Flexural Strength Measurement

In order to study the effects of dopant on the mechanical strength of a thin (0.4 to 0.7 mm) YSZ electrolyte, an ASTM standard of piston-on-three-balls configurations has been selected to determine the bi-axial flexural strengths. A hydraulically driven loading frame (MTS 810) was used to conduct the quasi-static experiments. As examples of the results, the bi-axial strengths (modulus of rupture, MOR) of baseline 8YSZ and 10% 3YSZ doped 8YSZ are shown in Tables 1 and 2, respectively. The thin-sheet specimens are 31.75 mm in diameter. In each group, twenty specimens were tested. The Tables list the results from successful tests.

The results in Tables 1 and 2 show that, 1) The strength data are rather scattered, with the modulus of rupture (bi-axial flexural strength) roughly proportional the number of broken pieces after failure. 2) The strength of 3YSZ-doped 8YSZ is consistently lower than that of the baseline 8YSZ, which is the counter of our objective of attaining increased strength.

A regrouping of the strength data using results from the tests where the specimen broke into four (4) or more pieces results in a much less scattering strength data collection. However, the microscopic mechanisms that determine the number of broken pieces remain to be revealed. More importantly, the mechanisms for the reduced strength of the doped material need to be investigated.

III. Research Planned

Research activities in the following areas are planned to develop a scientific understanding of the strengthening mechanisms of YSZ through doping.

Table 1 Modulus of Rupture (MOR) of Baseline 8YSZ.

Specimen	Diameter (mm)	Thickness (mm)	MOR (MPa)	Deflection (mm)	Broken pieces
PB8ysz_01	32.03	0.419	354	~0.330	5
PB8ysz_02	31.99	0.401	340	~0.330	5
PB8ysz_03	31.97	0.399	444	~0.432	8
PB8ysz_04	32.03	0.399	325	~0.305	5
PB8ysz_11	32.02	0.432	301	~0.381	5
PB8ysz_12	32.00	0.432	426	~0.356	8
PB8ysz_13	32.00	0.411	309	~0.330	4
PB8ysz_14	32.01	0.414	318	~0.330	7
PB8ysz_15	32.03	0.419	223	~0.279	3
PB8ysz_16	32.01	0.414	366	~0.305	7
PB8ysz_17	32.02	0.411	235	~0.229	2
PB8ysz_18	31.92	0.401	258	~0.279	4
PB8ysz_19	31.98	0.406	386	~0.381	6
PB8ysz_10	32.02	0.419	366	~0.305	7
Average	32.00	0.411	332	~0.330	5.4

Table 2 Modulus of Rupture (MOR) of 10% 3YSZ Doped 8YSZ.

Specimen	Diameter (nun)	Thickness (mm)	MOR (MPa)	Deflection (mm)	Broken pieces
1090ysz_01	31.76	0.617	292	0.229	5
1090ysz_02	31.79	0.605	220	0.203	3
1090ysz_03	31.70	0.610	184	0.152	2
1090ysz_04	31.72	0.643	274	0.178	6
1090ysz_05	31.76	0.635	273	0.203	5
1090ysz_06	31.77	0.589	256	0.178	4
1090ysz_07	31.72	0.627	276	0.203	5
1090ysz_08	31.73	0.627	276	0.229	4
1090ysz_09	31.76	0.630	176	0.152	3
1090ysz_10	31.73	0.643	285	0.178	6
1090ysz_11	31.72	0.617	286	0.203	5
1090ysz_13	31.72	0.627	253	0.178	5
1090ysz_14	31.78	0.602	301	0.203	5
1090ysz_15	31.75	0.602	269	0.178	4
1090ysz_16	31.74	0.630	250	0.178	4
1090ysz_17	31.80	0.643	257	0.152	4
1090ysz_18	31.77	0.665	90	0.076	2
1090ysz_19	31.74	0.615	152	0.114	2
1090ysz_20	31.80	0.630	163	0.127	2
Average	31.75	0.624	9	4	4

- Complete mechanical tests of all doped materials will be conducted to expand the strength database.
- Conduct bi-axial flexural tests on baseline and selected doped 8YSZ at high temperatures to determine the strengths of doped materials at working temperature.
- Conduct dynamic bi-axial flexural tests on baseline and selected doped 8YSZ materials to examine the effects of loading rate on the strength.
- Examine fracture surface using Scanning Electron Microscopy (SEM) to reveal the microstructural features such as grains, phases, crack initiation sites, crack propagation path and its interaction with the microstructures.
- Measure ionic conductivity of the promising materials.
- X-Ray Diffraction analysis (XRD) will be used to detect what phases are in presence for each composition.

Based on the knowledge learned from this investigation, superior materials will be developed with better mechanical and electrical properties for improving the structural integrity and oxygen conductivity of solid oxide electrolyzers for space missions.

REFERENCES

1. Zubrin, R. And Price, S., "Low Cost Mars Sample Return with ISPP," NASA Contract Report NAS-9-19145, Lockheed Martin, Denver, CO. 1995.
2. Sridhar, K. R., "Mars Sample Return With ISPP," *J. British Interplanetary Society*, 49, 435-440, 1996.
3. Ciacchi, F.T., Crane, K.M., Badwal, S.P.S., "Evaluation of Commercial Zirconia Powders for Solid Oxide Fuel Cells," *Solid State Ionic*, 73, 49-61, 1994.
4. Radford, K.C., Bratton, R.J., "Zirconia Electrolyte Cells," *Journal of Materials Science*, 14, 59-69, 1979.
5. Feighery, A.J., Irvine, J.T.S., "Effect of Alumina Additions upon Electrical Properties of 8 mol.% Yttria-Stabilised Zirconia," *Solid State Ionics*, 121, p.p. 209-216, 1999.
6. Colomer, M.T., Traqueia, L.S.M., Jurado, J.R., Marques, F.M.B., "Role of Grain Boundaries on the Electrical Properties of Titania Doped Yttria Stabilized Zirconia," *Materials Research Bulletin*, 30(4), 515-522, 1995.
7. Keizer, K., Burggraaf, A.J., De With, G., "The effect of Bi_2O_3 on the electrical and mechanical properties of ZrO_2 - Y_2O_3 ceramics," *J. of Materials Science*, 17, p.p. 1095-1102, 1982.
8. Sammes, N.M., Zhihong Cai, "Ionic Conductivity of Ceria/Yttria Stabilized Zirconia Electrolyte Materials," *Solid State Ionics*, 100, p.p. 39-44, 1997.
9. Badwal, S.P.S., Ciacchi, F.T., Ho, D.V., "A Fully Automated Four-Probe D.C. Conductivity Technique for Investigating Solid Electrolytes," *J. of Applied Electrochemistry*, 21, p.p. 721-728, 1991.

PARTICLE ENGULFMENT AND PUSHING BY SOLIDIFYING INTERFACES

D.M. Stefanescu¹, S. Mukherjee¹, F.R. Juretzko¹, A.V. Catalina², S. Sen², P.A. Curreri³

¹ The University of Alabama, Tuscaloosa, AL 35487

² University Space Research Alliance, Huntsville, AL 35806

³ NASA Marshall Space Flight Center, Huntsville, AL 35812

INTRODUCTION

The phenomenon of interaction of particles with solid-liquid interfaces (SLI) has been studied since the mid 1960's. While the original interest stemmed from geology applications (frost heaving in soil), researchers soon realized that fundamental understanding of particles behavior at solidifying interfaces might yield practical benefits in other fields, including metallurgy. In materials engineering the main issue is the location of particles with respect to grain boundaries at the end of solidification. Considerable experimental and theoretical research was lately focused on applications to metal matrix composites produced by casting or spray forming techniques, and on inclusion management in steel. Another application of particle SLI interaction is in the growing of $Y_1Ba_2Cu_3O_{7-\delta}$ (123) superconductor crystals from an undercooled liquid. The oxide melt contains $Y_2Ba_1Cu_1O_5$ (211) precipitates, which act as flux pinning sites.

The experimental evidence on transparent organic materials, as well as the recent *in situ* observations on steel demonstrates that there exist a *critical velocity* of the planar SLI below which particles are *pushed* ahead of the interface, and above which particles are *engulfed*. The engulfment of a SiC particle in succinonitrile is exemplified in Figure 1.

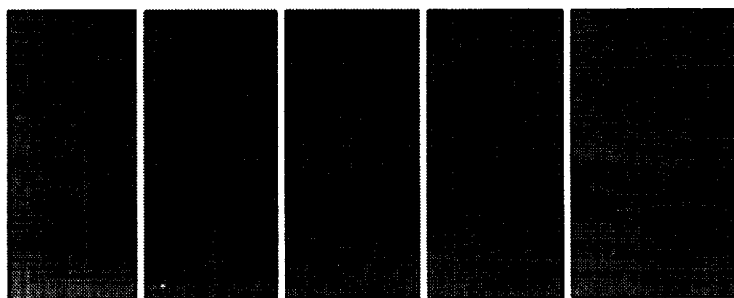


Figure 1. Engulfment of SiC particles by the SLI in succinonitrile. Gradual velocity increase from 9.2 to 21 $\mu\text{m/s}$.

However, in most commercial alloys dendritic interfaces must be considered. Indeed, most data available on metallic alloys are on dendritic structures. The term *engulfment* is used to describe incorporation of a particle by a planar or cellular interface as a result of local interface perturbation, as opposed to *entrapment* that implies particle incorporation at cells or dendrites boundaries. During entrapment the particles are pushed in the intercellular or interdendritic regions and then captured when local solidification occurs. The physics of these two phenomena is fundamentally different.

I. Dynamic Model (Analytical) – No Convection

Most models proposed to date^{2,3,4,5,6} ignore the complications arising from the liquid convection ahead of the SLI. They simply solve the balance between the attractive drag force exercised by the liquid on the particle and the repulsive interfacial force assuming steady-state. However, as demonstrated by experimental work, the process does not reach steady state until the particle is pushed for a while by the interface. The theoretical weakness of the steady state models is that the force balance can be satisfied for any sub-critical solidification velocity and therefore additional assumptions must be introduced to predict the critical velocity for engulfment. Recently we have proposed a dynamic model⁷ (non-steady-state). The non-steady state approach is based on the fact that a particle, initially at rest, must have an accelerated motion in order to reach the steady-state velocity, which is the solidification velocity.

The governing equation is the equation of particle motion^{8,9}:

$$\text{Equation 1} \quad \frac{4\pi}{3} \rho_p R_p^3 \frac{dV_p}{dt} = F_i - F_d - \tilde{C}_A \frac{4\pi}{3} \rho_L R_p^3 \frac{dV_p}{dt}$$

where, ρ is density, R_p is the particle radius, V_p is the particle velocity, dV_p/dt is the particle acceleration, F_i is the interface force, F_d is the drag force, and C_A is the added mass coefficient. The term on the LHS is the force required to accelerate the particle. The third term on the RHS is the force to accelerate the virtual "added" mass of the particle relative to the liquid. This allows for the fact that not only the particle has to be accelerated, but also a portion of the fluid that adheres to the particle.

As the solidification proceeds and the SLI approaches the particle, the gap width, d , will vary in time according to the relationship:

$$\text{Equation 2} \quad \frac{dd}{dt} = -\frac{dRI}{dL} (VS - V_p)$$

where RI_i is the distance between the center of the particle and the tip of the bump (or trough) on the SLI interface under the particle, L is the distance between the center of the particle and the unperturbed SLI, and VS is the solidification velocity.

The evolution of particle velocity can be analyzed by solving the system of equations composed by Equation 1 and Equation 2. Experiments performed during the USMP-4 mission were used for validation (Figure 2). It can be seen that the model results match very well with the experimental results at higher particle radii and reasonably well at lower particle sizes.

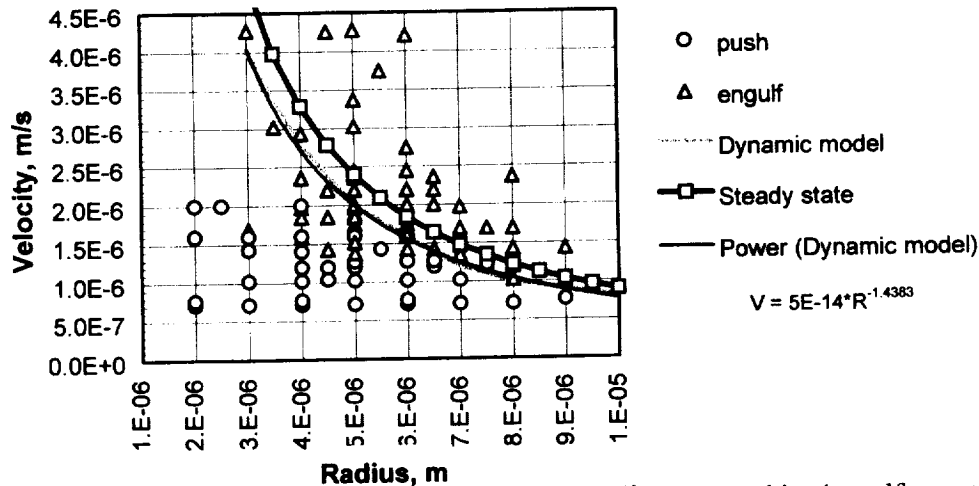


Figure 2. Calculated critical velocities and experimental values¹⁰ for the pushing/engulfment transition in the SCN-polystyrene system.

The dynamic model can be used to demonstrate the interplay between the particle velocity and the SLI velocity. Figure 3. shows the variation in time of V_p and of the velocity of the tip of the bump (or trough) of the SLI, V_t , for a case when the particle is continuously pushed by the SLI that has a solidification velocity $V_S = 0.3 \mu\text{m/s}$ for the aluminum-zirconia system. It can be observed that initially the particle is at rest. As the interface approaches it, the tip velocity increases to values far exceeding the value of V_S . At the same time, the particle begins to move because it is being pushed by the SLI. Its movement is also accelerated in the first stage. In the second stage, when the particle velocity reaches a certain value, the tip velocity begins to decrease rapidly, passing through zero, to some negative value. This is happening when the particle velocity exceeds the solidification velocity V_S , and therefore the perturbation of the SLI becomes unstable and begins to remelt. However, this process is accompanied by an increase of the gap width, which leads to a decrease of the pushing force acting on the particle. The result is that V_p begins to decrease while V_t increases again. This interplay continues with a decreasing amplitude until a steady state is achieved, *i.e.*, $V_p = V_t = V_S$. Note that steady state can be achieved only for sub-critical values of V_S .

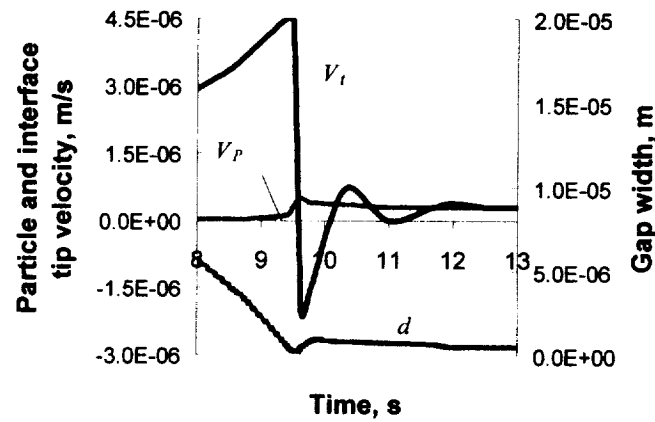


Figure 3. Particle velocity (V_p), SLI tip velocity (V_t), and particle - interface distance (d) versus time, for a sub-critical solidification velocity $V_S = 3 \cdot 10^{-5} \text{ m/s}$ (Al-ZrO₂ system, $R_p = 2.5 \cdot 10^{-4} \text{ m}$)

II. Analysis of Liquid Convection Effects

Besides the drag force, the interaction force, and the virtual added mass force, the particles are affected by three principal lifting forces. They are: 1) forces resulting from random velocity components greater than the terminal velocity of the particles; 2) Saffman force¹¹ due to velocity gradient in the liquid and relative translation velocity between the liquid and the particles; 3) Magnus force¹² due to relative translation and rotation velocity between the liquid and the particle. Equation 1 was rewritten in non-dimensional form with the further addition of the Saffman and Magnus forces (Equation 3):

$$\frac{dV_p}{dt} = \frac{3k^* \left[\left(\frac{a_o}{a_o + d} \right)^2 \frac{\text{Re}}{\text{We}} - 3k^* R_p \frac{V_p}{d} \right]}{2 \left(\frac{\rho_p}{\rho_L} + C_A \right) R_p^2} + \frac{V_{rel}}{R_p \left(\frac{\rho_p}{\rho_L} + C_A \right)} \left[1.54 \sqrt{\text{Re} S_{avg}} + \frac{3}{4} \text{Re} R_p \omega_{rel} \right]$$

where a_o is the atomic size, k^* is the thermal conductivity ratio, ω_{rel} is the rotational velocity of the particle relative to the liquid, V_{rel} is the translation velocity of the particle relative to the liquid, and S_{avg} is the average liquid velocity gradient ahead of the SLI. It was assumed that the particle and the liquid have the same density. Consequently the calculations are independent of the orientation of the gravity vector with respect to the solidification velocity vector. The Reynolds number and Weber number are given respectively as:

$$Re = \frac{VL\rho}{\eta}$$

$$We = \frac{V^2L\rho}{\Delta\gamma_0}$$

In the above equations, V is the characteristic velocity (taken as the maximum convection velocity), L is the characteristic length (taken as the boundary layer width of the liquid velocity), ρ is the liquid density, η is the dynamic viscosity of the liquid and $\Delta\gamma_0$ is the surface energy difference. A dimensionless equation like Equation 3 allows for comparison of “dynamically similar” systems.

Three different interaction regimes are identified for various ranges of convection velocities. For high convection velocities, there is no interaction between the SLI and the particle because the lift forces are much higher than the interaction force (Figure 4a). This is observed at normal gravity levels. As the gravity level decreases, the convection velocity also decreases and allows for interaction between the SLI and the particle because the lift and interaction forces are of the same order of magnitude (Figure 4b). The critical velocity for engulfment is higher as compared with the case of no convection. As convection further decreases, the lift forces become much smaller than the interaction force (Figure 4c) and convection does not influence the critical velocity anymore. The forces in these figures have been obtained for zirconia particles in a pure aluminum melt. The convection velocities at different gravity levels have been obtained from reference¹³. A parabolic liquid velocity profile has been assumed and the quantities S_{avg} and V_{rel} in Equation 3 have been obtained for this velocity profile.

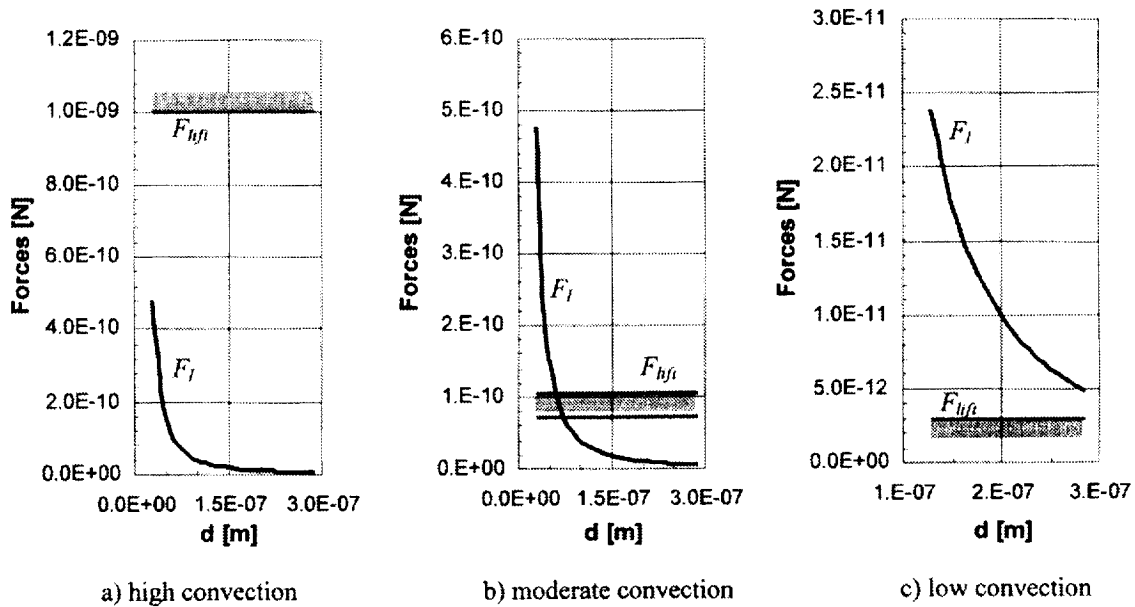


Figure 4. Comparison between lift and interaction forces for various convection levels.

Equation 3 was used to calculate the range of Reynolds numbers corresponding to the three convection regimes. The following results were obtained:

High convection regime	no particle-interface interaction	$Re > 0.6$
Moderate convection regime	increased critical velocity	$0.1 > Re > 0.6$
Low convection regime	no effect on critical velocity	$Re < 0.1$

III. Numerical Model – No Convection

The complicated problem of particle engulfment and pushing (PEP) can be simplified by minimizing convection ahead of the SLI. This is the rationale for microgravity experimentation. Under the assumption of no-convection we have also developed a numerical model that accounts for the influence of the solutal field¹⁴.

The 2-D numerical model for SLI tracking during the solidification of pure substances and alloys has been developed. The model is based on the finite difference formulation and uses a fixed Cartesian grid. The SLI is represented by a discrete set of markers that are moving according to the material thermophysical properties and the values of the transport variables (heat, solute concentration) in the vicinity of the interface. The model is capable to simulate solidification of pure substances as well as binary alloys. The model also accommodates changes of the interface temperature because of capillarity or solute redistribution. Another important feature of the model is that it is capable to describe the change of the solid/liquid interface shape and the development of segregation regions in the gap between an inclusion and the interface. This is a particularly difficult problem because of the length scales involved in the calculation. Indeed, the transport equations must describe events at the submicron level in the gap as well as at the macrolevel in the volume surrounding the particle.

Calculations for directional solidification of an Al-2wt%Cu alloy in the vicinity of a zirconia particle are shown in Figure 5. Specifically, the figure depicts the time evolution of the SLI as it approaches the particle at a velocity $V = 0.2 \mu\text{m/s}$. It can be observed that at $t = 7.19 \text{ s}$ from the beginning of simulation the interface forms a bump because the thermal conductivity of the particle is less than that of the melt, that is $k_p/k_L < 1$. At this stage, the particle/SLI distance is large and solute diffusion is not obstructed. The thermal field determines the outcome. However, as solidification proceeds, solute diffusion is partially blocked by the particle. The localized solute accumulation decreases the melting temperature and a trough begins to form on the interface bump ($t = 12.7 \text{ s}$). This solute accumulation increases as the interface further approaches the particle. Consequently, the depth of the trough also increases ($t = 20.1 \text{ s}$). The concentration profile presented in Figure 5 demonstrates solute trapping in the particle / interface gap.

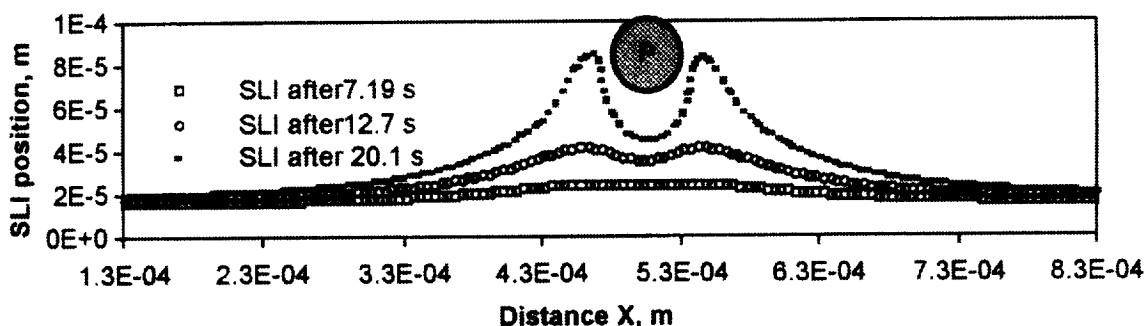


Figure 5. Time evolution of the SL interface (Al-2 wt% Cu alloy, ZrO_2 particle $R_p = 22.5 \mu\text{m}$, $V = 0.2 \mu\text{m/s}$)

IV. Experimental Work

Extensive ground and limited microgravity (μg) directional solidification experiments were performed to evaluate the critical velocity of engulfment of insoluble particles by an advancing SLI. The μg experiments were performed during shuttle flights in 1996 (LMS) and in 1997 (USMP4) in preparation for more intricate Space Station experimentation. For the experiments performed during the first flight, metallic matrices (aluminum and Al-Ni alloy with zirconia particles) were used. During the second flight we used transparent metal analogue materials (succinonitrile/polystyrene particles and biphenyl/glass particles). The latter allowed for observation of the interaction of the particles with the advancing solid/liquid interface *in-situ* and in *real-time*.

During ground experiments with the aluminum/zirconia particles ($500 \mu\text{m}$ diameter) system the observed critical velocity of engulfment was between 1.9 and $2.4 \mu\text{m/s}$. For subsequent μg experiments, each sample containing a high purity aluminum matrix with about 2 vol.% zirconia particles, was subject to three different

solidification velocities ranging from 0.5 to 20 $\mu\text{m/s}$. X-ray transmission microscope pictures of all samples were taken before and after flight. This allowed for a non-destructive characterization of the particle distribution and the possibility to check the samples for soundness in the pre-flight stage. By comparing the pre- and post-flight particle distribution, pushing was observed at a solidification velocity of 0.5 to 1 $\mu\text{m/s}$. The management of free surfaces was solved in one sample by a spring and piston mechanism. In the other one an expansion void was provided at the hot end. In both cases sound samples were obtained.

The drawback of metallic matrices is their opaqueness. Since analysis is limited to a *post-mortem* comparison, no direct observation of the SLI-particle interaction is possible. During the USMP-4 mission, a total of eight experiments were performed with transparent matrices in the μg glovebox facility. These experiments allowed for the observation in real time. The particle sizes ranged from 1 to 20 μm for polystyrene and 2-10 μm for glass. The data indicated the existence of a lower and upper bound for the critical velocity of engulfment. Comparison with ground data demonstrated again that a lower critical velocity is obtained in the absence of convection during μg experiments.

V. Acknowledgments

This work has been supported by NASA's Microgravity and Applications division through grant NAS8-39715.

REFERENCES

1. D.M. Stefanescu, R.V. Phalnikar, H. Pang, S. Ahuja and B.K. Dhindaw, *ISIJ International*, 35 (1995) 700-707
2. D.R. Uhlmann, B. Chalmers and K.A. Jackson, *J. Appl. Phys.*, 35, 10 (1964) 2986-2993
3. A.A. Chernov, D.E. Temkin, and A.M. Mel'nikova, *Sov. Phys. Crystallogr.*, 21, 4 (1976) 369-373 and 22, 6 (1977) 656
4. J. Pötschke, V. Rogge, *J. Crystal Growth*, 94, (1989) 726-738
5. D.K. Shangguan, S. Ahuja, D.M. Stefanescu, *Metall. Trans. A*, 23A (1992) 669-678
6. L. Hadji, in *Solidification 99*, W.H. Hofmeister, J.R. Rogers, N.B. Singh, S.P. Marsh and P.W. Vorhees, TMS, Warrendale, PA, (1999) 263-279
7. A.V. Catalina, S. Mukherjee and D.M. Stefanescu, *Metall. and Mater. Trans.* (2000) in print
8. J. O. Hinze, *Turbulence*, Mc-Graw-Hill, (1975) 463.
9. R. J. Brodkey, *The Phenomena of Fluid Motions*, Adison-Wesley, Reading, (1967) 621.
10. D. M. Stefanescu, F. R. Juretzko, B. K. Dhindaw, S. Sen, and P. A. Curreri: *NASA Microgravity Materials Science Conference*, D. C. Gillies, and D. E. McCauley editors, NASA Marshall Space Flight Center, Huntsville, Alabama, (1999) 599-604.
11. P.G. Saffman, *J. Fluid Mech.*, 22 (1965) 385-400.
12. Y. Tsuji, Y. Morikawa and O. Mizuno, *J. Fluids Eng.*, 107 (1985) 484
13. A. V. Bune et al., *J. Crystal Growth* 211 (2000) 446-451
14. A.V. Catalina and D.M. Stefanescu, in *Proceedings of the 4th Pacific Rim International Conference on Modeling of Casting & Solidification Processes*, C.P. Hong, J.K. Choi and D.H. Kim editors, CAMP, Seoul, Korea (2000) 3-12
15. F. R. Juretzko, B. K. Dhindaw, D. M. Stefanescu, S. Sen and P.A. Curreri, *Metall. and Mater. Trans.*, 29A (1998) 1691-96
16. D. M. Stefanescu, F. R. Juretzko, A.V. Catalina, S. Sen, P.A. Curreri, C. Schmitt and S. Gilley, in *Fourth United States Microgravity Payload: One Year Report*, E.C. Ethridge, P.A. Curreri and D.E. McCauley compilers, 1999, NASA/CP-1999-209628 (1999) 161-178

STRUCTURAL FLUCTUATIONS AND THERMOPHYSICAL PROPERTIES OF MOLTEN II-VI COMPOUNDS

Principal Investigator: Dr. Ching-Hua Su¹

Co-Investigators: Dr. Shari Feth, University of Alabama in Huntsville/MSFC

Dr. Sandor Lehoczky, SD40, NASA/MSFC

Dr. Herb Mook, Oak Ridge National Laboratory

Dr. Rose Scripa, University of Alabama at Birmingham

Dr. Shen Zhu, USRA/MSFC

¹SD47 NASA/Marshall Space Flight Center, Huntsville, AL 35812

Tel: (256) 544-7776 Fax: (256) 544-8762; E-mail Address: ching.hua.su@msfc.nasa.gov

INTRODUCTION

Recently, in support of the microgravity experiment entitled "Crystal Growth of Selected II-VI Semiconducting Alloys by Directional Solidification," the viscosity of HgZnTe pseudobinary melt was measured using an oscillating-cup viscometer [1] at NASA/Marshall Space Flight Center (MSFC). An unexpected time drift of the measured viscosity, which shows a slow relaxation phenomena at temperatures near the liquidus point, was reproducibly observed. Two sets of data were obtained by cooling the $\text{Hg}_{0.84}\text{Zn}_{0.16}\text{Te}$ melt from 850°C and stabilizing at temperatures of 790°C, which is just above the liquidus temperature, and stabilizing at temperature of 810°C. While it took one day to reach equilibration at 810°C, five days were required at 790°C. A similar relaxation phenomenon was also observed in the measured density of the same liquid [2]. Furthermore, in the density measurements of the HgCdTe melts, which is the pseudobinary system studied in another flight experiment entitled "Growth of Solid Solution Single Crystals," a negative thermal expansion was reported [3]. The liquid density increases from the liquidus point to a maximum value at a temperature approximately 70°C above the liquidus, where normal thermal expansion progressively resumes.

Possible mechanisms for the observed relaxation phenomena during temperature cycling in the HgZnTe melts and for the anomalous thermal expansion observed in the HgCdTe melts could be attributed to either macroscopic or microscopic inhomogeneities. Macroscopic inhomogeneities can be present, for instance, due to insufficient mixing during sample preparation. In fact, any local departure from stoichiometry will significantly change the thermophysical properties of the melts. An inhomogeneity can also arise from the evaporation/condensation of mercury into/from a free volume in the ampoule. This could create a thin mercury boundary layer around the sample, thus modifying the wetting condition of the melt to the ampoule wall and changing the surface tension of the top free surface of the melt. It is, however, unlikely that this effect would be present only in the small temperature range of 790 to 810°C and not be observed at higher temperatures. Finally, bubble formation in the melt may cause significant effects. Although direct observation of the melt during the density measurement [2] did not show any, the existence of small bubbles was still possible.

The nature of the relaxation effect more likely can be attributed to microscopic inhomogeneities. Density and composition fluctuations in the melts near the liquidus point can be significantly different from those at higher temperature. For instance, heterophase fluctuations in the form of subcritical clusters of the second phase can be present [4]. For the ionic binary and ternary systems, as compared to single-element melts, heterofluctuations would be more likely to occur. Any changes in the temperature will induce a redistribution in the cluster size and composition. This is a diffusion-controlled process of heat and mass transfer, which may be similar to the Ostwald ripening phenomenon and can be very slow.

High quality single crystals of compound semiconductors are needed for various electro-optical applications. At present, the majority of the semiconducting crystals are grown from the melt. Consequently, the pre-crystallization phenomena in the liquid phase are critical because the state and structure of the melt affects the structure and properties of the crystals formed from it. A fundamental understanding of molecular structural dynamics in melts will be helpful in understanding the relations between the interfacial flows and molecular attachment mechanisms, including those generating lattice defects. If the relationship between the processing conditions of the melt and the microstructural development of the solid is well understood then a first-principles design of materials with the desired properties can be realized. Therefore, an in-depth study on the time-dependent structural dynamic processes taking place in the vicinity of the solid-liquid phase transition as well as the *in-situ* structural analysis of the alloy homogenization process in the melt is needed to understand and to improve the crystal growth processes.

Thermophysical properties of the melts are required for any meaningful investigation of the crystal growth processes, in particular for testing the detailed predictions of numerical models. Thermal and electrical conductivity, viscosity and density are basic thermophysical properties of semiconductor melts. The experimental values of these properties as functions of temperature and composition are required for virtually all melt systems in the field of microgravity materials processing as well as in the area of fluid physics. However, because of restrictions, such as toxicity, high vapor pressure and contamination, imposed by the II-VI melts at elevated temperatures, the samples are required to be sealed inside closed ampoules. Hence, the thermophysical data on an overwhelming majority of the technologically important II-VI melts are scarce and inaccurate due to the difficulties, the complexity in operation and the serious performance limitations of existing techniques. The ability to accurately measure these properties of semiconductor melts as functions of temperature and composition would significantly increase the quality of the research and would make numerical modeling work more meaningful. For instance, accurate data on thermal conductivity for the ternary solid and liquid systems as functions of temperature and composition are needed for the detailed numerical simulation of the solid-liquid growing interface during the microgravity solidification experiment. Such data will also be valuable in the area of fundamental fluid physics.

Therefore, it is proposed to conduct ground-based experimental and theoretical research on the structural fluctuations and thermophysical properties of molten II-VI compounds to enhance the basic understanding of the existing flight experiments in microgravity materials science programs and to study the fundamental heterophase fluctuations phenomena in these melts by:

- 1) Conducting neutron scattering analysis and measuring quantitatively the relevant thermophysical properties of the melts such as viscosity, electrical conductivity, thermal diffusivity and density as well as the relaxation characteristics of these properties to advance an understanding of the structural properties and the relaxation phenomena in these melts and
- 2) Performing thermodynamic analyses on the melts to interpret the experimental results.

I. Experimental

To support the two microgravity materials science flight experiments entitled “Crystal Growth of Selected II-VI Semiconducting Alloys by Directional Solidification,” and “Growth of Solid Solution Single Crystals” we propose to perform measurements on the II-VI melts, which include the HgTe binary as well as the pseudobinaries of the HgCdTe and HgZnTe systems. The measurements include neutron scattering, viscosity, electrical conductivity, thermal diffusivity, density and volumetric expansion coefficient. Measurements will be performed under two sets of experimental conditions. Firstly, the measurements as a function of time near the liquidus point, including temperatures below the liquidus temperature on the supercooled liquid, will provide the basic information on heterophase fluctuations in the vicinity of the solid-liquid phase transition. Secondly, the measurements as a function of temperature from the liquidus to higher temperatures will be performed to study the structural transition as well as the semiconductor-metal transition, which typically cover a wide temperature range.

A. Neutron scattering analysis

Neutron scattering will be employed to study the heterophase fluctuations near the liquidus temperature as well as at higher temperatures in the HgTe binary as well as in the HgCdTe and HgZnTe pseudobinary melts of various compositions. The samples will be prepared inside a fused silica crucible. The initial experiments will involve the determination of the radial distribution function using a low wavelength or high momentum transfer setup. Two sets of experimental measurements will be performed: measurements as a function of time near the liquidus point and measurements as a function of temperature from the liquidus to higher temperatures. The results will provide basic information on the liquid structure and will dictate the selection of further experiments.

B. Viscosity and electrical conductivity

It is proposed to employ the rotating magnetic field technique to monitor the viscosity and electrical conductivity of HgTe, HgCdTe and HgZnTe melts under two different experimental conditions: (1) the viscosity and electrical conductivity measurements as a function of time near the liquidus point; *i.e.* about 30°C below and above the liquidus temperature and (2) the measurements as a function of temperature from the liquidus to higher temperatures. The results will provide basic information on the heterophase fluctuations near the liquidus temperature as well as the semiconductor-metal transition in the melt over a wide temperature range.

C. Thermal diffusivity measurements

A dynamic measurement of the thermal diffusivity using the laser flash method [5,6] has been employed previously to determine the thermal conductivity of various composite materials as well as those systems that have to be enclosed in closed ampoules due to their high vapor pressures or toxic nature. In this method, the front surface of a small disk-shaped sample is subjected to a very short burst of radiant energy from a laser pulse with a radiation time of 1 ms or less. The resulting temperature rise of the rear surface of the sample is measured and thermal diffusivity values calculated from the data of temperature rise versus time. The thermal diffusivities of $\text{Hg}_{1-x}\text{Cd}_x\text{Te}$ solids and melts [7], pure Te, Te-rich HgCdTe and Te-rich HgZnTe melts [8] were determined using this technique. Recently, using the technique we have also measured the thermal diffusivities for $\text{Hg}_{1-x}\text{Zn}_x\text{Te}$ solids and melts [9]. However, the relax-

ation characteristics of the measured thermal diffusivities on these melts were not investigated. It is therefore proposed that the laser flash technique will be established at MSFC to study the heterophase fluctuations and the relaxation characteristics in the molten II-VI systems. The samples will be prepared inside a fused silica crucible. Two sets of experimental conditions will be performed: the measurements as function of time near the liquidus point and measurements as function of temperature from the liquidus to higher temperatures. The results will provide basic information on the heterophase fluctuations near the liquidus temperature as well as on the semiconductor-metal transition over a wide temperature range.

D. Density and volume expansion coefficient

The density and volume expansion coefficients for the $\text{Hg}_{1-x}\text{Cd}_x\text{Te}$ ($x \leq 0.2$) [3] and $\text{Hg}_{1-x}\text{Zn}_x\text{Te}$ ($x \leq 0.16$) melts [2] were established at MSFC using a pycnometric method. The measurements were carried out in thermometer-shaped fused silica ampoules, which were placed vertically inside a transparent furnace and the meniscus heights measured using a cathetometer. From our experience with the measurements on HgZnTe melts, the shape of the meniscus was highly curved and changed abruptly with time, precluding the employment of a more accurate technique such as optical interferometry. As pointed out earlier, the measured density vs. temperature plot for the HgCdTe [3] melts exhibited a maximum, and an inhomogeneous structure model for the liquid [10] was adopted to explain this anomalous volume expansion. On the other hand, a relaxation phenomenon similar to the measured viscosity of HgZnTe melts was observed in the measured density for HgZnTe melts [11]. It is proposed to measure the density of these pseudobinary melts with specific improvements in the ampoule design, the isothermality and the stability of the furnace. Beside HgCdTe and HgZnTe melts, the two sets of measurements, as described in previous sections, will also be performed on the HgTe binary system.

II. Theoretical

A. Associated solution model for the liquid phase

The general theory of the associated solution model presented by Brebrick et al., which was employed for the In-Ga-Sb and Hg-Cd-Te systems [12] will be adopted. In the treatment of the Hg-Cd-Te system, the liquid is assumed to consist of Hg, Cd, Te, HgTe and CdTe species. The mole fraction of each species is determined by the atomic fraction of each element, i.e. Hg, Cd and Te, and the equilibrium constants for the association/dissociation reaction. The theory will be generalized to apply to a liquid consisting of any type and number of species as suggested by the neutron scattering analysis. Having chosen the species in the liquid phase, the thermodynamic characterization will be completed by assuming an equation for the excess Gibbs energy of mixing, ΔG_m^x of forming the solution from the liquid elements:

$$\Delta G_m^x = \sum \sum (\alpha_{ij} + \beta_{ij} y_j) y_i y_j + \sum \sum \sum \gamma_{ijk} y_i y_j y_k - \sum y_i^M \Delta G_i^M \quad (1)$$

where y_i is the mole fraction of species i . The α_{ij} , $\beta_{ij} y_j$ and γ_{ijk} are the composition-independent, temperature-dependent interaction parameters, and ΔG_i^M is the dissociation energy for the molecular species with mole fraction y_i^M .

B. Thermodynamic analyses for the heterophase

The previous thermodynamic analysis of these systems was treated under conditions of thermodynamic equilibrium. To modify this analysis such that it can represent a mixture, in which phases can coexist in a finite temperature range, we will include the concept of effective equilibrium. First, the analysis of equilibrium thermodynamics will be reviewed briefly.

(i) Equilibrium thermodynamics.

For simplicity, we will consider a one-component two-phase system. The temperature, T , and pressure, P , are constant through the whole system as a result of thermal and mechanical equilibrium. Let the number of particles in each phase be N_i with $i = 1$ or 2 so that the total number of particles in the system is fixed as $N = N_1 + N_2$. The Gibbs energy, G , is a function of T , P , N_1 and N_2 , i.e. $G = G(T, P, N_1, N_2)$ and is given by

$$G = G_1(T, P, N_1) + G_2(T, P, N_2). \quad (2)$$

Each of the phases can be treated as uniform – its Gibbs energy satisfies the property of uniformity:

$$G_i(T, P, N_i) = N_i \mu_i(T, P), \quad (3)$$

where $\mu_i(T, P)$ is the chemical potential of phase i . From the equilibrium condition at constant T and P , when

$$\delta G = 0, \delta N_1 = -\delta N_2, \quad (4)$$

which yields the Gibbs phase rule:

$$\mu_1(T, P) = \mu_2(T, P). \quad (5)$$

The equilibrium condition given by the Gibbs phase rule implies that two phases can coexist only along the line $T_0 = T_0(P)$. Therefore, under constant pressure, two phases under equilibrium conditions can only exist at the transition point T_0 , and no coexistence in a finite temperature region around the transition point is possible.

(ii) Effective equilibrium.

One method to construct the thermodynamics effective equilibrium of a mixture in which phases can coexist in a finite temperature range is to abandon the property of uniformity, equation (3). In this case, the effective chemical potential is introduced as

$$\mu_i^e(T, P, C_i) = (\delta/\delta N_i)G_i(T, P, N_i), \quad (6)$$

which depends on the number of particles, N_i , through the concentration C_i defined as $C_i = N_i/N$ with $C_1 + C_2 = 1$. From equation (4) it follows that

$$\mu_1^e(T, P, C_1) = \mu_2^e(T, P, C_2) \quad (7)$$

Thus the condition for effective equilibrium is the equality of the effective chemical potentials. Notwithstanding the similarity between the conditions of equilibrium and effective equilibrium, there is a drastic difference between them in that the phase concentrations under effective equilibrium are functions of temperature and pressure

$$C_i = C_i(T, P) \quad i = 1, 2. \quad (8)$$

Consequently, under constant pressure the phases can exist in a finite range of temperatures.

In the case of heterophase systems of many components, an added term for the entropy of mixing, $-N(C_1 \ln C_1 + C_2 \ln C_2)$, will be included in the excess Gibbs energy of mixing, equation (1).

III. Analyses

The neutron scattering measurements will provide the basic information of heterophase fluctuations such as the sizes, structures, chemical identities and lifetimes of the clusters existing in the melts. Based on the neutron scattering results the generalized associated solution model will be adopted to analyze the liquid phase. All of the thermodynamic data for the elements, the binary and the ternary systems will be gathered and selected discriminatively and the interaction parameters between the species will be determined by fitting the calculated results to the experimental data. Then, all of the thermodynamic properties as functions of composition and temperature, including those that are difficult to measure experimentally, can be generated.

After the interaction parameters for the liquid model are fixed, a theoretical description of the associated liquid phase can be established. The theoretical description will be employed to interpret the results of the thermodynamic and thermophysical property measurements (viscosity, electrical conductivity, thermal diffusivity and volumetric expansion coefficient) with proper modification or refinement to the model. Finally, a fundamental understanding of the molecular structural dynamics in these melts will enable us to interpret the various experimental results on the crystal growth of II-VI semiconducting compounds by directional solidification from both the ground-based and space-flight processing. Then, the ultimate goal of utilizing the first-principles design to obtain materials with desired properties can be realized as the relationship between the processing conditions of the melt and the microstructural development of the solid is well established.

REFERENCES

1. K. Mazuruk, Ching-Hua Su, Yi-Gao Sha and S. L. Lehoczky, J. Appl. Phys. 79 (1996) 9080.
2. Ching-Hua Su, Yi-Gao Sha, K. Mazuruk and S. L. Lehoczky, J. Appl. Phys. 80 (1996) 137.
3. D. Chandra and L. R. Holland, J. Vac. Sci. Technol A1 (1983) 1620.
4. V. I. Yukalov, Phys. Rep. 208 (1991) 395.
5. W. J. Parker, R. J. Jenkins, C. P. Butler and G. L. Abbott, J. Appl. Phys. 32 (1961) 1679.
6. R. E. Taylor, High Temp.-High Pressures 11 (1979) 43.
7. Y. Tsuchiya, J. Phys. C 20 (1987) 1209.
8. H. Maleki and R. Holland, J. Appl. Phys. 76 (1994) 4022.
9. Y.-G. Sha, C.-H. Su, K. Mazuruk and S. L. Lehoczky, J. Appl. Phys. 80 (1996) 752.
10. D. Chandra, Phys. Rev. B31 (1985) 7706.
11. V. I. Yukalov, Physica A 144 (1987) 369.
12. R. F. Brebrick, Ching-Hua Su and Pok-Kai Liao, "Semiconductors and Semimetals", Vol. 19, Ch.3 Academic Press (1983).

CRYSTAL GROWTH OF ZnSe AND RELATED TERNARY COMPOUND SEMICONDUCTORS BY VAPOR TRANSPORT

Principal Investigator: Ching-Hua Su¹

Co-Investigators: Prof. Robert F. Brebrick, Marquette University

Dr. Arnold Burger, Fisk University, NASA Center for Photonic Materials and Devices

Prof. Michael Dudley, State University of New York at Stony Brook

Prof. Richard J. Matyi, University of Wisconsin, Madison

Drs. Narayanan Ramachandran and Yi-Gao Sha, USRA, NASA/MSFC

Dr. Martin Volz, SD47, NASA/MSFC

Industrial Co-Investigator: Dr. Hung-Dah Shih, Central Research Laboratories, TI

¹SD47 NASA/Marshall Space Flight Center, Huntsville, AL 35812

Tel: (256) 544-7776 Fax: (256) 544-8762; E-mail Address: ching.hua.su@msfc.nasa.gov

INTRODUCTION

Crystal growth by vapor transport has several distinct advantages over melt growth techniques. Among various potential benefits from material processing in reduced gravity the followings two are considered to be related to crystal growth by vapor transport: (1) elimination of the crystal weight and its influence on the defect formation and (2) reduction of natural buoyancy-driven convective flows arising from thermally and/or solutally induced density gradient in fluids. The previous results on vapor crystal growth of semiconductors showed the improvements in surface morphology, crystalline quality, electrical properties and dopant distribution of the crystals grown in reduced gravity as compared to the crystals grown on Earth. But the mechanisms, which are responsible for the improvements and cause the gravitational effects on the complicated and coupled processes of vapor mass transport and growth kinetics, are not well understood.

The materials to be studied in this project are ZnSe and the related ternary compound semiconductors such as ZnSeTe, ZnSeS and ZnCdSe. The scientific objectives and priorities of this investigation are:

(1) Grow ZnSe crystals in reduced gravity using Physical Vapor Transport (PVT) processes:

- to establish the relative contributions of gravity-driven fluid flows to (i) the non-uniform incorporation of impurities and defects and (ii) the deviation from stoichiometry observed in the grown crystals as the results of buoyancy-driven convection, irregular fluid-flows and growth interface fluctuations.
- to assess the amount of strain developed during processing at elevated temperatures and retained on cooling caused by the weight of the crystals.
- to obtain a limited amount of high quality space-grown materials for various thermophysical and electrical properties measurements and as substrates for device fabrication and thus assess device performance as influenced by a substantial reduction in gravity-related effects.

- (2) Perform in-situ and real-time optical measurements during growth to independently determine:
 - the vapor concentration distribution by partial pressure measurements using optical absorption.
 - the evolution of growth interface morphology and instantaneous growth velocity by optical interferometry.
 - and thus help to simplify the complexity of the coupled mass transport and growth kinetics problem.
- (3) Evaluate the additional effects of gravity on the PVT process in the future flight experiments by examining:
 - the dopant segregation and distribution in the Cr doped ZnSe.
 - the compositional segregation and distribution in the ternary compounds grown by PVT.

I. Experimental

The main disadvantage of PVT growth technique is that the growth rate is usually low and inconsistent. Therefore, a systematic and complete study was performed to optimize the mass flux in the ZnSe PVT system. Firstly, from the results of a one-dimensional diffusion analysis [1,2], four experimentally adjustable parameters, the source temperature, the deposition temperature, the partial pressure ratio over the source (vapor phase stoichiometry) and the residual gas (CO, CO₂ and H₂O) pressure, determine the diffusive mass flux in a PVT system. However, two of these four parameters, the partial pressure ratio over the source and the residual gas pressure, are more critical than the others. These two parameters are critically dependent on the proper heat treatments of the starting materials for optimum mass flux. Secondly, the pertinent thermodynamic properties were determined. The partial pressures of Zn and Se₂ over ZnSe(s) were measured for several samples by the optical absorption technique [3] and the standard Gibbs energy of formation of ZnSe(s) from Zn(g) and 0.5Se₂(g) was found to be independent of the sample stoichiometry. The Zn-Se phase diagram was described using an associated solution model for the liquid phase and the behavior of the thermodynamic properties of the system pertinent to the PVT process, such as the partial pressures of Zn and Se₂ along the entire three-phase curve, were calculated [4]. The associated solution model was then extended to the Zn-Se-Te system and the thermodynamic properties, such as the partial pressures of Zn, Se₂ and Te₂ along the three-phase curve for various ZnSe_{1-x}Te_x (0 < x < 1) pseudobinary systems were established. Thirdly, an *in-situ* dynamic technique [5] was set up for the mass flux measurements which has the advantages over the previous techniques in that (1) instantaneous flux (instead of average value) was measured and (2) multiple data points were determined from one ampoule. The mass fluxes in the ZnSe PVT system were measured for source materials provided by various vendors and treated with different heat treatment procedures. Fourthly, the residual gas pressures and compositions in the processed ampoules were measured and it was found that (1) carbon and oxygen in the residual gas were mainly originated from the ZnSe source materials and (2) the oxygen content can be significantly reduced by an hydrogen reduction treatment [6]. Fifthly, various heat treatments were conducted to control the partial pressure ratio over the source and the effectiveness of the treatments was evaluated by partial pressure measurements [7]. Finally, the optimum hydrogen reduction and vacuum heat treatment procedures were established for the source to maximize the mass flux in the ZnSe PVT process.

The crystal growth activities were concentrated on a novel three thermal-zone translational growth in a closed system. In order to study the effects of gravity on the various properties of the grown crystals the growth experiments were performed with the growth direction at the angle of 0° (vertical destabilized configuration), 90° (horizontal configuration) and 180° (vertical stabilized configuration) to the gravity vector direction. The self-seeded and seeded growths of ZnSe as well as the self-seed growths of

ZnSeTe and Cr doped ZnSe were conducted. The grown crystals were characterized by various techniques. These methods included spectroscopy (atomic absorption, spark source mass spectroscopy and secondary ion mass spectroscopy), X-ray diffraction (Laue reflection, rocking curve and reciprocal lattice mapping), synchrotron radiation images from a white X-ray beam (reflection and transmission), microscopy (optical, electron, and atomic force), sample polishing and etching and optical transmission. The electrical and optical characterization was performed by optical transmission and photoluminescence measurements.

The effects of gravity vector orientation were studied by comparing the following characteristics of the vertically and horizontally grown ZnSe crystals:

- (1) Grown crystal morphology: the morphology of the as-grown, self-seeded ZnSe crystals grown in the horizontal configuration grew away from the ampoule wall and exhibited large (110) facets which tended to align parallel to the gravitational direction [8]. Crystals grown in the vertical configuration grew in contact with the ampoule wall to the full diameter and when the furnace translation rate was too high for the mass flux, the crystal growing surface became morphologically unstable with voids and pipes embedded in the crystal. The as-grown seeded ZnSe crystals in both the horizontal and vertical configurations showed similar characteristics in the morphology as described above for the self-seeded growth.
- (2) Surface morphology [8,9]: the as-grown surfaces of the horizontally grown ZnSe and Cr doped ZnSe crystals were dominated by (110) terraces and steps. On the other hand, the as-grown surface of the vertically grown ZnSe crystals showed granular structure with tubular features (200nm OD, 75nm ID and 25nm in height) on the top. The as-grown surface of the vertically grown Cr doped ZnSe crystals showed a network of high plateaus with each island 30-70nm in diameter and 3.5nm in height. Numerous nuclei with diameters around 20-50nm and heights of 1-7nm were observed on top of these islands.
- (3) Segregation and distribution of defects and impurities [10]: from secondary ion mass spectroscopy mappings, for the horizontally grown self-seeded ZnSe crystal, [Si] and [Fe] showed clear segregation toward the bottom of the wafer cut axially along the growth axis. For the vertically grown seeded ZnSe crystal, [Si] and [Cu] showed segregation toward the peripheral edge of the wafer cut perpendicular to the growth axis. From the photoluminescence mappings of near band edge intensity ratios, it was determined that all of the horizontally grown crystals showed the following trends in the radial and axial segregation of [Al] and $[V_{Zn}]$ due to buoyancy driving force and diffusion boundary layer: [Al] segregates radially toward the top and axially toward the first grown region and $[V_{Zn}]$ segregates radially toward the bottom and axially toward the first grown region. The as-grown surface of the seeded vertically stabilized grown crystal showed [Al], [Li and/or Na] and $[V_{Zn}]$ segregate radially toward the center. Finally, the as-grown surface of the self-seeded vertically destabilized grown crystal showed [Al] and $[V_{Zn}]$ segregate radially without an apparent pattern. The Cr concentration in the horizontally and vertically grown Cr doped crystals was determined by optical absorption and the segregation coefficients, $[Cr_{crystal}]/[Cr_{source}]$, were 0.015 and 0.085, respectively [9].
- (4) Axial compositional variation in ZnSeTe [11]: the mole fraction of ZnTe in the grown $ZnSe_{1-x}Te_x$ crystals, x, was determined from precision density measurements on slices cut perpendicular to the growth axis. The vertically (stabilized) grown crystals showed less axial variations and better agreement with the source compositions than the horizontally grown crystals. The composition of the initial grown crystals and the compositional variations in the horizontally grown samples were not consistent with the one-dimensional diffusion model.

The experimental results clearly showed that the convective irregular flows caused by the buoyancy-driven perturbation in the flow field in the vicinity of the growing surface resulted in non-uniformity in the axial and radial incorporation of impurities and defects as well as a deviation from stoichiometry.

In-situ and real-time measurements of partial pressure using optical absorption and measurements of the growth interface morphological evolution and instantaneous growth velocity using optical interferometry during growth were performed to study the coupled mass transport and growth kinetics problem. The growth furnace, optical monitoring set-up and growth ampoule design for *in-situ* optical monitoring during the PVT growth of ZnSe were constructed and optimized [12]. The results of the partial pressure measurements during the growth of ZnSe(1S)-5 ampoule [12] indicated that (1) partial pressures of Se_2 measured along the ampoule length was inconsistent with the results of the one-dimensional diffusion model and (2) the source composition shifted toward Se-rich conditions during the run, i.e. the grown crystal was more Zn-rich than the source.

Michelson and Fabry Perot optical interferometers were set up for *in-situ* monitoring of the growing surface of the crystal. The Michelson setup was flexible, i.e. the optics were easily adjusted both before and during growth, however the fringe patterns were not stable due to the thermal convection of the surrounding air. It was shown that a modification of the ampoule significantly suppressed this noise. Also, this effect is not expected to be of significant consequence in the reduced gravity environment. The Fabry-Perot interferometer provides good quality fringe patterns, but the optics were rigid and difficult to adjust during the crystal growth run. Using the interferometric techniques, the thermal expansion coefficient of ZnSe was measured between 25°C and 1080°C. Phase maps of the growing crystal surface were constructed in real-time using fringe data from both interferometric set-ups. A visual observation of the growing crystal was performed and the results can be correlated with the phase map results [12].

Other characterization techniques were also performed on the grown single crystals of ZnSe [13]. The impurities and defects in the grown crystals were studied by glow discharge mass spectroscopy (GDMS) and low temperature photoluminescence (PL) measurements. The PL results on the starting material and the grown crystals are consistent with the low impurity levels measured by GDMS. The crystalline quality of the grown crystals were examined by synchrotron white beam X-ray topography (SWBXT) and high resolution triple X-ray diffraction (HRTXD). The SWBXT shows that, aside from twins, the overall crystalline quality of the vapor grown ZnSe crystals, especially in the contactless grown region, was quite high. The HRTXD results are in line with the SWBXT findings. The comparison between the HRTXD on a chemical-mechanically polished and a cleaved surface seems to indicate that polishing damage can obscure the true microstructure in the as-grown ZnSe crystals.

II. Theoretical

Besides the one-dimensional diffusion model, the transport process modeling also included:

- (1) two-dimensional analytical description of fluid flow using thermal conditions (no solutal effects) for a typical growth experiment to estimate the maximum flow velocities for the vertical and horizontal configurations. The calculated maximum shear (perpendicular to growth direction) flow velocity was 5.2 $\mu\text{m/s}$ for the horizontal configuration and 0.22 $\mu\text{m/s}$ for the vertical configuration under $1g_0$ condition (where g_0 is the gravity level on Earth).
- (2) two-dimensional numerical modeling of the thermal environment of the growth furnace and a seeded ampoule, including both radiative and conductive heat transfer, predicted a temperature drop of 2.2°C from the edge to the center on the seed surface.

- (3) two and three-dimensional numerical modeling of physical vapor transport process using finite element technique to treat both thermal and solutal induced buoyancy forces [14]. Both compressible and Boussinesq fluids were assumed for a system of multiple transport species with residual gas. The results of the two and three-dimensional calculation agreed well with the benchmark studies. The effects of gravity on the flow field were examined by plotting the differences between the calculated flow velocities for various gravity levels and that for zero gravity. The calculated maximum shear flow velocity difference under $1g_0$ condition was $50\mu\text{m/s}$ for the horizontal configuration and $9.4\mu\text{m/s}$ for the vertical configuration. The maximum allowable acceleration level during the flight experiments was established by taking the criterion that the maximum shear velocity is equal or less than 10% of the crystal growth rate. This resulted in the requirement of a maximum residual longitudinal acceleration level of $2.7 \times 10^{-3} g_0$ and a transverse level of $1.0 \times 10^{-4} g_0$ for the flight experiments.

REFERENCES

1. M. M. Faktor and I. Garrett, Growth of Crystals from the Vapour, Chapman & Hall, London, 1974.
2. Ching-Hua Su, J. Crystal Growth 80 (1987) 333.
3. R. F. Brebrick and H.-C. Liu, High Temp. Mater. Sci. 35 (1996) 215.
4. R. F. Brebrick and H.-C. Liu, J. Phase Equilibria 17 (1996) 495.
5. Yi-Gao Sha, Ching-Hua Su, W. Palosz, M. P. Volz, D. C. Gillies, F. R. szofran, S. L. Lehoczky, H.-C. Liu and R. F. Brebrick, J. Crystal Growth 146 (1995) 42.
6. Ching-Hua Su, Yi-Gao Sha, K. Mazuruk, S. L. Lehoczky, H.-C. Liu, R. Fang and R. F. Brebrick, J. Crystal Growth 166 (1996) 736.
7. Ching-Hua Su, W. Palosz, S. Feth and S. L. Lehoczky, J. Crystal Growth 192 (1998) 386.
8. Ching-Hua Su, M. A. George, W. Palosz, S. Feth and S. L. Lehoczky, J. Crystal Growth (2000) in press.
9. Ching-Hua Su, S. Feth, M. P. Volz, R. Matyi, M. A. George, K. Chattopadhyay, A. Burger and S. L. Lehoczky, J. Crystal Growth 207 (1999) 35.
10. Ching-Hua Su, S. Feth, D. Hirschfeld, T. M. Smith, Ling Jun Wang, M. P. Volz and S. L. Lehoczky, J. Crystal Growth 204 (1999) 41.
11. Ching-Hua Su, Yi-Gao Sha, M. P. Volz, P. Carpenter and S. L. Lehoczky, J. Crystal Growth (2000) in press.
12. Ching-Hua Su, S. Feth and S. L. lehoczky, J. Crystal Growth 209 (2000) 687.
13. Ching-hua Su, M. Dudley, R. Mayti, S. Feth and S. L. Lehoczky, J. Crystal Growth 208 (2000) 237.
14. N. Ramachandran, Ching-Hua Su and S. L. Lehoczky, J. Crystal Growth 208 (2000) 269.

REDUCTION OF DEFECTS IN GERMANIUM-SILICON

F.R. Szofran^{1*}, K.W. Benz², S.D. Cobb¹, A. Cröll^{3,4}, P. Dold², N. Kaiser^{2,3}, S. Motakef⁵,
M. Schweizer², M.P. Volz¹, L. Vujisic⁵, and J.S. Walker⁶

¹NASA, Marshall Space Flight Center,

²Albert-Ludwigs University, Freiburg, Germany,

³University of Alabama in Huntsville,

⁴Technical University, Freiberg, Germany,

⁵CAPE Simulations, Inc.,

⁶University of Illinois at Urbana-Champaign

OBJECTIVES OF THE INVESTIGATION

Crystals grown without being in contact with a container have superior quality to otherwise similar crystals grown in direct contact with a container, especially with respect to impurity incorporation, formation of dislocations, and residual stress in the crystals. In addition to float-zone processing, detached Bridgman growth, although not a completely crucible-free method, is a promising tool to improve crystal quality. It does not suffer from the size limitations of float zoning and the impact of thermocapillary convection on heat and mass transport is expected to be negligible. Detached growth has been observed frequently during μg experiments [1]. Considerable improvements in crystalline quality have been reported for these cases [2]. However, neither a thorough understanding of the process nor a quantitative assessment of the quality of these improvements exists. This project will determine the means to reproducibly grow GeSi alloys in a detached mode and seeks to compare processing-induced defects in Bridgman, detached-Bridgman, and floating-zone growth configurations in GeSi crystals ($\text{Si} \leq 10 \text{ at\%}$) up to 20mm in diameter.

Specific objectives include:

- measurement of the relevant material parameters such as contact angle, growth angle, surface tension, and wetting behavior of the GeSi-melt on potential crucible materials;
- determination of the mechanism of detached growth including the role of convection;
- quantitative determination of the differences in defects and impurities for crystals grown using normal Bridgman, detached Bridgman, and floating zone (FZ) methods;
- investigation of the influence of a defined flow imposed by a rotating magnetic field on the characteristics of detached growth;
- control of time-dependent Marangoni convection in the case of FZ growth by the use of a rotating magnetic field to examine the influence on the curvature of the solid-liquid interface and the heat and mass transport; and growth of benchmark quality GeSi-single crystals.

I. Microgravity Relevance

Prior to the beginning of this investigation, the most reliable environment for obtaining detached Bridgman growth was reduced gravity. At this time, we and others are repeatedly growing partially detached Bridgman samples in unit gravity. Nonetheless, the reasons for completing the microgravity parts of this investigation still remain viable:

- The comparison of samples grown by detached growth with float-zone samples of the same diameter is fundamental to this study because the float-zone technique is truly and completely containerless in contrast to detached Bridgman growth. Terrestrial floating zones of this material are limited to diameters of about 8 mm. Therefore, these larger diameter floating-zone experiments can only be conducted in a reduced gravity environment.
- The occurrence of detachment during Bridgman growth is postulated to be dependent upon the difference in gas pressures in the crucible above and below the melt and it is further believed that the evolution of gases at the growth interface is required to maintain the necessary pressure difference [3, 4, 5]. Determining whether this pressure difference is essential in all cases is one of the objectives of this investigation. If the growth and contact angles are favorable, detachment will take place without a pressure difference. This will only be possible for very few material-crucible combinations. Gas evolution and the resulting maintenance of the pressure difference will be strongly effected by convection in the melt, which is dominated in the Bridgman configuration by buoyancy-driven flows. Thus, to the extent that this phenomenon is necessary for detachment, the conditions for detached growth will differ significantly between unit gravity and microgravity because of the influence of gravity on convection in the melt.
- The effect of an intentional pressurization of the volume below the meniscus either by using pressurized gas [6] or by changing the temperature profile, as in this project, is limited by the emission of bubbles under gravity once the pressure of the hydrostatic head is attained.
- Segregation effects due to significant differences in density between Ge and Si have to be considered during the growth of GeSi alloys. Experiments have shown that the orientation of the gravity vector is essential in respect to the segregation profile of GeSi Bridgman-grown crystals. In order to avoid gravitational effects it is essential to grow GeSi crystals under microgravity.
- Finally, the FZ growth of GeSi alloys is accompanied by interesting differences in the shape of the growth meniscus (compared to Ge or Si) due to the interaction between thermocapillary and solutocapillary effects. The specifics are discussed later but the full understanding of the interaction of these two effects, which might also influence detached growth, will require comparison between 1g and microgravity results.

II. Results

There is a common understanding that the main factors influencing detachment include the previously mentioned pressure differences along the meniscus, a high growth angle, and high contact angles between the sample material and the crucible/ampoule. In addition to the surface tension and its temperature and composition dependence, the wetting angles θ of $\text{Ge}_{1-x}\text{Si}_x$ melts with a variety of crucible materials are therefore of great interest for investigating detached Bridgman growth. To obtain this information sessile drop measurements of Ge (36 experiments) and $\text{Ge}_{1-x}\text{Si}_x$ ($x \leq 12$ at.%) (23 experiments) on different substrate materials (fused silica, sapphire, AlN, Si_3N_4 , pBN, SiC, glassy carbon, coated graphite, diamond) in active vacuum, slight overpressure of Argon, and forming gas (2% hydrogen in 5N argon) were conducted. These have shown that at least for Ge-Si melts, pyrolitic boron nitride (pBN) has the highest contact angle (Figure 1) and is therefore most likely to promote detach-

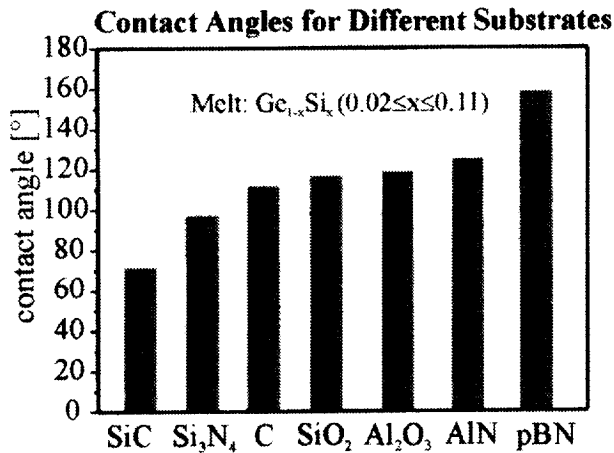


Figure 1. Contact angles on different substrate materials from sessile drop measurements.

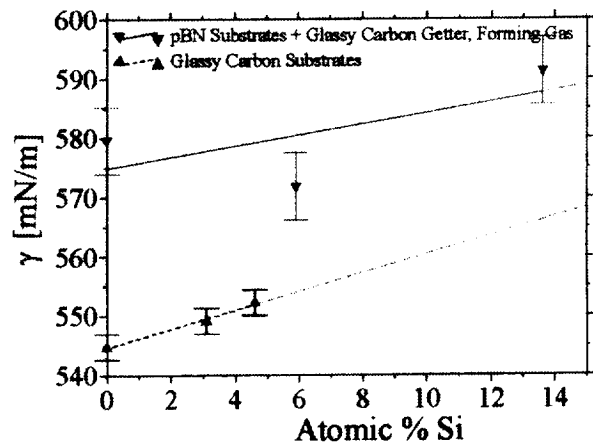


Figure 2. Concentration dependence of the surface tension of Ge-Si-melts at 1090°C for pBN and glassy carbon substrates. The slopes are 1 and 1.5 mN/m·at%, respectively. Additional measurements on pBN are under way.

ment during Bridgman growth. The experiments also showed that it is necessary to use forming gas and have an additional carbon getter in the system to maintain these angles over several days. All substrates reacted with the Si-containing melts to a certain extent, including pBN. In the latter case the effect on the contact angle was small.

Correspondingly, the boron content, measured by glow discharge mass spectrometry, reached values of only 10^{17} - 10^{18} cm⁻³ after 3 days of processing.

Surface tensions, including both temperature and compositional dependences, were determined from these measurements, also. These parameters are required to model the float-zone growth of Ge_{1-x}Si_x as well as the meniscus shape and the possible influence of Marangoni convection during detached-Bridgman growth. The compositional dependence of the surface tension is shown in figure 2 and has a value of about 1-1.5 mN/m·at%. The values for the temperature dependence of the surface tension were on the order of 0.08-0.12 mN/m·K.

The growth angle is the second parameter along with the contact angle that is important for detached crystal growth [7]. It was possible to determine the growth angle of GeSi by evaluating video images of GeSi floating zone crystal growth. The result for a 5 at% Si sample was $9.5 \pm 1^\circ$. Thus, the measured growth angle of GeSi corresponds well with the measured angle of Si (8-11°) [8, 9] and Ge (7-12°) [9, 10].

Partially detached Bridgman growth of Ge_{1-x}Si_x ($x \leq 2$ at.%) has been achieved repeatedly in both Freiburg and Huntsville for samples up to 15 mm in diameter. The best results, in accordance with the sessile drop contact angle measurements have been obtained using pBN as the crucible material, but detachment also has occurred in one case in a fused silica ampoule. There is no single typical characterization of the detachment, but there are some similarities. Some ingots have been detached over 90% of the circumference for an axial length ~2 cm while others have been completely or nearly completely detached around the circumference for lesser axial lengths. Detachment near the initial growth interface, reattachment for a short distance (~1-3 mm) and a second detachment followed by a final reattachment near the last-to-freeze part of the ingot have been repeated numerous times. Recently, several samples

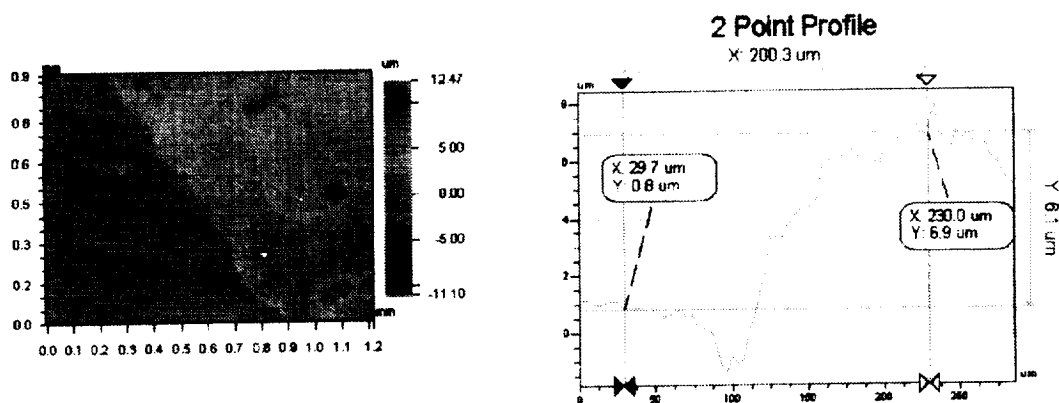


Figure 3. Profilometer measurements of a $0.9 \times 1.2 \text{ mm}^2$ surface area (left) and a plot of the height along the red line.

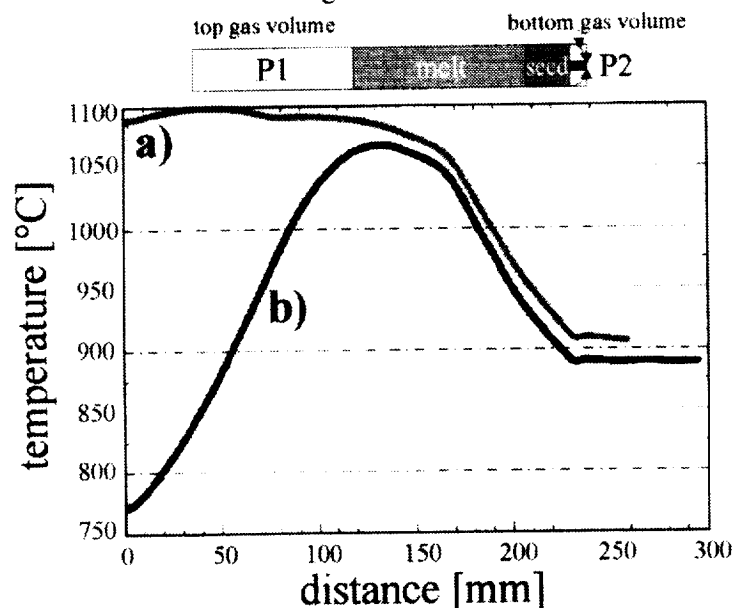


Figure 4. Temperature profile for the detached-Bridgman technique. a) Profile while melting the feed material and sealing the ampoule. b) Growth profile after establishing a pressure difference in the ampoule.

have been grown with 5 or more cm of detached growth. Detachment is detectable by changes in the surface features of the ingot including the appearance of growth facets and by a reduction in the radius where detachment occurs. This reduction has been observed to be up to $30 \mu\text{m}$ in Ge with smaller reductions in GeSi alloys. Profilometer measurements confirm the identification of attached and detached regions (figure 3).

GeSi crystal growth experiments with up to 2 at% Si were conducted in a 7-zone furnace. The temperature profiles are shown in figure 4. The initial gas pressure in the ampoule was 600 mbar forming gas. After melting the feed material to separate the top gas reservoir from the bottom gas volume (profile a in figure 4), the temperature in zones 1 and 2 were lowered and the temperature profile b in figure 4 resulted. Using this procedure, it is possible to achieve a pressure difference inside the ampoule with $P1 < P2$. With these profiles, growth experiments were conducted in closed end pBN and fused silica ampoules. In both cases, partially detached crystals were obtained. Crystals grown in closed end pBN tubes were detached over as much as 90% of the length.

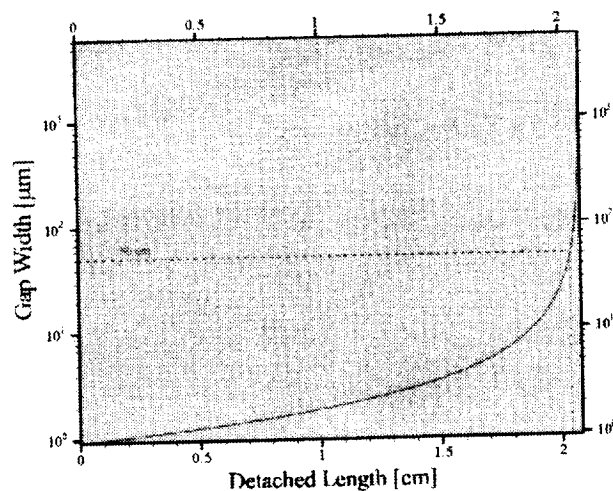
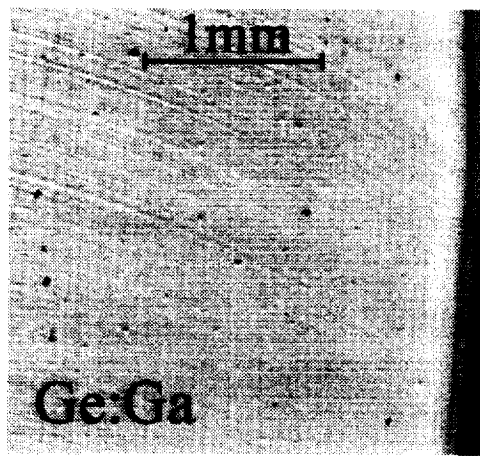


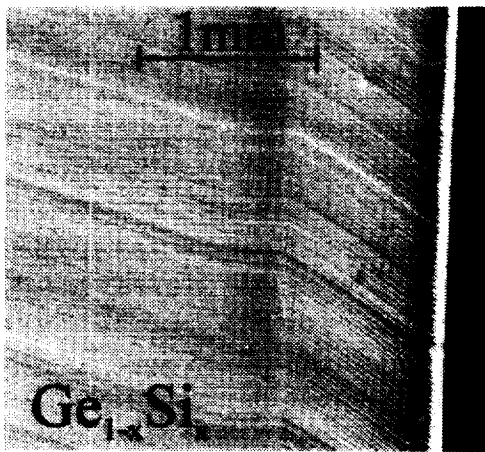
Figure 5: Calculated increase of gap width with detach growth length.

The theoretical analysis of this arrangement is well advanced. It is based on the hypothesis that the pressure in the trapped gas volume must support the sum of the hydrostatic head of the melt column, the gas pressure at the top free surface of the melt, and the capillary pressure drop across the meniscus. A thermal model of the growth system including the furnace, ampoule, and sample has been developed to track the solidification process. This model permits the calculation of the temperature distribution in the lower gas cavity and in the gas volume above the melt. The calculated pressure in the gas volumes is based on the initial mass of gas in the cavities, the perfect gas law, and the instantaneous temperature distribution in the cavities. The pressure in the lower gas volume does not include any contributions from the possible evaporation of dissolved gases from the melt into the gas volume, and thus represents a conservative estimate of the pressure in that cavity. As the ampoule is translated through the thermal environment and with increasing crystal length, the temperatures of the two gas reservoirs as well as the volume of the lower reservoir change. This leads to a time-dependant variation of the pressure in the two gas reservoirs and thus a variation in the thickness of the detached gap and shape of the meniscus. Figure 5 is a plot of the gap thickness versus the length of detached growth for one of the experimental conditions. Results indicate that detachment starts with a relatively small gap thickness and increases steeply at about 2 cm of detached growth where the gap thickness is about 50 μm . Detached growth beyond this point is calculated to require a significant increase in the gap thickness that may not be achievable in practice due to potential thermo-capillary instabilities. These are two-dimensional axisymmetric calculations and contact between the sample and ampoule at any point would permit increased (partially) detached lengths.

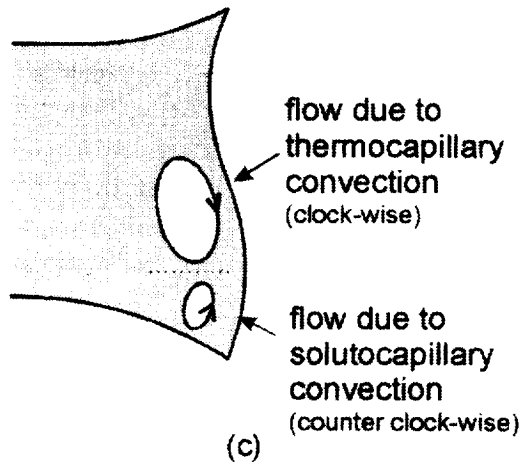
$\text{Ge}_{1-x}\text{Si}_x$ ($x \leq 10 \text{ at.}\%$) single crystals have been grown by the float-zone technique applied within a radiation heated monoellipsoid mirror furnace [11]. The boron-doped ($\geq 1-2 \cdot 10^{17} \text{ at/cm}^3$) feed crystal consisted of synthesized $\text{Ge}_{0.95}\text{Si}_{0.05}$ polycrystalline material. All crystals were grown using a $\langle 100 \rangle$ Ge seed. The etch pit density is about one order of magnitude lower than the EPD of Bridgman grown crystals. Compositional axial and radial profiles have been determined. The maximum silicon concentration was 10 at %. All crystals show a characteristic distortion of the interface morphology near the crystal edge (figure 6). This disturbance was not observed in silicon-free Ge:Ga-doped ($\geq 10^{18} \text{ at/cm}^3$) reference crystals and is thus likely to be caused by concentration-dependent (solutal) convection. Because this type of interface morphology does not appear in Bridgman samples, it is thought to be caused by solutocapillary convection due to the concentration dependence of surface tension and a segregation coefficient larger than one. The effect of solutocapillary convection is also evident in corre-



(a)



(b)



(c)

Figure 6. Floating zone growth of Ge and GeSi. (a) Interface morphology of gallium-doped Ge reference sample showing smooth, convex interface morphology. (b) Enlarged view of the edge of a GeSi sample showing the structure not seen in the Ge sample grown under similar conditions. (c) Half of a GeSi melt zone showing the flow rolls in the thermocapillary and the solutocapillary dominated regions.

sponding numerical simulations of the melt zone. In essence, we assume an additional, smaller solutocapillary convective cell immediately ahead of the growing interface. This cell is driven by the concentration gradient in the concentration boundary layer, similar to the mechanism described in [12, 13]. The main effect of this cell is a change in the morphology of the solid-liquid interface at the crystal edge. The radial concentration distribution does not change noticeably within the resolution limits of the EDX system used. By using a static axial magnetic field ($B \leq 400\text{mT}$) this radial distortion can be reduced and the irregular bending of the interface curvature is shifted toward the crystal edge but can not be eliminated completely.

REFERENCES

1. L.L Regel, W.R. Wilcox, Improved crystal quality by detached solidification in microgravity, NASA Microgravity Materials Science Conference Proceedings (1999) 533-539
2. D.J. Larson, J.I.D. Alexander, D. Gillies, F.M. Carlson, J. Wu, D. Black. NASA Conference Publication 3272, Vol. 1, 129-161
3. D. I. Popov, L. L. Regel, and W. R. Wilcox, Detached solidification. 1. Steady-state results at zero gravity, J. Materials Synthesis and Processing, vol. 5, pp. 283-297, 1997
4. D. I. Popov, L. L. Regel, and W. R. Wilcox, Detached solidification. 2. Stability, J. Materials Synthesis and Processing, vol. 5, pp. 299-311, 1997.
5. D. I. Popov, L. L. Regel, and W. R. Wilcox, Detached solidification. 3. Influence of acceleration and heat transfer, J. Materials Synthesis and Processing, vol. 5, pp. 313-336, 1997
6. T. Duffar, P. Dusserre, F. Picca, S. Lacroix, N. Giacometti: Bridgman growth without crucible contact using the dewetting phenomenon. J. Crystal Growth 211 (2000) 434-440
7. T. Duffar, P. Boiton, P. Dusserre, J. Abadie, Crucible de-wetting during Bridgman growth in microgravity, Part 2: smooth crucibles, J. Crystal Growth 179 (1997) 397-409
8. T. Surek, B. Chalmers, The direction of growth of the surface of a crystal in contact with its melt, J. Crystal Growth 29 (1975), 1
9. G.A. Satunkin, V.A. Tatarchenko, V.I. Shaitanov, Determination of the growth angle from the shape of a crystal lateral face and solidified separation drops, J. Crystal Growth 50 (1980), 291
10. H. Wenzel, A. Fattah, D. Gustin, M. Mihelcic, W. Uelhoff, Measurements of the contact angle between melt and crystal during Czochralski growth of gallium and germanium, J. Crystal Growth 43 (1978), 607
11. T. A. Campbell, M. Schweizer, P. Dold, A. Cröll, and K. W. Benz, Float-zone growth of $\text{Ge}_{1-x}\text{Si}_x$ ($x < 10\text{at}\%$) single crystals: Influence of thermocapillary and solutocapillary convection submitted to: J. Crystal Growth, 2000
12. P. Tison, D. Camel, I. Tosello, and J.-J. Favier, Proc. First Int. Symp. on Hydromechanics and Heat and Mass Transfer in Microgravity, Eds. Gordon and Breach, (Perm, Moscow) (1991) 121-131.
13. S. Kaddeche, H. Ben Hadid, and D. Henry, J. Crystal Growth 141 (1994) 279-290.

THE FEATURES OF SELF-ASSEMBLING ORGANIC BILAYERS IMPORTANT TO THE FORMATION OF ANISOTROPIC INORGANIC MATERIALS IN MICROGRAVITY CONDITIONS

Daniel R. Talham,^{1*} Rénal Backov,¹ and James H. Adair^{2*}

¹Department of Chemistry, University of Florida, Gainesville, FL 32611-7200

²Materials Research Laboratory, Pennsylvania State University, University Park, PA 16802

I. Hypothesis and Objective

Materials with directional properties are opening new horizons in a variety of applications including chemistry, electronics, and optics. Structural, optical, and electrical properties can be greatly augmented by the fabrication of composite materials with anisotropic microstructures or with anisotropic particles uniformly dispersed in an isotropic matrix. Examples include structural composites, magnetic and optical recording media, photographic film, certain metal and ceramic alloys, and display technologies including flat panel displays. The new applications and the need for model particles in scientific investigations are rapidly outdistancing the ability to synthesize anisotropic particles with specific chemistries and narrowly distributed physical characteristics (e.g. size distribution, shape, and aspect ratio).

While there has been considerable progress toward developing an understanding of the synthesis of powders composed of monodispersed, spherical particles, these efforts have not been transferred to the synthesis of anisotropic nanoparticles. Amphiphilic molecules can be used to prepare either “water-in-oil” or “oil-in-water” micelles, and these organic “template” structures have been used to control the size of growing inorganic particles. Larger concentrations of the segregated phase leads to the formation of bilayer structures. In our laboratories, we have demonstrated that these anisotropic micellular structures can be used as templates to prepare anisotropic particles in both metallic and inorganic salt systems.^{1,2} This project aims to extend the methods that have been developed to other inorganic particle systems and to increase our level of understanding of how anisotropic particles are formed at lamellar templates.

As part of our studies, we make extensive use of model membrane systems prepared by Langmuir-Blodgett (LB) methods in order to efficiently survey possible template systems and establish the important chemical and geometric features of the templates that influence particle growth.³⁻⁶ Motivation for studying single-layer systems is two-fold. First, the chemical and structural properties of LB films are easily manipulated and characterized, allowing us to tailor the template system to the inorganic material being formed. Secondly, LB films on surfaces are less subject to the convectional shear, sedimentation, and agglomeration normally experienced by particles synthesized in the bulk solution. The surface confined bilayers can be used to establish how particle growth is limited by chemical and geometric considerations in the absence of

convection and sedimentation effects. Results from the surface confined studies are continuously utilized in the design and choice of solution micellar systems as they are tailored to the desired inorganic materials. The program uses what is learned on the model systems to develop larger-scale preparations of the targeted inorganic materials at bilayer structures formed from “oil-in-water” segregated phase systems. It is these systems that will eventually lead to high yield, monodisperse preparations.

II. Justification for Microgravity Experiments

The advantages of a microgravity environment for studying crystallization, nucleation and growth processes are well documented.^{7,8} In the present project, minimizing convectional induced fluid shear and sedimentation in the microgravity environment should allow extended organic templates to form rather than fragments or “rafts” that result at normal Earth’s gravity. Convection limits the size of uniform template domains and also creates a non-uniform size dispersion. These imperfections in the template structures make it difficult to assess the role that the chemical and geometric identities of the template play in controlling particle size and dispersion. Reducing convection will also minimize the agglomeration of particles that are produced. Sedimentation is less of a problem than convection in the synthesis and processing of nanoscale particles or particles with nanometer scale in at least one dimension. Analysis⁹ demonstrates that the displacement due to gravity becomes less dominant as the particle size becomes smaller than about 0.25 μm . In contrast, sedimentation will begin to mask template effects as particle sizes increase beyond several hundred nanometers.

III. Metal Particles Formed in Free Standing Bilayer Templates

Templating in free standing bilayers can be used to produce metal platelets as well as the semiconductors previously described.^{1,2} Figure 1A shows the effect of preparing silver and platinum particles in a bilayer system with little or no metal ion binding at the polar head group. In contrast the amine co-surfactant system (pentylamine/sodium dodecylsulfonate-toluene-water) and a bilayer composed of water and octylamine produces tabular-shaped Pt and Ag particles, respectively (Figures 1B and 1C). A variety of metallic platelets have been prepared in the water-octylamine system including Au, Cu, and Ag/Pd alloys of special interest to the electronics community.

IV. Langmuir-Blodgett Model Studies

To further study the templating effect, gold, silver and platinum particles have been grown at Langmuir-Blodgett templates. The growth of gold and silver particles have been reported previously,⁶ so the templating of platinum particles is reported here. Particles were formed by photoreduction of $[\text{PtCl}_4]^{2-}$ trapped within LB bilayers. LB films were formed from the following surfactants: octadecylamine (ODA), benzyldimethylstearylammmonium chloride monohydrate (BDSA), 4-hexadecylaniline (HDA), and dipalmitoyl-DL- α -phosphatidyl-L-serine (DPPS). The series of films, each with different N-containing headgroups, allows us to study the influence of specific interactions on particle templating. Figure 2 shows Pt particles grown from each of these LB films. Only the ODA film produces plate-like single crystal particles with well-defined faces. This observation is consistent with results from the free-standing templating described above, where plate-like particles were only observed when the bilayer templates contained amines.

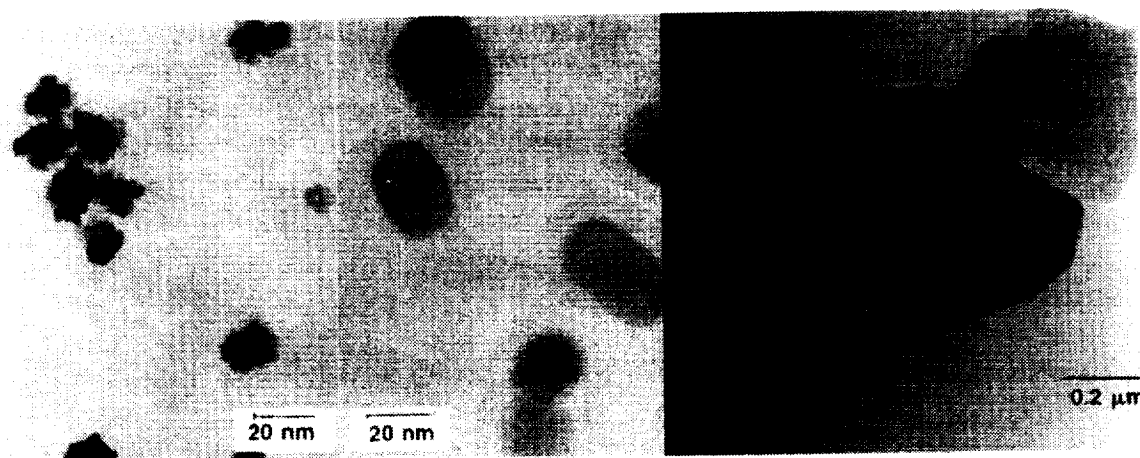


Figure 1. TEM photomicrographs of Pt and Ag particles produced in bilayer systems. (A) Pt particles produced in an AOT-heptane-water bilayer system without specific polar group templating; (B) Pt particles produced in a pentylamine/sodium dodecylsulfonate-toluene-water bilayer system with specific polar group templating and; (C) Ag particles produced in an octylamine-water bilayer with templating.

Specific interactions between the amine and the surface of Pt stabilize the single crystal plate-like particles. It should be noted that, in principle, HDA and DPPS could provide similar specific interactions, but DPPS reacts with Pt^{2+} to form a stable complex, and HDA polymerizes during the photoreduction of Pt^{2+} .

V. Mechanism of Particle Growth at Lamellar Templates

The results on metal particles, along with our previous work on semiconductor systems, has now led us to a better, yet still incomplete, understanding of how the layered templates lead to anisotropic particles.¹⁻⁶ The organic assembly regulates particle growth through a combination of three different processes, which vary in relative importance for any given template/particle system. The first process is that of *confinement*. The template defines a space in which the particle can grow. A second process is through *specific interactions* between the template and the particle. Here, the template acts similarly to an adsorbate or poison in homogeneous preparations and stabilizes certain crystallographic faces at the template interface. Finally, the template controls *mass transport* to the growing particle. The diffusion is easier parallel to the template walls, and particles will grow in the directions that material is supplied.

We have observed that there are at least two general mechanisms that lead to the templating of two different classes of platelike particles. Each mechanism takes advantage of the processes of confinement, specific interactions and mass transport. The first we will call *crystal templating*, where the products are anisotropic single crystal particles. These particles result from a slow nucleation event, giving relatively few nuclei, and subsequent growth of the individual crystals.¹⁰ The anisotropic shape results from a combination of crystallization physics (determined from the solid-state structure of the material), specific interactions between the template and growing crystal faces, and directional transport of the reactant to the crystal.¹¹ Using micellar templates, we have observed single crystal metal platelets with dimensions up to several hundred nanometers and the size dispersion is broad. Using LB templates, particle sizes are somewhat larger, up to several microns, but there is also substantial polydispersity. The factors that control the size

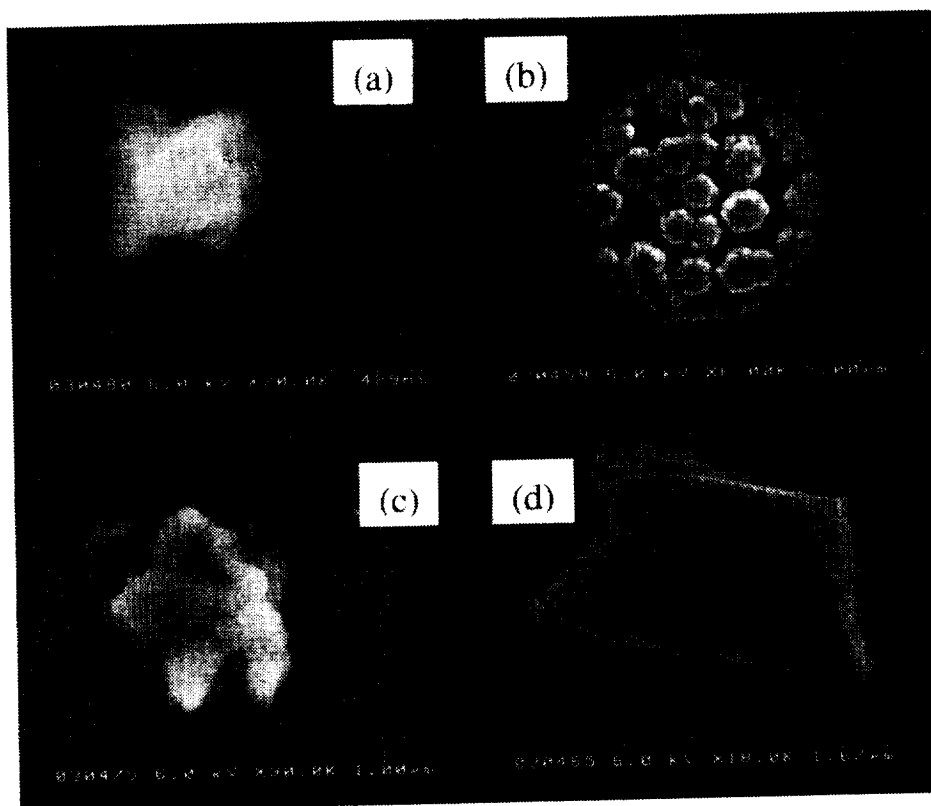


Figure 2. Platinum particles grown by photoreduction of $[\text{PtCl}_4]^{2-}$ in LB films of (a) DPPS, (b) BDSA, (c) HDA, and (d) ODA. Only the ODA film produces plate-like particles with flat faces that are similar to the metal particles formed from free standing templates (see Figure 1).

and polydispersity are not yet clear, yet we hypothesize that the size and uniformity of the template domains are important.

The second mechanism we will call *aggregate templating*. Here, the products are assemblies of smaller single crystal particles that aggregate in the shape of a platelet. The constituent particles need not have the same shape of the final product, and are most often spherical. The mechanism involves rapid nucleation followed by diffusion of the nuclei to form the platelets. The ultimate particle shape is limited by the vectorial diffusion of nuclei, which in turn is controlled by the shape of the template. At first glance, the influence of specific interactions on particle shape would appear to be less important in this mechanism, however, the chemical make-up of the template can affect the rapid nucleation event which in turn influences the polydispersity of the product. Particles formed through aggregate templating have a smaller dispersity than the single crystal particles. Preparations yielding particle sizes ranging from a few nanometers up to hundreds of nanometers have been developed for CdS in micelle templates.¹

VI. Some New Directions

In addition to the templated synthesis of metal particles we have begun studies on two additional facets of self-assembled systems, enzyme catalyzed particle synthesis¹² and room temperature synthesis of metal oxides. In the former work a urea-urease substrate-enzyme couple was used to synthesize aluminum basic sulfate from 15°C to 40°C by exploiting the pH increase created by the urease mediated breakdown of urea to ammonia and carbonate. Under certain conditions

discrete, submicron, spherical $\text{Al}(\text{OH})_x(\text{SO}_4)_y$ particles were produced via precipitation from homogeneous solution in contrast to the large particles of broad size distribution produced by the more traditional thermal breakdown of urea. It was shown in extended kinetic studies at 25°C that the anhydrous metal oxide is the stable phase of both undoped and Y-doped zirconia, an important material for a variety of applications including structural ceramics and high temperature fuel cells. Experiments are anticipated that will combine the enzyme-induced precipitation reactions with low temperature synthesis within bilayer self-assembly systems to produce unique particles of heretofore thermodynamically intractable materials such as Y-doped zirconia and optoelectronic materials such as CuInSe_2 .

VII. Acknowledgements

The P.I.'s would like to acknowledge co-workers T. Li and S. Ravaine.

REFERENCES

1. J. H. Adair, T. Li, T. Kido, J. Moon, K. Havey, J. Mecholsky, A. Morrone, D. R. Talham, M. H. Ludwig and L. Wang *Mat. Sci. Eng. Reports* **1998**, *R23*, 139-242.
2. T. Li, J. Moon, A.A. Morrone, J.J. Mecholsky, D.R. Talham, and J.H. Adair, *Langmuir* **1999**, *15*, 4328-4334.
3. Pike, J. K.; Byrd, H.; Morrone, A. A.; Talham, D. R. *Chem. Mater.* **1994**, *6*, 1757-1765.
4. Pike, J. K.; Byrd, H.; Morrone, A. A.; Talham, D. R. *J. Am. Chem. Soc.* **1993**, *115*, 8497-8498.
5. Pike, J. K.; Byrd, H.; Morrone, A. A.; Talham, D. R. *Thin Solid Films* **1994**, *243*, 510-514.
6. S. Ravaine, G. E. Fanucci, C. T. Seip, J. A. Adair and D. R. Talham *Langmuir* **1998**, *14*, 708-713.
7. *Materials Processing in the Reduced Gravity Environment of Space*; Doremus, R. H.; Nordine, P. C., Ed.; Materials Research Society: Pittsburgh, 1987; Vol. 87, pp 366.
8. Vaderhoff, J. W.; Micale, F. J.; El-Aasser, M. S.; Sudol, E. D.; Tseng, C. M.; Sheu, H. R. *J. Disp. Sci. Tech.* **1984**, *5*, 231.
9. Allen, T. *Particle Size Measurement*; 4th ed.; Chapman Hall: New York, 1990.
10. S. Whipples, S. R. Khan, F. J. O'Palko, R. Backov and D. R. Talham *J. Cryst. Growth* **1998**, *192*, 243-249.
11. (a) Calvert, P.; Mann, S. *J. Mat. Sci.* **1988**, *23*, 3801-3815. (b) Heywood, B. R.; Mann, S. *Adv. Mater.* **1994**, *6*, 9-20. (c) Mann, S. *Nature*, **1993**, *365*, 499-505. (d) Archibald, D. D. and Mann, S. *Nature*, **1993**, *364*, 430-433.
12. (a) Mittal, K. L.; Mukerjee, P. In *Micellization, Solubilization and Microemulsions*; K. L. Mittal, Ed.; Plenum Press: New York, 1977; pp 1-21. (b) Tadros, T. F. *Adv. Coll. Int. Sci.* **1993**, *46*, 1-47.

INTERFACIAL ENERGY DETERMINATION OF SUCCINONITRILE AND SUCCINONITRILE-ACETONE ALLOY USING SURFACE LIGHT SCATTERING SPECTROMETER

Padetha Tin¹, David T. Frate², Henry C. de Groh III²

¹National Center for Microgravity Research for Fluids and Combustion

²NASA Glenn Research Center

The objectives of this ground based research is to measure the liquid/vapor interfacial surface energies of succinonitrile (SCN) and alloys of succinonitrile and acetone using Surface Light Scattering Spectrometer. Liquid/vapor interfacial energy measurements will be made near and above the melting point and are the primary goal of this proposal. A measurement of viscosity also results from the Surface Light Scattering technique employed. Interfacial free energies between the phases enters into many analysis of phase transformation and flow, including nucleation, dendritic growth, interface stability, Ostwald ripening, and Marangoni flow.

Succinonitrile (SCN) is useful as a model for the study of metal solidification, although it is an organic material, it has a BCC crystal structure and solidifies dendritically like a metal. It is also transparent and has a low melting point (58.08°C). Succinonitrile has been and is being used extensively in NASA's Microgravity Materials Science and Fluid Physics programs and as well as in several ground-based and microgravity studies including the Isothermal Dendritic Growth Experiment (IDGE) due to Glicksman and co-workers and subsequently in several theoretical and numerical studies of dendritic growth. Previous measurements of succinonitrile (SCN) and alloys of succinonitrile and acetone surface tensions are extremely limited. We believe the data sought through this proposal have significant basic physical property data value and thus the work proposed will provide needed data in support of NASA's Microgravity program research.

Under the sponsorship of NASA's Advanced Technology Development program, the Surface Light Scattering spectroscopic technique to measure surface tension/energy and viscosity has been developed. This relatively new and unique technique has several advantages over the classical methods such as, it is non invasive, has good accuracy and measures the surface tension and viscosity simultaneously. The accuracy of interfacial energy values obtained from this technique is better than 1% and viscosity about 10%. Succinonitrile and succinonitrile-acetone alloys are well-established model materials with several essential physical properties accurately known - except the liquid/vapor surface tension at different elevated temperatures. We will experimentally determine liquid/vapor surface energy and liquid viscosity of succinonitrile and succinonitrile-acetone in the temperature range from their melting point to around 100°C. Preliminary studies in our laboratory at Glenn Research Center demonstrated that the surface light scattering spectrometer is capable of measuring SCN liquid/vapor surface tension at different temperatures. This method is not only limited to liquid/vapor systems but also to liquid/liquid interfaces also and thus we plan a feasibility study of solid/liquid surface tension measurements using this novel technique. The success here will represent a significant advancement to the materials research and development community.

INTERFACE PATTERN SELECTION IN DIRECTIONAL SOLIDIFICATION

R. Trivedi¹ and S.N. Tewari²

¹Iowa State University

²Cleveland State University

OBJECTIVE

The central focus of this research is to establish key scientific concepts that govern the selection of cellular and dendritic patterns during the directional solidification of alloys. Ground-based studies have established that the conditions under which cellular and dendritic microstructures form are precisely where convection effects are dominant in bulk samples. Thus, experimental data can not be obtained terrestrially under pure diffusive regime. Furthermore, reliable theoretical models are not yet possible which can quantitatively incorporate fluid flow in the pattern selection criterion. Consequently, microgravity experiments on cellular and dendritic growth are designed to obtain benchmark data under diffusive growth conditions that can be quantitatively analyzed and compared with the rigorous theoretical model to establish the fundamental principles that govern the selection of specific microstructure and its length scales.

In the cellular structure, different cells in an array are strongly coupled so that the cellular pattern evolution is controlled by complex interactions between thermal diffusion, solute diffusion and interface effects. These interactions give infinity of solutions, and the system selects only a narrow band of solutions. The aim of this investigation is to obtain benchmark data and develop a rigorous theoretical model that will allow us to quantitatively establish the physics of this selection process.

I. Introduction

Cellular and dendritic patterns are most dominant for metallic alloys processed by solidification techniques. The formation of a cellular or a dendritic structure is accompanied by microsegregation of solute, which results in a nonhomogeneous material. This nonhomogeneity in composition not only influences mechanical properties, but it can also generate stresses or lead to the formation of a new stable or metastable phase in intercellular region that can significantly alter the properties of the material. Thus the reliability of products made by solidification techniques such as casting, welding, melt spinning, atomization and laser processing of materials largely depends upon our ability to control the microstructure.

A sequence of directional solidification experiments has been designed to quantitatively establish the fundamental principles that govern cell/dendrite microstructure selection. As the solidification velocity is increased, or the temperature gradient decreased, the interface undergoes several transitions: planar to small amplitude cells, to deep cells, and finally to dendrites. We shall first

show that these changes in microstructures occur at low velocities where thermosolutal convection is dominant. We shall then present the results of a numerical model that predicts microgravity level required to obtain diffusive growth. Ground-based experimental studies in the Al-4.0 wt % Cu system, and the analysis of the results will then be described.

II. Need for Microgravity

In order to establish the presence of convection, we have developed a detailed numerical model for the directional solidification process [1,2]. We considered the vertically upward solidification of a binary liquid of initial composition C_0 (in % solute) inside a two-dimensional rectangular cavity. The vertical walls are rigid solid walls that represent the three-zone thermal assembly and are impervious to mass flux. The three-zone assembly consists of an isothermal cold zone wall at temperature T_c , an isothermal hot zone wall at temperature T_H , and a no-flux adiabatic zone between them. The system of coupled nonlinear equations were written in coordinate frame fixed with the uniformly moving solid-liquid interface, and it included Boussinesq approximated Navier-Stokes equations, and the heat and solute transport equations. These equations are completely described by thermal and solutal Rayleigh numbers, the ratio of vertical to horizontal temperature gradients, the Peclet number based on growth rate, the partition coefficient, the Prandtl number, the Lewis number and the aspect ratio. The proper choice of the heat transfer coefficients was done through regression analysis of computed axial and radial temperature profiles with measured experimental data in our ground-based system. Numerical calculations were carried out for conditions characteristic of solidification of Al-4.0% Cu alloys. The growth rate of 1.0 $\mu\text{m/s}$ was selected since it was the smallest growth rate in our planned experimental study, and it would give the largest fluid flow effect. The extent of convection was examined by considering solidification in tubes of different inner diameters, varying from 0.6 mm to 6 mm. These calculations show that the convective velocity is orders of magnitude larger than the diffusive velocity for samples of diameter larger than 6 mm. One needs to use sample diameter smaller than 1 mm to obtain conditions for which the convective velocity is smaller than the diffusive velocity in the Al-4.0 wt % Cu system under 1g conditions. The use of smaller than 1 mm diameter under terrestrial condition shows that one would require microgravity level of 10^{-4} g to directionally solidify 1 cm diameter samples under diffusive conditions. These calculations were validated by an independent set of experiments carried out in samples of different diameters that were grown in the same experiment. These ground-based experimental results will now be described.

III. Ground-Based Experiments

Ground-based experiments have been carried out to study following aspects of cellular growth. (1) Establish the conditions under which cellular and dendritic microstructures are influenced by convection effects, (2) Quantitatively characterize the velocity-thermal gradient regime in which cellular structures would be stable under purely diffusive growth conditions, *i.e.* under microgravity conditions. These data were used to define the experimental matrix for microgravity experiments. (3) Determination of system parameters for Al-4.0 wt % Cu alloys. (4) A methodology for the post-solidification analysis of samples. This included three-dimensional reconstruction of the microstructure and the effect of quenching on the displacement of the interface.

(1) The effect of convection

An experimental technique was developed to reduce convection under 1g conditions by solidifying alloys in tubes of smaller diameters. Several experiments were carried out in the Al-4wt% Cu alloy system using thin tubes of diameters varying from 6.0 mm down to 0.4 mm [3,4]. A bundle of thin samples of varying diameters was placed inside the 5.0 mm diameter tube, and all samples were directionally solidified simultaneously in a single experiment. Thus, the thermal profile and the translation rate imposed on the samples were identical except for the degree of convection that varied with the tube diameter. Since convection effects are gradually reduced with decreasing sample size, quantitative evaluation of convection on microstructural development can be obtained.

In the presence of convection, a significant curvature of the interface was observed with the interface protruding in the center. This was due to convective transport that gave rise to a higher concentration at the walls than at the center. From the experimental measurements of the height of the protrusion, coupled with the known value of G , the difference in interface temperature between the center and the wall, ΔT , was calculated for different sample diameters, as shown in Figure 1. The steepening effect becomes negligible when the diameter is reduced below 0.6 mm.

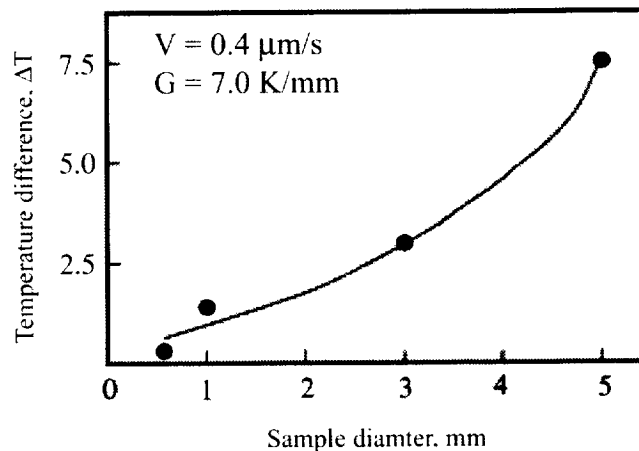


Figure 1. The difference in interface temperature between the center and the wall as a function of sample diameter showing that the steepening effect becomes larger as the sample diameter is increased. Planar interface growth at $V=0.4 \mu\text{m/s}$, $G=7.0 \text{ K/mm}$.

The effect of convection giving rise to steepening is also accompanied by solute segregation [5,6]. Quantitative composition measurements for planar and cellular growth were carried out which conclusively showed that fluid flow effects become negligible only when the sample diameter is equal to less than 1.0 mm. The composition profiles for planar interface growth, Figure 2, show that the profiles become identical when the sample diameter is less than one, which is consistent with our results of the numerical analysis.

Reducing the sample diameter (decreasing the extent of convection) results in the following: The tip temperature decreases, the primary arm spacing increases, and the planar-to-cellular and cellular-to-dendritic transitions occur at lower growth speeds for a given temperature gradient. The critical velocity for these transitions were found to be higher in the presence of convection, although the effect on cellular to dendritic transition was quite small because of the higher velocity at which this transition takes place. Figure 3a shows the experimental results in Al-Cu

system in which a thin sample was directionally solidified inside a large sample, and it is clearly observed that the interface in the outside region where convection effects are significant stabilizes the planar growth. In the finer sample, where diffusive growth occurs, a cellular structure is seen. Similar results were also observed in the Sn-Cd alloy, shown in Figure 3b.

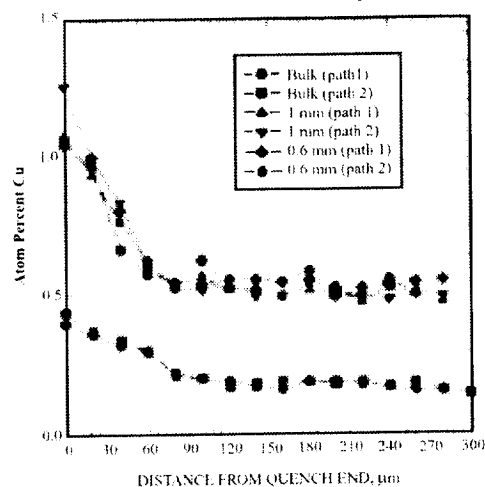


Figure 2. Composition ahead of a planar interface in samples of different diameters. Al-4.0 wt % Cu directionally solidified at $V = 0.4 \mu\text{m/s}$, $G = 7.0 \text{ K/mm}$. [4].

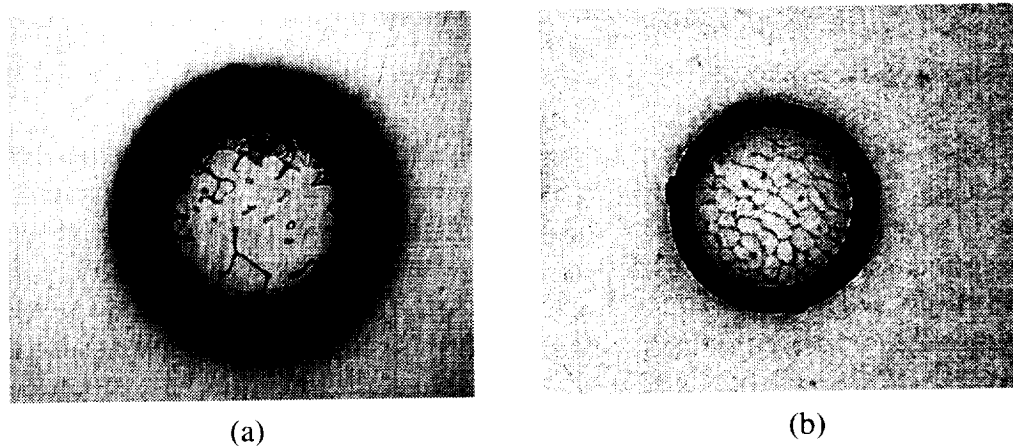


Figure 3. The formation of a cellular structure inside a thin tube, whereas a planar front is present in the larger outside region where convection effects were found to stabilize the planar front growth. (a) Al-Cu alloy, (b) Sn-Cd alloy. The transverse section was taken just below the solid-liquid interface [4].

(2) Experimental matrix

Since diffusive growth could be obtained only in samples of diameter 1.0 mm or less in Al-Cu system, detailed experiments were carried out in thin samples of 0.6 mm diameter to identify planar, cellular and dendritic microstructures as a function of G and V in Al-4.0 wt % Cu alloys. The results are shown in Figure 4, which shows that cellular structures at $G=100 \text{ K/cm}$ are observed for the velocity range of 0.43 to $9.0 \mu\text{m/s}$. Consequently, our first experiments are planned in the cellular regime close to the cell-dendrite transition to include both the cellular and dendritic microstructures. Ten different experiments at fixed $G=100 \text{ K/cm}$ will be carried out at velocities of $5.0, 6.0, 7.0, 8.0, 8.5, 9.0, 9.5, 1.0, 2.0$ and $3.0 \mu\text{m/s}$. This will give five data in the deep cell regime, one in the cell-dendrite transition region, and three in the dendritic regime.

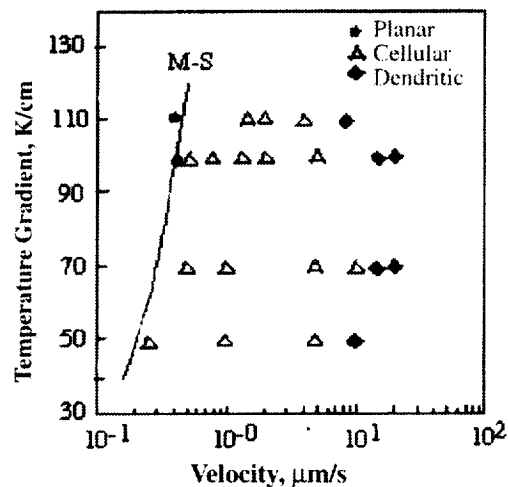


Figure 4. Microstructures observed in samples of 0.6 mm diameter in Al-4.0 wt % Cu as function of G and V . The line M-S represents the prediction of the linear stability analysis.[4].

The samples will be quenched after steady state is reached, and they will be analyzed to characterize the shape of the interface including the tip radius, primary spacing, and composition profiles. Subsequent experiments will be carried out in the planar to shallow-cell transition region and in the dendritic region.

(3) System parameters for the Al-4.0 wt % Cu system

Accurate values are available in the literature for the phase diagram, thermal parameters and interface energy. Two major parameters whose values have not been obtained precisely are the anisotropy in interface energy and the diffusion coefficient in the liquid. Detailed ground-based studies have been carried out to examine the shape of a fine liquid droplet in solid on the (001) plane of the solid, and the shape of the droplet was found to deviate only slightly from a circle indicating that the anisotropy value is quite small. Precise measurements of the shape are now being carried out. The value of the diffusion coefficient in the liquid has been reported between 3.0 to $5.0 \times 10^{-9} \text{ m}^2/\text{s}$. We have carried out detailed composition measurements in the quenched liquid ahead of the interface in samples of different diameters that provided the compositions in the liquid and solid at the interface and the composition gradient at the interface [7]. By using the flux balance equation at the interface, based on diffusive transport only, the value of the effective diffusion coefficient, D_{eff} , was calculated. The results are shown in Figure 5. A larger value was obtained when convection effects were present in larger diameter samples. The diffusion coefficient in thin samples was found to be $1.5 \times 10^{-9} \text{ m}^2/\text{s}$. These results again show that the convection effects become important when the diameter becomes larger than 1 mm, and they significantly influence the value of the diffusion coefficient obtained by assuming no fluid flow.

(4) Post-solidification analysis of samples

Detailed ground-based studies were carried out to analyze the accuracy of the reconstruction of the three-dimensional shapes of cells from the images of successive sections obtained from micromilling. Detailed experimental studies are described by Yu *et al.* [8].

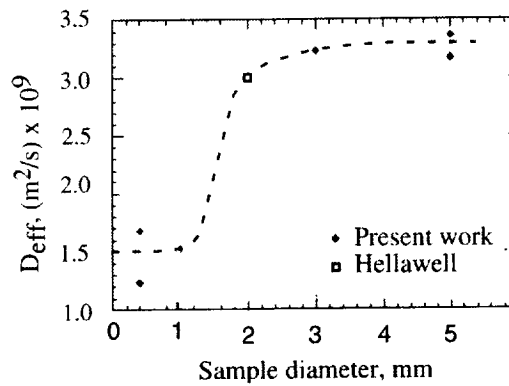


Figure 5. The variation in the calculated diffusion coefficient as a function of the sample diameter. The diffusion coefficient value is influenced by fluid flow in larger diameter samples. [7].

Another important factor in the precise analysis of the shape of the interface is the effect of quenching. Detailed studies of quenching were thus carried out and the cooling rate was measured for each quenching experiment. Detailed composition measurements were also carried out to obtain the change in composition in the solid induced by quenching. The displacement of the interface was then determined as a function of the quenching rate [9]. An optimum quenching rate of 100 K/s was found to give a minimum displacement of the interface. Higher quenching rates changed very little the interface displacement. It was shown that the displacement always occurs along the growth direction with each element of the interface largely moving in the growth direction. Thus, the shape of the interface, as well as the tip radius, in the quenched sample was found to differ only negligibly from their values before quenching.

IV. Conclusions

These ground-based experimental studies clearly demonstrated the presence of significant convection in bulk samples. Although this experimental method permits access of the diffusive regime, this technique cannot be used to characterize microstructures for which the microstructural length scale is of the order of the sample diameter. Since sample diameters of 1 mm or less is required for diffusive growth under 1g conditions, only a single cell can form. There is no selection for the formation of a single cell, so that it is not possible to obtain diffusive growth terrestrially in bulk alloy samples that are large enough to establish the selection criterion or to obtain statistically meaningful distribution of spacing of cell/dendrite arrays. Microgravity experiments are thus planned to obtain cellular and dendritic microstructures under diffusive growth conditions. Numerical models using the boundary integral and the phase field methods are being developed to precisely obtain the steady state shape of cellular interface and the variation in primary spacing and tip radius as a function of G and V . A comparison of the benchmark data with these model will allow us to establish the fundamental principle that dictates the selection of primary spacing. Furthermore, it will allow us to develop appropriate criterion for the cell to dendrite transition.

V. Acknowledgements

S. Liu, P. Mazumder, E. Simsek, G. Ding and H. Miyahara contributed to this work. This work was supported by NASA microgravity research, Division of Materials Science, grant # NCC8-98.

REFERENCES

1. P. Mazumder and R. Trivedi, "Convection Induced Pattern Formation in Directional Solidification", in: Fluid Flow Phenomenon in Metal Processing, Ed. by N. El-Kaddah, D. G. C. Robertson, S. T. Johansen and V. P. Voller, TMS, Warrendale, PA (1999), 459-456.
2. R. Trivedi, P. Mazumder and S. N. Tewari, "Primary Spacing Disorder in Directional Solidification", Materials Transactions (Submitted).
3. R. Trivedi, S. N. Tewari, and D. Kurtze, "Interface Pattern Selection Criterion for Cellular Structures in Directional Solidification", Proc. of NASA Microgravity Materials Science Conference, Ed. by D. C. Gillies and D. E. McCauley, NASA (1998) 635-640.
4. R. Trivedi, H. Miyahara, P. Mazumder, E. Simsek and S. N. Tewari, "Directional Solidification Microstructures in Diffusive and Convective Regimes", J. Cryst. Growth (Submitted).
5. R. Trivedi and W. Kurz, "Solidification Microstructures", in: Erstarrung Metalischer Smeltzen in Forschung und Giessereipraxis", Deutsche Gesselshaft, (1999), 3-14.
6. R. Trivedi, S. Liu, P. Mazumder and E. Simsek, "Microstructure Development in the Directionally Solidified Al-4.0 wt% Cu Alloy System", J. Mat. Proc., (in press).
7. E. Simsek and R. Trivedi, "Measurement of diffusion coefficient in the Liquid in the Al-4.0 wt% Cu system", Unpublished work, Iowa State University, Ames, IA (2000).
8. L. Yu, G.L.Ding, J.Reye, S.N. Ojha, and S.N.Tewari, "Cellular/Dendritic Array Tip Morphology during directional solidification of Pb-5.8 wt pct Sb alloy", Metall. Mater. Trans. 30 A (1999) 2463-2472.
9. S. Liu and R. Trivedi, "The Effect of Quenching on Microstructure Perturbation", Materials Trans. (Submitted).

DYNAMICAL SELECTION OF THREE-DIMENSIONAL PATTERNS IN DIRECTIONAL SOLIDIFICATION

R. Trivedi¹, R. Napolitano¹ and Alain Karma²

¹Iowa State University

²Northeastern University

OBJECTIVES

The central focus of this research is to establish fundamental principles that govern the dynamical selection of interface patterns during the directional solidification of model transparent materials. Several ground-based studies on primary cellular/dendritic spacing have clearly established that the primary spacing does not have a unique value under given growth conditions. Rather, the selection of the spacing is governed by the history, and experiments with the same history lead to a reproducible pattern. Thus, the precise understanding of the pattern evolution requires the knowledge of the dynamics of spacing selection. The goal of this research is to quantitatively establish the complete dynamics of interface pattern selection. In addition, the conditions for transitions from planar to cellular and cellular to dendritic structures under dynamical conditions of growth will also be established.

In order to obtain benchmark data on the dynamics of pattern formation, a transparent model system will be used in which the time-evolution of the pattern can be continuously imaged and analyzed. These experimental results will be coupled with a detailed modeling of the pattern evolution by using the phase field approach. The benchmark data obtained under microgravity conditions will allow us to validate the model so that a predictive theory of pattern formation can be formulated. This study is in collaboration with French Space Agency (CNES), and we intend to use the DECLIC hardware that is now being built by CNES.

I. Background

The importance of tailoring microstructures to obtain desired properties of solidified materials has been well established in the literature. In all important commercial solidification techniques, such as casting and welding, cellular or dendritic structure form, and both the mechanical properties and the defect structures are governed by the microstructural characteristics of cells and dendrites.

The difficulty in the development of a fundamental understanding of the evolution of solidification morphologies arises from the complex dynamic interactions between cooperative phenomena such as thermal and solutal diffusion, fluid flow, and anisotropy of both interfacial energy and atomic attachment kinetics. Numerical models are being developed which could take into account all of these factors, provided that independent description of each is available. Complex

fluid flow effects on pattern formation, cannot however, yet be modeled quantitatively, and benchmark experimental data under diffusive growth conditions are not possible under terrestrial conditions because of the strong influence of convection on pattern evolution.

In order to minimize convection, several experimental studies have been carried out in transparent systems constrained in two-dimensions. These studies have provided valuable information on the dynamics of pattern evolution and the selection of morphologies and their wavelengths. However, they can not be used to validate the quantitative three-dimensional pattern evolution because of the wall constraints.

An integrated experimental and modeling program is thus proposed in the present study to provide a quantitative description of the dynamics of pattern selection in three-dimensions. This will include simulation of time-dependent three-dimensional pattern evolution using the phase field method to establish the dynamic conditions of planar to cellular and cellular to dendritic transitions, and to provide detailed predictive results on the time-evolution of wavelengths as a function of the history of the growth conditions. In order to validate the model, a comprehensive set of benchmark data in diffusive regime will be obtained under microgravity conditions.

II. Microgravity Relevance

Significant experimental studies have been carried out in thin samples of succinonitrile (SCN) - acetone by the P.I. A detailed and systematic study of microstructure evolution as a function of the thickness of the sample was carried out by Somboonsuk et al. [1], who found that convection effects became important when the sample thickness was larger than 0.3 mm. More detailed studies in bulk samples, 6.0 mm square sides, using vertically upwards growth showed a significant fluid motion during growth [2]. The CNES team has carried out extensive work on the directional solidification of succinonitrile-acetone in the DECLIC prototype, and they have mapped out the significant fluid flow that occurs during solidification in 12 mm samples [3].

Extensive experimental studies in the diffusive regime have been carried out in thin samples (150 μm thick) where the pattern evolution is controlled by diffusive transport [1,4]. Although these studies have provided valuable results on the mechanisms and on wavelength selection, the wall effects significantly influenced the cell shape so that these results in the diffusive regime cannot be quantitatively compared with either 2-D or the 3-D models. Experimental studies in large diameter samples, $d > 3$ mm, in metallic and organic systems have clearly shown the presence of a highly disordered spatial arrangement of cells or dendrites [2,5], and this disorder is related to the presence of significant convection effects in the melt.

For primary spacing studies, samples of diameters larger than 3 mm are generally used, providing a reasonably large array of cells or dendrites. For these larger specimens, however, it is found that 1g gravity level yields growth conditions dominated by convective transport [5]. These convection effects, for heavier solutes, may give rise to a high degree of radial segregation at the interface and significant nonuniformity in spacing that masks the diffusion controlled wavelength selections. Convection effects can be minimized by utilizing thin specimens (less than 1 mm), even in 1 g conditions [6]. This experimental alternative to reduced gravity effects is limited, however, in that thin samples preclude the experimental observation of evolving cellular or dendritic arrays, since only one or two cells or dendrites can grow. Hence, if the interactions arising between structures of an array which are critical in the spacing selection process, are to be

considered, microgravity experimental facilities are left as the only means of experimental observation of the dynamics of cellular and dendritic growth in the diffusive regime.

Recently, we have developed a rigorous two-dimensional numerical model of thermo-solutal convection in vertical Bridgman system for solidification of low Pr fluid [7]. This model showed that a microgravity level of $\sim 10^{-4}$ g is required to establish diffusive growth conditions in binary metallic specimens of 12 mm diameter with stable axial solute gradients. The thermal Grashoff number, which is a measure of the driving force for thermal convection, is much smaller in a transparent system than in a metallic system. Also, the characteristic temperature difference between the hot and cold zone of the furnace is much smaller in the transparent system due to its low melting point. The viscosity of the transparent system is also much higher, and the thermal conductivities of the solid and liquid are nearly identical. These factors make the transparent system have a lower level of convection than the metallic systems. Thus, the minimum microgravity level required for metal systems could be used as an upper bound for the transparent system. More detailed numerical studies for a transparent system are now being carried out during the first phase of this project. These numerical studies will be supplemented with experimental studies in thin samples to establish the microgravity level required for diffusive growth in 12 mm diameter samples.

III. Ground-Based Studies

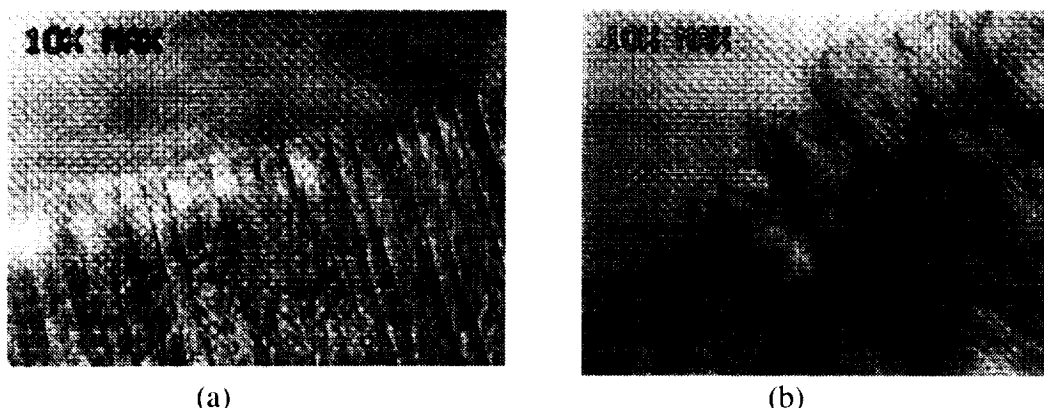
The ground-based studies have been focused on the development of the apparatus, and on the use of thin samples to characterize the importance of the orientation of the solid and the determination of the experimental matrix for our microgravity experiments.

A. Experimental apparatus

For ground-based studies, an experimental unit is designed in which a sample of 12 mm diameter can be solidified vertically upwards. In addition to the basic directional solidification unit used for metallic systems, this apparatus has several important modifications.

- (1) In order to observe and record interface pattern evolution with time, two CCD cameras will be used: one from the side to obtain longitudinal growth and one from the top to obtain a transverse view. The camera at the side is mounted on an independent translating stage so that it can be positioned and maintained near the interface during growth. Our initial results show that high quality images of three-dimensional growth structures can be obtained, Figure 1. We are also incorporating an endoscope, placed inside the liquid at the top, to obtain images of interface. In addition to the cameras, ground-based studies will also incorporate laser interference technique to reconstruct the shape of the low amplitude cell.
- (2) In order to take proper images, it is necessary to have a larger region for the observation of the interface. Thus, instead of using the traditional heater and cooler, we have designed our sample tubes with a thin ITO coating which is transparent.
- (3) In ground-based experiments, the presence of fluid flow causes a significant curvature of the interface. The interface is depressed at the center, so that one could only image the pattern that is close to the wall and the wall significantly influences this pattern. Thus, a planar interface front is required. Accordingly we have designed a small booster heater, to be placed

near the cold zone that can give a flat interface. We have completed the design of this heater and incorporated it into our system. The images obtained without and with the booster heater are shown in Figure 1.



(a) (b)
Figure 1. Observation of a three-dimensional cell/dendrite from the side.
Succinonitrile-1.0 wt% salol, $V = 0.8 \mu\text{m/s}$. (a) Non-planar interface shows only the array at the wall. $G = 2.3 \text{ K/mm}$. (b) Use of a booster heater allows a three-dimensional view, $G = 1.2 \text{ K/mm}$.

B. Experiments in thin samples

Several experiments have been carried out in thin samples to characterize the dynamics of pattern evolution in the succinonitrile system. First, we have examined the importance of interface anisotropy on pattern formation.

In order to examine the effect of orientation on interface pattern development, several experiments were carried out in the succinonitrile - acetone and the Pivalic acid-ethanol systems under different growth conditions that gave the final cellular or dendritic patterns [8]. The basic effects of anisotropy in both these systems under different growth conditions were found to be the same. Figure 2 shows a typical result obtained in the succinonitrile-acetone system. Of the two grains, the right grain that became unstable first had $\psi=0$, which is the angle between the preferred crystallographic direction, *i.e.* [001], and the heat flow direction. Also, the initial instability amplifies faster for $\psi=0$, as seen in Figure 2b. As the perturbed interface propagates, the spacing selection begins to occur in the right grain by the process of cell elimination, and some characteristic spacing distribution is established shortly. In contrast, the grain on the left, $\psi=25^\circ$, shows that the initial spacing is smaller, but as cells become inclined and go through the tip-splitting instability process, a more chaotic structure results, which after a long time gives a significant disorder in spacing. In order to characterize the wavelength selection, results of experiments in the cellular regime were analyzed. Figure 3a and 3b show the Fourier transforms of two patterns that were growing at different values of ψ . After a short time, a single wavelength was dominant for the orientation $\psi=0$. Two dominant peaks are observed for the case in which $\psi=25^\circ$. Thus, we conclude that: (i) the critical velocity for the planar interface instability appears to increase as ψ deviates from zero, (ii) the initial spacing of cells is coarser when ψ is smaller, and (iii) more disorder in spacing is observed as ψ increases. These studies indicate that it is important to control the orientation of the crystal for the quantitative studies of pattern formation, and our initial microgravity experiments will require the crystal orientation close to $\psi=0$. A technique for producing single crystal of required orientation is now being developed.

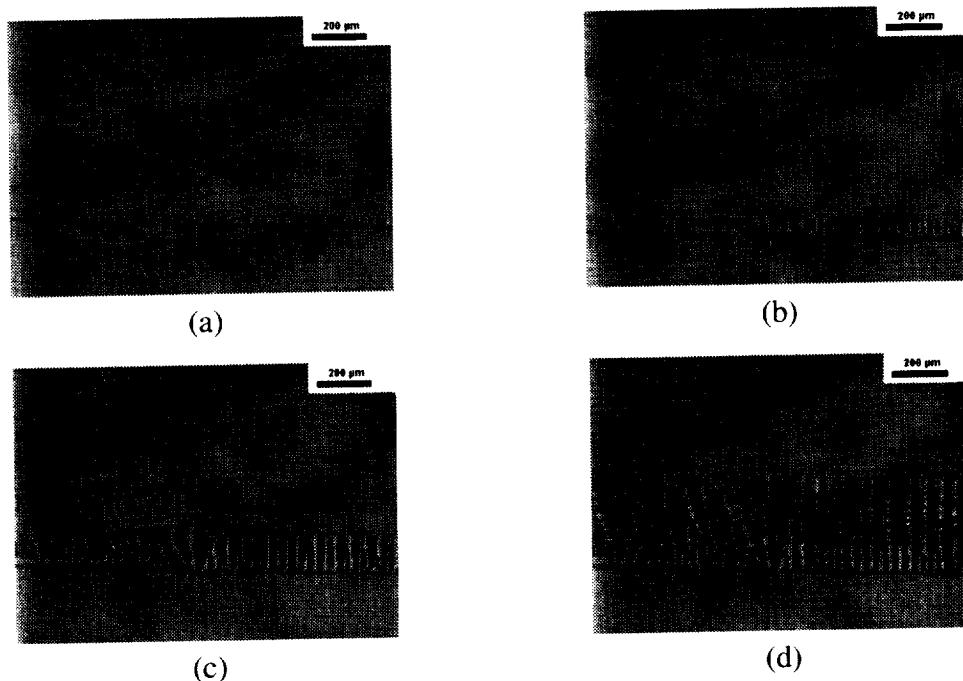


Figure 2. Interface pattern evolution in two grains in which $\psi=0$ in the right grain, and $\psi=25^\circ$ in the left grain. SCN-1.2 wt% acetone, $G=3.1$ K/mm, $V=25.4$ $\mu\text{m/s}$.

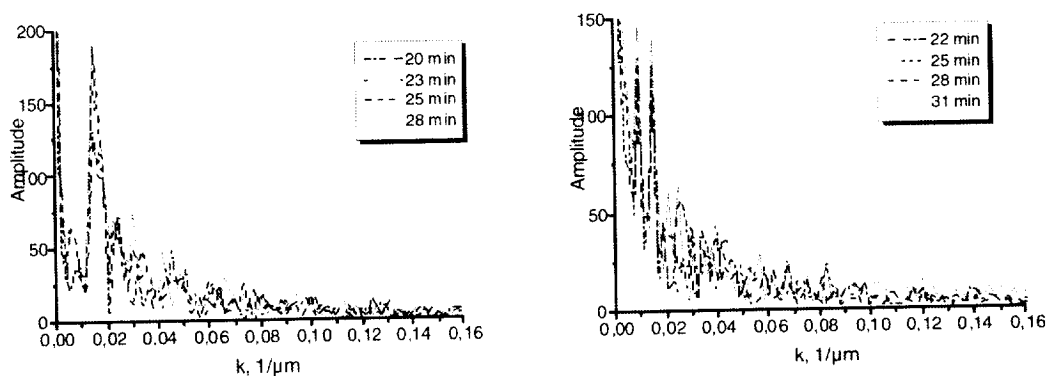


Figure 3. Fast Fourier transform of interface shapes with (a) $\psi=0$, and (b) $\psi=25^\circ$. Succinonitrile- 1.7 wt % acetone, $V = 0.53$ $\mu\text{m/s}$, $G = 2.3$ K/mm.

IV. Theoretical Modeling

The computationally efficient phase-field approach developed by Karma and Rappel [9] for equiaxed thermal dendrites has been extended to the directional solidification of a dilute binary alloy. The extension to directional growth has already been carried out for an idealized symmetric model with equal solute diffusivity in the solid and liquid phases and parallel solidus and liquidus slopes. In order to obtain quantitative predictions, this approach will be extended to the standard one-sided model of a dilute binary alloy with negligible solute diffusion in the solid phase and non-equal solidus and liquidus slopes. Preliminary results indicate that it is possible to construct a dilute alloy phase-field model that yields the same dramatic increase in computational efficiency as for thermal equiaxed dendrites using the reformulated asymptotics of the thin interface limit of Karma and Rappel [9]. Initial results for the time evolution of interface pattern are shown in Figure 4 in which $\psi=0$ is considered. Calculations in 2-dimensions were carried out assuming zero anisotropy and a finite anisotropy. The absence of anisotropy gives a very disor-

dered array, whereas a small amount of anisotropy is shown to sharpen the pattern selection. Phase-field computations are now being extended to 3-dimensional patterns.

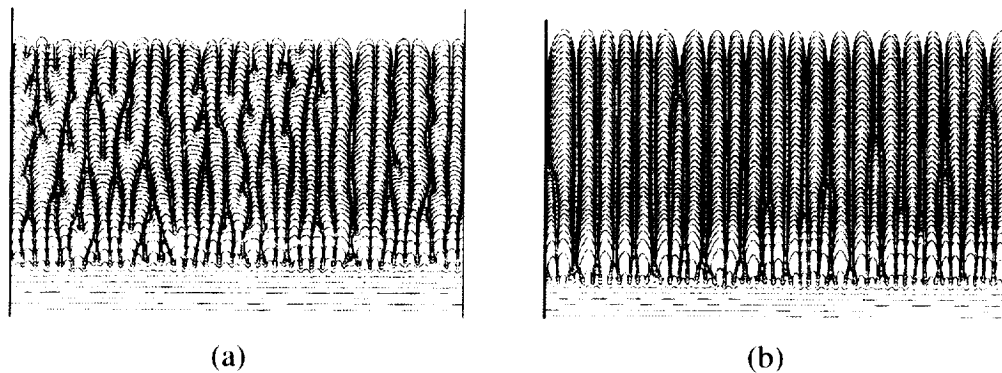


Figure 4. Phase field calculations of the cellular pattern evolution with time.
(a) Isotropic interface energy, (b) small anisotropy in interface energy.

REFERENCES

1. K. Somboonsuk, J.T. Mason, and R. Trivedi, *Metall. Trans. A*, 15 (1984) 967.
2. H. Song and S. N. Tewari, *Metall. Mat. Trans. A*, 27 (1996) 1111.
3. H. Jamgotchian and B. Billia, Private Communication, Marseille, France (1999).
4. S.H. Han and R. Trivedi, *Acta Metall. Mater.*, 41 (1994) 25.
5. R Trivedi, P Mazumder, S. N. Tewari, (submitted to *Met. Trans.*)
6. R Trivedi, H Miyahara, P. Mazumder, E. Simsek and S. N. Tewari, (submitted to *J. Cryst. Growth*)
7. P. Mazumder and R. Trivedi, in: *Fluid Flow Phenomenon in Metal Processing*, Ed. by N. El-Kaddah et al., TMS, Warrendale, PA (1999), 459-456.
8. B. Kauerauf and R. Trivedi, Unpublished work, Iowa State University (2000).
9. A. Karma and W.J. Rappel, *Phys. Rev. E*, 53 (1996) R3017.

SHIVA
(Spaceflight Holography Investigation in a Virtual Apparatus)

James D. Trolinger¹, Ravindra B. Lal², Roger Rangel³, Carlos Coimbra⁴, William Witherow and
Jan Rogers⁵

¹MetroLaser Incorporated, email: jtrolinger@metrolaserinc.com

²Alabama A&M University

³University of California Irvine

⁴Drexell University

⁵Marshall Spaceflight Center

Symbols

a	Radius of the particle
\mathbf{f}_H	History force
\mathbf{f}_{St}	Stokes force
\mathbf{f}_{VM}	Virtual mass force
\mathbf{g}	Local gravity acceleration
S	Scaling number $\frac{\alpha\omega}{2} = \frac{\Omega}{\nu} \left(\frac{a}{3}\right)^2$
α	Fluid-to-particle density ratio
η	Particle-to-fluid amplitude ratio $(1 + b_i / a_i)$
ν	Kinematic viscosity
ρ	Density
τ_p	Characteristic time $2\rho_p a^2/9\mu$
Ω	Angular frequency of the fluid surrounding the particle
ω	Dimensionless angular frequency = $\Omega\tau_p$

I. Introduction and Summary

SHIVA (Spaceflight Holography Investigation in a Virtual Apparatus) will expand our understanding of the fundamental physics of particle movement in fluids by exploiting the power of holography in a spaceflight experiment¹. In addition, the study will exploit the movement of particles in fluids to observe and quantify microgravity phenomena that are extremely important in materials sciences with applications both in space and on earth. The regime under scrutiny is the low Reynolds number, Stokes regime or creeping flow, which covers particles and bubbles moving at very low velocity. The equations describing this important regime have been under development and investigation for over 100 years and yet a complete analytical solution of the general equation had remained elusive yielding only approximations and numerical solutions. In the course of the ongoing NASA NRA, the first analytical solution of the general equation was produced by members of the investigator team using the mathematics of fractional derivatives. This opened the way to an even more insightful and important investigation of the phenomena in microgravity.

The proposed flight experiments have several closely related objectives directed towards understanding and exploitation of the movement of particles in fluids. One is to validate the new

analytical solution to the equation of motion for a particle in the Stokes flow regime and to gain an understanding of its limits of validity. A second objective is to provide experimental knowledge that will allow us to push the limits of the solutions. Consequently, the experiments have been designed also to provide empirical data for conditions that have escaped accurate theoretical modeling. This includes interacting particles, particle-wall interactions, bubbles, and Reynolds numbers larger than unity. The flight experiments will provide an opportunity to collect data that can be used not only to validate, but to expand our existing theoretical foundation.

Another important objective of the experiment is to exploit our understanding of the movement of particles in fluids and new advanced diagnostics tools made available by this research² to observe and measure effects of residual acceleration and g-jitter in the space station. These tools will allow us to accurately quantify the quasi-steady acceleration and its variations that are believed to be extremely important in materials processing experiments such as crystal growth. This is achievable by accurately measuring the movement of a sphere in a known fluid over time. An even more accurate technique developed during this study is to measure the time varying separation between spheres that are lighter and heavier than the fluid; this provides a direct measure of residual acceleration and low frequency g-jitter. In selected cases, the separation between the two spheres varies by as much as four times the movement of the fluid; providing an amplification effect for the measurement. This will provide valuable information to compare with and to complement other acceleration measuring equipment under development for the Space Station.

The objectives of SHIVA will be achieved by recording a large number of holograms of carefully selected particle fields and fluids in space under controlled conditions, bringing the holograms back to earth and extracting the precise three-dimensional position of all of the particles as a function of time. We have demonstrated that having the holograms to study on earth is essentially equivalent to being back in the space environment for the particle tracking operation. (Leading to the term "virtual spaceflight chamber".) The accuracy needed to achieve the objectives of the project has been demonstrated in ground experiments. A limited amount of data will be recorded in video to provide real time data as a back up and allow ground based scientists to monitor the progress of the experiment.

A variety of forcing functions for the particle field will include both natural forces of the Space Station environment and applied forces. A sinusoidal movement will provide a fundamental forcing function for validating the equations.

The Space Station provides an ideal environment for SHIVA. Potential for conducting limited parts of the experiment in a ground-based laboratory has been identified and some of these have been carried out. In general the space environment is required for the overall experiment, especially for cases containing very heavy particles, very light particles, bubbles, collections of particles and for characterization of the space environment and its effect on particle experiments. Lightweight particles and bubbles typically rise too fast in a gravitational field and heavy particles sink too fast. In a microgravity environment, heavy and light particles can be studied side-by-side for long periods of time.

II. Theory

During the theoretical effort, we developed a procedure to solve the equation of motion exactly (to the approximations made in the derivation of the equation) for a generic, uniform flow field³. Of the various special cases we have treated, the one selected for the experiment is concerned with the motion of a sphere that is allowed to move under the forces generated by a sinusoidal surrounding field⁴. Three force terms in the equation are considered, the Stokes force, the virtual mass force, and the history term. The history term is usually neglected because it is the most difficult to include. Therefore, we have concentrated somewhat on regimes where the history term is not negligible since these are the least understood of cases of interest.

A scaling analysis on the forces that depend on the fluid-to-particle density ratio yielded the value of a critical forcing frequency for which the history term effects are maximized in harmonic Stokes flows. Depending on the forcing frequency, the forces acting on the particle can be dominated by either the steady-state Stokes drag (low frequencies) or by virtual mass effects (at high frequencies). When the forcing frequency is of the order of the critical frequency $9\nu/a^2$, all forces are of the same order of magnitude and must be considered. Figure 1 shows graphically the scaling of the individual forces. As an example, a case under study is when the fluid (Dupont Krytox) is twice as dense as the particle (polystyrene), *i.e.* $\alpha=2$. For this case, theory shows that the history term is most important at an oscillatory frequency of 60 Hz. ($\omega=1$).

The analysis shows that when $S=1$ ($\alpha\omega=2$) the amplitude of the history drag force is three times larger than the amplitude of the virtual mass and the Stokes drag forces. When the value of the product $\alpha\omega$ is much smaller than 2, the Stokes drag dominates. For values of $\alpha\omega$ much larger than 2, the virtual mass force is dominant. Based upon these results we have designed the experiment to operate around the value of $S=1$.

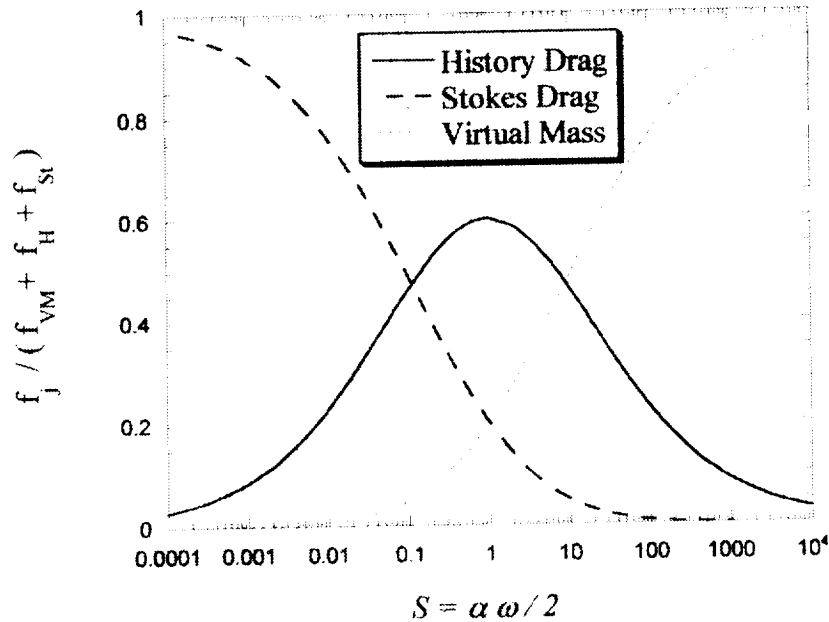


Figure 1. Relative scaling of the forces for harmonic particle motion.

One experiment, therefore, is to measure the amplitude of the particle in an oscillating fluid verses the scaling parameter, S . In particular we are interested in the ratio of the particle-to-fluid amplitude ratio and its comparison with and without inclusion of the history term. Figure 2

shows the predicted particle-to-fluid amplitude ratio for the case described above. For a fluid amplitude of 100 micrometers, the usual solution for the particle amplitude would predict 150 micrometers, while the new solution predicts 125 micrometers. Our experimental accuracy for amplitude measurement, therefore, must be better than 25 micrometers to detect the difference. Experiments so far show that we are well within this limit.

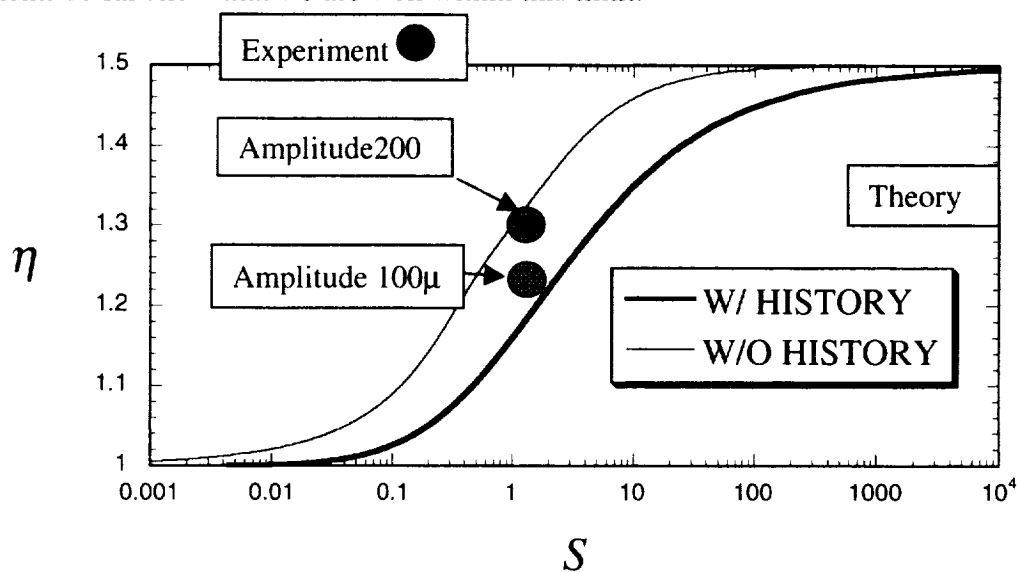


Figure 2. Amplitude ratio for $\alpha = 2$.

III. Experiments

Figure 3 illustrates one of the ground experiments that have been done in preparation for flight experiments. The particle is released at the bottom of a fluid filled cell. The fluid is constrained to move with the cell. The cell is vibrated in a sinusoidal motion with an amplitude up to 200 microns at 60 and 120 Hz. Therefore, we can measure precisely where the fluid and particle are at all times. As the particle rises, it attempts to follow the sinusoidal movement of the fluid; however, it follows a quasi-sinusoidal path with negative phase difference and larger amplitude (see particle and fluid motion in the figure).

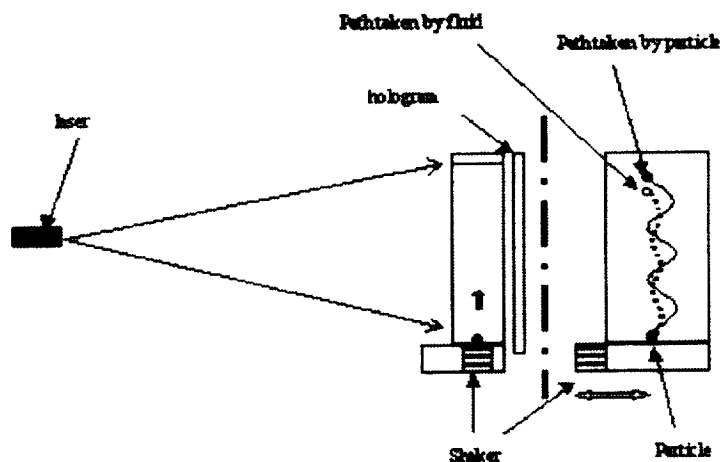


Figure 3. Ground Experiment Apparatus.

Figure 4 shows the edge of a 2 mm diameter particle reconstructed from a doubly exposed hologram where the particle is captured at its amplitude extremes. The amplitude of vibration is 100 microns. Clearly the center of the line representing the edge of the particle can be located to better than 5 microns, which is the desired resolution.

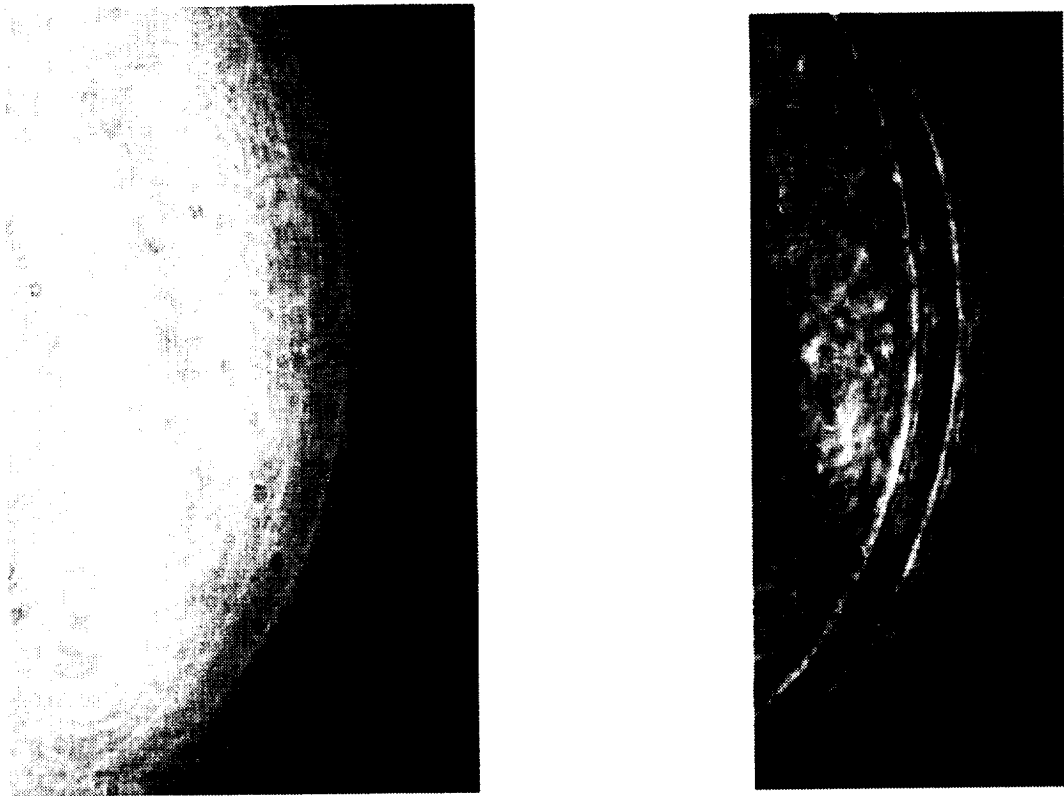
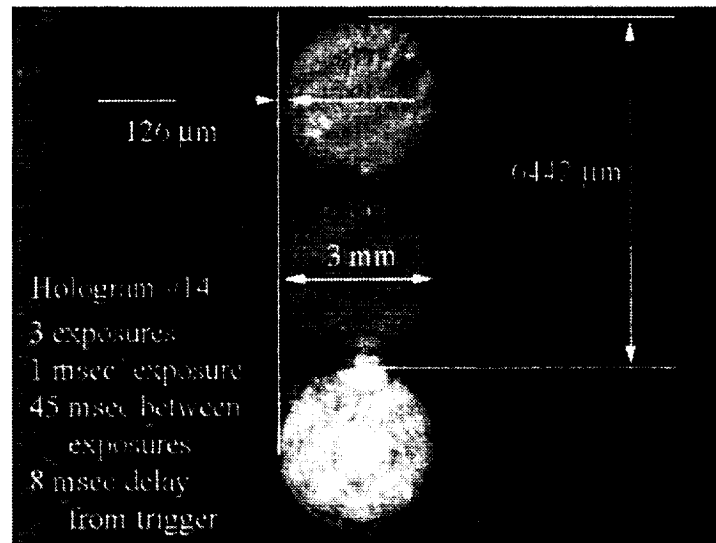


Figure 4. Reconstructed image of the edge of a particle from a doubly exposed hologram. The particle moved 100 microns between exposures. The image in the right figure has been optically high pass filtered to enhance the edge image.

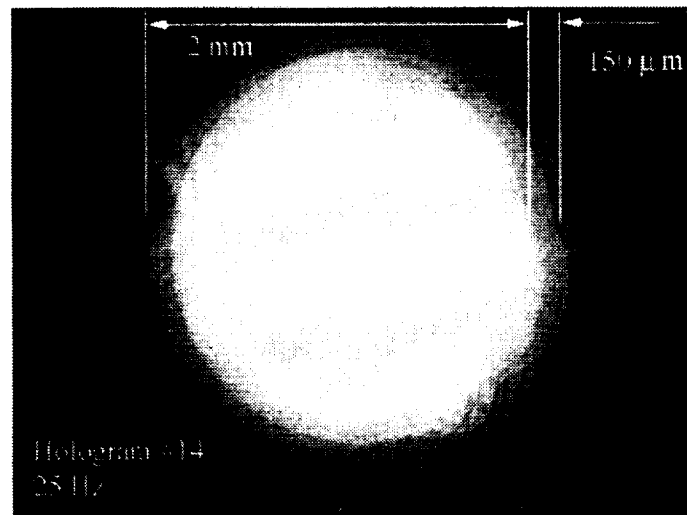
In a parallel set of experiments the cell is mounted on a traverse that is driven by a stepper motor. The system is capable of moving the cell by up to 200 microns at frequencies up to about 20 Hz. A particle was dropped into the cell and the position of the particle was monitored by a separate laser trigger that starts a timer when the particle passes through the beam. The timer is then used to fire a shutter after a preset time delay.

Figure 5 shows images for a falling 3mm diameter ceramic sphere taken from a triply exposed hologram made with one-millisecond exposures. Figure 5a is the image of a sphere that is attached to the cell window, while Figure 5b is the falling particle in the fluid. The edge of the particle can easily be located in these images to a few microns.

Future experiments will include particles that are lighter than the fluid launched at the bottom of the cell. This will also provide testing of launching concepts that will be used in the spaceflight experiment.



a.



b.

Figure 5. Vibrating three-millimeter diameter ceramic sphere recorded at two ends of the vibration amplitude in a triple exposure, in-line hologram. Edge location resolution is better than five microns. a) Three exposure image of falling 3mm ceramic sphere. b) Image of 3mm ceramic sphere attached to window.

Figure 6 and Figure 7 illustrate the preliminary instrument concept. A laser diode will produce a diverging light that illuminates the test cell after collimation. As the light passes through the chamber, it will pick up particle and crystal profile information and in-line holograms will be recorded on 70-mm film. This ability will allow the particle's position to be precisely tracked, thus permitting the detection of very small motions.

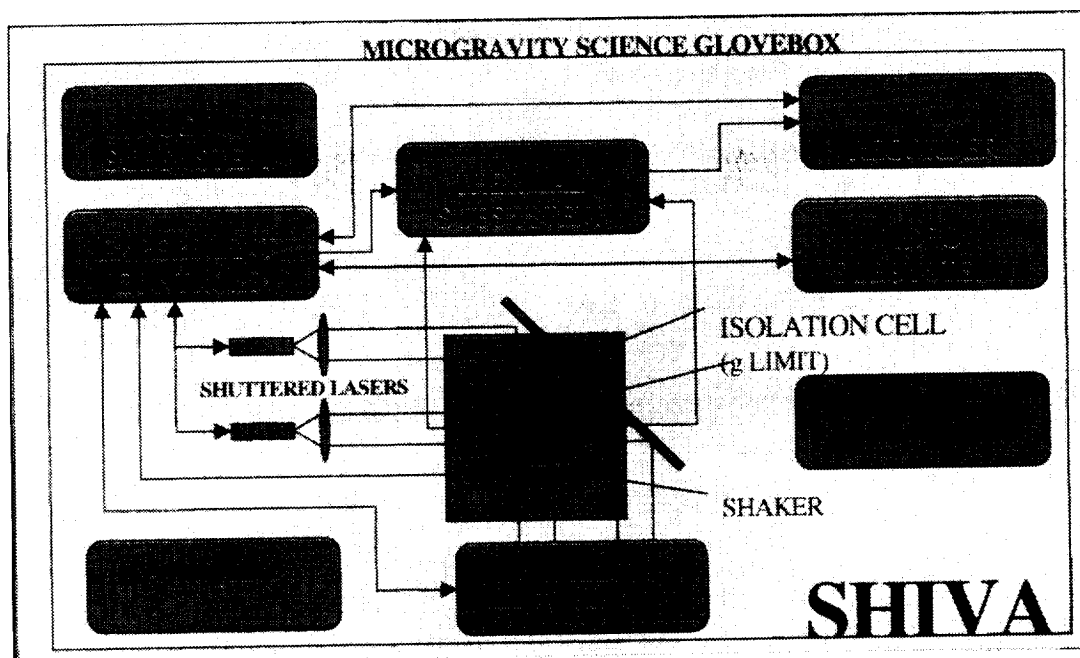


Figure 6. Spaceflight system concept.

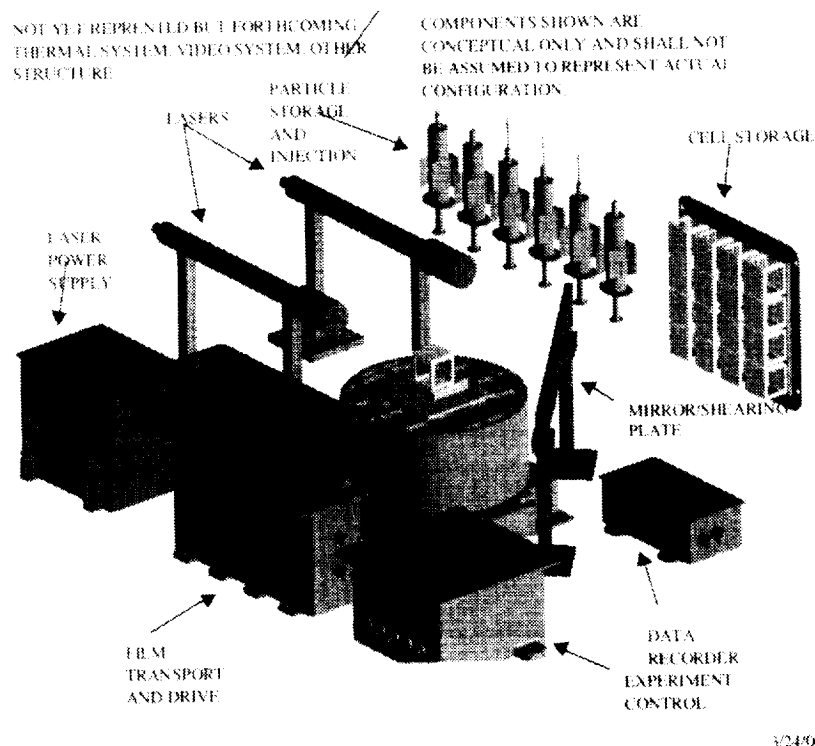


Figure 7. Perspective view of the flight hardware.

Figure 8 shows how the shearing plate is installed in the system. The wave shearing plate splits the beam that has passed through the test cell into two beams that are laterally shifted in space. The two beams interfere with each other providing a measurement of the gradient in phase across the wavefront. The wavefront that has passed through the depletion zone surrounding a particle will be interfered with a wave that is adjacent to the particle providing an infinite fringe inter-

ferogram of the depletion zone. The amount of the shift will be approximately 0.8 the thickness of the shear plate for glass. We require a shift of at least 0.5 centimeters. The shearing plate and the mirror can be formed on the same optical element for rigidity. The shear plate can be a piece of glass that is coated for 50% reflection on the first surface and 100% reflection on the second surface. This mode of operation will allow us to perform not only waveshearing interferometry but also digital holography.

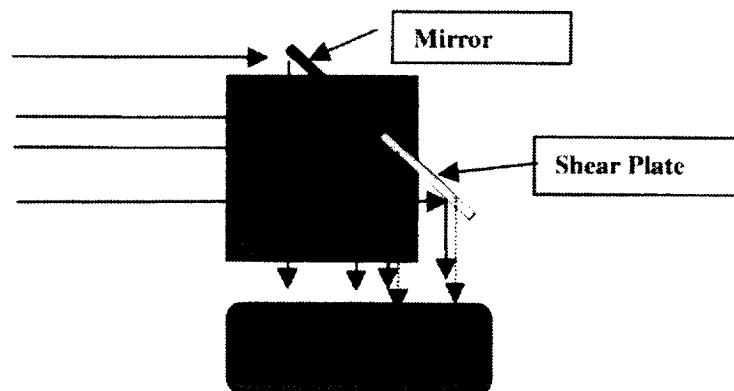


Figure 8. Wave Shearing Interferometer Configuration.

The purpose of adding waveshearing interferometry and digital holography capability to the system is to allow observation and measurement of temperature and concentration gradients that will be purposely introduced into the cell for part of the experiment. In the most general case, we will investigate the movement of a growing and/or dissolving crystal in the fluid. Such a crystal has a depletion zone associated with it that will complicate the situation. Figure 9 shows such a crystal observed during the Spacelab 3 crystal growth experiment.

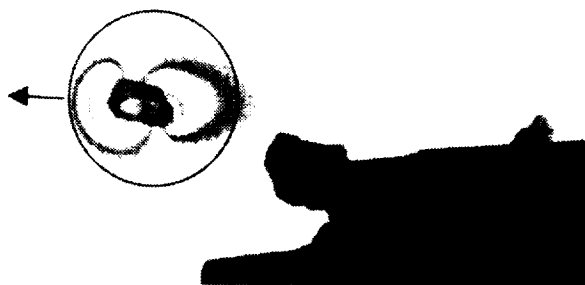


Figure 9. Free floating crystal observed in Spacelab 3 experiment.

A small free-floating crystal (inside the circle denoting the depletion layer) has broken away from the main seed and moves through a TGS solution in a Spacelab 3 crystal growth experiment. Double exposure holographic interferometry clearly shows the depletion zone around the growing crystal as well as the effects of the motion on the growth rate. The higher concentration of the fringe frequency on the leading edge indicates a higher concentration gradient and higher growth rate as it moves through the solution (in the direction of the arrow). This was the first time the long theorized depletion zone and effects of movement on growth rate had been observed in space. This crystal was monitored for many hours during (and after) Spacelab 3 providing much of the inspiration for the SHIVA project.

IV. Summary and Conclusions

The objectives of the experiment are to:

1. Collect a sufficient amount of data describing the movement of particles in fluids in microgravity to allow us to validate our analytical solution of the general equation of motion.
2. Collect data on the movement of particles in fluids in microgravity that will be useful in extending the current theory beyond presently available theory.
3. Develop, test, and apply the method for measuring quasi-steady acceleration by tracking particles in fluids.
4. Quantify the low frequency acceleration environment of the space station.
5. Observe and quantify quasi-steady g and g -jitter effects and microconvection on particles in fluids.
6. Characterize the ability of isolation tables to isolate experiments containing particles in liquids.
7. Understand the interaction between the particle and fluid sufficiently to allow particles to be used to track fluid movement.

The feasibility for achieving these results has already been established in the ongoing, ground-based NASA Research program, which led to the "virtual spaceflight chamber" concept.

REFERENCES

1. J.D. Trolinger, R.B. Lal, D. McIntosh, and W.K. Witherow "Holographic Particle Image Velocimetry in the First International Microgravity Laboratory aboard the Space Shuttle Discovery", *Applied Optics*, Vol. 35, No. 4, pp. 681-689 (1 Feb. 1996).
2. J.D. Trolinger, M. Rottenkolber, and F. Elandaloussi "Development and Application Of Holographic Particle Image Velocimetry Techniques For Microgravity Applications", *J. of Measurement Sciences and Technology*, Vol. 8 pp. 1573-1583 (1997).
3. C.F.M. Coimbra and R.H. Rangel "General Solution of the Particle Momentum Equation in Unsteady Stokes Flows", *J. Fluid Mech.*, 370, pp. 53-72 (1998).
4. C.F.M. Coimbra and R.H. Rangel "Spherical Particle Motion in Unsteady Viscous Flows", AIAA 99-1032, 37th AIAA Aerospace Sciences Meeting, January 1999.

GROWTH STUDIES OF SILICALITE-1 CRYSTALS AND THIN FILMS

M. Tsapatsis*, D.G. Vlachos*, V. Nikolakis and G. Bonilla

Department of Chemical Engineering
University of Massachusetts Amherst
Amherst, MA 01003

Zeolites and molecular sieve materials, in general, are ordered framework structures with highly regular, ordered cages and channels of nanometer scale. Their tailored structure, stability and activity led to the development of numerous, traditional applications in hydrocarbon conversion, size/shape selective catalysis and separation processes. Molecular sieve thin films are highly desirable for the preparation of novel chemical reactors, selective chemical sensors and membranes. However, the preparation of zeolite films and membranes for demanding applications, like membrane reactors and hydrocarbon or permanent gases separations, is hindered by the lack of suitable membrane formation processes leading to films with controlled microstructures, and by the limited fundamental understanding linking microstructure with separation properties. Our research objective focuses on addressing the critical issues of microstructure control and predictive mathematical modeling linking processing and microstructure with separation performance. We are developing simulations with the ultimate goal of developing predictive models based on fundamentals of crystal growth, colloidal interactions, and transport phenomena. Along with these fundamental studies, we are exploring potential applications of zeolite films for separation of close boiling hydrocarbons.

The feasibility of selective separations has been demonstrated by several research groups, by using thin (several microns) zeolite films on porous supports. One successful method for synthesizing those films is the secondary grain growth technique, which has the advantage of decoupling zeolite nucleation from the film growth. In that method, a coating of crystals is initially deposited on the support, which is further treated hydrothermally.

The growth of the zeolite silicalite-1 (structure type MFI) crystals, either deposited on supports or in dilute suspensions, has been studied both experimentally and theoretically.

Seeded growth of TPA-silicalite-1 seeds in suspension was studied using Dynamic Light Scattering (DLS) as the primary experimental technique. The effect of the total silica concentration, temperature, and total seed concentration was examined. The molar compositions of the synthesis solution examined are $x\text{SiO}_2$: 9TPAOH: 9500 H_2O : $4x\text{EtOH}$, with $x=5,10,20,40,50,60,80,120$. Those compositions are correspondingly referred as C1~C8 from hereon. It has been shown, in agreement with other reports in the literature¹⁻³, that primary units (subcolloidal particles) having a size of approximately 2.8 nm are present in the synthesis mixture. These particles are believed to be pre-organized inorganic-organic composite structures, and their role in nucleation and growth of silicalite-1 is still poorly understood. It is desired to examine whether silicalite growth

by addition of subcolloidal particles is a possible mechanism. From the DLS results it has been observed that at high concentrations (C2~C8) of silica in the solution, growth is observed, with a linear growth rate that is practically independent of the total silica added to the system. Growth is activated with an activation energy of ~90 kJ/mol which is also independent of the silica concentration. The seed concentration over the range ($0.1 \times 10^9 \sim 5.9 \times 10^9$ seeds/cm³ of sol) does not affect the above conclusions.

To describe growth of diluted suspensions of seeds (ideally an isolated particle), we employ a transport growth model using the DLVO^{4,5} theory to account for the presence of an energy barrier to coagulation. For interacting particles performing Brownian motion, the general transport equation of the colloidal particles, with respect to a central static sphere of radius R is

$$\frac{\partial c}{\partial t} = \frac{1}{r^2} \frac{\partial}{\partial r} \left[D r^2 \frac{\partial c}{\partial r} + r^2 c \frac{D}{kT} \frac{\partial V}{\partial r} \right], \quad (1)$$

where c is the subcolloidal particle concentration, D is the diffusion coefficient of the subcolloidal particles, k is the Boltzman constant, V is the potential describing the effect of an externally applied force field to the mutual diffusion, and r is the distance from the center of the seed. In deriving the above equation, it has been assumed that (i) the superposition principle is applicable to both hydrodynamic and colloidal forces, (ii) neither temperature nor density gradients exist, and (iii) the particles are spherical, non rotating, and isotropic.

In order to solve Equation 1, boundary conditions have to be specified. The most common boundary condition at the surface, referred to as the *perfect sink model*⁶, assumes that all the subcolloidal particles arriving at the surface of the static particle get irreversibly incorporated into it. The flux of the subcolloidal particles arriving at the static particle attains a quasi-steady-state value when $t \gg R^2/D$, which is the characteristic time for diffusion of the subcolloidal particles over a length R. The time t needed for the crystal size to increase by R is R/k_{growth} , where k_{growth} is the linear growth rate. In order for the quasi-steady-state approximation to be valid, the characteristic time for growth has to be much larger than the diffusion one. Using typical values for the radius of the silicalite seeds and the diffusion coefficient of the subcolloidal particles, the time necessary to achieve quasi-steady-state is estimated to be of the order of milliseconds which is much smaller than the characteristic time of growth estimated from our experiments. Considering that the mass rate of growth is equal to the arriving mass flux, the expression for the growth rate has been derived. The rate of radius change of the seed is

$$\frac{dR}{dt} = \frac{D c_0 (R+r_s)}{R^2 W} \frac{4}{3} \pi r_s^3. \quad (2)$$

where W is the stability ratio.

The stability ratio is a measure of the difference between the number of collisions in the absence of interactions between two particles and the actual number when interactions are taken into account. The decrease in the frequency of collisions, between interacting particles compared to the one for non-interacting particles performing Brownian motion, is caused by an energy barrier the subcolloidal particles have to overcome before they come in contact with the growing crystal. Due to the existence of this barrier, a growth mechanism through the addition of subcolloidal particles will appear to be activated, with an activation energy that depends on the potential used. The stability ratio is obtained from

$$W = 2 \int_0^{\infty} \frac{e^{V/KT}}{(u+2)^2} du, \quad (3)$$

where $u=2d/(R+r_s)$, and d is the closest distance between the surfaces of the two particles.

In order to apply the above analysis to the growth of silicalite seeds, the interactions between particles have to be described. When we come to consider the long-range interactions between macroscopic particles in liquids, the two most important forces are the van der Waals and electrostatic (DLVO theory). The interactions between a glass sphere and the surface of a silicalite membrane have been quantified by using Atomic Force Microscopy force measurements⁷. It is shown that they can be fitted with a model that assumes constant surface charge as the particles approach each other. Same type of interactions was further assumed between the subcolloidal particles and the silicalite seeds, with their parameters measured by independent experiments (zeta potential, conductivity) at the conditions of the growth.

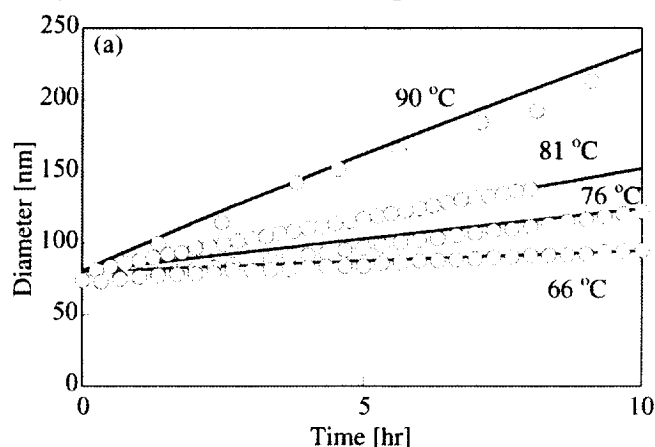


Figure 1. Comparison of experimentally measured growth curves (open symbols) with simulated ones (lines)

In Figure 1 the experimental results are compared with the simulation ones for one synthesis composition, at four different temperatures. Despite the variation of the model input parameters (the error bars indicate the standard deviation due to fitting of growth rate curves in an Arrhenius graph), Figure 2 depicts a very good agreement between the calculated and the experimental activation energies over the range of synthesis compositions examined. This result shows that over the range of the compositions examined, the activation energy is practically independent of composition. The activation energy was calculated from the fitted linear growth rates of the simulation results. These results strongly indicate that association of subcolloidal particles with the crystal, followed by fast rearrangements on the crystal surface, is a possible mechanism of silicalite growth. In such a case, the apparent activation energy observed during the silicalite growth can be attributed to the repulsion that is caused by the overlap of the electrical double layers of the silicalite seeds and the subcolloidal particles as they approach each other. The constant charge or constant potential approximations that have been used are the two limiting cases for the interactions, but they are a first good approximation when no detailed information about the surface behavior is available.

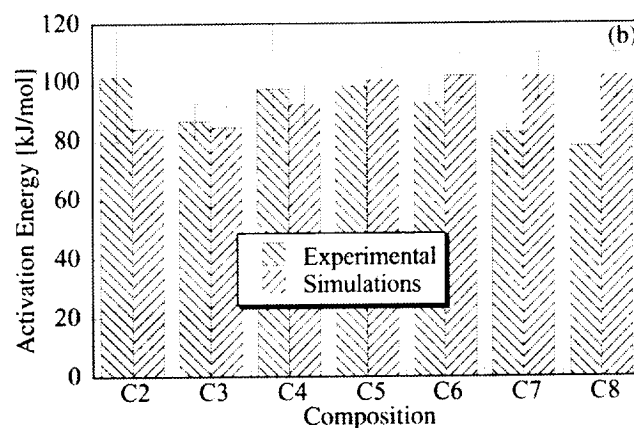


Figure 2. Comparison of measured and calculated activation energies at different compositions.

By considering the effects of size in the interaction potentials, it is also possible to explain the stability of the seeded suspension and understand why the smaller subcolloidal particles (of diameter ~ 2.8 nm) are more likely the ones contributing to the growth. Our results support a mechanism where the rate-limiting step for growth of silicalite is the addition of subcolloidal particles.

The final size of the nanocrystals studied by DLS was around 300 nm. It is not possible to examine growth by DLS at larger sizes due to crystal precipitation and multiple scattering problems. This is not the case, though, for the film growth studies. As the initially spherical crystals grow bigger, (mesoscopic length size) they start exhibiting distinct facets. As the faceted seeds grow further, they impinge upon each other, creating a continuous, polycrystalline film. Starting with randomly oriented seeds, we have been able to prepare preferentially oriented membranes during secondary growth. The preferred orientation is due to the anisotropic growth rates of the zeolite grains that lead to an evolutionary selection process during columnar growth according to the classical van der Drift model⁸. We have performed a series of simulations on the growth of polycrystalline, faceted MFI using a front tracking technique in two spatial dimensions. The growth in two dimensions is modeled by considering a simplified description of the shape of silicalite crystals based on a single growth rate parameter, α , describing the relative crystal facet velocities. Our model simulates the growth of the zeolite membrane, starting from seeds with initial random orientation and position, by tracking the motion of all corners where facets from the same grain and different grains meet. The temporal evolution of film growth shows that grain boundaries are straight, but undergo abrupt changes in direction when two grains from different crystals meet. The computer simulation clearly captures the two major characteristics of the evolutionary grain selection, i.e., with increasing film thickness (i) a preferential orientation of the crystallites develops, and (ii) the average grain size increases. Consequently, the grains become increasingly columnar. Such columnar microstructures are common features of polycrystalline MFI films⁹. This can be attributed to the competitive growth among adjacent crystal grains. Much of the growth is understood by considering its dependence on the growth rate parameter, α . For example, as the parameter is increased, we observe a significant increase in the surface roughness. Figure 3 clearly shows good qualitative agreement of the growth simulations with a typical silicalite membrane as observed with the Scanning Electron Microscope (SEM).

The distribution of grains in the final film grown is also studied in order to quantify the development of the preferred orientations during vertical growth. Specific for the case of silicalite, the crystallographic orientation distribution (texture) analysis shows two peaks that sharpen during film growth. The first peak position is common to all idiomorphs and may be derived directly from the orientation of the largest radial vector (c-axis) perpendicular to the substrate. The second peak position is dependent on the growth rate parameter and is derived from the orientation of the second largest radial vector in two dimensions.

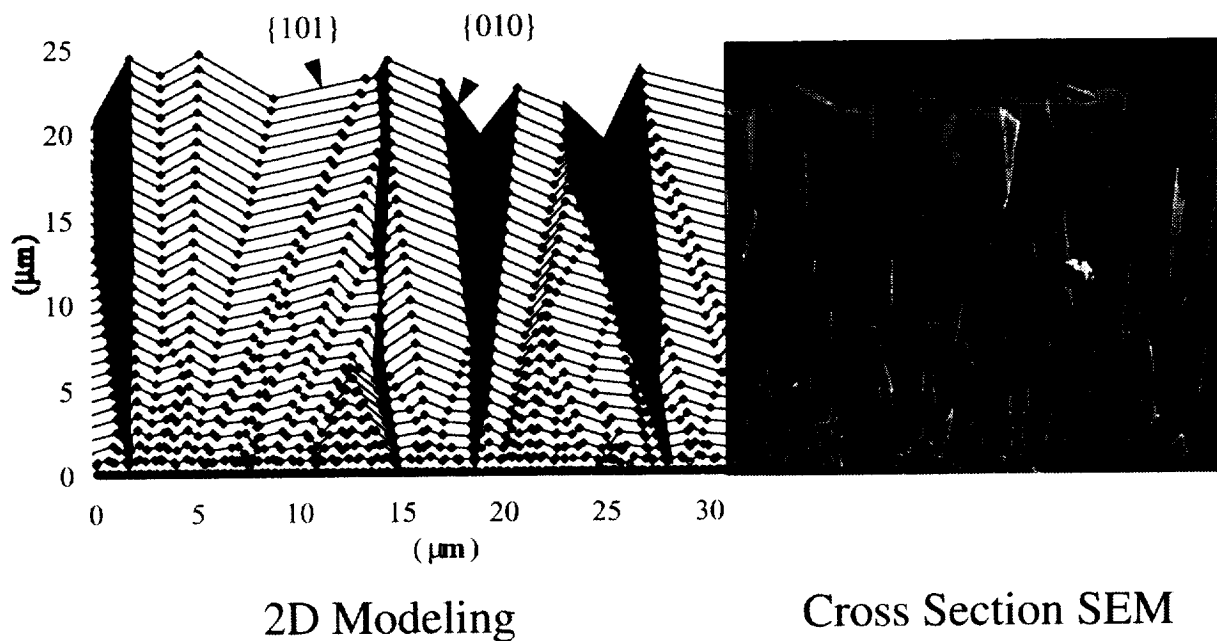


Figure 3. Qualitative comparison of computer simulations of growth of an MFI membrane with an SEM image of MFI grown by the secondary growth technique under hydrothermal synthesis.

X-ray diffraction (XRD) pole figure measurements were performed on MFI membranes grown by secondary growth under hydrothermal synthesis. This type of measurement is used to obtain direct information on the orientational distribution of specific lattice planes in the membrane. The results obtained also show two peaks that are consistent with the peaks observed in the orientational distribution function obtained from the simulations. Therefore, while this second peak had been experimentally observed, the mechanisms that give rise to its existence were not well understood until now.

During the ground based studies we will further develop the mathematical models guided from growth experiments and microstructural characterization. Microgravity experiments will help bridging the gap between the *in-situ* submicrometer crystal growth studies and the film evolution studies by extending the DLS measurements (*e.g.* by limiting precipitation). Membranes prepared under microgravity will be valuable in linking processing methods with the microstructure of molecular sieve films. This will allow for clear benchmarking for the practical benefits of the potential for defect elimination when growth takes place in microgravity by comparing the microstructure and the performance in membrane applications for films developed in microgravity with films grown in our lab.

REFERENCES

1. N. J. Watson, E. L. Iton, R. I. Keir, J. C. Thomas, T. L. Dowling, and J. W. White, *J. Phys. Chem. B* 1997, *101* 10094-10104.
2. P.-P. E. A. de Moor, T. P. M. Beelen, B. U. Komanschek, L. W. Beck, P. Wagner, M. E. Davis, and R. A. van Santen, *Chemistry-A European Journal* 1999, *5* 2083-2088.
3. P.-P. E. A. de Moor, T. P. M. Beelen, R. A. van Santen, K. Tsuji, and M. E. Davis, *Chem. Mater.* 1999, *11* 36-43.
4. E. J. W. Verwey and J. T. G. Overbeek, *Theory of stability of lyophobic colloids* (Elsevier, Amsterdam, 1948).
5. B. V. Derjaguin and L. Landau, *Acta Physicochim. URSS* 1941, *14* 733-762.
6. M. Elimelech, *J. Chem. Soc. Faraday Trans.* 1990, *86* 1623-1624.
7. V. Nikolakis, E. Kokkoli, M. Tirrell, M. Tsapatsis, and D. G. Vlachos, *Chem. Mater.* 2000, *12* 845-853.
8. A. van der Drift, *Philips Research Report* 1967, *22* 267.
9. A. Gouzinis and M. Tsapatsis, *Chem. Mater.* 1998, *10* 2497-2504.

COARSENING IN SOLID-LIQUID MIXTURES

J. Alkemper, V.A. Snyder and P.W. Voorhees

Department of Materials Science and Engineering
Northwestern University
Evanston, IL 60208

INTRODUCTION

The late-stages of a first-order phase transformation process are usually characterized by the growth of second-phase domains with low interfacial curvature at the expense of domains with high interfacial curvature. This process, also known as Ostwald ripening or coarsening, occurs in a wide variety of two-phase mixtures ranging from multiphase solids to multiphase liquids, and has a significant impact on the high temperature stability of many technologically important materials. Unfortunately, an understanding of the dynamics of ripening processes is not in hand. Many of the recent theories for the effects of a finite volume fraction of coarsening phase on the kinetics of Ostwald ripening have proposed divergent expressions for the dependence of the coarsening rate of the system on the volume fraction of coarsening phase, for a review see [1]. As there are virtually no experimental data of sufficient quality to differentiate between these theories, or even provide qualitative information on the coarsening dynamics of low volume fraction systems, the controversy over the dependence of the coarsening rate of the system on the volume fraction remains unresolved.

Previous NASA sponsored work showed clearly that solid-liquid mixtures consisting of Sn-rich particles in a Pb-Sn eutectic liquid are ideal, and perhaps unique, systems in which to explore the dynamics of the Ostwald ripening process. The high coarsening rate in these systems permit accurate kinetic data to be obtained and the thermophysical parameters necessary to make a comparison between theory and experiment are known. However, in a terrestrial environment experiments can be performed only at the relatively high volume fractions of solid where the presence of a solid skeletal structure prevents large-scale particle sedimentation. This precludes experiments aimed at testing theories that predict the coarsening kinetics in low volume fraction systems. Even in these high volume fraction solid solid-liquid mixtures, however, it is unclear that the particles are truly motionless. As the theory assumes that the particles do not move during the coarsening process, an unambiguous comparison between theories of diffusion controlled Ostwald ripening and experiment is difficult, if not impossible, using terrestrial-based experiments.

The primary objective of the Coarsening in Solid-Liquid Mixtures (CSLM) experiment was to measure the temporal evolution of the average size-scale of a solid-liquid mixture during coarsening and then use this data to test theory without any adjustable parameters. In addition, the experiment was designed to provide information on the effects of gravity on the morphology of solid-liquid, the mixtures that are found during coarsening.

I. Spaceflight Results

The Coarsening in Solid-Liquid Mixtures experiment was flown on STS-83 and STS-94. We performed seven coarsening experiments on STS-83, and nine on STS-94. A considerable amount of data was acquired from these experiments. All totaled, approximately 25,000 micrographs have been taken. In the course of performing these experiments a great deal has been learned about the system and its behavior in a microgravity environment. The success of these experiments shows clearly that Pb-Sn solid-liquid mixtures, along with a microgravity environment, can be used to obtain unique data on the coarsening behavior of two-phase systems.

Most importantly, the experiments have shown that solid-liquid mixtures consisting of Sn-particles in a Pb-Sn eutectic liquid processed in microgravity are ideal systems in which to study the coarsening process. The microstructures of the 10% volume fraction solid samples processed on the ground shows extensive sedimentation and particle shape accommodation, see Figure 1. In contrast, an identical sample processed in microgravity displays nearly spherical, uniformly distributed, solid particles, see Figure 2. This result is of central importance as it indicates that performing experiments in space using the Pb-Sn system will enable us to produce the long-awaited data that can serve as a test of the theories of Ostwald ripening.

In addition to the Ostwald ripening experiments, we performed experiments to determine the temporal evolution of grain boundary grooves. These experiments provided a measurement of the entire thermophysical-parameter dependent portion of the coarsening rate constant, in particular, the product of the solid-liquid interfacial energy and the solute diffusion coefficient in the liquid. We find that to within the scatter of the data the grain boundary grooves develop at the same rate in microgravity as on the ground. Thus, we can conclude that the ground-based data originally taken by Hardy were not influenced by convection of the liquid.

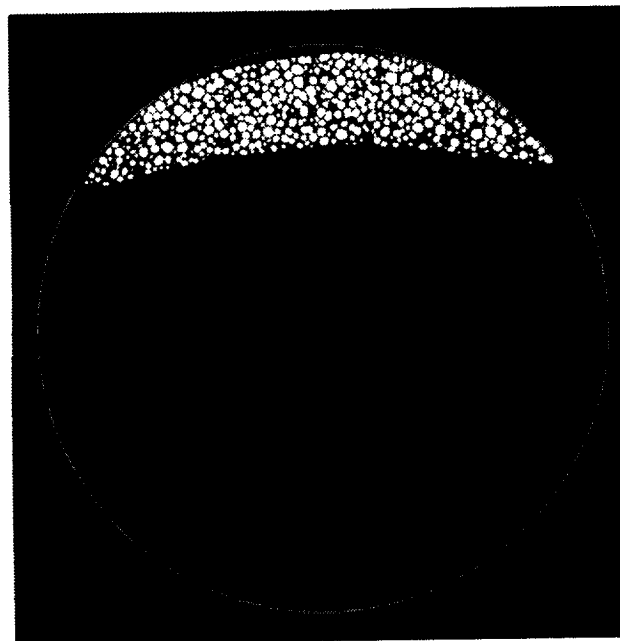


Figure 1. Microstructure of a ground-processed solid-liquid mixture after 36600s of coarsening. The particles are white and the matrix is black. The entire cross-section of a 1 cm diameter sample is shown.

The most successful series of experiments were those using samples with a 10% volume fraction of solid. This is quite fortunate as virtually all theories for Ostwald ripening make predictions at this volume fraction. For a more detailed description of the experiments see [2-4]. A summary of the results of the experiments using a 10% volume fraction of solid is given below:

- The experiments showed unambiguously for the first time that a system could coarsen via a transient Ostwald ripening process. This was detected by observing changes in the scaled particle size distribution, see Figure 3, and the radial distribution function during coarsening, see Figure 4.
- These experiments produced the first measurement of the radial distribution functions in a system with sufficiently low volume fraction that it can be compared to theory, see Figure 4. This result exceeded our expectations, as prior to flight we were concerned that the solidification process would disturb the spatial arrangement of the particles. It clearly does not on the length-scales sampled in the experiments.

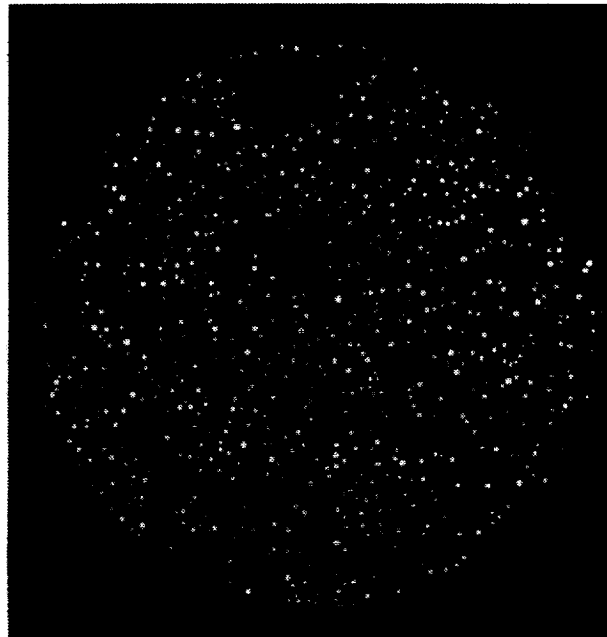


Figure 2. Microstructure of a space-processed solid-liquid mixture after 36600s of coarsening. The particles are white and the matrix is black. The entire cross-section of a 1cm diameter sample is shown.

- The absence of gravitationally induced sedimentation allows us to make measurements of the coarsening kinetics with unprecedented accuracy, far better than on the ground. The absence of sedimentation along with the large number of particles measured in the experiments allowed us to identify the presence of transient Ostwald ripening.
- The near-DC microgravity levels are sufficiently small that coarsening experiments for much longer times can be performed than were previously thought possible.
- The scaled particle size distributions are quite similar to those predicted by theories of transient coarsening, see Figure 3. These particle size distributions are, however, different from the steady state distributions, reinforcing our assertion that transient Ostwald ripening is present.
- The coarsening rate is slightly higher than that predicted by theory of transient Ostwald ripening.

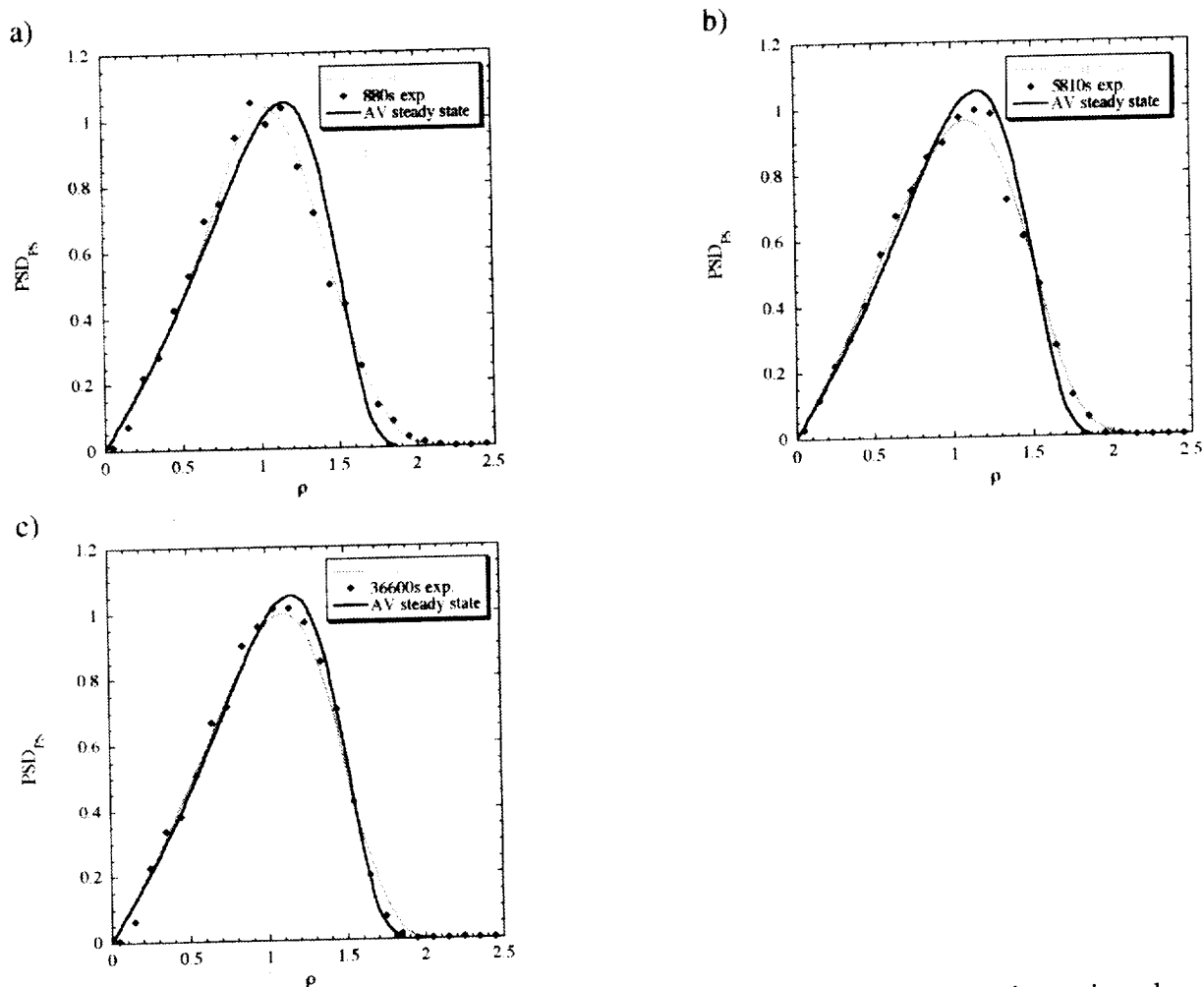


Figure 3: Experimentally measured and calculated particles size distributions using a time dependent theory for Ostwald ripening $\rho = R_{ps}(t)/\langle R \rangle_{ps}(t)$, where $R_{ps}(t)$ is the radius measured on a plane of section and $\langle R \rangle_{ps}(t)$ is the average particle radius measured on a plane of section for purposes of comparison a theoretically predicted steady state PSD also shown. a), b), and c) show the PSD's at 880s, 5810s, and 36600s respectively.

The analysis of samples with higher volume fractions shows that the rate constant increases with the volume fraction of solid. In addition similar transient coarsening has been observed in samples with volume fractions of 20% and 30%. We are continuing to analyze the high volume fraction samples. The major conclusion to be drawn from these experiments is that the steady state theories that are commonly used to analyze data are not applicable to this experiment. Since experimental artifacts easily mask such transient effects it is possible that previous experiments that report a disagreement with theory have been unknowingly performed in this regime.

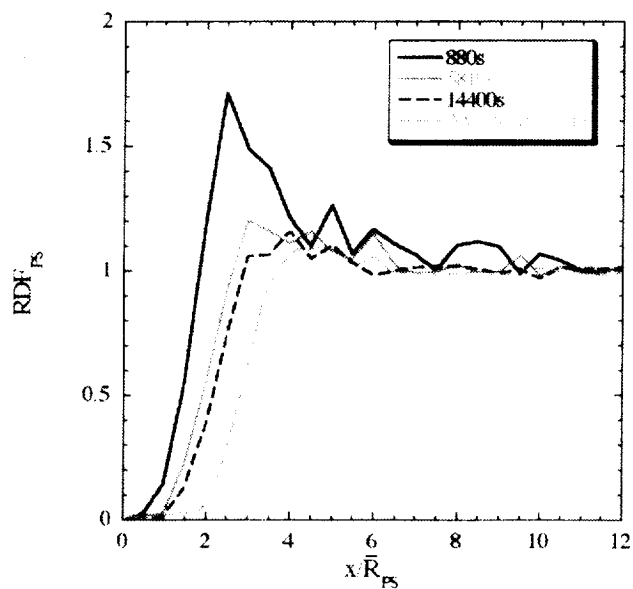


Figure 4. Radial distribution function (RDF) for four different coarsening times. The distance from a particle center is, x . The AV steady state RDF is the theoretical prediction for a steady state coarsening process.

REFERENCES

1. P.W. Voorhees, Ann. Rev. of Mat. Sci., **22**, 197, (1992).
2. J. Alkemper, V.A. Snyder, N. Akaiwa, and P.W. Voorhees, Phys. Rev. Lett. **82**, 2725 (1999).
3. V.A. Snyder, J. Alkemper and P.W. Voorhees, Acta. Mater. in press.
4. V.A. Snyder, N. Akaiwa, J. Alkemper and P.W. Voorhees, Metall. Trans. A, **30A**, 2341 (1999).

MODELLING THE EFFECTS OF MAGNETIC FIELDS IN CRYSTAL GROWTH

John S. Walker

Department of Mechanical and Industrial Engineering, University of Illinois at Urbana

During the last two years, we have developed a number of models to help optimize the benefits of applying steady or periodic magnetic fields during the bulk growth of semiconductor crystals on Earth or in microgravity.

I. Rotating Magnetic Field

A rotating magnetic field (RMF) is created by connecting the successive phases of a multiphase AC power source to inductors at equally spaced azimuthal positions around a crystal-growth furnace. The RMF has an essentially constant spatial pattern which rotates at a constant angular velocity around the centerline of the furnace. Recent experiments have indicated that an RMF with a magnetic flux density of 5-10 mT and a frequency of 50 or 60 Hz can lead to more uniform crystals. The body force produced by an RMF is three-dimensional and unsteady. Previous researchers averaged this body force over time. We presented the first calculations of the three-dimensional, unsteady melt motion driven by the entire body force¹. The results showed that the error in using the temporal average of the body force is indeed very small for the frequencies and field strengths being used in current experiments. Most experiments with RMF's have used frequencies of 50 or 60 Hz. While an RMF produces desirable mixing, it can also lead to undesirable hydrodynamic instabilities. There was a hypothesis that a high-frequency RMF, with the body force concentrated near the periphery of the melt, might yield the beneficial mixing without the deleterious instabilities. We investigated this hypothesis with modelling. First we developed an efficient method to determine the distributions of the magnetic field and electromagnetic body force for any frequency, including very high frequencies². Next we studied the melt motion driven by a high-frequency RMF³. The results showed that the flow pattern changes radically as the frequency is increased, leading to very strong flows confined to small parts of the melt. The model indicated that increasing the frequency reduces the desirable mixing, while increasing the undesirable instabilities, so that the 50 or 60 Hz currently in use is optimal for the current small experiments and lower frequencies will be optimal for future larger experiments.

II. Rotation with a Steady, Weak, Transverse Magnetic Field

An RMF produces radially inward flow near the crystal-melt interface. For many semiconductors, rejected dopant becomes concentrated near the centerline because the crystal-melt interface is concave into the crystal, and radially inward local flow increases this undesirable radial segregation. One way to produce an outward flow is to apply a steady, transverse magnetic field and to rotate the entire crystal-growth process about its centerline. There are two reasons why an RMF with a fixed process is different from a fixed magnetic field with a rotating process. First, creating a small azimuthal velocity in an otherwise quiescent melt with an RMF is different from

creating a small perturbation of a rigid body rotation with a steady, weak, transverse magnetic field, because in the latter case the flow is dominated by the Coriolis force due to the rigid-body rotation. Second, the RMF can rotate at 3000 rpm (50 Hz), while crystal-growth processes cannot be rotated at more than 20 to 30 rpm in practice. In order to obtain comparable mixing, the field strength of 0.005-0.01T for the RMF must be increased to approximately 0.1T for the rotating process. Both differences make it more difficult to achieve an axisymmetry flow, while deviations from axisymmetry produce undesirable rotational striations. In our first paper on the subject, we treated the melt motion in a rotating cylinder with a steady transverse magnetic field⁴. We showed that there are practical combinations of angular velocities and magnetic field strengths that produce essentially axisymmetric radially outward flows with velocities which are large enough to modify the radial distribution of dopants. In our second paper⁵, we treated the floating-zone process with thermocapillary and buoyant convection, with crystal and feed-rod rotation and with a steady transverse magnetic field. With only buoyant and thermocapillary convection, there is radially inward convection over an outer annulus of the crystal-melt interface. Rotation or the transverse magnetic field separately decrease the magnitude of this inward flow, but cannot stop or reverse it. The combination of rotation and a transverse magnetic field produce an axial variation of the centrifugal force due to the azimuthal motion which easily overwhelms the buoyant and thermocapillary convection and produces radially outward flow over the entire crystal-melt interface. For a typical system, rotation at 20 rpm with a field of 0.1T leads to a strong and axisymmetric radial velocity, and crystals grown under these conditions do indeed have much less radial segregation.

III. Thermoelectromagnetic Convection

During crystal growth, variations of the absolute thermoelectric power and of the temperature can drive a circulation of thermoelectric current through the melt and crystal. If a magnetic field is used to damp the buoyant, thermocapillary or solutal convection, the interaction of the thermoelectric current and the externally applied magnetic field produce an additional melt motion called a thermoelectromagnetic convection (TEMC). A number of experimental results for crystal growth with very strong magnetic fields have been tentatively attributed to TEMC. In addition, if a weak magnetic field is used to control convection or to stir the melt during crystal growth in microgravity, TEMC may be very important. We began with two studies of TEMC with strong axial magnetic fields, one for the Bridgman process⁶ and one for the floating-zone process⁷. These studies showed that for an axisymmetric flow with magnetic field strengths of 1 to 5T, the radial and axial velocities are several thousand times smaller than the azimuthal velocity, *i.e.*, 1-2 $\mu\text{m/s}$ versus 5-10 mm/s. Our next study focused on crystal growth in microgravity. Of the magnetic damping furnaces currently being considered for future experiments on the International Space Station, one furnace would have a steady magnetic field with a flux density of approximately 0.2T and another would have a magnetic field with a flux density of 5 mT which could be either steady or periodic, *i.e.*, an RMF. We treated TEMC in a cylindrical Bridgman ampoule with either a moderate or weak magnetic field, *i.e.*, either 0.2T or 5mT, respectively⁸. For a moderate magnetic field, the thermoelectric current is intrinsically coupled to the melt motion, which is thus a true magnetohydrodynamic flow. For a weak magnetic field, the thermoelectric current and electromagnetic body force are decoupled from the melt motion, which is an ordinary hydrodynamic flow driven by a known body force. The results showed that indeed TEMC may be very important for any crystal growth in microgravity with magnetic damping or stirring.

Until recently all studies of TEMC, including our own, assumed an axisymmetric temperature. However the experiments which produced the unexpected results tentatively attributed to TEMC involved deviations from axisymmetry in the heat flux into the melt⁹. We developed the first model of TEMC with a nonaxisymmetric temperature and with a strong axial magnetic field. The results reveal that for each azimuthal Fourier component of the melt motion except the axisymmetric one, the radial, axial and azimuthal velocities are all comparable and are directly proportional to the magnitude of the corresponding Fourier component of the temperature variation. As a result, if there is even a very small deviation from axisymmetric in the heat flux to the melt, the nonaxisymmetric radial and axial velocities may be many times larger than those in the axisymmetric flow. These results help explain the unexpected experimental results and support the previous hypothesis that they are due to TEMC.

IV. Transient Mass Transport with a Strong Magnetic Field

A primary purpose of controlling the melt motion with an externally applied magnetic field is to produce uniform distributions of dopants and species in the crystal. Recent experiments involving the vertical Bridgman process with a steady, five-tesla, axial magnetic field produced the first bulk-grown alloyed crystals with radially uniform distributions of species. However much more understanding of the mass transport of dopants and species is needed in order to optimize the benefits of a magnetic field. Magnetic damping reduces mixing so that the mass transport never reaches a quasi-steady state and remains intrinsically unsteady for the entire period of twelve hours to two weeks needed to grow a crystal. The many models which assume a quasi-steady state are therefore not appropriate and lead to erroneous predictions. All previous treatments of transient mass transport have involved the simultaneous time integration of the Navier-Stokes, internal-energy and mass-transport equations. With such an approach, a numerical code must be run on a massively parallel supercomputer for several hundred hours in order to simulate about 15 minutes of actual crystal growth. Clearly such an approach cannot be extended to the actual crystal-growth period of twelve hours to two weeks and certainly cannot be used to investigate many different magnetic field strengths and configurations in order to optimize the benefits of the magnetic field. Fortunately a far more practical approach yields accurate predictions of the transient mass transport for the entire crystal-growth period. While the mass transport is intrinsically transient and never reaches a quasi-steady state, both the melt motion and the temperature reach quasi-steady states in a few seconds with a strong magnetic field. Thus quasi-steady state solutions for the melt motion and temperature can be used in an unsteady treatment of the dopant and species transport. The key element is that inertial effects and convective heat transfer are negligible for strong magnetic fields. One paper¹⁰ was focused on defining the error associated with the neglect of inertial effects and convective heat transfer for each magnetic field strength. For a relatively large system with the buoyant convection due to terrestrial gravity, the error due to neglect of inertial effects and convective heat transfer is less than 4% for a magnetic flux density of 0.4T and this error decreases rapidly as the flux density is increased from this value. For the vertical Bridgman process with mercury-cadmium-telluride or germanium-silicon, the magnetic flux density for a 4% error is smaller. For the Bridgman process in microgravity, the required magnetic flux density scales as the square root of the residual acceleration.

We developed the method to use quasi-steady state solutions for the melt motion and temperature in a transient treatment of the dopant transport for the entire period to grow a crystal¹¹. We then applied this method to Bridgman growth in microgravity with a steady axial magnetic field¹².

Next we presented an extensive parameter study of dopant distributions in crystals grown on Earth by the vertical Bridgman process with different magnetic field strengths and at different growth rates¹³. This study revealed that the key parameter reflecting the effects of varying both the magnetic field strength and growth rate is the number of complete circuits completed by the buoyant convection during the entire period to grow the crystal. As the magnetic field strength or the growth rate is increased, this number decreases and the dopant distribution in the crystal approaches that for diffusion-controlled growth. As the magnetic field strength or the growth rate is decreased, this number increases and the dopant distribution in the crystal approaches that for the well-mixed limit.

V. Peltier Marking with Magnetic Damping

In the Peltier marking process, an electric current is passed axially through the crystal and melt for a very short period of time. This creates a band of higher or lower dopant concentration in the part of the crystal solidified during the current pulse, and this band reveals the instantaneous shape of the crystal-melt interface when the crystal is later cut and etched. If a strong, steady, axial magnetic field is used to control the buoyant convection, the radial redistribution of the Peltier current due to the curved crystal-melt interface interacts with the axial magnetic field to produce a strong melt motion during the brief period of the Peltier pulse. We developed a model for the melt motion due to Peltier marking with a magnetic field¹⁴. This model helps explain the dopant distributions in crystals grown by the vertical Bridgman process with a strong axial magnetic field and with Peltier marking. In addition this method can be used to produce a controlled amount of mixing at any time during crystal growth. Some microgravity experiments involve crystallizing and remelting the same sample under different conditions with *in situ* methods to measure the properties of each crystal before remelting. In these experiments it is often necessary to wait a long time after remelting in order to allow the dopant distribution in the melt to become uniform before growing the next crystal. A magnetic field and an electric current like the Peltier pulse can be used to mix the melt after each remelting, thus eliminating the long wait between experiments.

VI. Magnetic Stabilization of Thermocapillary Convection

While the floating-zone process has advantages over the Bridgman process, its biggest disadvantage is the striations produced by the periodic flow arising from the thermocapillary instability. A magnetic field can be used to stabilize the thermocapillary convection and eliminate the striations. We developed a model for the stabilization due to a strong magnetic field which is parallel to the free surface¹⁵. The results showed that the primary effect arises from the electric currents produced inside the thin Hartmann layers adjacent to the crystal-melt and feed-rod-melt interfaces. The results showed that the critical Marangoni number increases linearly with increasing Hartmann number, and this corrects the previous erroneous conclusion that it varies as the square of the Hartmann number which was based on a model which neglected the electric field.

REFERENCES

1. L. Martin Witkowski, J. S. Walker and P. Marty, "Nonaxisymmetric flow in a finite length cylinder with a rotating magnetic field," *Physics of Fluids*, 11, 1821-1826, 1999.

2. L. Martin Witkowski, P. Marty and J. S. Walker, "Multidomain analytical-numerical solution for a rotating magnetic field with a finite length conducting cylinder," *IEEE Transactions on Magnetics*, 36, 452-460, 2000.
3. L. Martin Witkowski, P. Marty and J. S. Walker, "Liquid metal flow in a finite length cylinder with a high frequency rotating magnetic field." To be published in *Journal of Fluid Mechanics*, 2000.
4. L. Martin Witkowski and J. S. Walker, "Liquid metal flow in a rotating cylinder with a weak transverse magnetic field." Submitted to *Physics of Fluids*, 2000.
5. N. Ma, J. S. Walker, A. Lüdge and H. Riemann, "Silicon floating zone process with a weak transverse magnetic field and crystal rotation." To be published in *Journal of the Electrochemical Society*, 2000.
6. Y. Y. Khine and J. S. Walker, "Thermoelectric magnetohydrodynamic effects during Bridgman semiconductor crystal growth with a uniform axial magnetic field," *Journal of Crystal Growth*, 183, 150-158, 1998.
7. Y. Y. Khine and J. S. Walker, "Thermoelectrically driven melt motion during floating zone crystal growth with an axial magnetic field," *Journal of Fluids Engineering*, 120, 839-843, 1998.
8. Y. Y. Khine, J. S. Walker and F. R. Szofran, "Thermoelectric magnetohydrodynamic flow during crystal growth with a moderate or weak magnetic field." To be published in *Journal of Crystal Growth*, 2000.
9. J. S. Walker, A. Cröll and F. R. Szofran, "Thermoelectromagnetic convection during floating zone crystal growth with a nonaxisymmetric temperature." Submitted to *Journal of Crystal Growth*.
10. N. Ma and J. S. Walker, "Inertia and thermal convection during crystal growth with a steady magnetic field." To be published in *Journal of Thermophysics and Heat Transfer*, 2000.
11. N. Ma and J. S. Walker, "A model of dopant transport during Bridgman crystal growth with magnetically damped buoyant convection," *Journal of Heat Transfer*, 122, 159-164, 2000.
12. N. Ma and J. S. Walker, "Segregation during Bridgman crystal growth in space with an axial magnetic field," *Magnetohydrodynamics*, 35, 155-159, 1999.
13. N. Ma and J. S. Walker, "A parametric study of segregation effects during vertical Bridgman crystal growth with an axial magnetic field," *Journal of Crystal Growth*, 208, 757-771, 2000.
14. C. C. Sellers, J. S. Walker, F. R. Szofran and S. Motakef, "Melt motion due to Peltier marking during Bridgman crystal growth with an axial magnetic field." To be published in *Flow, Turbulence and Combustion*, 2000.
15. T. E. Morthland and J. S. Walker, "Instabilities of dynamic thermocapillary liquid layers with magnetic fields," *Journal of Fluid Mechanics*, 382, 87-108, 1999.

PROCESS-PROPERTY-STRUCTURE RELATIONSHIPS IN COMPLEX OXIDE MELTS

Richard Weber and Paul Nordine

Containerless Research, Inc.
Evanston, IL 60201-3149
Phone: 847/467-2678; e-mail: weber@containerless.com

I. Introduction and Background

Investigation of process-property-structure relationships in high temperature liquids is essential to a scientific understanding of the liquid state and technological advances in liquid-phase processing. This research is concerned with the effects of processing variables on the behavior and properties of molten oxides. It uses containerless experimental methods to eliminate container-derived contamination, allow equilibration with controlled $p(O_2)$ atmospheres, and avoid heterogeneous nucleation by container walls to access highly non-equilibrium liquids.

Research during the first four years (June 1996-June 2000) included investigation of binary alumina-silica (Al_2O_3 - SiO_2), alumina-magnesia (Al_2O_3 - MgO), and alumina-yttria (Al_2O_3 - Y_2O_3) materials. The major emphasis of the research was on fragile undercooled alumina-yttria melts. These melts exhibit a highly non-Arrhenian viscosity vs temperature dependence [1], large heat capacity relative to the crystalline solid, and a polyamorphic phase transition. A separate Flight Definition project is in progress to perform microgravity experiments that determine the viscosity in this fragile liquid and the mechanism of polyamorphic phase transition. The research on alumina-magnesia melts has for the first time provided pure and homogeneous glass samples of the forsterite. This result is of special interest because forsterite is a member of the very abundant olivine family of minerals.

Accomplishments described in this report were to:

1. Investigate liquid-phase processing, undercooling, and solidification of binary alumina-silica, alumina-magnesia, and alumina-yttria materials under non equilibrium conditions.
2. Investigate the temperature dependence of the viscosity of deeply undercooled melts.
3. Measure the structure of YAG- and mullite- composition liquids.
4. Characterize processed materials using optical and scanning electron microscopy and X-ray diffraction analysis.
5. Develop collaborative research activities in the processing of oxide liquids and the characterization of novel products.
6. Publish and present results.

II. Experimental Methods

The compositions investigated were 40.0-90.0 mole% alumina with 10-60 mole% silica, 50-66 mole% magnesia with 33-50 mole% silica and 50-80 mole % alumina with 20-50 mole% yttria. Binary alumina-yttria materials with other rare earth oxides substituted for yttrium oxide were also investigated. Spheroidal specimens *ca.* 0.3 cm. in diameter were made by laser hearth melting of high purity oxide powders [2]. The specimens were levitated in an aero-acoustic or aerodynamic levitator in argon, oxygen or metered gas mixtures. Levitated specimens were heated with a cw CO₂ laser beam. Progress of the melting experiments was observed optically or with a video camera and the specimen temperature was measured using optical pyrometry. Temperature data were recorded at rates up to 100 Hz using LabView computer programs developed in the work.

III. Results

A. Liquid-Phase Processing Experiments

Alumina-silica: Containerless processing enabled glass formation from binary alumina-silica compositions containing up to 72 mole% aluminum oxide. Compositions close to that of mullite, Al₆Si₂O₁₃, readily formed glass at cooling rates of approximately 200 C/s.

Alumina-magnesia: Glasses were synthesized from several compositions containing from 50-66 mole% MgO including forsterite (Mg₂SiO₄) and enstatite (MgSiO₃). The critical cooling rate for glass formation from molten forsterite was on the order of 700 K/s under containerless conditions. Figure 1 shows representative cooling curves for Mg₂SiO₄ samples of different sizes processed under containerless conditions. This was the first successful synthesis of bulk forsterite glass, even splat quenching experiments which employed cooling rates on the order of 10⁶ K/s yielded only a few percent glass [3]. Forsterite is the Mg-rich end-member of the olivine family (iron-magnesium silicates) which is considered to be the most abundant mineral in the universe, and principal component of interstellar material [4]. The fact that glass formed relatively easily from this "island" silicate under containerless conditions suggests a mechanism by which such non-equilibrium phases can form in the "containerless environment" of outer space.

Measurements of the enthalpy of vitrification and crystallization behavior of the glasses are being performed by Dr. Jean Tangeman and Professor Alexandra Navrotsky at the Thermochemistry Facility at the University of California-Davis, preliminary evaluation of the data including NMR studies, shows that the forsterite glass has a relatively high enthalpy of vitrification and is composed of an expanded silicate structure.

Neutron diffraction measurements were completed on the glass by Dr. Chun Loong at Argonne National Laboratory. The diffraction data are being reduced to yield the radial distribution function, G(r), for the glass. Structural studies by synchrotron X-ray scattering have also been performed by Dr. Kentaro Suzuya at the SPRing 8 in Japan.

Alumina-yttria: Compositions centered around yttrium aluminum garnet (YAG, Y₃Al₅O₁₂) followed different solidification paths depending on the process conditions. Melts processed in oxygen undercooled by 800-900 C and spontaneously crystallized to form YAG, or undercooled

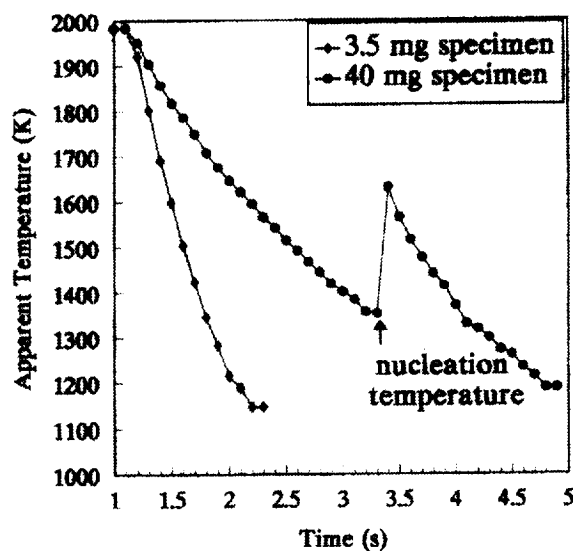


Figure 1. Cooling curves for liquid of the Mg_2SiO_4 composition. Specimens weighing *ca.* 40 mg, 0.3 cm diameter, nucleated crystals at a temperature of approximately 1350 K. Smaller specimens, on the order of 0.1 cm diameter, cooled to form glass.

by 600-650 C and spontaneously crystallized to form a mixture of yttrium aluminum perovskite (YAlO_3) and aluminum oxide. Crystallization of YAG was favored if the liquid was superheated by >200 C above the equilibrium melting point for several minutes. YAG-composition glasses contained two glassy phases with identical chemical composition, this is a manifestation of a polyamorphic liquid phase transition which has been proposed to occur in metastable liquids. Aasland and McMillan observed a similar transition in undercooled alumina-yttria binary material containing up to 24-32 molar % yttria. The current investigations have demonstrated an increased composition range for polyamorphism of 23-42 molar% yttria [5].

Conditions for formation of single and two-phase glasses formed from rare-earth oxide-alumina materials were established. Liquids formed from $\text{Y}_3\text{Al}_5\text{O}_{12}$ and $\text{Er}_3\text{Al}_5\text{O}_{12}$, and from $\text{Lu}_3\text{Al}_5\text{O}_{12}$ exhibit the liquid-liquid phase transition. The glasses have a cloudy appearance, due to the formation of spheroids of one glass phase in a matrix of a second glass phase.

Clear, brilliant, single phase glasses were obtained from $\text{La}_3\text{Al}_5\text{O}_{12}$, $\text{ErLaYAl}_5\text{O}_{12}$, LaAlO_3 , and YAG compositions containing 5 or more molar % La_2O_3 substituted for Y_2O_3 . Formation of two glasses is attributed to nucleation and growth of the second liquid at a temperature below the equilibrium liquid-liquid transition temperature. Addition of lanthanum depressed the phase transition temperature and/or the nucleation temperature below the glass transition temperature so that the liquid-liquid phase transition was not observed. The results were analyzed in the context of first order liquid-liquid phase transitions and the enhancement of single phase glass formation in melts that contain a high proportion of 4-coordinate aluminum ions [5].

The aluminate glasses were characterized by hardness and spectral transmission measurements. The materials have a Vickers hardness in the range 700-900. The spectral transmission extends to wavelengths *ca.* 5 μm .

Glass formation from liquids containing La^{3+} cations partially or completely substituted for Y^{3+} in the $\text{Ln}_3\text{Al}_5\text{O}_{12}$ composition was investigated. Substitution of La greatly enhanced glass formation. Based on the structural measurements on pure $\text{Y}_3\text{Al}_5\text{O}_{12}$ material described later in this report, we hypothesize that the larger cation stabilizes four-fold coordination of aluminum in the liquid which tends to result in longer range order and easier glass formation.

B. Investigation of Melt Viscosity

Formation of glass demonstrates that the viscosity of the melt increases significantly when it is undercooled. This observation prompted experiments to pull fibers from the undercooled melt at intermediate temperatures [1]. The fiber pulling experiments provide an indirect measure of the viscosity of the undercooled melt. This technique has been applied to study the viscosity of various molten aluminates over a wide range of temperatures. The results confirm that undercooled molten YAG is an extremely fragile liquid [6] with the onset of increased viscosity occurs at a temperature *ca.* 600 C below the melting point.

Similar measurements on materials containing lanthanum substitute for yttrium suggest that these lanthanum-bearing materials form significantly “stronger” liquids which are relatively good glass formers. Fiber pulling is supported over a wider range of temperature from the La-substituted materials. Conversely, substitution of erbium for yttrium makes the liquid more fragile.

C. Liquid Structure

$\text{Y}_3\text{Al}_5\text{O}_{12}$: The total structure factor, $S(Q)$, and radial distribution function, $G(r)$, of liquid $\text{Y}_3\text{Al}_5\text{O}_{12}$ (YAG) were determined over the temperature range from 1770-2230 K by synchrotron X-ray scattering from samples held under containerless conditions in argon and oxygen atmospheres [7]. The $S(Q)$ shows two peaks at 2.18 \AA^{-1} and 4.0 \AA^{-1} , indicative of chemical and topological short-range order, respectively. Nominal coordination numbers were 4 for Al^{3+} and 6 for Y^{3+} ions. The $G(r)$ has peaks at $r \text{ 1.8 \AA}$ for Al-O, $r \text{ 2.25 \AA}$ for Y-O, and $r \text{ 3.3-3.6 \AA}$ assigned to metal ions in adjacent AlO_4^{5-} and YO_6^{9-} polyhedral ions that are joined by shared O^{2-} ions. Relative to pure aluminum and yttrium oxides, $G(r)$ for molten YAG has smaller half-widths for the Al-O and Y-O peaks, and an increased sensitivity to temperature and the ambient gas composition. Results are shown in Figure 2.

The results support the idea that tetrahedral coordination of Al^{3+} is preserved even in the deeply undercooled liquid in oxygen atmospheres. In argon, the Al^{3+} coordination increases when the liquid is undercooled, tending towards octahedral. The results are consistent with reported density and viscosity data for liquid $\text{Y}_3\text{Al}_5\text{O}_{12}$.

$\text{Al}_6\text{Si}_2\text{O}_{13}$: The structure factor, $S(Q)$, and the pair distribution function, $G(r)$, of $\text{Al}_6\text{Si}_2\text{O}_{13}$ (3:2 mullite) was measured in the normal and supercooled liquid states in the temperature range 1776-2203K [8]. Measurements were obtained by synchrotron X-ray scattering on levitated, laser beam heated liquid specimens.

The $S(Q)$ shows a pre-peak at 2.0 \AA^{-1} followed by a main peak at 4.5 \AA^{-1} and a weak feature at 8 \AA^{-1} . The $G(r)$ shows a strong (Si,Al)-O correlation at 1.80 \AA at high temperature which moves to 1.72 \AA as the liquid is supercooled. The second and third nearest neighbor peaks at 3.0 and

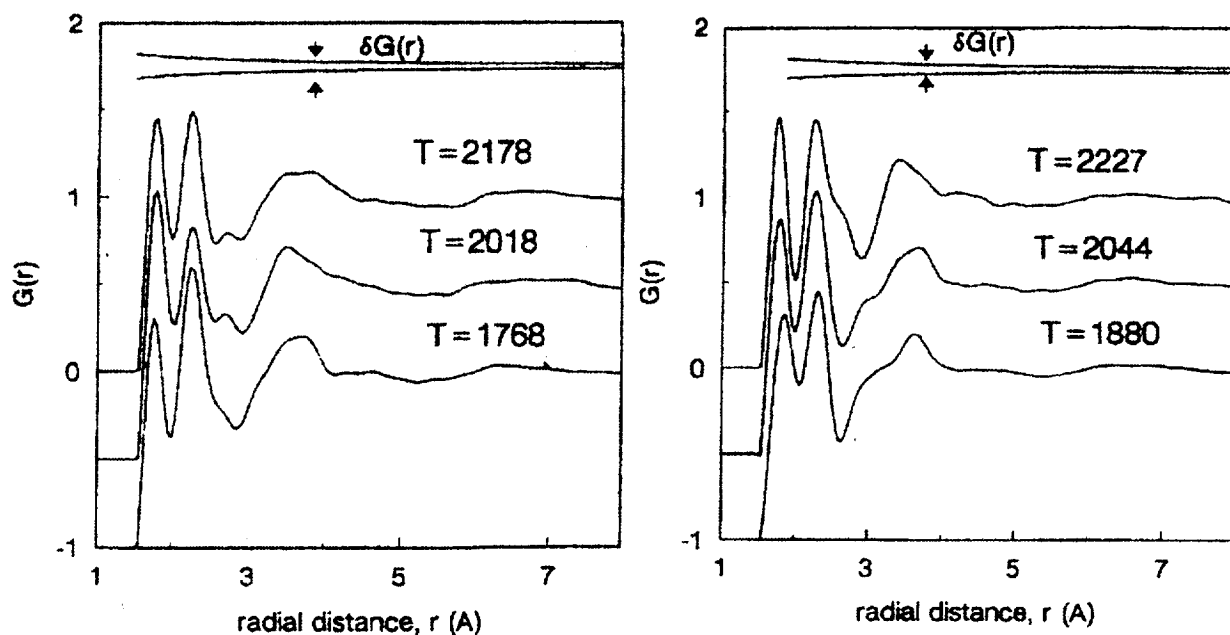


Figure 2. Radial distribution function for undercooled molten $\text{Y}_3\text{Al}_5\text{O}_{12}$ processed in oxygen (left) and argon (right), error bar is shown inset at the top of the figure. From reference 7.

4.25 Å sharpen with supercooling. The short-range structure of the high temperature liquid is similar to that of the corresponding glasses produced by rapid quenching.

D. Characterization of Processed Material

Processed materials were examined by a variety of analytical techniques. Scanning and optical microscopy were used to investigate the morphology of bulk specimens after processing. X-ray diffraction analysis was used to determine the lattice parameters and identify crystalline phases. The SEM experiments were performed at NASA MSFC by Dr. Greg Jerman.

E. Collaborative Research

This project has permitted collaborative research on the processing and properties of oxide materials with scientists at Argonne National Laboratory, Arizona State University, Marshall Space Flight Center, Northwestern University, University of California-Davis and the University of Illinois Urbana-Champaign.

Specialized materials characterization facilities at the collaborating institutions have been used in the analysis and measurements of materials properties. The results help to guide the research and the development of new applied materials in independently supported work. The project has supported work at CRI by three undergraduate students in Northwestern University's Cooperative Science and Engineering Program.

F. Publication and Presentation of Results

Results were prepared for submission to peer reviewed journals and presented at international conferences, workshops, and seminars. CRI has filed a patent application on the new single phase glass materials.

III. Plans

The project was completed in May, 2000. Further work in this area will continue in a follow on project. The new work will investigate effects of anion substitution in the melts by substituting nitrogen for oxygen in the materials. The new work will include experiments to levitate molten materials at elevated pressure in controlled atmospheres.

REFERENCES

1. J.K.R. Weber, J.J. Felten, B. Cho and P.C. Nordine, "Glass Fibers of Pure and Erbium or Neodymium-Doped Yttria-Alumina Compositions," *Nature*, accepted April, 1998.
2. J.K.R. Weber, J.J. Felten and P.C. Nordine, "New Method for High Purity Ceramic Synthesis," *Rev. Sci. Instrum.*, 67, 522-24 (1996).
3. Q. Williams, P.F. McMillan and T.F. Cooney, "Vibrational Spectra of Olivine Composition Glasses: The Mg-Mn Join," *Phys. Chem. Miner.*, 16, 352-59 (1989).
4. P. Richet, "Melting of Forsterite and Spinel with Implications for the Glass Transition of Mg_2SiO_4 Liquid," *Geophys. Res. Lett.*, 20, 1675-78 (1993).
5. J.K.R. Weber, A.D. Hixson, J.G. Abadie, P.C. Nordine and G.A. Jerman, "Liquid-liquid Phase Transition and Polyamorphism in Undercooled Rare Earth-Alumina Compositions," *J. Am. Ceram. Soc.*, in press.
6. C.A. Angell, "Formation of Glasses from Liquids and Biopolymers," *Science*, 267, 1924-35 (1995).
7. J.K.R. Weber, S. Krishnan, S. Ansell, A.D. Hixson and P.C. Nordine, "Structure of Liquid $\text{Y}_3\text{Al}_5\text{O}_{12}$ (YAG)," *Phys. Rev. Lett.*, 84, 3622-66, (2000).
8. S. Krishnan, J.K.R. Weber, S. Ansell, A.D. Hixson and P.C. Nordine, "The Structure of Liquid Mullite (60% Al_2O_3 -40% SiO_2)," *J. Am. Ceram. Soc.*, in press.

MICROGRAVITY STUDIES OF LIQUID-LIQUID PHASE TRANSITIONS IN UNDERCOOLED ALUMINA-YTTRIA MELTS

Richard Weber and Paul Nordine

Containerless Research, Inc.
Evanston, IL 60201-3149

Phone: 847/467-2678; e-mail: weber@containerless.com

I. Introduction and Background

Experimental investigations of undercooled rare earth aluminate liquids have revealed scientifically and technologically interesting properties. These liquids can be deeply undercooled under containerless conditions. The liquids are highly fragile, evidenced by highly non-Arrhenian viscosity vs temperature [1] and a large heat capacity relative to the crystalline solids. A liquid-liquid phase transition has been demonstrated over a wide range of chemical compositions [2,3] and it has been demonstrated that this polyamorphism is suppressed if the liquid contains small amounts of the larger rare earth ions such as La^{3+} and Nd^{3+} . It has also been demonstrated that the ambient oxygen partial pressure has a significant influence on the behavior of undercooled aluminate liquids, and on the liquid structure.

Bulk glass can be formed at the cooling rates achieved in containerless experiments and glass fibers can be pulled from the viscous undercooled melts. These glass materials have photonic applications based on the lasing properties of rare earth ions. Crystalline materials formed from the liquid or by crystallization of the glass materials have potential high temperature structural applications based on their highly refractory, oxidation resistant, and creep properties.

The goal of this investigation is to perform microgravity experiments to (i) determine the mechanism of the polyamorphic phase transition, and (ii) obtain highly accurate viscosity versus temperature results to characterize the fragile liquid behavior. The approach is to (i) determine the kinetics of the liquid-liquid phase transition and (ii) measure viscosities over a wide range of temperatures using the oscillating drop technique in the low viscosity (under-damped) regime and drop relaxation measurements in the higher viscosity (over-damped) regime. The prototype material composition is $\text{Y}_3\text{Al}_5\text{O}_{12}$, with potential variations in Y:Al and rare-earth dopants that extend the temperature range in which polyamorphism can be observed, or avoided in the viscosity measurements. Control of the oxygen activities in the liquid is required.

The microgravity investigation is motivated by the facts that containerless conditions are required in the research and the phase transition kinetics cannot be accurately measured in earth-based experiments. Levitator-induced fluid motion, convection, stirring, and gravity-induced sedimentation mixes the two liquids, masks progress of the phase transition, and prevents control of the dissolved oxygen activity when the sample temperatures are changed. The experiments are

designed to exploit the high degree of mechanical, thermal, and chemical quiescence that can be achieved under microgravity conditions.

II. Ground-Based Experiments

Ground-based research using aero-acoustic [4] and aerodynamic levitation [5] techniques at CRI and electrostatic levitation [6] at NASA's Marshall Space Flight Center are being used to define requirements for the flight experiments. The containerless methods are being used in conjunction with CO₂ laser beam heating. Some results of the ground-based experiments are briefly discussed in the following sections.

Polyamorphic phase transition [2] in undercooled liquid YAG, under the rapid cooling conditions required to form glass, results in spheroids of one glass in a matrix of a second glass. Figure 1 presents optical and atomic contrast backscattered electron images (BEI) of sectioned and polished specimens. The images were obtained using an accelerating voltage of 15 kV.

Electron microprobe analyses were performed at ten points in the matrix, the lighter spheroids, and the darker spheroids revealed in the BEI images. Results of the analyses for a YAG-composition sample are summarized in Table I. The mean composition values and standard deviations of the mean values (SD) are given in the table. Each datum is the average of 10 measurements. The compositions of all phases are identical within the measurement errors.

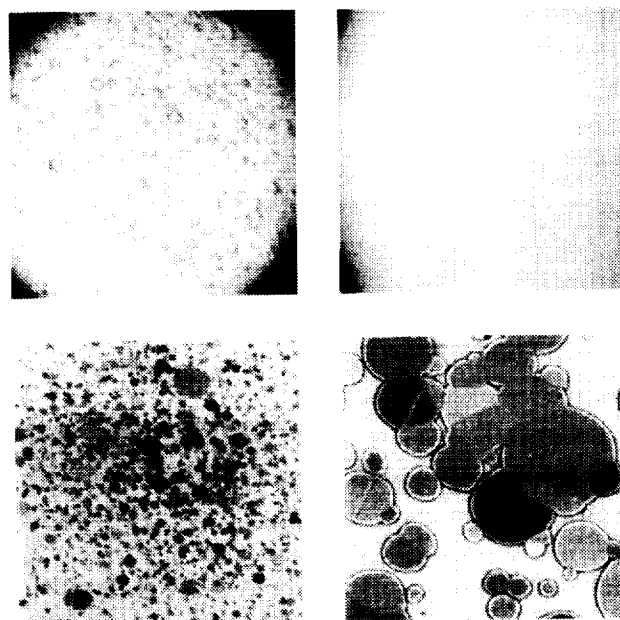


Figure 1. Top left - optical image of a polished section of a two phase Y₃Al₅O₁₂-composition glass. Top right - optical image of a polished section of a single phase La₃Al₅O₁₂-composition glass. Bottom left - low magnification BEI of a two phase Y₃Al₅O₁₂-composition glass. Bottom right - high magnification BEI of a two phase Y₃Al₅O₁₂-composition glass showing regions where the transformed liquid drops have coalesced.

Table I. Results of electron microprobe analysis of $Y_3Al_5O_{12}$ -composition glass material

Area of Specimen	O (At%)	SD	Al (At%)	SD	Y (At%)	SD
Matrix	58.91	0.12	26.34	0.08	14.75	0.09
Light spheroids	58.70	0.10	26.45	0.06	14.86	0.05
Dark spheroids	58.61	0.09	26.55	0.06	14.84	0.09

A. Effects of Ambient Oxygen Pressure

There is increasing evidence that the ambient oxygen partial pressure has a major influence on the behavior of aluminate melts. Pure liquid aluminum oxide exhibits a change in the spectral absorption coefficient with the ambient oxygen pressure and a minimum value at a $p(O_2)$ value *ca.* 5×10^{-5} atm. [7]. In undercooled liquid YAG, the Al^{3+} ions are primarily 4-fold coordination in oxygen and tend towards 6-fold coordination in UHP argon [8]. We have also observed that glass formation occurs more easily in oxygen than in argon. These results suggest that the liquid can more easily develop the extended range ordering associated with increased viscosity when the aluminum is in 4-fold coordination. Control of oxygen pressure in equilibrium with the melt may thus be used to modify melt properties and perhaps to control the liquid-liquid phase transition in molten aluminates.

B. Effects of Composition

Glass formation occurs from rapidly cooled yttria-alumina liquids under containerless conditions for compositions containing from 23 to 42 molar% yttrium oxide [2]. Outside this range, the maximum cooling rates investigated, on the order of 400 K/s were insufficient to suppress crystallization. All of the glasses in this range of composition show evidence the polyamorphic phase transition. The amount of second phase formed increased with increasing yttrium concentration.

The amount of the second glass phase also changes if other rare earth ions are substituted for yttrium. For example, glasses containing erbium and lutetium are difficult to synthesize and yield about 25% of the second phase. Substitution of lanthanum for yttrium suppresses the phase transition and decreases the critical cooling rate for glass formation. Figure 2 shows examples of four glasses formed under containerless conditions. The cooling rates required to form glass decreased with increasing lanthanum content in the glass materials.

Substitution of lanthanum leads to single phase glass either by making the second liquid unstable relative to the first, or by reducing the phase transition or nucleation temperature for the second liquid below the glass transition temperature. The effects of lanthanum substitution for yttrium have been attributed [2] to a decrease in 6-fold and increase in 4-fold coordination of Al^{3+} when the rare earth ion coordination is increased by substitution of a larger rare-earth ion for yttrium.

C. Temperature Range for Liquid-Liquid Transition

Results obtained in containerless experiments [2,9,10] show that the undercooled liquid with the YAG composition can be undercooled to a temperature of 1300 K before spontaneous nucleation

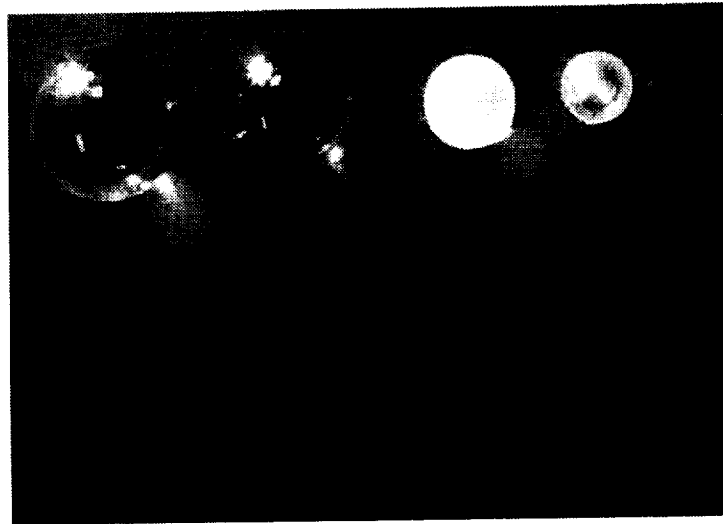


Figure 2. Photograph of (left to right); $\text{La}_3\text{Al}_5\text{O}_{12}$, $\text{ErLaYAl}_5\text{O}_{12}$, $\text{Y}_3\text{Al}_5\text{O}_{12}$, and $\text{Er}_3\text{Al}_5\text{O}_{12}$ composition glasses. The $\text{Er}_3\text{Al}_5\text{O}_{12}$ and $\text{Y}_3\text{Al}_5\text{O}_{12}$ glasses have a cloudy appearance due to formation of two glass phases. The $\text{ErLaYAl}_5\text{O}_{12}$ and $\text{La}_3\text{Al}_5\text{O}_{12}$ composition glasses are clear and transparent.

of crystalline YAG occurs. Experiments to hold the undercooled liquid in the temperature range above the nucleation temperature of crystals but below the nucleation temperature of the second phase are ongoing. Temperature gradients in the liquid have so far prevented extended duration experiments with the liquid in the "transition temperature" range.

Figure 3 shows our current estimate of the Time-Temperature-Transformation diagram for the YAG composition. The lower part of the TTT curve is based on DTA measurements of the crystallization kinetics of glass samples [11]. The upper section is estimated from the temperature measurements in slow cooling experiments that led to crystallization. The cooling curve shown to be tangent to the nose of the TTT curve is from undercooling experiments at cooling rates just sufficient to avoid crystallization. The shaded area of the figure is the region in which the polyamorphic phase transition is possible. Its upper limit is estimated from Aasland and McMillan [3] and the lower limit is the glass transition temperature observed for La-substituted YAG [12].

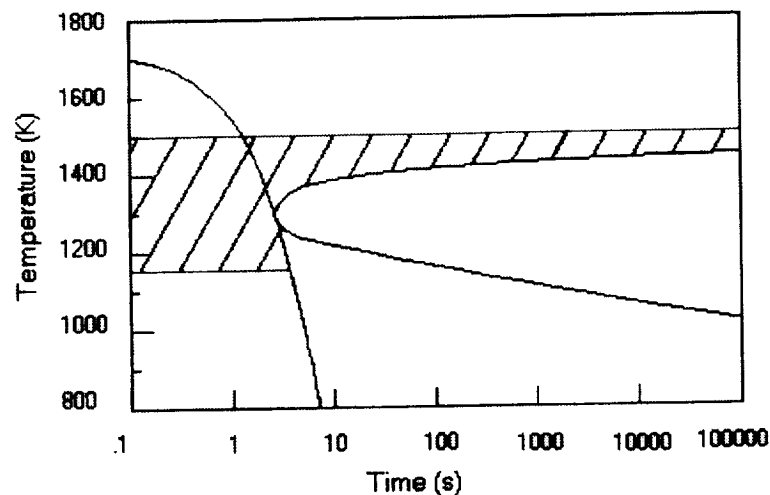


Figure 3. Time-Temperature-Transformation diagram for the YAG composition. The shaded area of the figure is the region in which the polyamorphic phase transition is possible.

Work is in progress to extend these measurements to additional compositions in the yttria-alumina system and to rare earth-doped yttria-alumina compositions. Compositions and experimental temperature ranges for the flight experiments to study phase transition kinetics will be specified.

II. Microgravity Experimental Protocol

Consider a drop of molten $Y_3Al_5O_{12}$ under mechanically, thermally, and chemically “quiescent” containerless conditions. This means that the liquid can be deeply undercooled without nucleation by container walls, is not stirred, and has uniform temperature and composition. The specimen temperature can be changed rapidly compared to the time required for diffusion-limited equilibration with the atmosphere because the thermal diffusivity is much greater than the diffusivity of oxygen. Thus, chemical quiescence can be maintained in the bulk liquid when the temperature is changed to investigate the undercooled melt. This would not be possible in a stirred sample. The experimental protocol envisioned for kinetic studies is:

1. Prepare the quiescent liquid drop by levitating a solid sample, melting it, equilibrating the liquid at a temperature above the melting point. Stirring may be used to accelerate the equilibration process but will then be stopped to achieve mechanical quiescence.
2. Reduce the liquid temperature to a value at which the phase transition is expected to occur (1300-1675 K). A period of 10-20 seconds will be required to achieve uniform temperature after the heating power is changed.
3. Hold the specimen at the selected temperature to allow partial transition of the liquid to occur. Cool and recover the specimen for later microstructural analysis.
4. Repeat the above procedure using different hold times and temperatures in the undercooled state.

The melt viscosity will be determined from measurements of liquid drop oscillation and deformation. Accurate viscosity data can be obtained on the undercooled liquid using the oscillating drop method [13], when the viscosity value is less than a few Poise. At higher viscosity values, where the liquid is no longer freely oscillating (overdamped), measurements of the relaxation of a deformed viscous drop may be used [14]. The deformed viscous liquid drop relaxes to a sphere when the shaping force is turned off. Changes in the rotation rate of the levitated liquid may be used to deform and allow relaxation of the liquid shape.

III. Science Concept Review

The Science Concept Review was held at NASA MSFC on 28 March, 2000. The review panel members were: Professor Michael Weinberg (Chair), Dr. Roger Araujo, Professor Himanshu Jain, and Dr. Michael DiGiuseppe. CRI scientists present were Dr. Richard Weber, PI, Dr. Paul Nordine, CoPI, Mr. Johan Abadie and Mr. Thomas Key. The presentation was made by Dr. Weber. The NASA Project Scientist, Dr. Mike Robinson presented information about hardware requirements.

The panel provided a summary oral debriefing at the conclusion of the SCR meeting. The panel considered that the project is of high scientific and technological importance and should be given a high priority. The precise requirements for microgravity were discussed in some detail. A key

issue raised by the panel was the need to more precisely define the temperature at which the polyamorphic liquid phase transition occurs. This will be investigated in the ground-based ESL experiments at NASA MSFC. The panel also recommended that two-phase glasses made from compositions with different rare earth oxide to aluminum oxide ratios be investigated.

IV. Publication and Presentation of Results

Results were prepared for submission to peer reviewed journals and presented at international conferences, workshops, and seminars. Additional publications are in preparation.

V. Plans

Research to obtain data on the viscosity of melts formed from alumina-yttria binaries and to establish the nature of the onset of increased viscosity in the undercooled liquids is continuing. The chemical effects resulting from changes in ambient $p(\text{O}_2)$ and melt chemistry are being investigated in ground-based experiments. Work is continuing towards the Requirements Definition Review phase of the project in which precise experimental conditions and hardware performance requirements will be defined.

REFERENCES

1. J.K.R. Weber, J.J.Felten, B. Cho and P.C. Nordine, "Glass Fibers of Pure and Erbium or Neodymium-doped Ytria-alumina Compositions," *Nature*, 393, 769-71 (1998).
2. J.K.R. Weber, J. Abadie, A.D. Hixson, P.C. Nordine and G.A. Jerman, "Liquid-liquid Phase Transition in Undercooled Rare Earth-Alumina Compositions," *J. Am. Ceram. Soc.*, in press.
3. S. Aasland and P.F. McMillan, "Density-driven Liquid-liquid Phase Separation in the Al_2O_3 - Y_2O_3 System," *Nature*, 369, 633 (1994).
4. J.K.R. Weber, D.S. Hampton, D.R. Merkley, C.A. Rey, M.M. Zatarski and P.C. Nordine, "Aero-acoustic Levitation - A Method for Containerless Liquid-phase Processing at High Temperatures," *Rev. Sci. Instrum.*, 65, 456-465 (1994).
5. J.K.R. Weber and P.C. Nordine, "Containerless Liquid-Phase Processing at High temperatures," *Microgravity Sci. and Tech.*, VII, 279-282 (1995).
6. W-K. Rhim, "Materials Processing by High Temperature Electrostatic Levitation," *Microgravity Sci. and Tech.*, VIII, 46-51 (1995).
7. J.K.R. Weber, S. Krishnan and P.C. Nordine, "Effects of Melt Chemistry on the Spectral Absorption Coefficient of Liquid Aluminum Oxide," *J. Am. Ceram. Soc.* 78, 3067-3071 (1995).
8. J.K.R. Weber, S. Krishnan, S. Ansell, A.D. Hixson and P.C. Nordine, "Structure of Liquid $\text{Y}_3\text{Al}_5\text{O}_{12}$ (YAG)," *Phys. Rev. Lett.*, 84, 3622-66, 2000.
9. P.C. Nordine, J.K.R. Weber and J.G. Abadie, "Properties of High Temperature Melts Using Levitation," 10th IUPAC International Conference on High Temperature Materials Chemistry, Julich, Germany 10-14 April, 2000, *Schriften des Forschungszentrums, Julich*.
10. J.K.R. Weber, P.C. Nordine, J.G. Abadie, T.S. Key and A.D. Hixson, "Investigation of Metastable Liquid Oxides in Microgravity," *Proc. Spacebound 2000*, May 14-18, 2000, Vancouver, in press.
11. B.R. Johnson, University of Illinois Urbana-Champaign, Private communication.
12. C.S. Ray, University of Missouri-Rolla, Private communication.

13. G. Trapaga, D.M. Matson, R.W. Hyers and M.C. Flemings, "Mathematical Modeling of Electromagnetically Levitated Metallic Melts," in Observation of Solidification Phenomena, Proc. J. Szekely Memorial Symp., TMS, Cambridge, MA, October 1997.
14. J-C. Barbé, C. Payayre, M. Daniel, M. Papoular and N. Kernevez, "High Temperature Containerless Viscosity Measurement by Gas Film Levitation," Int. J. Thermophys., 20, 1071-83 (1999).

PHASE SEPARATION AND SELF-ASSEMBLY OF LIQUID CRYSTALS AND POLYMER DISPERSIONS: A GROUND-BASED FEASIBILITY STUDY FOR MICROGRAVITY

J.B. Whitehead, Jr.^{1*} and G.P. Crawford²

¹University of Southern Mississippi

²Brown University

Polymer dispersed liquid crystals (PDLC) provide a unique opportunity to systematically study phase separation and microstructure development in terrestrial and microgravity environments. The microstructure or morphology of PDLC materials depends on concentration, viscosity, curing temperature, mechanism of phase separation, sample thickness, and gravitational effects. PDLC materials are fabricated using Polymerization Induced Phase Separation (PIPS), Solvent Induced Phase Separation (SIPS), and Thermally Induced Phase Separation (TIPS). Polymer dispersed liquid crystals, sometimes known as liquid crystal and polymer dispersions, are promising new materials for anti-reflective coatings, omni-directional reflectors, electrically switchable Bragg gratings, spatial light modulators, optical interconnects, optical data storage, dynamically variable lenses, and high intensity laser radiation attenuators. The microstructure of PDLC materials range from liquid crystal droplets dispersed in solid polymer matrix, commonly known as the "Swiss cheese" morphology, to alternating liquid crystal droplet and polymer planes, and to a polymeric membrane suspended in the liquid crystal solvent.

We propose a systematic study of polymerization induced phase separation of liquid crystal and polymer dispersions to elucidate the relationship between the process control parameters and the resultant PDLC morphology in the terrestrial environment, and to facilitate the design of a future reduced gravity investigation. The knowledge gained during the ground-based study is immediately applicable to enhancing the properties of current PDLCs. The ground-based study will include: 1) the development of phase diagrams for liquid crystal/prepolymer and/or monomer mixtures, 2) characterization of PDLC microstructure using thermal analysis, optical microscopy, scanning electron microscopy, and electro-optic measurements, and 3) real-time characterization of PDLC microstructure evolution using laser light scattering. The results of the ground-based studies will determine the design of the reduced gravity flight activities. The goal of the project is an enhanced understanding of phase separation processes. The results are applicable to the production of benchmark PDLCs and to the understanding of fluid flow in complex fluids under varying gravitational conditions.

RESIDUAL GAS EFFECTS ON DETACHED SOLIDIFICATION IN MICROGRAVITY

Liya L. Regel and William R. Wilcox

Clarkson University, Potsdam, NY 13699-5814

Detached solidification has been observed in many microgravity experiments [1]. When it occurred, the perfection of the resulting crystals was greatly increased, making them much more useful for electronic and opto-electronic devices. Although detachment has been common, it has also been non-reproducible and erratic, for unknown reasons. Our long term goal is to make it reproducible, which requires a full understanding of the mechanisms underlying it.

Detached solidification was first observed in Skylab experiments about 25 years ago. Our 1995 Moving Meniscus Model [2](Figure 1) provided the first real understanding of the mechanism. Residual gases play a major role in this model, dissolving in the melt at the vapor end of the ampoule, and being expelled across a meniscus into the gap between the growing solid and the ampoule wall. Modeling has shown that detachment is favored by a high dissolved gas concentration, high contact angle of the melt on the ampoule wall, high growth angle, and low melt-vapor surface tension [3-6]. However, many uncertainties remain in the model, primarily because the solubility of these gases in the melt and their influence on its properties are unknown. The objective of the research proposed here is to measure those properties which are most important to the detachment mechanism and with the most uncertainty in their values. Of most interest is the role of oxygen in detached solidification. Over the years it has been proposed that oxygen forms an oxide film, increases the contact angle of the melt on the ampoule wall, and avoids compositional inhomogeneities by stopping Marangoni convection arising from temperature and composition gradients along the meniscus. Thus far, these are only speculative.

Numerous experiments with liquid metals on oxide surfaces show, however, that dissolved oxygen always lowers the contact angle [e.g.,7-9] for liquid metals. (And most molten semiconductors have metallic properties.) This behavior can be understood by examining the terms in the Young equation (without debating the merits or validity of this classical relationship):

$$\cos\theta = \frac{\sigma_{vs} - \sigma_{ls}}{\sigma_{lv}}$$

The surface energy σ_{vs} between the vapor and the oxide solid should be relatively unaffected by the presence of trace amounts of oxygen. The surface tension σ_{lv} between liquid and vapor is lowered by oxygen adsorption on this surface, in accordance with the Gibbs relationship. (For example, the surface tension σ_{lv} of molten silicon shows a dramatic decrease in surface tension with increasing oxygen activity up to the solubility of SiO_2 , beyond which it increases slightly [10-13].) The solid-liquid surface tension σ_{ls} tends to be strongly lowered by oxygen in a metal melt, due to chemical interactions with the solid [7]. One mechanism involves formation of O^{2-}

and positive metal ions that are attracted to the negatively charged oxygen atoms at the oxide surface. In some cases, a new oxide phase forms at the interface. Thus, both σ_{lv} and σ_{ls} are decreased, thereby increasing $\cos\theta$ and so decreasing the contact angle θ .

Another role sometimes attributed to oxygen in detached solidification is the suppression of convection driven by surface tension gradients along the meniscus. Although we have shown [3] that such Marangoni convection has little effect on the transport of gas into the gap, it would be expected to perturb the distribution of impurity dopant in the resulting crystals. Oxygen adsorption on the meniscus could explain why some crystals solidified with detachment exhibited no such perturbations while others did [1].

We note that only a few measurements have been made for the contact angle of semiconductor materials [14-22]. These measurements were all made using the sessile drop method in sealed ampoules placed in high-temperature tube furnaces. There were no attempts made to measure O_2 concentration or contact angle hysteresis. Likewise, we found no references to measurements of contact angles versus the rate of movement of a contact line in either liquid metals or semiconductors.

We plan to measure the following properties of residual gases in molten semiconductors, with initial emphasis on oxygen in indium antimonide:

1. Solubility of the gas in the melt versus pressure and the temperature.
2. Interfacial reaction kinetics between species in the gas phase and in the melt, *e.g.* $O^=$ in the melt and O_2 in the gas.
3. Surface tension of the melt versus gas pressure.
4. Contact angle and contact angle hysteresis of the melt on the ampoule wall.

For experiments with oxygen, a special cell will be constructed with a zirconia oxygen sensor/pump (Figure 2). To measure solubility and interfacial reaction kinetics, the molten semiconductor will be placed in a small cup. The rate of change of oxygen pressure will be monitored after pumping oxygen in or out of the cell.

Surface tension and contact angle will be determined by the sessile drop technique, on surfaces typically used for ampoules, *i.e.* quartz, carbon-coated quartz, and boron nitride.

Contact angle hysteresis (contact line pinning) will be characterized by the tilting surface method. A sessile drop will be videotaped while the surface is slowly tilted. The frame just prior to sliding (rolling) of the drop down the incline will be used to estimate advancing and receding static contact angles. The apparatus will be placed on anti-vibration mounting in order to avoid vibration causing the drop to break free prematurely.

The information to be gained in this research is essential to the planning of future microgravity experiments on detached solidification. How well do we need to control and to measure the residual gas pressure in the ampoule? Is it desirable to have a high or low pressure of oxygen? of nitrogen? argon?

The information to be gained in this research is also of importance in other crystal growth techniques. In Bridgman growth without detachment, sticking of the crystal to the ampoule wall is

the primary mechanism for formation of dislocations and probably also of grain and twin boundaries. Nucleation of grains and twins depends strongly on the interface between the melt and the ampoule wall. Our prior research on CdTe has shown a strong correlation between the contact angle of the melt and the tendency of the resulting solid to adhere to the wall and for grains and twins to nucleate at the wall. Although it is strongly suspected that oxygen increases wetting by semiconductor melts, there are no data to support this. Surface tension and contact angle are important to the control and success of other crystal growth processes, including Czochralski crystal pulling, shaped crystal growth, and web-dendrite sheet growth..

REFERENCES

1. L.L. Regel and W.R. Wilcox, "Detached Solidification in Microgravity: A Review," *Microgravity Sci. Technol.* **14**, 152-166 (1999).
2. W.R. Wilcox and L.L. Regel, "Detached Solidification," *Microgravity Science and Technology* **8**, 56-61, (1995).
3. D.I. Popov, L.L. Regel and W.R. Wilcox, "Detached Solidification: 1. Steady-State Results at Zero Gravity," *J. Mat. Synth. & Proc.* **5**, 283-297 (1997).
4. D.I. Popov, L.L. Regel and W.R. Wilcox, "Detached Solidification: 2. Stability," *J. Mat. Synth. & Proc.* **5**, 299-311 (1997).
5. D.I. Popov, L.L. Regel and W.R. Wilcox, "Detached Solidification: 3. Influence of Acceleration and Heat Transfer," *J. Mat. Synth. & Proc.* **5**, 313-336 (1997).
6. Y. Wang, L.L. Regel and W.R. Wilcox, "Influence of Contact Angle, Growth Angle and Melt Surface Tension on Detached Solidification of InSb," *J. Crystal Growth* **209**, 175-180 (2000).
7. Ju.V. Naidich, "The Wettability of Solids by Liquid Metals," in Volume 14 of *Progress in Surface and Membrane Science*, edited by D.A. Cadenhead and J.F. Danielli, Academic Press, NY (1981) pp 354-484.
8. H. Taimastu, T. Tani and H. Kaneko, "Effect of oxygen on the wettability of sapphire by liquid palladium," *J. Mat. Sci.* **31**, 6383-6387 (1996).
9. A. Sharan and A.W. Cramb, "Surface Tension and Wettability Studies of Liquid Fe-Ni-O Alloys," *Met. Mat. Trans. B* **28B**, 465-472 (1997).
10. K. Mukai, Z. Yuan, K. Nogi and T. Hibiya, "Effect of oxygen partial pressure on the surface tension of molten silicon and its temperature coefficient," *ISIJ International* **40**, S148-S152 (2000).
11. Z. Niu, K. Mukai, Y. Shiraishi, T. Hibiya, K. Kakimoto and M. Koyama, "Effects of temperature and oxygen on the surface tension of molten silicon," *Proc. Int. Conf. High Temperature Capillarity*, edited by N. Eustathopoulos and N. Sobczak, Foundry Research Institute, Cracow, Poland (1997).
12. A. Niu, K. Mukai, Y. Shiraishi, T. Hibiya, K. Kakimoto and M. Koyama, "Temperature and oxygen dependences of surface tension of molten silicon," *Proc. Joint Xth European and Vith Russian Symposium on Physical Sciences in Microgravity*, edited by V.S. Avduyevsky and V.I. Polezhaev, Moscow, Vol. II, 48-55 (1997).
13. Z. Niu, K. Mukai, Y. Shiraishi, T. Hibiya, K. Kakimoto and M. Koyama, "Effect of oxygen and temperature on the surface tension of molten silicon," *J. Jap. Assoc. Crystal Growth* **24**, 31-40 (1997).
14. I. Harter, P. Dusserrer, T. Duffar, J.Ph. Nabot and N. Eustathopoulos, "Wetting of III-V melts on crucible materials," *J. Crystal Growth* **131**, 157-164 (1993).

15. R. Balasubramanian and W.R. Wilcox, "Surface Tension and Contact Angle of Molten Cadmium Telluride," *Int. J. Thermophys.* 11, 25-35 (1990).
16. R. Shetty, R. Balasubramanian and W.R. Wilcox, "Surface Tension and Contact Angle of Molten Semiconductor Compounds: 1. Cadmium Telluride," *J. Crystal Growth* 100, 51-57 (1990).
17. R. Shetty, R. Balasubramanian and W.R. Wilcox, "Surface Tension and Contact Angle of Molten Semiconductor Compounds: 2. Gallium Arsenide," *J. Crystal Growth* 100, 58-62 (1990).
18. A. Katty, P. Dusserre, R. Triboulet and T. Duffar, "Surface tension of II-VI compounds and contact angle on glassy carbon," *J. Crystal Growth* 118, 470-472 (1992).
19. B. LaPlane, "Mouillabilité et Tension Superficielle de Matériaux Semi-Conducteurs," Centre National de Recherche Scientifique, Meudon, France (1978).
20. R. Sangiorgi and M.L. Muolo, "Energetics and reactivity of liquid silicon-silica interface," *Mater. Sci. Forum (International Ceramics Conference)* (1998) pp 427-432.
21. B.R. Bathey, G.F. Hurley and H.E. Bates, "Observations of EFG die material interactions with liquid silicon," *J. Mater. Sci.* 15, 2192-6 (1980).
22. Y. Hayasaka, K. Edamura, M. Iwai, N. Onogawa and K. Kinoshita, "Evaluation of the Wettability of Molten InGaAs," *J. Jap. Soc. Microgravity Appl.* 14, 101-102 (1997).

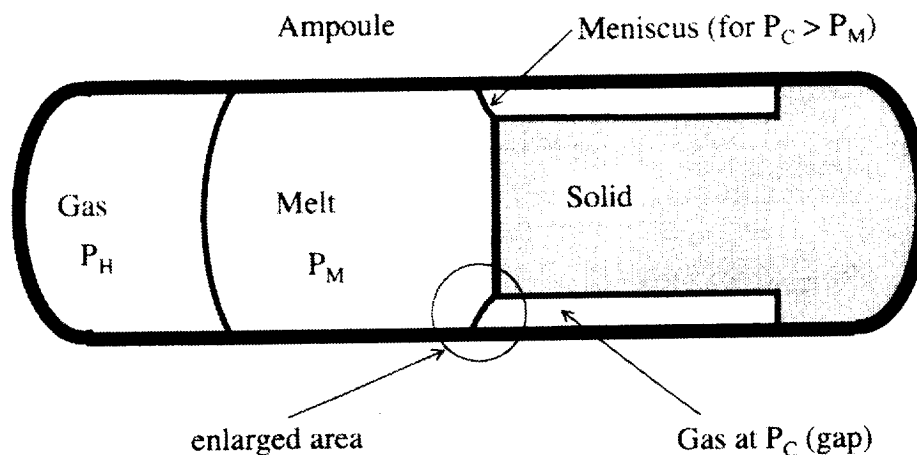


Figure 1a. Schematic diagram of detached solidification. Overall view. In this example, the freezing interface and the meniscus move from right to left.

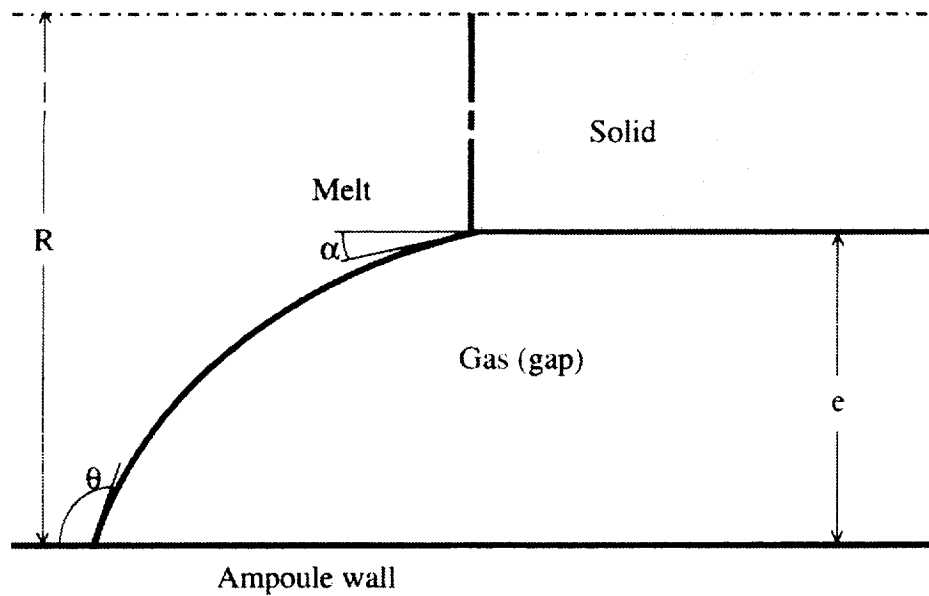


Figure 1b. Schematic diagram of detached solidification. Close-up of meniscus.

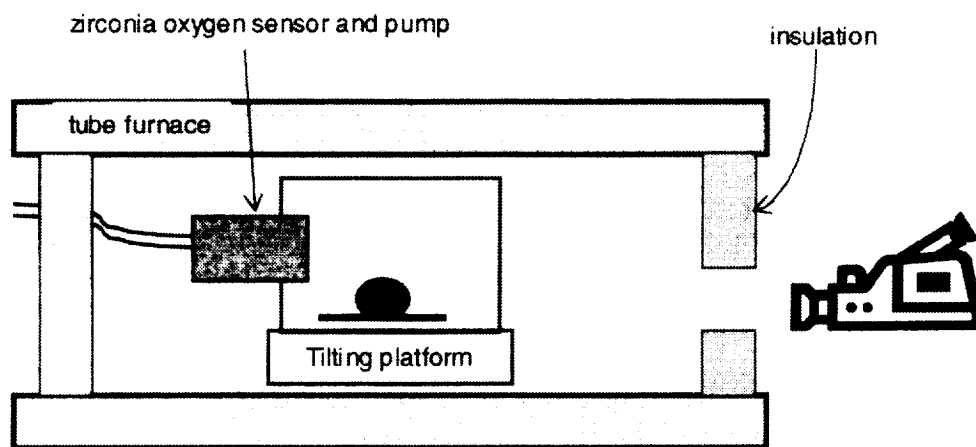


Figure 2. Diagram of apparatus to be constructed for measurements in molten semiconductors. Not shown is the light source at the left end and the rod connected to the platform and extending out of the furnace.

USE OF MICROGRAVITY TO CONTROL THE MICROSTRUCTURE OF EUTECTICS

Liya L. Regel, William R. Wilcox, Dmitri Popov, Fengcui Li and Ram Ramanathan

Clarkson University, Potsdam, NY 13699-5814

Directional solidification of eutectics in microgravity has frequently yielded changes in microstructure, particularly with fibrous eutectics [1,2]. Changes in microstructure have also been observed in some experiments performed on Earth in which the convection in the melt was altered. The causes for these changes are unclear, but worthy of investigation because microstructure determines the utility of these materials. Previous theoretical work at Clarkson University showed that buoyancy-driven convection alone should not influence eutectic microstructure. It was assumed that the composition of the melt was at the eutectic, both in the bulk and at the freezing interface. Consequently, for the present project it was hypothesized that convection alters the microstructure indirectly by causing freezing rate fluctuations. Combined with unequal kinetics of fiber termination and nucleation, such fluctuations would coarsen the microstructure of some systems, make it finer for some, and have negligible influence on others. In order to test this hypothesis, experimental and theoretical modeling studies were undertaken. Originally, we had planned to perform experiments on Mir in collaboration with Professor Reginald Smith of Queens University in Canada. Although flight ampoules were prepared and ground-based tests performed, difficulties with Mir forced us to abandon these plans.

In one set of experiments at Clarkson University, oscillations in the freezing rate of the MnBi-Bi eutectic were generated by periodically passing electric current through the system [3,4]. These fluctuations had several effects that had not been reported previously. As the current pulsing density was increased, more grains exhibited irregular structures with the MnBi present as broken lamellae or large irregular pieces (Figure 1). Sometimes MnBi was absent altogether from a grain. Among those grains that maintained a quasi-regular array of MnBi rods, with increasing pulsing current the rods decreased in size and spacing (Figure 2). Our hypothesis had been that a fluctuating freezing rate would increase the rod size and spacing. The rod roundness also increased with decreasing rod size, whether this was caused by current pulsing or by a higher freezing rate (Figure 3).

Directional solidification experiments were also performed on the Al-Si eutectic [5], in the hope that this alloy would be useful for microgravity experiments. Some ingots were solidified during application of the Accelerated Crucible Rotation Technique (ACRT) in order to generate convection. (ACRT not only causes vigorous convection, but also causes the freezing rate to fluctuate.) Some ingots had 0.01 wt% Sr added as a silicon habit modifier, which tends to convert the silicon from flakes to rods. Unfortunately, the scatter in the data did not permit any firm conclusions on the influence of ACRT on the microstructure, although its effect appeared to vary along the length of the ingot. This may indicate that the strong convection caused by ACRT causes the

composition and doping of the alloy to vary during solidification, leading to a variation in microstructure.

A sharp-interface model was developed that showed freezing rate oscillations can cause departures of the interfacial melt composition from the eutectic [6,7]. This effect becomes more pronounced when one phase projects in front of the other, as is expected in fibrous eutectics. Departures from eutectic composition also occur when nucleation occurs.

A phase-field model [6,8-10] was able to duplicate qualitatively the microstructural changes that were recorded on movie film many years ago by Jackson and Hunt, who observed solidification of eutectic mixtures of organic compounds under the microscope. The phase-field results showed nucleation, lamellar termination, oscillations in volume fractions, and formation of irregular structures. (See, for example, Figure 4. A video can be downloaded from <http://www.clarkson.edu/projects/eutectic/eutphfld.zip>.) Freezing rate variations caused the region of perturbed concentration to extend farther into the melt, which would cause the concentration field to be more influenced by convection.

A third model was developed that utilized the results of the previous two. The influence of freezing rate oscillations on entropy production was determined, in the absence of phase nucleation and termination [6,11]. Minimization of energy production led to the prediction that freezing rate oscillations should slightly reduce the eutectic spacing.

All of these observations, theoretical and experimental, tend to conflict with our hypothesis that convection causes changes in eutectic microstructure indirectly by generating freezing rate oscillations. It appears that departures of the interfacial composition from the eutectic may make the composition field, and thereby the microstructure, much more sensitive to convection. These departures from eutectic composition can be caused by freezing rate fluctuations, a stepped interface, or finite interface kinetics.

Acknowledgement

We are grateful to Barbara Facemire for arranging the use of the supercomputer at Marshall Space Flight Center.

REFERENCES

1. W.R. Wilcox and L.L. Regel, "Influence of Gravity on the Microstructure of Fibrous Eutectics," *Microgravity Quarterly* 4, 147-156 (1994).
2. W.R. Wilcox and L.L. Regel, "Influence of Convection on the Microstructure of Fibrous Eutectics," *Acta Astronaut.* 38, 511-516 (1996).
3. Fencui Li, "The Influence of a Fluctuating Freezing Rate on Directional Solidification of the MnBi/Bi Eutectic," PhD Thesis, Clarkson University (2000).
4. Fencui Li, L.L. Regel and W.R. Wilcox, "The Influence of Electric Current Pulses on the Microstructure of the MnBi/Bi Eutectic" (submitted).
5. Ramnarayanan Ramanathan, "Directional Solidification of the Al-Si Eutectic," MS Thesis, Clarkson University (1999).

6. Dmitri Popov, "Modeling of Detached Solidification and Unsteady Eutectic Solidification," PhD Thesis, Clarkson University (1999).
7. D.I. Popov, L.L. Regel and W.R. Wilcox, "Eutectic Solidification with a Fluctuating Freezing Rate: Sharp Interface Model" (submitted).
8. D.I. Popov, L.L. Regel and W.R. Wilcox, "Fourier Collocation and Fourier Galerkin Methods applied to the Phase-Field Model of Two-Dimensional Phase Transition Problems," *Physica* **31**, 1-9 (1998).
9. D.I. Popov, L.L. Regel and W.R. Wilcox, "One-Dimensional Phase-Field Model for Binary Alloys," *J. Crystal Growth* (in press).
10. D.I. Popov, L.L. Regel and W.R. Wilcox, "Phase-Field Model of Unsteady and Oscillatory Eutectic Solidification" (submitted).
11. D.I. Popov, L.L. Regel and W.R. Wilcox, "Application of the Theorem of Minimum Entropy Production to Growth of Lamellar Eutectics with an Oscillating Freezing Rate," *J. Crystal Growth* **209**, 181-197 (2000).

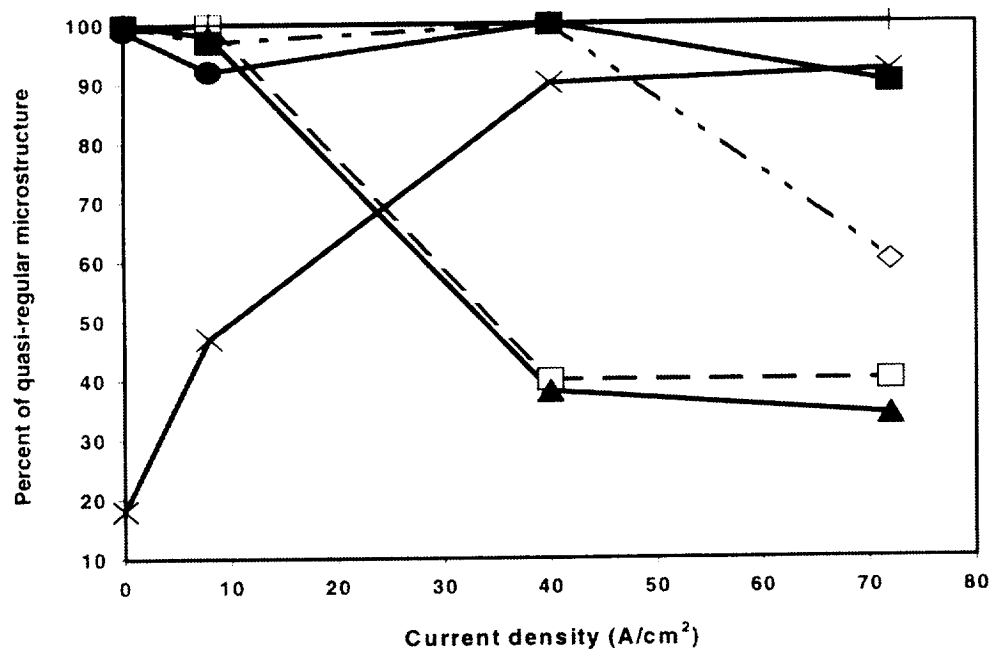


Figure 1. Percent of quasi-regular microstructure versus current density.

- ◇: $V = 2.1\text{cm/hr}$, positive current pulses, $t = 0.75\text{s}$, $T = 6\text{s}$
- : $V = 4.3\text{cm/hr}$, positive pulses, $t = 3\text{s}$, $T = 6\text{s}$
- ▲: $V = 2.1\text{cm/hr}$, positive pulses, $t = 4.5\text{s}$, $T = 18\text{s}$
- ×: $V = 1.1\text{cm/hr}$, positive pulses, $t = 0.25\text{s}$, $T = 2\text{s}$
- : $V = 4.4\text{cm/hr}$, negative pulses, $t = 3\text{s}$, $T = 6\text{s}$
- : $V = 5.5\text{cm/hr}$, negative pulses, $t = 3\text{s}$, $T = 6\text{s}$
- +: $V = 8.0\text{cm/hr}$, negative pulses, $t = 3\text{s}$, $T = 6\text{s}$

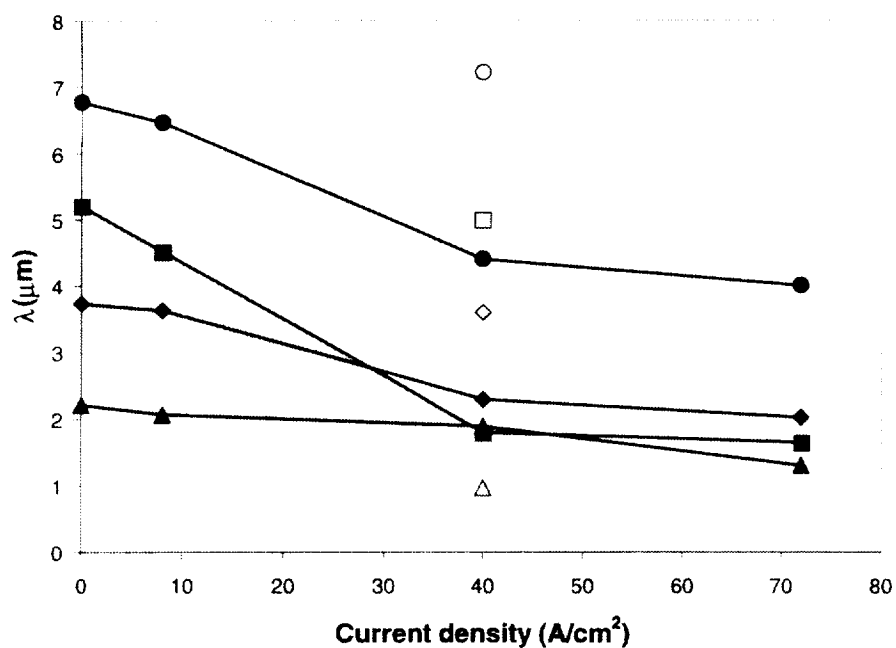


Figure 2. Average rod spacing λ versus positive current density.

- : $V = 1.1\text{cm/hr}$, $t = 0.25\text{s}$, $T = 2\text{s}$ ○: same, with continuous current
- : $V = 2.1\text{cm/hr}$, $t = 4.5\text{s}$, $T = 18\text{s}$ □: same, with continuous current
- ◆: $V = 4.3\text{cm/hr}$, $t = 3\text{s}$, $T = 6\text{s}$ ◇: same, with continuous current
- ▲: $V = 9.5\text{cm/hr}$, $t = 3\text{s}$, $T = 6\text{s}$ △: same, with continuous current

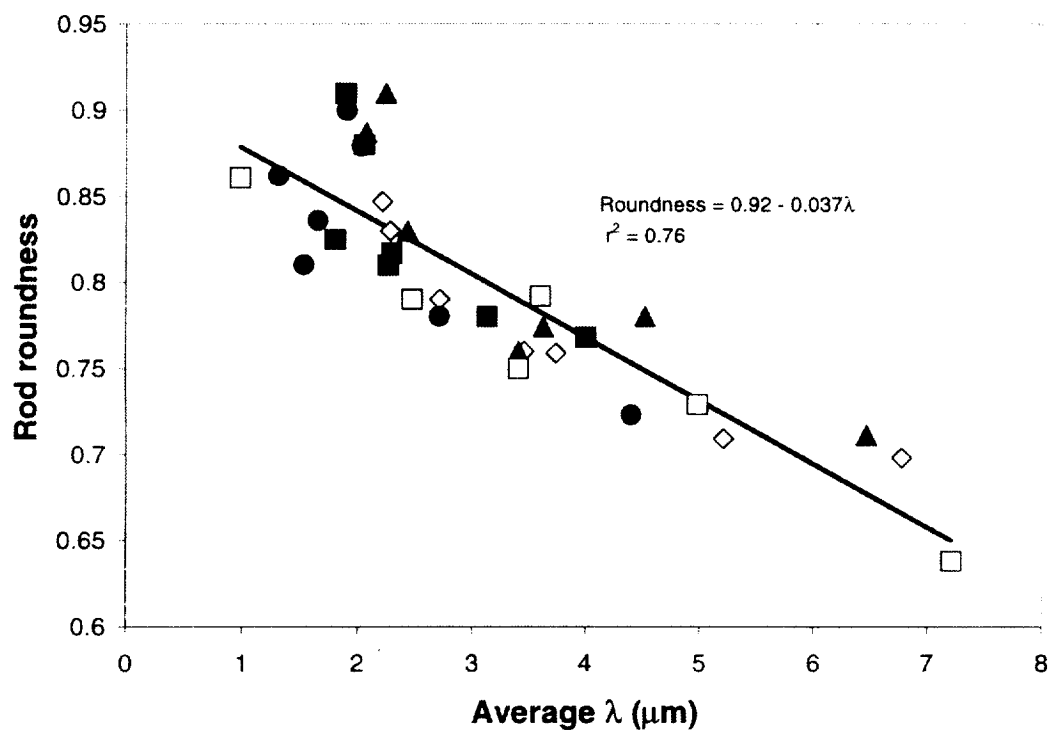


Figure 3. MnBi rod roundness versus λ .

- ◇: no current □: 40 A/cm² continuous current
- ▲: 8 A/cm² pulses ■: 40 A/cm² pulses ●: 72 A/cm² pulses

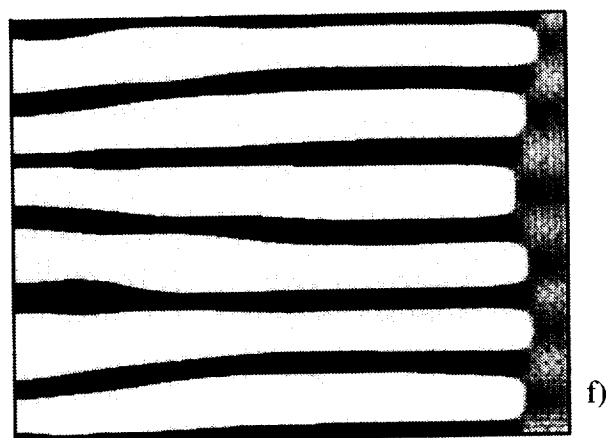
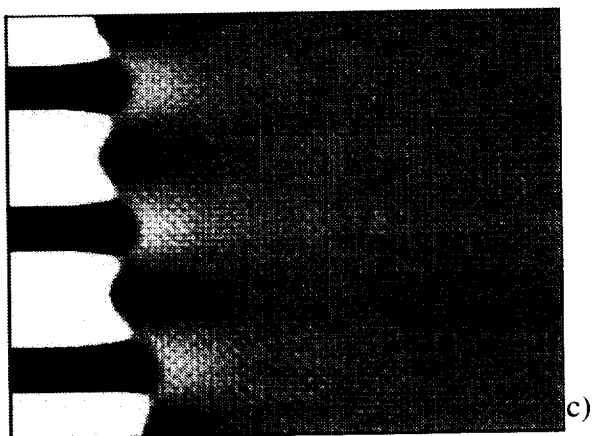
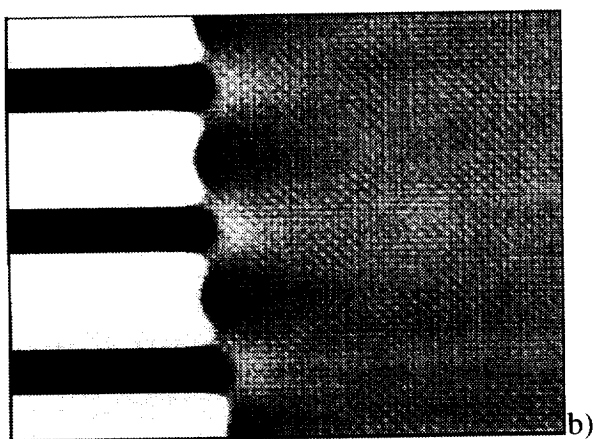
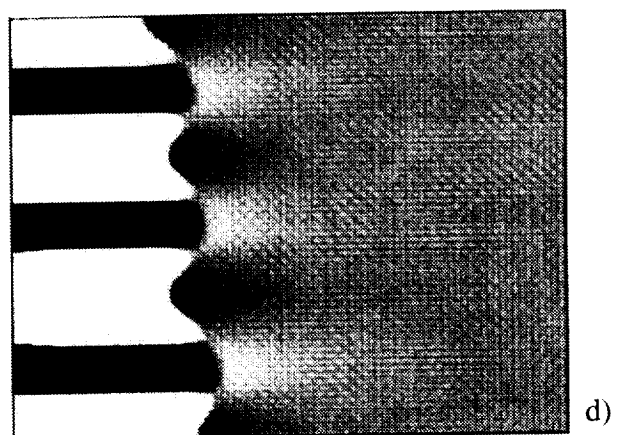
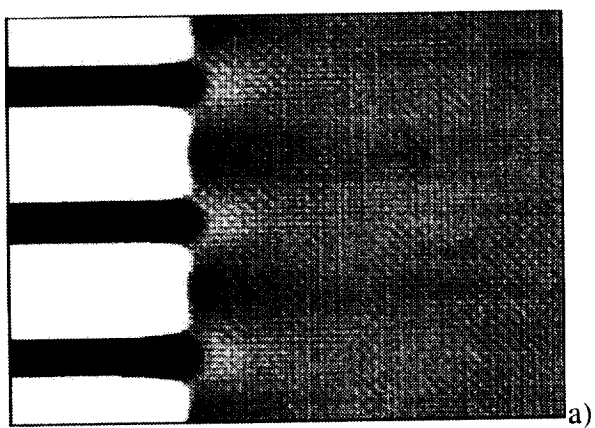


Figure 4. Phase-field simulation of sudden increase in freezing rate of eutectic.

IMPROVED SPACECRAFT MATERIALS FOR RADIATION PROTECTION

Shield materials optimization and testing

J.W. Wilson^{1*}, F.A. Cucinotta², R.K. Tripathi¹, M.S. Cloudsley¹, J.L. Shinn¹, R.C. Singleterry¹,
S.A. Thibeault¹, M.-H.Y. Kim³, J.H. Heinbockel⁴, G.D. Badhwar², F.F. Badavi⁵, J. Miller⁶,
C.J. Zeitlin⁶, and L.H. Heilbronn⁶

¹NASA Langley Research Center

²NASA Johnson Space Center

³ College of William and Mary

⁴ Old Dominion University

⁵ Christopher Newport University

⁶ Lawrence Berkeley National Laboratory

INTRODUCTION

Methods by which radiation shielding is optimized need to be developed and materials of improved shielding characteristics identified and validated. The GCR are very penetrating and the energy absorbed by the astronaut behind the shield is nearly independent of shield composition and even the shield thickness. However, the mix of particles in the transmitted beam changes rapidly with shield material composition and thickness. This results in part from the breakup of the high-energy heavy ions of the GCR which make contributions to biological effects out of proportion to their deposited energy. So the mixture of particles in the radiation field changes with shielding and the control of risk contributions from dominant particle types is critical to reducing the hazard to the astronaut. The risk of biological injury for a given particle type depends on the type of biological effect and is specific to cell or tissue type [1,2,3]. Thus, one is faced with choosing materials which may protect a given tissue against a given effect but leave unchanged or even increase the risk of other effects in the same tissue or increase the risks to other adjacent tissues of a different type in the same individual. The optimization of shield composition will then be tied to a specific tissue and risk to that tissue. Such peculiarities arise from the complicated mixture of particles, the nature of their biological response, and the details of their interaction with material constituents.

Aside from the understanding of the biological response to specific components, one also needs an accurate understanding of the radiation emerging from the shield material. This latter subject has been a principal element of this project. In the past ten years our understanding of space radiation interactions with materials has changed radically, with a large impact on shield design. For example, the NCRP estimated that only 2 g/sq. cm. of aluminum [4] would be required to meet the annual 500 mSv limit for the exposure of the blood forming organs (this limit is strictly for LEO but can be used as a guideline for the Mars mission analysis). The current estimates require aluminum shield thicknesses above 50 g/sq. cm. which is impractical. In such a heavily shielded vehicle, the neutrons produced throughout the vehicle also contribute significantly to the exposure and this demands greater care in describing the angular dependence of secondary

particle production processes. As such the continued testing of databases and transport procedures in laboratory and spaceflight experiments has continued. This has been the focus of much of the last year's activity and has resulted in improved neutron prediction capability [5]. These new methods have also improved our understanding of the surface environment of Mars. The Mars 2003 NRA HEDS related surface science requirements were driven by the need to validate predictions on the upward flux of neutrons produced in the Martian regolith and bedrock made by the codes developed under this project [6]. The codes used in the surface environment definition are also being used to look at *in situ* resources for the development of construction materials for Martian surface facilities. For example, synthesis of polyimides and polyethylene as binders of regolith for developing basic structural elements has been studied and targets built for accelerator beam testing of radiation shielding properties [7]. Preliminary mechanical tests have also been promising.

Improved spacecraft materials have been identified (using the criteria reported by this project at the last conference) as potentially important for future shielding materials. These are liquid hydrogen, hydrogenated nanofibers, liquid methane, LiH, Polyethylene, Polysulfone, and Polyetherimide (in order of decreasing shield performance). Some of the materials are multifunctional and are required for other onboard systems. We are currently preparing software for trade studies with these materials relative to the Mars Reference Mission as required in the project's final year.

I. Methodologies

The types and energy distributions of particles transmitted through a shield material requires the solution to a transport description of the process with appropriate boundary conditions related to the external space radiation environment. The relevant transport equations are the linear Boltzmann equations derived on the basis of conservation principles [8] for the flux density $\phi_j(x, \Omega, E)$ of type j particles moving in direction Ω with energy E as

$$\Omega \cdot \nabla \phi_j(x, \Omega, E) = \sum_k \sigma_{jk}(\Omega, \Omega', E, E') \phi_k(x, \Omega', E') d\Omega' dE' - \sigma_j(E) \phi_j(x, \Omega, E) \quad (1)$$

where $\sigma_j(E)$, $\sigma_{jk}(\Omega, \Omega', E, E')$ are the media macroscopic cross sections for various atomic and nuclear processes including spontaneous disintegration. In general, there are hundreds of particle fields $\phi_j(x, \Omega, E)$ with several thousand cross-coupling terms $\sigma_{jk}(\Omega, \Omega', E, E')$ through the integral operator in equation (1). The total cross section $\sigma_j(E)$ with the medium for each particle type of energy E may be expanded as

$$\sigma_j(E) = \sigma_{j,at}(E) + \sigma_{j,el}(E) + \sigma_{j,r}(E) \quad (2)$$

where the first term refers to collision with atomic electrons, the second term is for elastic nuclear scattering, and the third term describes nuclear reactive processes and are ordered as $10^8:10^5:1$. This ordering allows flexibility in expanding solutions to the Boltzmann equation as a sequence of physical perturbative approximations. Special problems arise in the perturbation approach for neutrons for which the nuclear elastic process appears as the first-order perturbation and has been the recent focus of research [5] as follows.

The double differential particle production and fragmentation cross sections $\sigma_{jk}(\Omega, \Omega', E, E')$ of equation (1) are separated into an isotropic contribution and a remainder as

$$\sigma = \sigma_F + \sigma_{iso} \quad (3)$$

where the remainder σ_F consists of only forward directed secondary particles and σ_{iso} is dominated by lower energy particles produced in the reaction. The low energy charged particles can be solved analytically [8] but the low energy neutrons require a different solution technique [5]. The solution to equation (1) can likewise be separated into two parts for which σ_F appears only in equation (1) with solution ϕ_F and a second equation in which σ_{iso} appears in equation (1) but with source terms from coupling to the ϕ_F field through σ_{iso} . The solution to equation (1) for ϕ_F can be written in operational form as

$$\phi_F = G_F \phi_B \quad (4)$$

where ϕ_B is the inbound flux at the boundary, and G_F is the Green's function associated with σ_F which reduces to a unit operator on the boundary. There remains the evaluation of the remainder terms σ_{iso} of equation (1), especially the low-energy neutron transport. The remainder of equation (1) following the separation given by equation (3) is

$$\Omega \cdot \nabla \phi_j(x, \Omega, E) = \sum \sigma_{iso,jk}(E, E') \phi_k(x, \Omega', E') d\Omega' dE' - \sigma_j(E) \phi_j(x, \Omega, E) + g_j(E, x) \quad (5)$$

where the source term $g_j(E, x)$ results from the collisional σ_{iso} source with the ϕ_F field. The charged particle fields of equation (8) can be solved analytically [8] leaving the low-energy neutrons fields to be evaluated using energy multigroup methods [5,9]. It requires a solution to a boundary value problem for the distribution of neutron sources along a 512 array of directions about each location within the vehicle where the fields are to be evaluated. The solution methodology implies a great deal of repeated operations (for each direction) with differences only in the distribution of source terms, distances to the boundaries, and boundary conditions which can be done efficiently with a parallel processor. Other parallel operations could also be used in the solution of the ϕ_F fields solved by marching procedures.

The extent of the nuclear interaction cross section database required for the transport of cosmic rays spans most nuclear-reaction physics from thermal energies to energies above tens of GeV/nucleon, including a large number of projectile and target material combinations. The types of cross sections required for the transport involve total yields and secondary energy spectra for one-dimensional transport and double differential cross sections in angle and energy for three-dimensional transport. The usual approach to database generation is the use of Monte Carlo models or hydrodynamic models with limited usefulness and success. The uniquely LaRC approach has been to develop solution procedures of the basic quantum mechanics using the multiple scattering formalism [10-15].

II. Validation

Laboratory validation with well defined ion beams and target geometries with high resolution test equipment allows the testing of the atomic/nuclear database and material transmission factors in great detail. One type of database test [16] is shown in Figure 1 for 1.05 GeV/nucleon iron beams on several targets. The results of the quantum multiple scattering model is shown here in comparison with the experiments. The cross section for removal of a few protons is strongly affected by the single particle model for the nuclear wave functions and the development of a cluster model database is required. Only a small sample of ion and material combinations have so far been tested.

Spaceflight testing allows validation of the full complement of methods (environmental models, materials interaction database, computational procedures, methods of analysis) required to produce exposure field estimates. Most validation is limited to measurements in a predominantly 2219-aluminum alloy structure (Shuttle). Earlier testing was with a particle telescope [17] and more recently with a tissue equivalent proportional counter (TEPC) [18] shown in Figure 2 with the model calculation [18]. The discrepancy in the lowest lineal energies in the GCR spectrum is believed in part due to the neglect of pions in the present shielding model and in part from wall effects in the TEPC not included in the detector response model but important for HZE ions [18]. Neutron measurements [19] using four Bonner spheres and activation foils on STS-31 and STS-36 have been very encouraging.

III. Optimization Methods

A large fraction of the shielding on human rated vehicles is from the basic structure and onboard systems [8]. Engineering design usually proceeds with little regard to radiation constraints until the latter stages of the design process, in part, due to the use of Monte Carlo methods which require great amounts of dedicated computer time resulting in design delays [7]. At such a late stage in the design process, a fix of a radiation problem usually involved adding shielding in less than optimum ways (for example, a 5,500 kg vault was added to Skylab requiring additional support structures). A similar problem now exists with the International Space Station in which redesign is in progress. Clearly, improved methods of design in which radiation constraints are entered early into the design process allowing optimum radiation risk mitigation are required. Since the basic structure and onboard systems provide much of the shielding, the optimization of the spacecraft shielding cannot be done in a vacuum and is inherently a multidisciplinary design process. With the rapid expansion of high performance computing and communication, there is increased emphasis on multidisciplinary optimization (MDO) methods and radiation constraints analysis needs to be added to the collection of tools available to mission design teams. It also requires that materials proposed for other mission design requirements (structure, thermal, noise reduction, expendables) are multifunctional in character since their radiation shielding properties impact the radiation constraints.

IV. Future Materials Research

Required materials research falls into three categories: First is the improvement of computational models and associated databases. Second is the development of multifunctional material properties for use in system optimization procedures. Third is the design of optimum radiation protective materials to finish out deficiencies in the shield design at minimum mass and costs.

A. Computational models and databases

The computational models required are the basic atomic and nuclear physics models for database evaluation and the associated transport models which combine these databases to evaluate material transmission properties. Three issues discussed in prior sections relate to needs in the nuclear database and transport procedures. First, the few proton removal cross sections depend on the representation of the outer shells of the nuclear models. Most reaction codes (*e.g.*, Monte Carlo) rely on single particle wave functions whereas the few proton removal cross sections depend on clustering effects and the direct knockout of such clusters. The QMSFRG code [13]

accounts for clustering but lacks a complete database of nuclear cluster models to perform the evaluation except in the case of a few light nuclei. Second, the mesons are in part responsible for the discrepancy in the low lineal energy GCR spectrum and needs to be added to the nuclear database and transport procedures and efforts on developing such a database has started. Third, there are several thousand energy and angle dependent cross sections for each material constitutive required in shielding analysis. Very few of these cross sections have been validated in laboratory experiments and a systematic measurements program is required. The requirements for such a measurements program is discussed elsewhere [8]. Finally, although the HZETRN codes are more than a 1,000 times faster than the corresponding Monte Carlo codes even greater speed by using massively parallel processors along the usual 512 angular rays will greatly enhance the computational efficiency. Such speed is critical to the early entry of radiation constraints in the design process and optimization procedures.

B. Multifunctional materials optimization

Radiation shield optimization requires an evaluation of the design materials and making appropriate design choices at each step of the design process. Many choices will be driven by design requirements other than shielding and will usually be among less than perfect shield materials. The shield performance of candidate materials for each specific application need characterized to allow optimum choices to be made in the design process. New materials for specific applications need developed with enhanced shielding characteristics. Many such choices have already been identified for future designs. For example, polymer composites are preferable to aluminum alloys. Food and water are known effective shield materials and have been utilized in past design considerations. Hydrogen or methane fuels are potentially important materials for protection. We have proposed developing sound absorbing materials which are efficient radiation shields for use in crew areas. Recent advances in hydrogen storage in graphite nanofibers may have a large impact (3-6 times better than aluminum) on radiation safety in future spacecraft design.

C. Optimum protective materials

The requirements for a high performance shield material is to maximize the number of electrons per unit mass, maximize the nuclear reaction cross section per unit mass, and minimize the production of secondary particles. Thus, the transmitted LET spectra of hydrogen shows almost universal attenuation above a few keV/ μ resulting in good attenuation of biological effects independent of biological model used. On the other hand, materials with less hydrogen content such as water experience attenuation only above 20 keV/ μ . The LET attenuated components of higher Z materials continues to increase to higher values reaching 50 keV/ μ for lead [1]. The maximum performance is for liquid hydrogen which we use to define the maximum performance limit of any material as shown in Figure 3. It is a challenge to materials research to develop materials approaching these performance levels.

V. Concluding Remarks

At the beginning of this project, the shield design technology was at Technology Readiness Level (TRL) 3-4. The laboratory testing with relevant particle types has provided valuable data for model improvements and database validation. Future improvements will be more evolutionary than revolutionary as interaction models are relatively mature, which was not the case a few

years ago and as confirmed by the blind test conducted by the LBNL group [16]. Future improvements are expected to be incremental. An opportunity for comparison with flight measurements on a large 2219 aluminum alloy structure allowed us to rapidly move the TRL to include level 6-7 elements in the project. The use of the tissue equivalent proportional counter (TEPC) with its broad spectral capability and the time resolved methodologies allows testing of codes and databases for both trapped proton spectra and galactic cosmic rays. This comparison added to the evidence that the pions may be the next most important component to add to the current technology, and consequently a low energy database for pion production has been prepared. The addition of higher energy multi-pion processes is in progress and will be funded out of another program. Only modest improvements to the exposure field are expected for spacecraft but the enhanced model may play a more important role for the Mars surface. Additional testing of the codes and database will take place on ISS in the near future. As a final note, the identification of polyethylene as a relatively efficient shield material under this project has resulted in an on-going activity with JSC for the augmentation of the ISS design to reduce the cancer risks of the astronauts in ISS operations.

REFERENCES

1. J. W. Wilson et al., Issues in space radiation protection.: Galactic Cosmic Rays. *Health Phys.* 68:50-58; 1995.
2. J. W. Wilson et al., Materials for shielding astronauts from the hazards of space radiation. *Mat. Res. Soc. Symp. Proc.* 551, 1999, pp. 3-15.
3. W. Schimmerling et al., Requirements for simulating space radiation with particle accelerators. *Risk Evaluation of Cosmic-Ray Exposure in Long-Term Manned Space Missions*. Eds. K. Fujitaka, et al., Kodansha Scientific Ltd., Tokyo, pp. 1-16, 1999.
4. National Council on Radiation Protection, *Guidance on Radiation Received in Space Activities*, NCRP Report No. 98, 1989.
5. J. H. Heinbockel et al. *An Improved Neutron Transport Algorithm for Space Radiation*. NASA TP-2000-209865, 2000.
6. J. W. Wilson et al. Mars surface ionizing radiation environment: Need for validation. In *Workshop on MARS 2001: Integrated Science in Preparation for Sample Return and Human Exploration*. J. Marshall and C. Weitz, eds. Lunar and Planetary Institute, Houston, LPI Contribution No. 991, pp. 112-114, 1999.
7. M.-H. Y. Kim et al. Development and testing of *in situ* materials for human exploration of Mars. *High Perform. Polym.* 12, 1-14, 2000.
8. J. W. Wilson et al., *Transport Methods and Interactions for Space Radiations*. NASA Reference Publication, RP-1257, 1991.
9. M.S. Cloudsley et al., A comparison of the multigroup and collocation methods for solving the low energy neutron Boltzmann equation. To be published *Can. J. Phys.*
10. J. W. Wilson, Multiple Scattering of Heavy Ions, Glauber Theory, and Optical Model. *Phys. Lett.* B52, 149, 1974
11. F. A. Cucinotta, L. W. Townsend, and J. W. Wilson, Model of Alpha-Nucleus Interaction Cross Sections. NASA TP-3285, 1993
12. F. A. Cucinotta and R. R. Dubey, Final-State Interactions and Inclusive Nuclear Collisions. NASA TP-3353, August 1993
13. F. A. Cucinotta, J.W. Wilson, R.K. Tripathi and L.W. Townsend, Microscopic fragmentation model for galactic cosmic ray studies, *Adv. Space Res.* 22: 533-537; 1998

14. R. K. Tripathi, F.A. Cucinotta, and J.W. Wilson, Medium modified nucleon-nucleon cross sections in a nucleus, Nucl. Instr. meth. Phys. Res. B152: 425-431; 1999
15. R. K. Tripathi, J.W. Wilson, and F.A. Cucinotta, Nuclear absorption cross sections using medium modified nucleon-nucleon amplitudes, Nucl. Instr. Meth. Phys. Res. B 145: 277-282; 1998
16. C. Zeitlin et al., Heavy fragment production cross sections from 1.05 GeV/nucleon ^{56}Fe in C, Al, Cu, Pb, and CH₂ targets. Phys. Rev. 56: 388-397; 1997.
17. G. D. Badhwar et al., Measurements of the secondary particle energy spectra in the space shuttle. *Radiat. Meas.* 24, pp. 129-138, 1994.
18. J.L. Shinn, et al., Validation of a comprehensive space radiation transport code. IEEE Nucl. Sci. 45: 2711-2719; 1998.
19. J. E. Keith, G. D. Badhwar, D. J. Lindstrom, Neutron spectrum and dose-equivalent in Shuttle flights during solar maximum. Nucl. Track and Radiat. Meas. 20(1), pp. 41-47, 1992.

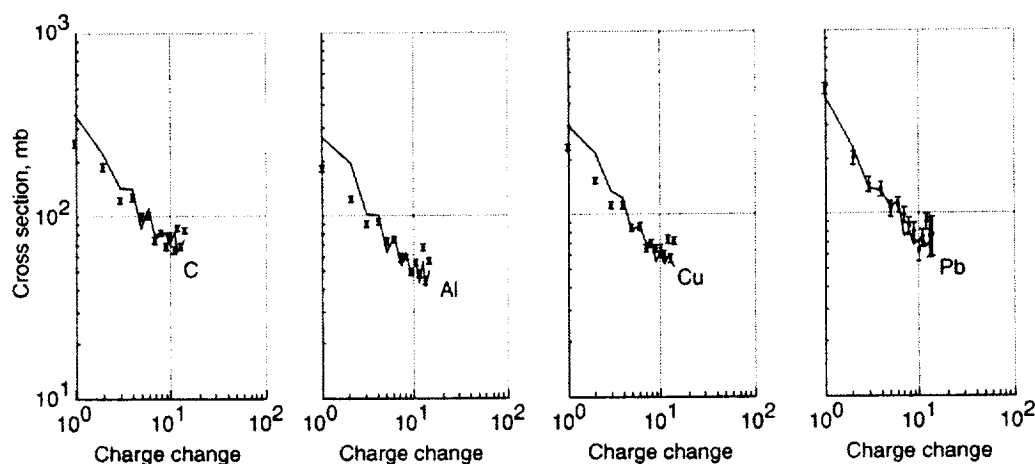


Figure 1. Charge-changing cross sections for ΔZ from -1 to -14 for 1.05 GeV/nucleon ^{56}Fe incident on C, Al, Cu, and Pb targets. The solid lines are predictions from QMSFRG.

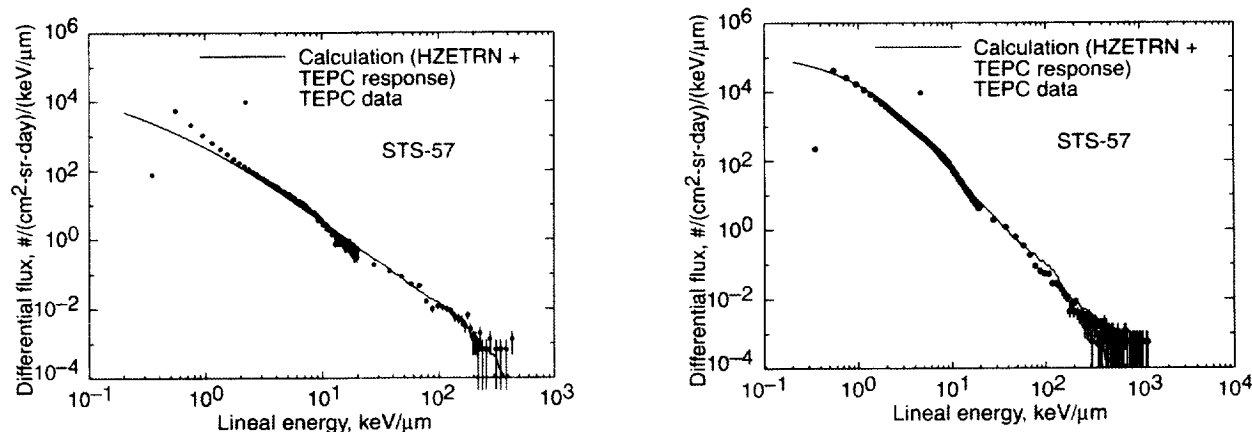


Figure 2. TEPC measurements on STS-57 compared to model calculations.

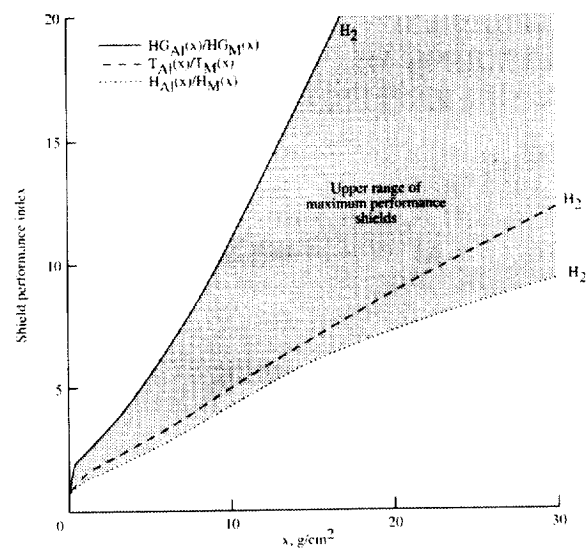


Figure 3. Maximum performance factors for any material relative to aluminum.

IDENTIFICATION AND CONTROL OF GRAVITY RELATED DEFECT FORMATION DURING MELT GROWTH OF ELECTRO-OPTIC SINGLE CRYSTALS: SILLENITES, BISMUTH SILICATE ($\text{Bi}_{12}\text{SiO}_{20}$)

M. Wiegel and A.F. Witt

Massachusetts Institute of Technology, Cambridge, MA 02139

OBJECTIVES

A research program is being conducted which is expected to lead to the identification and control of gravitational effects which adversely impact, through their interference with the growth process, critical application specific properties in the photorefractive sillenite system $\text{Bi}_{12}\text{SiO}_{20}$.

The research places focus on a class of materials with acousto-optic, piezo-electric and outstanding electro-optic properties, which suggest a broad spectrum of device applications. Realization of the full potential of these materials remains impeded, primarily because of our current inability, in ground-based experiments, to control during growth adequately composition (on a micro scale), critical crystal defect formation as well as confinement related contamination and appearance of lattice stress.

Selective reduction of the primary driving force for convective melt flows, achieved in micro gravity growth experiments, is expected to:

- greatly facilitate the establishment of cause and effect relationship for defect formation,
- advance our understanding of the crystal growth process and thus
- provide for enhanced property control during crystal growth and
- establish a basis for the development of effective defect engineering directed at the optimization of application-specific properties in BSO and in electro-optical materials in general.

Research results

1) When conducting BSO growth by the Czochralski technique it was observed that the growth behavior under conventional conditions, ambient uncontrolled open air or controlled flow of purified or synthesized air, differs significantly from that encountered in closed or dynamic systems with varying partial pressures of oxygen. It was found moreover that in closed systems with reduced oxygen partial pressure, the confinement material, platinum, becomes subject to embrittlement and severe intergranular corrosion. Considering the importance of melt confinement in space experiments, detailed studies of the melt-platinum interaction, in particular of the wetting behavior of BSO melts under varying ambient conditions were conducted.

2) A system was assembled which permits the photographic recording (CCD camera at 640x480 pixels) of sessile drops of BSO melts on Pt and alloyed Pt substrates under varying, controlled ambient conditions. Contact angles are measured when steady state was reached after expansion of the contact area between the BSO melt and the substrate. Images were stored in a computer and a Sobel edge detector was used to resolve the contour of the liquid vapor interface. Using a Matlab code the surface tension of the melt and the contact angles were extracted from the computed contour diagrams. The viability of the approach was tested with substances listed in CRC tables. The test results indicated excellent agreement with published data. It was found that in the partial pressure range from pure oxygen (1 atm) to ~ 10 torr the contact angle changes from ~10° to about 40°. For the same experimental conditions (10 minutes of melt confinement contact time), the mode of melt confinement interaction changes from no noticeable effect on the substrate to significant corrosion and embrittlement.

It was found that wetting of Pt by BSO melt is significantly reduced if platinum is alloyed with gold (Au). An extensive study of wetting, embrittlement and corrosion of the $\text{Pt}_{.95}\text{Au}_{.05}$ is currently being conducted.

Because of reports on differences in the wetting behavior on the ground and in space, wetting experiments have been designed for conduct during KC-135 flights. (Results were reported at this conference).

3) Related to design of adequately controllable and quantifiable growth experiments on the international space station, a Bridgman-type growth system has been designed, was characterized and tested. The heat pipe based system operates with two control T/Cs in the gradient (growth) region and permits growth interface stabilization as well as growth interface morphology control from convex through planar to concave. The system has been used for growth of BSO, both undoped and doped. Single crystal growth (seeded) was confirmed, significant reduction of off core striation formation was observed, as was absence of central coring. In two growth experiments the grown single crystals exhibited filamentary second phase formation (previously predicted from thermal measurements but not as yet reported to be observed in growth experiments).

ON THE CONTROL OF THE EFFECTS OF GRAVITY ON SOLIDIFICATION MICROSTRUCTURES USING OPTIMALLY DESIGNED BOUNDARY HEAT FLUXES AND ELECTROMAGNETIC FIELDS

Nicholas Zabaras * and Rajiv Sampath

Sibley School of Mechanical and Aerospace Engineering
Cornell University, 188 Frank H.T. Rhodes Hall
Ithaca, NY 14853-3801
Email: zabaras@cornell.edu

The main objective of this work is to design and test computational techniques that can be used to control the microstructures that are developed during directional solidification processes.

Gravity plays an important role in the obtained microstructures mainly by influencing the melt flow mechanisms as well as the solute diffusion processes. Since these effects remain present even under a reduced gravity environment, we address inverse design solidification problems that result in desired microstructures at various gravity levels.

Our main design variables are the thermal mold/furnace conditions as well as the strength and orientation of an externally applied electromagnetic field. We select these continuous variables such that a desired growth velocity V and temperature gradient G are achieved near the freezing interface that correspond to desired microstructures. In our preliminary work, we are interested to design processes with spatially uniform growth velocity under stable growth conditions.

These design problems are inverse problems with overspecified thermal conditions (temperature and flux) on one part of the boundary and no-thermal conditions on another part of the boundary. They are posed as functional optimization problems. The exact gradient of the cost functional is obtained via the solution of an adjoint continuum problem. A sensitivity problem is also defined and is used in the implementation of the conjugate gradient method.

Since electromagnetic fields have a direct effect on the strength of the melt flow, the consideration of designing appropriate strengths and direction of electromagnetic fields simultaneously with continuous boundary heating/cooling conditions for various strengths of gravity enhances the success of the solidification design process.

These design techniques are useful for the development of the next generation of furnaces for controlled crystal growth. In particular, the availability of mathematical models for solidification control via optimally designed thermal boundary fluxes and electromagnetic fields is essential for the development of multiple-zone automated furnaces. Further development of such inverse techniques will enhance our ability to develop new advanced directional solidification process designs for cast microstructure control.

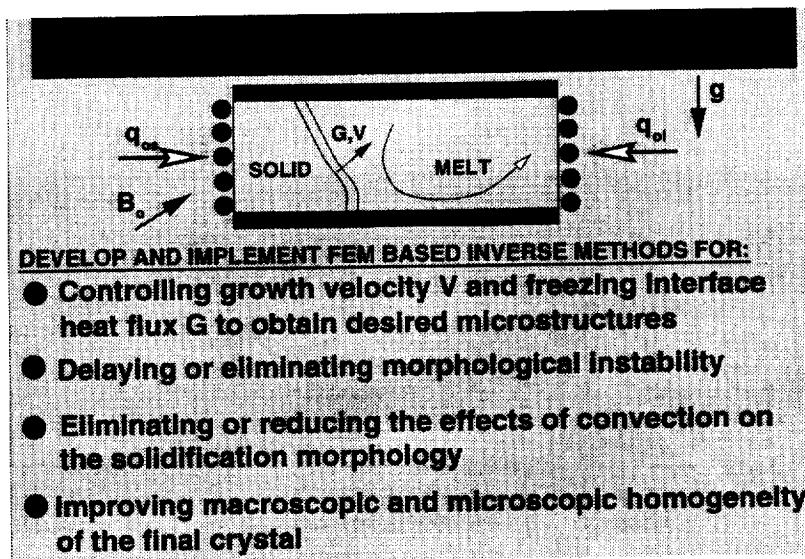


Figure 1.

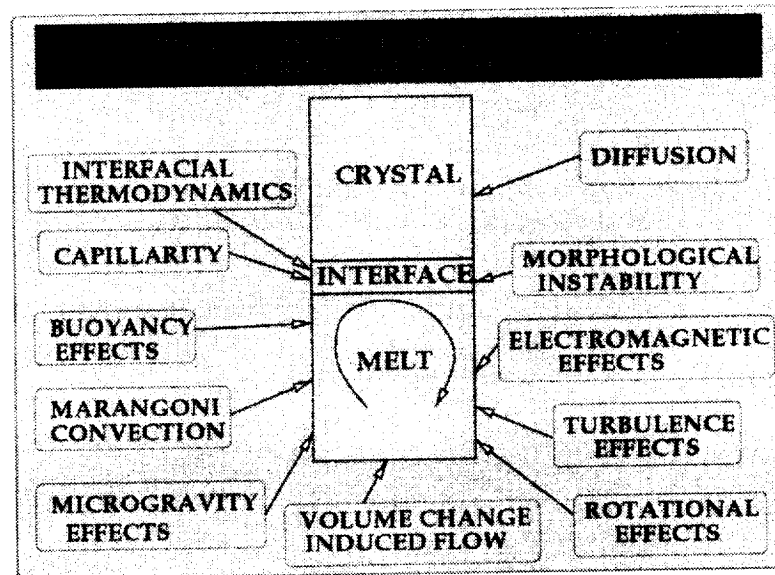


Figure 2.

- Proper adjustment of the cooling/heating furnace conditions
- Controlled variation of the solid-liquid interface growth velocity
- Use of electromagnetic fields for conducting melts in order to suppress or control the melt flow
- Proper rotation of the furnace/crucible to control the melt flow and solute distribution
- Solidification in reduced or gravity free environment to reduce the effects of buoyancy driven melt flow

Figure 3.

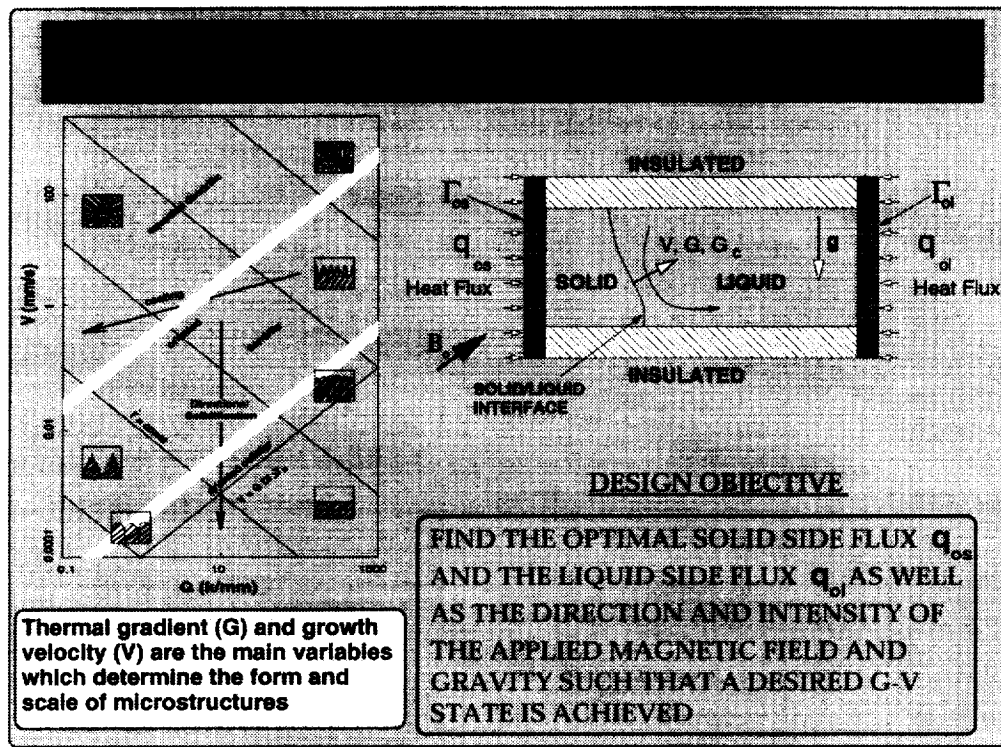


Figure 4.

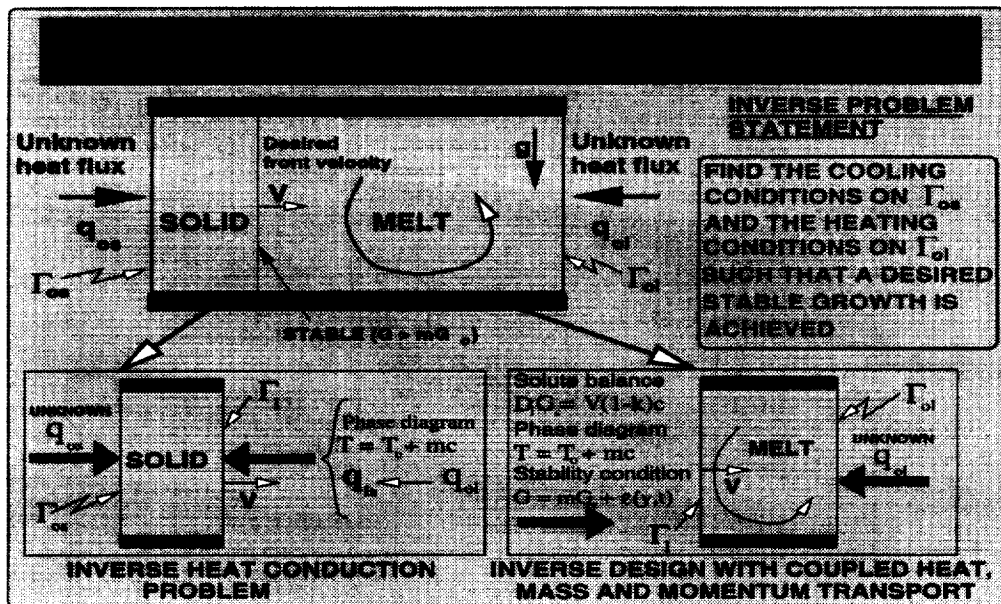


Figure 5.

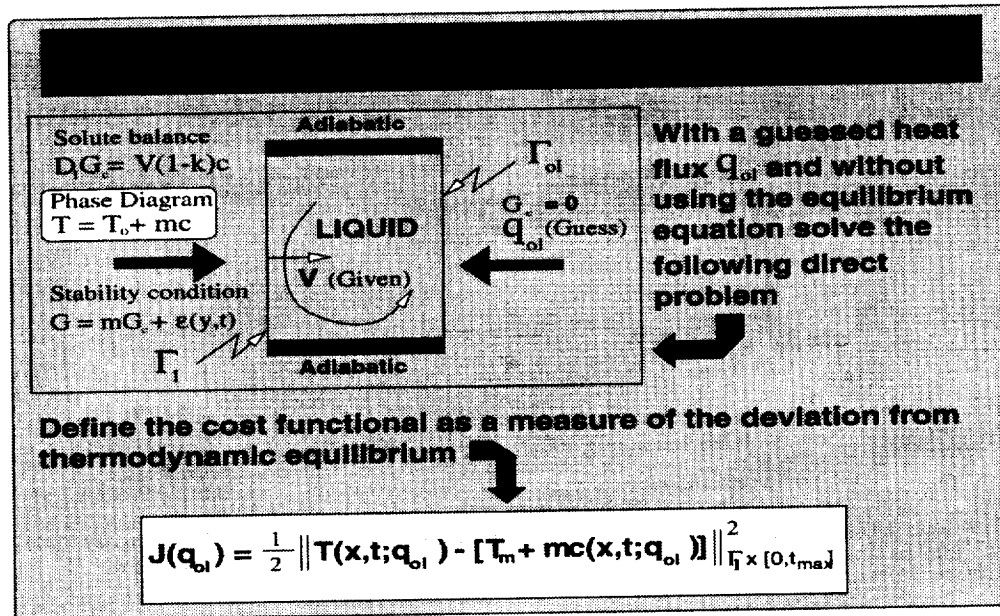


Figure 6.

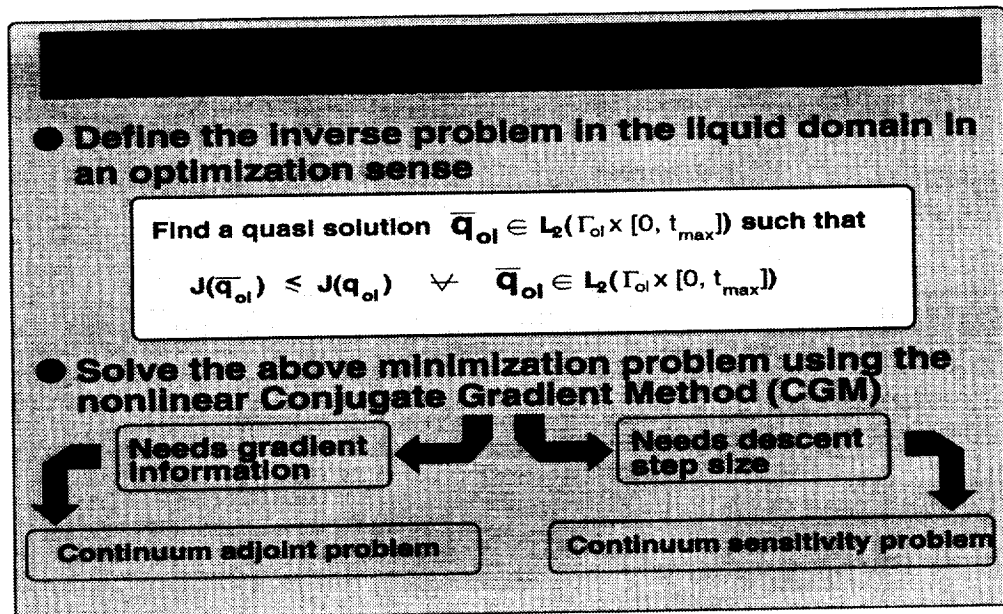


Figure 7.

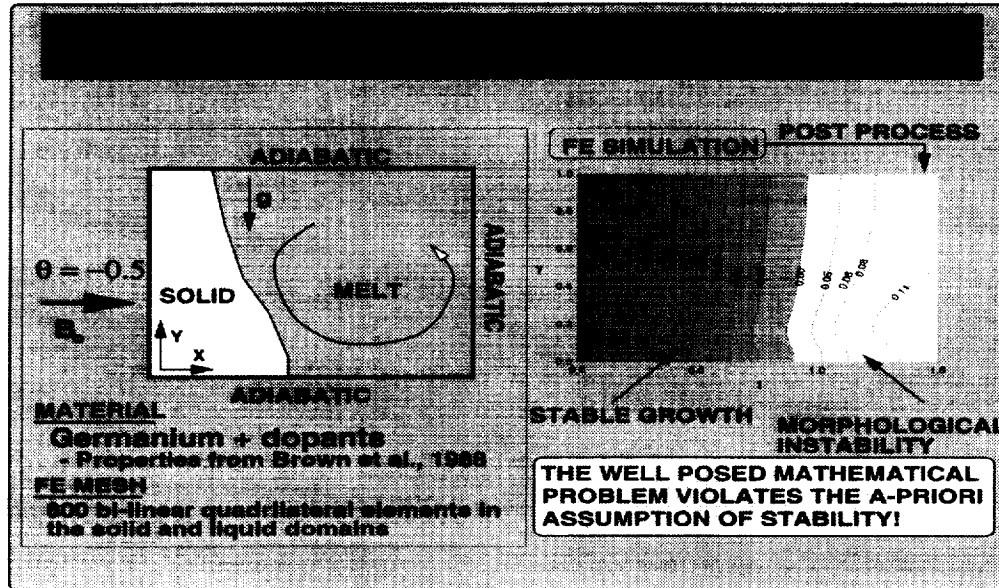


Figure 8.

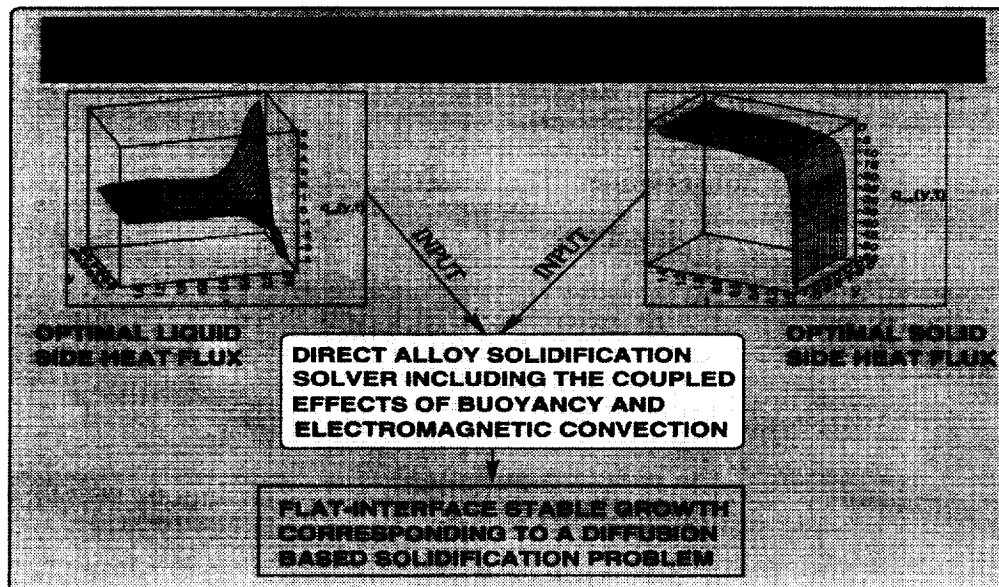


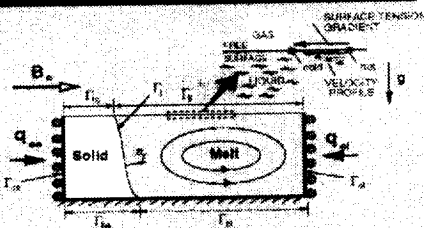
Figure 9.

- In low-gravity environment the action of Marangoni convection is significant
- A preliminary design study has shown that thermal flux design combined with appropriate magnetic field and microgravity strength and orientation can lead to a desired flat-interface growth

SOLIDIFICATION SIMULATION
MATERIAL: Germanium-Antimony



Normal gravity
 No magnetic field



Reduced gravity
 Horizontal magnetic field

Figure 10.

- Implement design methods for desired interface growth conditions for several metallurgical and semiconductor materials
- Address flow control problems to stratify or restrict the melt flow to achieve macroscopic homogeneity
- Develop computational methods for simultaneous design of magnetic fields and thermal fluxes
- Incorporate microstructure evolution models to achieve desired microstructures based on optimal macroscopic design solutions
- Develop inverse methods for computational design of eutectic solidification models

Figure 11.

- Yang, G. Z. and Zabaras, N. 'The adjoint method for an inverse design problem in the directional solidification of a binary alloy', J. Comp. Phys., (1998) 432-452.
- Yang, G. Z. and Zabaras, N. 'An adjoint method for the inverse design of solidification processes with natural convection', Int. J. Numer. Methods Engr., (1998) 1121-1144.
- Sampath, R. and Zabaras, N. 'Numerical study of convection in the directional solidification of a binary alloy driven by the combined action of buoyancy, surface-tension and electro-magnetic fields', J. Comp. Phys., submitted.
- Zabaras, N. 'Adjoint methods for inverse free convection problems with applications to solidification processes', Computational Methods for Optimal Design and Control, (1998) 391-426.
- Hurle, D. T. J., Handbook of Crystal Growth, Vol 1a-3b, North-Holland, Amsterdam, 1992.

Figure 12.

MEASUREMENT OF CHARGED PARTICLE INTERACTIONS IN SPACECRAFT AND PLANETARY HABITAT SHIELDING MATERIALS

C. Zeitlin¹*, L. Heilbronn¹, J. Miller¹, R.C. Singleterry², J.W. Wilson²

¹Lawrence Berkeley National Laboratory

²NASA Langley Research Center

The Microgravity Materials Program, through its 98-HEDS-04 Research Announcement, has called for research to support “enhanced human radiation protection through the development of light weight soft goods with high radiation protection characteristics.” Given the nature of the particle flux from the Galactic Cosmic Radiation (GCR), and the many constraints on the depth and type of shielding in spacecraft and planetary habitats, it is clear that the health risks these particles present to astronauts in deep space cannot be entirely eliminated. It is the objective of this project to develop a highly accurate model of GCR transport so that NASA can develop and validate the properties of protective shielding materials with the best available information. The validity of the GCR transport model depends in large part on having accurate and precise input data in the form of the charge-changing and fragment production cross sections for the heavy ions of greatest biological significance. The accuracy of the transport model can be evaluated and enhanced by employing the following a three-step strategy. (1) New cross section data will be made available to the NASA-Langley scientists responsible for the transport codes, and will be used as inputs to the codes. (2) The codes will be used to predict additional cross sections and/or details of the radiation field behind realistic shielding arrangements, where the materials and configurations may be quite complex. Mock-ups of the shielding configurations suitable for use in accelerator experiments will be obtained by the NASA-Langley co-investigators. (3) The transport model predictions will be tested in accelerator-based experiments. The time scale for one pass through these steps is well-suited to a four-year schedule. Over a longer term, these steps may be repeated, leading to still further refinements of the transport code, new predictions, and an additional round of measurements, until the desired predictive accuracy is achieved. The focus of this work is primarily on the first of these steps, the determination of fragmentation cross sections, which will be the main task in years one and two. The detailed strategy for carrying out the remainder of the program is more difficult to specify, as it depends on unpredictable factors such as the extent to which the transport model must be modified, schedules for accelerator time, target fabrication, etc.

Energetic high energy heavy ions particles comprise only a small fraction of the charged particle flux in the Galactic Cosmic Radiation (GCR), but the fact that they produce extremely dense tracks of ionization in matter makes them a source of risk to astronauts on long-duration missions outside the geomagnetosphere. Owing to practical limitations on shielding mass, many such ions and their fragmentation products will penetrate a spacecraft or planetary habitat wall and deliver

a radiation dose to personnel inside. An incident particle deposits a dose proportional to its Linear Energy Transfer in water (LET), which goes as the square of the charge Z of the particle. Iron ions ($Z = 26$) are the highest- Z particles found to be abundant in the GCR. They have LETs in the range 150-300 keV/ μ m and contribute significantly to the "free space" dose (the dose in the absence of shielding), despite the fact that protons are about 2000 times more prevalent in the GCR flux. Other heavy ions present in significant numbers in the GCR include silicon ($Z = 14$), oxygen ($Z = 8$) and carbon ($Z = 6$). Because the risk from high-LET radiation has long been recognized by NASA to be a potentially serious problem, a wide-ranging program encompassing research in nuclear physics, radiation biology, and microdosimetry has been underway for several years. Significantly, several recent radiobiology experiments show important biological effects – including genomic instability – arising from irradiation with GCR-like particles, iron in particular. Some of these appear to be unique effects of high-LET particles. Also, a recent model calculation (*Health Physics*, 68(1), 50-8, 1995) suggests that at some depths of certain shielding materials, dose equivalent and rates of cell transformation induced by the GCR are greater than they would be with no shielding. These results underscore the need for an accurate model of the transport of GCR particles through shielding, in order to properly assess and, insofar as is possible, minimize their effects.

Uncertainty in nuclear cross sections leads to a large uncertainty (a factor of 2-3) in specifying the attenuation characteristics of shield materials (NASA Conference Publication 3360, 1997). For example, estimates of the attenuation of the dose equivalent behind aluminum shielding vary widely, depending on the choice of model. On the basis of a calculation by Letaw et al. (*Adv. Sp. Res.*, 9(10), 1989), it appears that only 2.5 g/cm² of aluminum is required to reduce the annual GCR exposures at solar minimum to an acceptable value of 0.45 Sv. However, using the NUCFRG2 model (*Nucl. Instr. and Meth. B* 94 95-102, 1994), the required depth of aluminum is over 50 g/cm².

Some of the quantities of fundamental importance to GCR transport, such as charge-changing cross sections and heavy-fragment production cross sections for high-energy iron particles, have been published by the LBNL group (*Phys. Rev. C* 56, 388-397, 1997). These results resolve discrepancies between two previous measurements and thus greatly reduce the uncertainties on the reported cross sections. Other relevant data have been published by Weber et al. (*Phys. Rev. C* 41, 520-532, 1990), but with only low-mass targets pertinent to heavy-ion transport through interstellar space. Many relevant cross sections remain unmeasured, or measured with large uncertainties. Analysis of data already obtained by the LBNL group will yield many new data points, particularly in the area of light-fragment production, and will reduce the uncertainties in others.

This project is entirely ground-based, with no need for flight experiments or the use of NASA's reduced-gravity facilities.

GROUND BASED EXPERIMENTS IN SUPPORT OF MICROGRAVITY RESEARCH RESULTS - VAPOR GROWTH OF ORGANIC NONLINEAR OPTICAL THIN FILM

M.Ittu Zugrav¹, W.E. Carswell², G.B. Haulenbeek² and F.C. Wessling³

¹Center for Microgravity and Materials Research

²Alliance for Microgravity Materials Science and Applications

³Department of Mechanical and Aerospace Engineering

University of Alabama in Huntsville

Huntsville, AL 35899

INTRODUCTION

This work is specifically focused on explaining previous results obtained for the crystal growth of an organic material in a reduced gravity environment. On STS-59, in April 1994, two experiments were conducted with N,N-dimethyl-p-(2,2-dicyanovinyl) aniline (DCVA), a promising nonlinear optical (NLO) material. The space experiments were set to reproduce laboratory experiments that yielded small, bulk crystals of DCVA. The results of the flight experiment, however, were surprising. Rather than producing a bulk single crystal, the result was the production of two high quality, single crystalline thin films. This result was even more intriguing when it is considered that thin films are more desirable for NLO applications than are bulk single crystals. Repeated attempts on the ground to reproduce these results were fruitless.

A second set of flight experiments was conducted on STS-69 in September 1995. This time eight DCVA experiments were flown, with each of seven experiments containing a slight change from the first reference experiment. The reference experiment was programmed with growth conditions identical to those of the STS-59 mission. The slight variations in each of the other seven were an attempt to understand what particular parameter was responsible for the preference of thin film growth over bulk crystal growth in microgravity. Once again the results were surprising. In all eight cases thin films were grown again, albeit with varying quality. So now we were faced with a phenomenon that not only takes place in microgravity, but also is very robust, resisting all attempts to force the growth of bulk single crystals.

The space growth parameters and samples were analyzed and the results were used to guide a systematic terrestrial investigation through the optimization and control of the growth cell orientation to the gravity vector, substrate temperature, deposition rate, and background pressure. The task was extended to include experiments with other NLO organic materials related to DCVA, vapor pressure measurements for the evaluation of the experimental transport situation, nitrogen background pressure variation during the heat-up and steady-state growth, thermal profile variation during the heat-up period, heat-up rates variation, supersaturation modification during the steady-state growth, and the substrate material variation.

1999 has been a breakthrough year for our ground based experiments in support of microgravity research results. Results of our work in 1999, since January when the first DCVA thin film was successfully grown on the ground, have yielded many encouraging and revealing results. A series of ground experiments launched an investigation into the parameters that control the thin film growth, revealing a very complicated system. We have established two thresholds behind which we must stay in order to grow these films. The first is a threshold for background nitrogen pressure below which bulk crystals grow rather than thin films. The second is related to the limiting conditions in terms of temperature.

The typical NLO organic material has at least one benzene ring, but more often will contain two benzene rings, which are either directly joined together or joined via an ethylene or azo linkage. A strong donor of electron density, such as a dialkyl amino group and strong acceptor of electron density, such as cyano group, are placed at the extreme ends of the conjugated molecule. This is done so that when placed in an electromagnetic field, such as a laser beam, electron density can flow from one end of the molecule to the other, creating a change in dipole moment and refractive index. It is this property that makes these materials useful for NLO applications. The NLO response is fast because the effects are derived almost exclusively from the movement of electrons, as opposed to setting the ions in motion as in LiNbO_3 , KD_2PO_4 , or BaTiO_3 . Growth of large, highly-ordered organic crystals is very difficult, and very few groups are continuing work in this area. In addition, the final shaping of the NLO material into a device favors the organic thin films. Therefore, the results of our ground work may have technological significance and may lead to new pathways to produce crystalline organic thin films in a variety of electronic and optical applications.

I. Material Properties

The DCVA is a donor/acceptor-substituted aromatic compound. The NLO properties of this new material have been recently [1] characterized by the Alliance for Nonlinear Optics in USA. The experimental second harmonic generation (SHG) powder test [1] using the YAG:Nd laser at 1064 nm revealed a weak and barely visible 532 nm signal, even at high power. These results were published in 1998 and they confirmed the results of our SHG experiments carried out on the DCVA space-grown thin films and published in 1997 [2,3]. At that time, our explanation was given based on the visible absorption spectrum of DCVA. The spectrum showed the onset of absorption around 532 nm. Using a Raman shifter at 1907 nm, DCVA gave a strong signal that is about 10 times that of urea [1]. The material displays thermal stability with no glassy state, polymorphism or polymerization in the melting-solidification cycles of the Differential Scanning Calorimetry (DSC) repeated scans [3]. The five year old space-grown DCVA thin films proved to have thermodynamic and photochemical stability. All these features are important to withstand many conventional semiconductor fabrication processes.

II. Description of the Crystal Growth Facility

A versatile flight-qualified Moderate Temperature Facility (MTF) has been developed for materials processing in space [4]. The MTF is capable of growing crystals and thin films on Earth and in space on a wide variety of carriers, including the International Space Station. The four successful flights on the United States Space Shuttles (STS-40, STS-57, STS-59, and STS-69) have demonstrated the MTF materials processing capability. Follow-up flight experiments

with electro-optic device-quality prepared substrates, are manifested for June 2001, on the STS-105, and on the 12A.1 mission in October 2002 on the International Space Station (ISS). The NLO Station hardware is presently being designed for the integration into the EXPRESS (Expedite the PROCESSING of Experiments to Space Station) Rack of the ISS. During the ground or space experiments the MTF is housed in a sealed canister and consists of a mounting structure, a vacuum vent valve assembly, a backfill assembly, a temperature controller, and the PVT (Physical Vapor Transport) hardware.

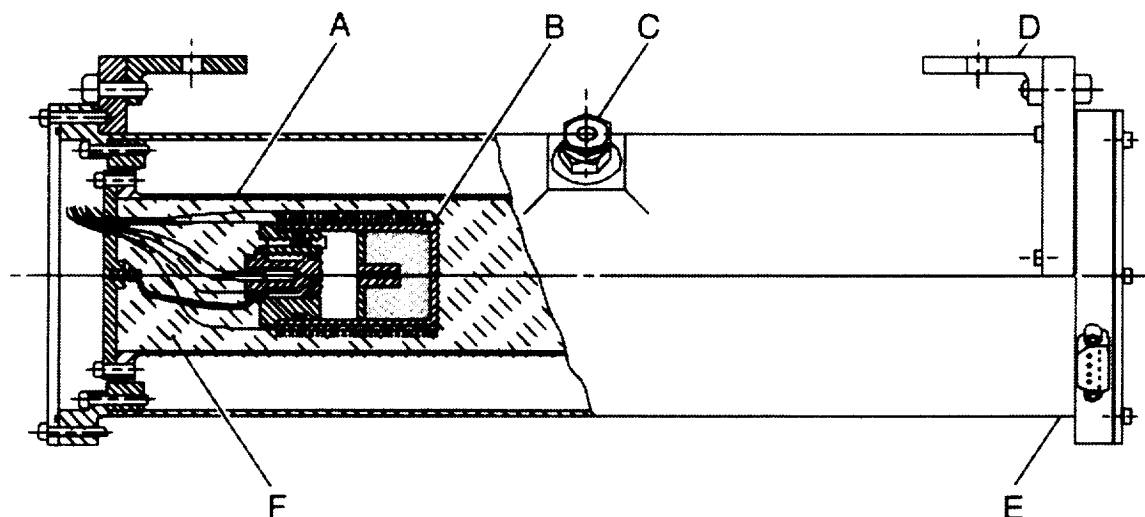


Figure 1. Cut-away view of assembled Moderate Temperature Facility oven. Primary components are: (A) inner cylinder, (B) crystal growth cell, (C) vacuum vent port, (D) mounting brackets, (E) outer cylinder, and (F) polyimide foam insulation.

The PVT hardware consists basically of six ovens. Construction of each of the ovens is identical, and is shown in a cut-away view in Figure 1, with a crystal growth cell installed in one end. The oven's power consumption is less than 3 W at 140°C. This thermal efficiency was achieved by addressing all three forms of heat loss: radiative, convective, and conductive. Radiative heat loss was minimized by using concentric cylinders with high reflectance and low emissivity. Convective heat loss was reduced by evacuating the area between the aluminum cylinders through the vent port in the outer cylinder. Conductive heat loss through the concentric metal cylinders was minimized by a special support mechanism consisting of a set of aramid strands impregnated with a high temperature, low viscosity epoxy. The polyimide foam insulation also plays a role in reducing conductive heat losses by thermally insulating the growth cell from the inner aluminum cylinder. The crystal growth cell is a semi-closed ampoule [5,6]. The source material is sublimed in the hot end of the ampoule and transported without chemical transformation in a temperature gradient to the growing interface. Continuous removal of (rate limiting) gaseous impurities is achieved by placing a calibrated leak to vacuum adjacent to the growing interface. The growth process of crystals is fully automated and consists of five essential sequences: outgassing and warm-up, growth, backfilling, and cool-down.

III. Significant Findings

For valid comparison, the space experiments must have, by definition, only the presence of reduced gravity as the factor differing from the ground control experiment. In our experiments

we identified two other factors as being different and both of them are related to the fluid transport. They are interdependent and difficult to control precisely. One of them is the temperature profile represented in Figure 2. Such a temperature profile may be an indication of a much higher background nitrogen pressure than the millitorr range used in the laboratory. This may be due to the presence of a 60 μm effluence filter and a small quantity of molecular sieve material

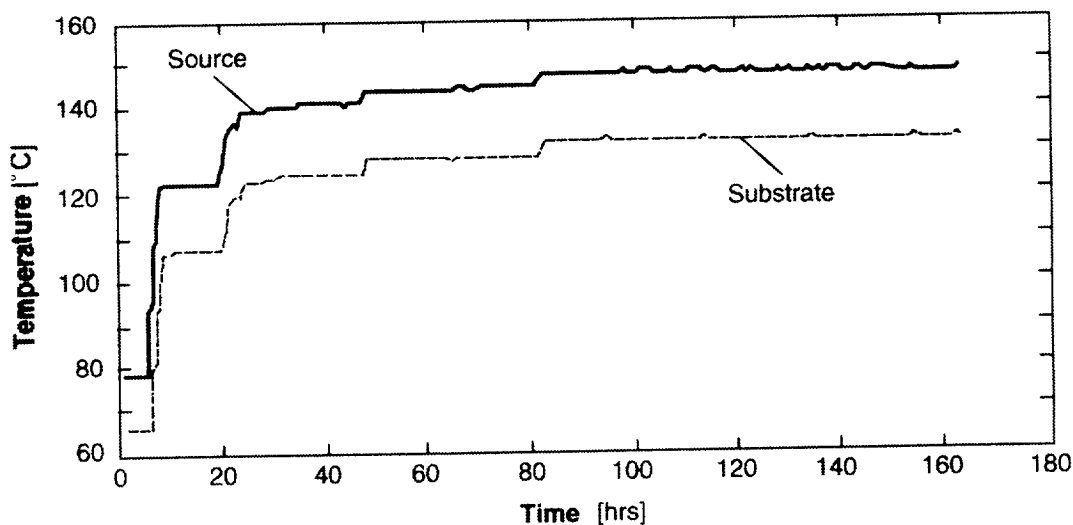


Figure 2. Temperature profile of a representative growth cell which flew on STS-59. The space samples tended to heat up in stages followed by plateaus, whereas the ground samples went directly to the set points in only 2 hours.

placed in our vacuum vent line, as required by NASA for safety. This changes in an uncontrolled way the background nitrogen pressure, the actual internal growth cell gas pressure and also affects the temperature profile. Laboratory tests with ground control hardware showed efficient, if somewhat moderately slower, evacuation with the 60 μm filter and molecular sieve material in place. Therefore, initial laboratory experiments were run with low nitrogen pressure conditions, on the order of millitorrs. It is under these conditions that bulk crystals form.

Eventually, however, it was realized that a unique condition existed on orbit that was not reproduced by ground control experiments. During the space shuttle launches, vibrations caused some of the molecular sieve material to powderize. This did not happen in the laboratory. Furthermore in the weightless environment the powder, small in quantity though it was, did not settle to the "bottom" of the evacuation tube but was swept into the 60 μm filter by the vacating gasses, effectively clogging the filter. This would not have happened in the laboratory even if the powder had been formed. Thus the evacuation rate in the space experiment was much, much less than the evacuation rate in the ground control experiment. Once these conditions became apparent it was decided to examine the opposite extreme of vacuum conditions and laboratory growth runs were carried out at higher pressures including the full atmospheric nitrogen pressure. Experiments at varying pressures and ΔT s (the difference in temperature between the substrate and the source material) appear to indicate that there is a transition region at which growth changes from thin films to bulk crystals [7-10]. One particular experiment dramatically made this point at $\Delta T = 15^\circ\text{C}$ and $P = 2 \times 10^{-1}$ torr.

Past efforts have been successful in growing DCVA thin film on the ground, but only on copper substrates. Very recent test results showed thin films grown on glass and transparent substrates for the first time. This significant development opens the way for better characterization of the films by transmission methods, and for use of these films in NLO devices. Future experiments will include the additional capability of *in situ* observation through the installation of a fiberscope, permitting visualization of the growth process in real time, and yielding significant understanding of the mechanisms for the two different types of crystal formation. The fiberscope is an important feature lacking in previous experiments. It will add considerable insight into the "Van der Waals" nature of the epitaxial growth process for DCVA.

IV. Conclusions

Background nitrogen pressure appears to be the key to transforming from the bulk crystal growth morphology to the thin film crystal growth morphology. The question now becomes one of understanding the role being played by the nitrogen gas and optimizing the growth process. A possible explanation could be that at higher pressures the nucleation could be controlled to the point that only a few nuclei, perhaps just one, will grow into a thin film or a thin-plate like crystal. The successful development of the ground thin film technology is a direct result of information gleaned from experiments conducted in microgravity on two space shuttle missions.

V. Acknowledgement

Support of this work under NASA grant NAG8-1456 is gratefully acknowledged.

REFERENCES

1. Antipin, M. Yu, Timofeeva, T. V., Clark, R. D., Nesterov, V. N., Sanghadasa, M., Barr, T. A., Penn, B., Romero, L., and Romero, M. "Molecular crystal structures and nonlinear optical properties in the series of dicyanovinylbenzene and its derivative" J. Phys. Chem. A, 102, (1998) 7222.
2. Ittu Zugrav, M., Wessling, F. C., Carswell, W. E., Leslie, T. M., Watson, C., and Lundquist, C. A. "Vapor deposited organic thin film in microgravity" J. Crystal Growth 174, (1997) 130.
3. Ittu Zugrav, M., Carswell, W. E., Lundquist, C. A., Wessling, F. C., and Leslie, T. M. "Physical vapor transport experiments on board the Space Shuttle Endeavour" in Materials Research in Low Gravity, SPIE 3123, (1997) 110.
4. Wessling, F. C. and Carswell, W. E. "Moderate temperature facility for materials processing in space", Microgravity Sci. Technol. VIII/3, (1995) 196.
5. Ittu Zugrav, M. and Rosenberger, F. "Ground-based vapor crystal growth experiments", in Materials Research in Low Gravity, SPIE 3123, (1997) 135.
6. Ittu Zugrav, M. and Rosenberger, F. "Towards efficient crystal growth of 4-(N,N-dimethylamino)-3-acetamidonitrobenzene (DAN) in space - Vapor pressure measurements and growth morphology studies", in Space Processing of Materials, SPIE 2809, (1996) 271.
7. Carswell, W. E., Ittu Zugrav, M., and Wessling, F. C. Disclosure of a novel technique for growing organic thin films for probable patents and trade secrets was signed on May 6, 1999. Patent in process.

8. Carswell, W. E., Ittu Zugrav, M., Haulenbeek, G. and Wessling, F. C., "Ground and space processing of single-crystalline organic thin films" *J. Crystal Growth*, in print.
9. Ittu Zugrav, M. I., Wessling, F. C., and Carswell, W. E. "Vapor transport growth of organic crystals: Morphology versus microgravity," *Proceedings of the XVIIIth International Union of Crystallography Congress, Glasgow, Scotland*, C. C. Willson, K. Shankland, and T. Csoka, eds., *Acta Crystallographica*, A55, (1999) 535.
10. Ittu Zugrav, M., Carswell, W. E., and Wessling, F. C. "Ground and Space Processing of Nonlinear Optical Organic Materials", in the Book "Recent Developments in Crystal Growth Research", K. Benz, D. Schwabe and I. Higashi, eds., Transworld Research Network. Invited. In print.

Appendix A: Author Index

A

Abbaschian, R. 1, 21
Abid, M. 510
Adair, James H. 580
Adam, J.D. 548
Advincula, Rigoberto 422
Agladze, N.I. 539
Ainsworth, William 477
Alemozafar, Ali Reza 310
Alexander, J. Iwan D. 22, 63, 70
Alexandrou, A.N. 517
Alkemper, Jens 24, 614
Altan, M. C. 27
Altgilbers, A.A. 76
Anderson, D.M. 435
Anderson, Timothy J. 33
Andrews, J. B. 39, 45
Anilkumar, A.V. 279
Apfel, Robert E. 52
Asherie, Neer 98
Ayers, M.R. 316
Ayyaswamy, P.S. 188
Aziz, Michael J. 57

B

Bachmann, K.J. 176
Backov, Rénal 580
Badavi, F.F. 648
Badhwar, G.D. 648
Baker, S. 516
Banish, R. Michael 63, 70
Bates, F.S. 293
Baughman, R.H. 407
Bayuzick, R.J. 76, 301
Beckermann, C. 82, 86
Bellizia, G. 440
Benard, A. 92
Benedek, George B. 98
Benz, K.W. 573
Bermudez, H. 293
Bernholc, Jerry 103
Berns, David 116
Bhowmick, J. 279
Boboridis, Konstantinos 531
Boettinger, W.J. 435
Bonilla, G. 608
Booth, N. A. 127
Bowman, Christopher 409
Brady, J. F. 109
Brannan, A. 293
Brebrick, Prof. Robert F. 568
Brezinsky, Kenneth 113

Brown, M.E. 308
Brun, R. 465
Burger, Dr. Arnold 568
Burkhard, Craig 487

C

Carminati, F. 465
Carswell, W.E. 666
Catalina, A.V. 556
Cebe, Peggy 116
Cha, Soyoung Stephen 121
Chait, A. 360
Chekanov, Yuri 477
Chelikowsky, J.R. 170, 174
Chen, P.Y.P. 1
Chen, W. 551
Chernov, A. A. 127
Cima, Michael J. 133
Clark, Noel A. 409
Claude, Juan Pablo 422
Clowdsley, M.S. 648
Cobb, S.D. 573
Coimbra, Carlos 599
Cooper, Reid F. 135
Coriell, S.R. 45, 430, 548
Courtney, T.H. 141
Crawford, G.P. 637
Croat, T.K. 353
Cröll, A. 573
Cronise, R. 288
Crunkleton, Daniel W. 33
Cucinotta, F.A. 149, 295, 648
Curreri, P.A. 556

D

Dantzig, Jonathan A. 150, 157
Davis, G. de Vahl 1, 21
Day, Delbert E. 158
de Groh III, H.C. 1, 82, 86, 346, 388, 585
Debelak, Kenneth A. 164
Derby, J.J. 170, 172, 174
Dhanaraj, G. 308
Diaz, A.R. 92
Dietz, N. 176
Discher, B. 293
Discher, D.E. 293
Dold, P. 573
Downey, J. Patton 259
Dreizin, E.L. 182
Du, Y. 141
Ducheyne, P. 188
Dudley, M. 194, 308, 568
Duffar, T. 451

Dumont, Thierry 477
Dutta, Prabir K. 199
Duval, W.M.B. 548

E

El-Shall, M.S. 204
Engel, H.P. 244
Ethridge, Edwin C. 210
Evans, J.W. 213
Everman, Rebecca L.A. 135

F

Fedoseyev, A.I. 216, 282
Feigelson, R.S. 222
Ferrari, A. 465
Feth, Dr. Shari 562
Flemings, M.C. 228
Frate, David T. 585
Frazier, Donald O. 259
Frei, J.E. 246, 253
Friedli, Andrienne C. 234
Fripp, A. 346

G

Gangopadhyay, A. 353
Gao, H. 188
Gatsonis, N.A. 517
Ge, Yi 121
Georgiev, Georgi 116
German, Randall M. 239
Geyer, U. 332
Gillies, Donald C. 244, 375
Giummar, C. 246
Glaser, Matthew A. 409
Glicksman, M.E. 246, 253, 259, 360
Gokhale, A.M. 267
Goldenfeld, Nigel 150, 157
Golyshev, V.D. 21
Gonik, M. 21
Grady, B. P. 27
Greenberg, A.R. 273
Grugel, R.N. 279, 282, 423
Guimarra, C. 253
Gupta, P. K. 283
Gür, Turgut M. 310
Gustafson, D.E. 301
Gustafson, R.J. 499

H

Halas, N.J. 288
Hammer, D.A. 293
Haulenbeek, G.B. 666
Hays, C. 332
Heilbronn, L. 295, 419, 446, 648, 664
Heinbockel, J.H. 648

Heinrich, J.C. 471
Hofmeister, W.H. 76, 301
Holland-Moritz, D. 353
Hollingsworth, M.D. 308
Homsy, George M. 310
Hu, Z. 283
Hunt, A.J. 316
Hyers, Robert W. 353

I

Iacocca, Ronald G. 239
Izmailov, A.F. 447

J

Jackson, Kenneth A. 322, 323
Jalbert, Lyle B. 63
Jeter, L. 451
Johnson, David R. 325
Johnson, W.L. 332
Jones, W.K. 213
Jordan, J. 499
Jouravlev, O. 407
Juretzko, F.R. 556

K

Kaforey, M.L. 413
Kaiser, N. 573
Kang, Nam Hyun 543
Kaplan, David L. 334
Karma, A. 82, 86, 340, 345, 593
Kartavykh, A. 407
Kassemi, M. 22, 346
Kaszynski, Piotr 234
Keefer, L.A. 413
Kelton, K.F. 353
Kerle, T. 516
Khayrullin, I.I. 407
Kim, M.Y. 295, 648
Kim, S. 282
Kinnison, J.D. 419
Kizito, J. P. 22
Klabunde, K.J. 359
Koochesfahani, M.M. 92
Koss, M.B. 246, 253, 360
Kou, S. 366
Krane, Matthew John M. 325
Krantz, W.B. 273
Krishnan, Shankar 372, 531
Kulkarni, Anil K. 543

L

LaCombe, J.C. 246, 253, 360
Lai, F.-C. 27
Lal, Ravindra B. 599
Larson, Dr. David J., Jr. 374

Lee, C.-M. 293
 Lehoczky, Sandor L. 375, 562
 Lemdiasov, R.A. 517
 Leonardi, E. 1, 21
 Leslie, F. 213
 Lewis, J.A. 377
 Li, Ben Q. 382, 388
 Li, Fengcui 643
 Lian, Y. 1
 Limmaneevichitr, C. 366
 Lin, X.M. 359
 Lin, Z. 516
 Lomakin, Aleksey 98
 Löser, W. 228
 Lowry, S. 394
 Lu, S.Z. 141
 Lupulescu, A.O. 246, 253
 Luz, P. 451

M

Ma, Nancy 401
 MacKnight, A. 407
 Magda, Jules J. 409
 Malarik, D.C. 253
 Manka, Jason T. 234
 Marin, C. 451
 Martin, Raquel 334
 Masere, Jonathan 477
 Mason, L.W. 411
 Matson, D.M. 228
 Matthiesen, D.H. 413
 Matyi, Prof. Richard J. 194, 568
 Maurer, R.H. 419
 Mays, J. 422, 516
 Mazumder, S. 394
 Mazuruk, Dr. Konstantin 423
 McCall, S. 176
 McFadden, G.B. 430, 435
 McGrath, J.J. 92
 McNallan, M. 440
 Megaridis, C.M. 440
 Meiburg, E. 510
 Miller, J. 295, 419, 446, 648, 664
 Mook, Dr. Herb 562
 Morris, R. 407
 Motakef, Dr. Shariar 423
 Motakef, S. 573
 Mukherjee, S. 556
 Mullins, W.W. 505
 Murray, B.T. 430
 Myerson, A.S. 447

N

Napolitano, R. 593
 Narayanan, Ranga 33
 Naumann, Robert J. 449

Nikolakis, V. 608
 Nordine, Paul 624, 630

O

Ohsaka, K. 519
 Oldenburg, S.J. 288
 O'Rear, E. A. 27
 Ostrogorsky, A.G. 451

P

Pankajavalli, R. 33
 Peignier, T. 451
 Pekny, M.R. 273
 Perepezko, J.H. 458
 Peterson, M.L. 308
 Pines, V. 360
 Pinsky, L.S. 465
 Pithawalla, Y.B. 204
 Poirier, D.R. 471
 Pojman, John A. 477
 Popov, Dmitri 643
 Pourpoint, Timothee 70
 Price, David L. 372

R

Radin, S. 188
 Radzihovsky, Leo 409
 Rafailovich, Miriam H. 483
 Raghothamachar, B. 308
 Rakov, V. 407
 Ramachandran, Narayanan 568
 Ramanathan, Ram 643
 Rangel, Roger 599
 Rashidnia, N. 346
 Rathz, Thomas J. 353
 Ray, Chandra S. 158
 Regel, Liya L. 487, 638, 643
 Rhim, Won-Kyu 493
 Rice, E.E. 499
 Robinson, Michael B. 353
 Rogers, Jan R. 228, 259, 353, 599
 Rohrer, G.S. 505
 Roland, Christopher 103
 Ronney, P.D. 510
 Roth, D.R. 419
 Roth, John A. 164
 Russell, T.P. 516
 Rusyniak, M. 204

S

Saboungi, Marie-Louise 372
 Sacco, A., Jr. 517
 Sadhal, S.S. 519
 Sadoway, Donald R. 525
 Sala, Paola 465

Sampath, Rajiv 658
 Sanders, Paul G. 57
 Schaefer, Robert 531
 Schroers, J. 332
 Schweizer, M. 573
 Scripa, Dr. Rose 562
 Sekerka, Robert F. 533
 Sen, S. 556
 Sengupta, D. 394
 Serrano, Brenda 33
 Seybert, C. 213
 Sha, Yi-Gao 568
 Shavers, M.R. 149
 Shih, Dr. Hung-Dah 568
 Shin, In-Seok 449
 Shinn, J.L. 648
 Sibille, L. 288, 316
 Sievers, A.J. 539
 Singh, Jogender 543
 Singh, N.B. 548
 Singleterry, R. 295, 419, 446, 648, 664
 Slepicka, James S. 121
 Smith, D.D. 288, 316
 Snyder, V.A. 614
 Song, KwangJin 52
 Sorensen, C.M. 359
 Sridhar, K.R. 551
 Stefanescu, D.M. 556
 Steinbach, I. 82, 86
 Stoeva, S. 359
 Su, Ching-Hua 562, 568
 Szofran, F.R. 375, 573

T

Talham, Daniel R. 580
 Tewari, A. 267
 Tewari, S.N. 471, 586
 Thibeault, S. 295, 446, 648
 Timchenko, V. 1
 Tin, Padetha 585
 Todd, P. 273
 Townsend, L.W. 295
 Tripathi, R.K. 149, 648
 Trivedi, R. 345, 586, 593
 Trolinger, James D. 599
 Trznadel, Mirosław 234
 Tsapatsis, M. 608
 Tsvetivsky, V. 21
 Tucker, Dennis S. 210

U

Ufimtsev, V. 407

V

Valluzzi, Regina 334
 Vekilov, P. 127
 Vlachos, D.G. 608
 Vlasse, M. 411
 Volpert, Vitaly 477
 Volz, Dr. Martin 451, 568, 573
 Voorhees, P.W. 24, 614
 Vujisic, L. 573

W

Walker, J.S. 573
 Walker, John S. 619
 Wallace, D.B. 440
 Wang, Yazhen 487
 Way, J.D. 411
 Weber, Richard 624, 630
 Wessling, F.C. 666
 Wheeler, A.A. 435
 Whitehead, J.B., Jr. 637
 Wiegel, M. 656
 Wilcox, William R. 487, 638, 643
 Wilke, Hermann 477
 Wilson, Donna 334
 Wilson, J. 295
 Wilson, J.W. 149, 446, 648, 664
 Wilson, T.L. 465
 Witherow, William 259, 599
 Witt, A.F. 656
 Wolfe, D. 288
 Won, Y.-Y. 293

Y

Yeckel, A. 172

Z

Zabaras, Nicholas 658
 Zaccaro, J. 447
 Zakhidov, A.A. 407
 Zartman, J. 273
 Zeitlin, C.J. 295, 419, 446, 648, 664
 Zhang, Dr. Hui 374, 548
 Zharikov, E.V. 222
 Zhu, Dr. Shen 562
 Zugrav, M.Ittu 666

Appendix B: Acronyms and Abbreviations

AADSF	Advanced Automated Directional Solidification Furnace
AAL	Aero-Acoustic Levitation
AAS	Atomic Absorption Spectroscopy
ACCESS	Advanced Cosmic Ray Composition Experiment
ACRT	Accelerated Crucible Rotation Technique
AGHF	Advanced Gradient Heating Facility
AHP	Axial Heat Processing
ALICE	Heavy ion experiment being built for the Large Hadron Collider (LHC) project at CERN, Geneva, Switzerland
ALN	Aluminum Nitride
AOTF	Acousto-Optic Tunable Filter
AP	Ammonium persulfate
ASD	Accelerated Stokesian Dynamics
ATD	Advanced Technology Development
ATLAS	Atmospheric Laboratory for Applications and Science
BCC	Body Centered Cubit
BEI	Backscatter Electron Images
BG	Bioactive Glass
BMG	Bulk Metallic Glasses
BODIPY	A fluorescein derivative
BRYNTRN	Radiation transport code
BUU	Boltzmann-Uehling-Uhlenbeck
CA	Cellular Automata
CAM	CO ₂ Acquisition Membrane
CCD	Charge-Coupled Device
CDC	Container-Less Directional Solidification
CERN	European Laboratory for Particle Physics (Geneva, Switzerland)
CFD	Computational Fluid Dynamics
CFX	Commercial Flow Code
CGB	Crystal Growth with a Baffle
CGH	Coupled Growth in Hypermonotectics
CMDS	Center for Materials Development in Space (at the University of Alabama in Huntsville, AL)
CMMR	Center for Microgravity Materials Research (at the University of Alabama in Huntsville, AL)
CNES	Centre National d'Etudes Spatiales (France)
CNES	Centre Nationale d'Études Spatiales ("National Center for Space Studies," French Space Agency)
CRI	Containerless Research Incorporated
CSLM	Coarsening in Solid-Liquid Mixtures
CSM	Colorado School of Mines
CT	Computed Tomography
CTE	Coefficient of Thermal Expansion
CVS	Coupled Vibrational Stirring
DCC	Diffusion Cloud Chamber

DCVA	N,N-dimethyl-p-(2,2-dicyanovinyl) aniline
DDC	Dynamic Decompression and Cooling
DECLIC	Dispositif pour l'Etude de la Croissance et des Liquides Critiques (DECLIC) (Facility for the Study of the Growth and the Fluids near Critical Point)
DIT	Diffusion Interface Theory
DLS	Dynamic Light Scattering
DLVO	Derjaguin, Landau, Verwey, Overbeek
DMSO	High temperature solvent
DNS	Direct Numerical Simulations
DODMAC	Dimethyldioctylammonium chloride
DOE	Department of Energy
DPIMS	Diffusion Processes in Molten Semiconductors
DSC	Differential Scanning Calorimetry
DTA	Differential Thermal Analysis
EBW	Electron-Beam Welding
ED	Electron Diffraction
EDG	Electro Dynamic Gradient
EDGE	Equiaxed Dendritic Solidification Experiment
EDS	Energy Dispersion Spectroscopy
EDS	Energy Dispersive X-ray Spectroscopy
EIS	Electrochemical Impedance Spectroscopy
EIT	Effective Interfacial Tension
EITIC	Effective Interfacial Tension Induced Convection
EKTAPRO	A Kodak camera
ELMS	Evolution of Local Microstructures
ELT	Electrodynamic Levitator Trap
EML	Electromagnetic Levitator
EPD	Etch Pit Density
EPMA	Electron Probe Micro-Analyzer
ESL	Electrostatic Levitation/Levitator
EXPRESS	(Expedite the Processing of Experiments to Space Station)
FCC	Face Centered Cubit
FDLB	Finite Difference Lattice Boltzmann
Fe-MAS	Fe-bearing Magnesium Aluminosulphate
FLUENT	Computational fluid dynamics software
FLUKA	A Monte-Carlo simulation code for radiation transport
FTIR	Fourier Transform Infrared Spectrometry
FZ	Float/floating Zone
GCR	Galactic Cosmic Ray
GDMS	Glow Discharge Mass Spectroscopy
GEANT	A Monte-Carlo simulation code for radiation transport
GF-AA	Graphite Furnace- Atomic Absorption Spectroscopy
GFL	Gas Film Levitation
GOSAMR	Gelation of Sols; Applied Microgravity Research
GTAW	Gas-Tungsten Arc Welding
GUI	Graphical User Interface
HAD	High-density Amorphous

HARV	High Aspect Ratio Vessel
HBT	High Performance Transistors
HD	Hoop Direction
HDDA	hexane diol diacrylate
HDIV	Holographic Diffraction Image Velocimetry
HDPE	High-Density Polyethylenes
HECT	High Energy Transport Code
HEDS	Human Exploration and Development of Space
HEMA	hydroxyethyl methacrylate
HETC	A Monte-Carlo simulation code for radiation transport
HPCVD	High Pressure Chemical Vapor Deposition
HPMS	High Pressure Mass Spectrometry
HRTXD	High Resolution Triple Crystal X-ray Diffractometry/Diffraction
HTESL	High Temperature Electrostatic Levitator
HTSC	High Temperature Superconductor
HZETRN	Radiation transport code
ICP-AES	Inductively Coupled Plasma-Atomic Emission Spectroscopy
ICP-MS	Inductively Coupled Plasma-Mass Spectrometry
IDGE	Isothermal Dendritic Growth Experiment
IML	International Microgravity Laboratory
INFN	Instituto Nazionale di Fisica Nucleare (Italian National Nuclear Physics funding agency)
IR	Infra Red
ISCP	<i>In-Situ</i> Consumables Production
ISPP	<i>In-Situ</i> Propellant Production
ISRU	<i>In-Situ</i> Resource Utilization
ISS	International Space Station
ITO	Indium-Tin-Oxide
JPL	Jet Propulsion Laboratory (Pasadena, CA, managed by the California Institute of Technology)
JSC	NASA Johnson Space Center (Houston, TX)
KC-135	A NASA aircraft that performs parabolic maneuvers to produce short durations (20 seconds) of reduced gravity (0.01 g) environment.
KDP	Potassium Dihydrogen Phosphate
KSC	NASA Kennedy Space Center (Cape Canaveral, FL)
LAHET	A Monte-Carlo simulation code for radiation transport
LaRC	NASA Langley Research Center (Hampton, VA)
LB	Langmuir-Blodgett
LB	Lattice Boltzmann
LBNL	Lawrence Berkeley National Laboratory
LBW	Laser Beam Welding
LC	Liquid Crystal
LCP	Liquid Crystalline Polymeric
LDA	Low-density Amorphous
LDPE	Low-Density Polyethylenes
LED	Light Emitting Diode
LEO	Low Earth Orbit

LET	Linear Energy Transfer
LF	Low Frequency
LIF	Laser-Induced Fluorescence
LM	Lockheed Martin
LMS	Life and Microgravity Spacelab
LPS	Liquid Phase Sintering
MCA	Membrane Casting Apparatus
MCA	Multi-Channel Analyzer
MD	Molecular Dynamics
MDO	Multidisciplinary Optimization
MEPHISTO	Matériau pour l'Étude des Phénomènes Intéressants de la Solidification sur Terre et en Orbite ("Apparatus for the Study of Interesting Phenomena of Solidification on Earth and in Orbit")
MeV	One million electron volts
MGB	Materials Science Glovebox
MI	Melt Indices
MIT	Massachusetts Institute of Technology
MITH	Millikelvin Thermostat
MNR	Nuclear Magnetic Resonance
MOCVD	Metal Organic Chemical Vapor Deposition
MOR	Modulus of Rupture
MRD	Microgravity Research Division
MSAD	Microgravity Science and Applications Department
MSFC	NASA Marshall Space Flight Center (Huntsville, AL)
MSL	Microgravity Sciences Laboratory
MSL-1R	Materials Sciences Laboratory (R represents the reflight)
MST	Microscopic Solvability Theory
MST	Minimum Spanning Tree
MTF	Membrane Test Facility
MTF	Moderate Temperature Facility
MTV	Molecular Tagging Velocimetry
MV	Macrovoids
MVPD	Macrovoid Penetration Depth
NAA	Neutron Activation Analysis
NCS	Nucleation of Crystals from Solution
NCSL	Nanocrystal Superlattices
ND	Normal Direction
NIST	National Institute of Standards and Technology
NLO	Nonlinear Optical
NMR	Nuclear Magnetic Resonance
NRA	NASA Research Announcement
NSF	National Science Foundation
NUCFRG	A radiation transport code
OB	Oberbeck-Boussinesq
OMCVD	Organometallic Chemical Vapor Deposition
OO	Object Oriented
ORBITEC	Orbital Technologies Corporation

OSD	Office of the Secretary of Defense
PAW	Physics Analysis Workstation
PB	Polybutadiene
PBT	Polybutylene terephthalate
PC	Personal Computer
PD	Penetration Depth
PDLC	Polymer Dispersed Liquid Crystals
PDM	Power Distribution Module
PE	Polyethylene
PEE	Polyethylethylene
PEO	Polyethylene Oxide
PEP	Particle Engulfment and Pushing
PI	Principal Investigator
PID	Proportional Integral Derivative
PIPS	Polymerization Induced Phase Separation
PIV	Particle Image Velocimetry
PL	Photoluminescence
PMMA	polymethylmethacrylate
POCC	Payload Operations Control Center (NASA MSFC)
Pr	Prandtl Number
PS	polystyrene
PVA	Pivalic Acid
PVT	Physical Vapor Transport
QMSFRG	Quantum Multiple Scattering Fragmentation Model, a radiation transport code
QMST	Quantum Multiple Scattering Theories
R2PI	Resonant-Two-Photon-Ionization
RDF	Radial Distribution Function
RDR	Requirements Definition Review
RE	Rare Earth
Re	Reynolds Number
REMPI	Resonance Enhanced Multiphoton Ionization
RIDGE	Rensselaer Isothermal Dendritic Growth Experiment
RMF	Rotating Magnetic Field
ROMP	Ring Opening Metathesis Polymerization
ROOT	An object-oriented physics analysis infrastructure
RQC	Rotating Quench Cell
RWV	Rotating Wall Bioreactor Vessel
SAMS	Space Acceleration Measurement System
SAXS	Small-Angle X-ray Scattering
Sc	Schmidt Number
SCN	Succinonitrile
SCN-ACE	Succinonitrile-acetone
SCN-E	Succinonitrile-ethanol
SCN-GLY	Succinonitrile-glycerol
SCN-W	Succinonitrile-water
SCR	Science Concepts Review
SD	Standard Deviations

SD	Stokesian Dynamics
SEM	Scanning Electron Microscopy
SEP	Société Européenne de Propulsion
Sh	Sherwood Number
SHG	Second Harmonic Generation
SHIVA	Spaceflight Holography Investigation in a Virtual Apparatus
SHS	Self-propagating High-temperature Synthesis
SIMS	Secondary Ion Mass Spectrometry
SIPS	Solvent Induced Phase Separation
SIV	Stereoscopic Imaging Velocimetry
SLI	Solid-liquid Interface
SOPC	Stearoyl, Oleoyl Phosphatidylcholine
SPE	Solar Particle Event
STM	Scanning Tunneling Microscopy
STS	Space Transportation System (Shuttle/external tank/solid rocket booster system, also a Shuttle mission designation)
SUBSA	Solidification Using the Baffle in Sealed Ampoules
SWBXT	Synchrotron White Beam X-ray Topography
TDSE	Transient Dendritic Solidification Experiment
TEM	Transmission Electron Microscopy
TEM	Tunneling Electron Microscope
TEMC	Thermoelectromagnetic Convection
TEMPUS	Tiegelfreies Elektromagnetisches Prozessieren Unter Schwerelosigkeit (German Electromagnetic Containerless Processing Facility)
TEOS	Tetraethylorthosilicate
TEPC	Tissue Equivalent Proportional Counter
THM	Traveling Heater Method
TIPS	Thermally Induced Phase Separation
TLS	Two Level System
TMF	Traveling Magnetic Field
TRL	Technology Readiness Level
TRR	Time-Resolved Relativity
TSL Theory	Classical Theory of Phase Coarsening by Todes, Lifshitz, and Slyozov
TTT	Time-Temperature-Transformation
UAH	University of Alabama in Huntsville
UF	Utilization Flight
USAXS	Ultra-Small Angle X-ray Scattering
USML	United States Microgravity Laboratory
USMP	United States Microgravity Payload
UV	Ultra Violet
UW	University of Wisconsin
VB	Vertical Bridgman
VFMV	Flow-Visualized Microvoid
WAXS	Wide Angle X-Ray Scattering
WCI	Wetting Characteristics of Immiscibles
XCAP	Image analysis software
XRD	X-ray Diffraction

XRF	X-ray Fluorescence
YAG	Yttria Aluminum Garnet
YSV	Yttria Stabilized Zirconia
YSZ	Yttria-stabilized zirconia
ZBLAN	A glass which contains the fluorides of zirconium, barium, lanthanum, aluminum, and sodium

Appendix C: Contributor Address List

Prof. Reza Abbaschian
University of Florida
Department of Materials Science and Engineering
P.O. Box 116400
132 Rhines Hall
Gainesville, FL 32611-2066
T 352-846-3300; F 352-392-7219
rabba@mse.ufl.edu

Dr. M. Abid
University of Southern California
Department of Aerospace and Mechanical
Engineering
Los Angeles, CA 90089-1453

Prof. James H. Adair
Pennsylvania State University
Materials Science and Engineering
217 Materials Research Laboratory
University Park, PA 16802
T 814-863-6047; F 814-863-9704
JAdair@mrl.psu.edu

Dr. J. D. Adam
Northrop Grumman Corporation
Science and Technology Center
ESSS MS-3D14, ATL
1212 Winterson Road
Linthicum, MD 21090
F 410-765-7652

Prof. Rigoberto Castillo Advincula
University of Alabama, Birmingham
Department of Chemistry
CHEM Building, Room 201
901 14th Street South
Birmingham, AL 35294-1240
T 205-934-8286; F 205-934-2543
gobet@uab.edu

Dr. N. I. Agladze
Cornell University
Laboratory of Atomic and Solid State Physics
517 Clark Hall
Ithaca, NY 14853-2501
F 607-255-6428

Mr. William Ainsworth
University of Southern Mississippi
Department of Chemistry and Biochemistry
P. O. Box 5043
Hattiesburg, MS 39406-5053
F 601-266-6045

Prof. Ali Reza Alemozafar
Stanford University
Laboratory for Advanced Materials
McCullough Building
476 Lomita Mall
Stanford, CA 94305-4045

Prof. Iwan Alexander
Case Western Reserve University
Department of Mechanical and Aerospace
Engineering
416 Glennan Building
10900 Euclid Avenue
Cleveland, OH 44106
T 216-368-6045; F 216-368-6445
ida2@po.cwru.edu

Dr. Andreas Alexandrou
Worcester Polytechnic Institute
Mechanical Engineering Department
100 Institute Road
Worcester, MA 01609-2280
T 508-831-5147; F 508-831-5680
andalexa@wpi.wpi.edu

Prof. Jens Alkemper
Northwestern University
Department of Materials Science and Engineering
2225 North Campus Drive
Evanston, IL 60208-3108
T 847-491-5943; F 847-491-7820
j-alkemper@nwu.edu

Prof. M. Cengiz Altan
University of Oklahoma
School of Aerospace and Mechanical Engineering
865 Asp Avenue, Room 212
Norman, OK 73019
T 405-325-1737; F 405-325-1088
altan@ou.edu

Mr. Alex Altgilbers
Vanderbilt University
5527 Kenadall Drive
Nashville, TN 37209
T 615-322-2756; F 615-343-8645
asa@vuse.vanderbilt.edu

Prof. D. M. Anderson
George Mason University
Department of Mathematical Sciences
Fairfax, CA 27599

Prof. Timothy J. Anderson
University of Florida
Department of Chemical Engineering
P.O. Box 116005
Gainesville, FL 32611
T 352-392-0881; F 352-392-9513
tim@nersp.nerdc.ufl.edu

Prof. J. Barry Andrews
University of Alabama, Birmingham
Department of Materials and
Mechanical Engineering, BEC 254
1150 10th Avenue Southwest
Birmingham, AL 35294
T 205-934-8452; F 205-934-8485
bandrews@Engr.uab.edu

Prof. A. V. Anilkumar
Vanderbilt University
1743 Station B
Nashville, TN 37235
T 615-343-7293; F 615-343-8730
nil@vuse.vanderbilt.edu

Prof. Robert E. Apfel
Yale University
Department of Mechanical Engineering
Room M-1
9 Hillhouse Avenue
P.O. Box 208286
New Haven, CT 06520-8286
T 203-432-4346; F 203-432-7654
robert.apfel@yale.edu

Dr. Neer Asherie
Massachusetts Institute of Technology
Department of Physics
Center for Materials Science and Engineering
Material Processing Center
77 Massachusetts Avenue
Cambridge, MA 02139

Dr. Michael R. Ayers
Lawrence Berkeley National Laboratory
1 Cyclotron Road
MS 70-110A
Berkeley, CA 94720
T 510-486-4292; F 510-486-7303
mrayers@inreach.com

Prof. Portonovo S. Ayyaswamy
University of Pennsylvania
Department of Mechanical Engineering and
Applied Mechanics
Philadelphia, PA 19104-6315
T 215-898-8362; F 215-573-6334
ayya@eniac.seas.upenn.edu

Prof. Michael J. Aziz
Harvard University
Division of Engineering and Applied Sciences
29 Oxford Street
Cambridge, MA 02138-2901
T 617-495-9884; F 617-495-9837
maziz@harvard.edu

Prof. Klaus J. Bachmann
North Carolina State University
Department of Materials Science and Engineering
Research Bldg.-1, Room 219
Box 7919, Centennial Campus
100 Capability Drive
Raleigh, NC 27695-7919
T 919-513-1926; F 919-515-3419
k_bachmann@ncsu.edu

Prof. Renal Backov
University of Florida
Department of Chemistry
P.O. Box 117200
Gainesville, FL 32611-7200
F 352-392-3255

Prof. F. F. Badavi
Christopher Newport University
1 University Place
Newport News, VA 23606

Dr. Gautam D. Badhwar
NASA JSC
Solar System Division
Mail Code SN
2101 NASA Road One
Houston, TX 77058-3696
T 281-483-5065; F 281-483-5276
gautam.d.badhwar1@jsc.nasa.gov

Dr. S. Baker
University of Massachusetts
Polymer Science and Engineering Department
Amhurst, MA 01003-4530

Prof. R. Michael Banish
University of Alabama, Huntsville
CMMR, VBRH, D-11
301 Sparkman Drive
Huntsville, AL 35899
T 256-824-6969; F 256-824-6944
banishm@email.uah.edu

Prof. Frank S. Bates
University of Minnesota
Department of Chemical Engineering and
Materials Science
Amundson Hall
421 Washington Avenue, S.E.
Minneapolis, MN 55455-0132

Prof. R. H. Baughman
New Jersey Institute of Technology
University Heights
Newark, NJ 07102-1982

Prof. Robert J. Bayuzick
Vanderbilt University
Department of Chemical Engineering
303A Olim Hall
Nashville, TN 37235
T 615-322-7047; F 615-343-8645
bayuzick@vuse.vanderbilt.edu

Prof. Christoph Beckermann
University of Iowa
Department of Mechanical Engineering
2412 SC Engineering Building
Iowa City, IA 52242-1527
T 319-335-5681; F 319-335-5669
becker@Engr.uiowa.edu

Mr. Giulio Bellizia
University of Illinois, Chicago
2828 North Pine Grove, Apt. 317
Chicago, IL 60657
T 312-413-7601; F 312-413-0447

Prof. Andre Benard
Michigan State University
Department of Mechanical Engineering
2555 Engineering Building
East Lansing, MI 48824
T 517-432-1522; F 517-353-1750
benard@egr.msu.edu

Prof. George B. Benedek
Massachusetts Institute of Technology
Department of Physics
Room 13-2005
77 Massachusetts Avenue
Cambridge, MA 02139-4307
T 617-253-4828; F 617-225-2585
gbb@mit.edu

Dr. K. W. Benz
Kristallographisches Inst.
Der Universitat
Hebelstrasse 25 D-7800
Freiberg, Germany

Prof. H. Bermudez
University of Pennsylvania
120 Hayden Hall
3320 Smith Walk
Philadelphia, PA 19104

Prof. Jerry Bernholc
North Carolina State University
Department of Physics
Box 8202
Raleigh, NC 27695-8202
T 919-515-3126; F 919-515-7331
bernholc@ncsu.edu

Dr. David Berns
Tufts University
Department of Physics and Astronomy
Science and Technology Center, Room 208
4 Colby Street
Medford, MA 02155
F 617-627-3744

Dr. J. Bhowmick
Vanderbilt University
1743 Station B
Nashville, TN 37235
F 615-343-8730

Dr. Konstantinos Boboridis
National Institute of Standards and Technology
100 Bureau Drive
MS 8555
Gaithersburg, MD 20899-8555

Dr. William J. Boettinger
National Institute of Standards and Technology
Metallurgy Division
Materials Science and Engineering Lab.
Bldg. 223, Room A153
Gaithersburg, MD 20899
T 301-975-6160; F 301-975-4553
wboettinger@nist.gov

Prof. G. Bonilla
University of Massachusetts, Amherst
Department of Chemical Engineering
Goessmann Laboratory
Amherst, MA 01003

Prof. Nicholas Booth
University of Alabama in Huntsville
CMMR, VBRH, D-29
Huntsville, AL 35899
T 256-824-6019; F 256-824-6499
boothn@email.uah.edu

Prof. Christopher Bowman
University of Colorado, Boulder
Department of Chemical Engineering
Campus Box 424
Boulder, CO 80309-0424
T 303-492-3247; F 303-492-4341
bowmanc@colorado.edu

Prof. John F. Brady
California Institute of Technology
Division of Chemistry and Chemical Engineering
210-41
Pasadena, CA 91125
T 626-395-4183; F 626-568-8743
jfbrady@caltech.edu

Prof. A. Brannan
University of Minnesota
Department of Chemical Engineering and Materials
Science
Amundson Hall
421 Washington Avenue S.E.
Minneapolis, MN 55455-0132

Prof. Robert F. Brebrick
Marquette University
Department of Mechanical and Industrial
Engineering
P.O. Box 1881
Milwaukee, WI 53201-1881
robert.brebrick@marquette.edu

Prof. Kenneth Brezinsky
University of Illinois, Chicago
Department of Chemical Engineering
810 South Clinton Street
Chicago, IL 60607-7000
kenbrez@uic.edu

Prof. M. E. Brown
Kansas State University
Department of Chemistry
311 CHEM-BIOCHEM
Manhattan, KS 66506
mpeterso@ksu.edu

Dr. R. Brun
CERN
EP/AIP
Bat. 12 1-013
CH-1221 Geneva 23, Switzerland
F 41 22 767 9480

Prof. Arnold Burger
Fisk University
Center for Photonic Materials and Devices
Department of Physics
1000 17th Avenue N
Nashville, TN 37208-3051
T 615-329-8516; F 615-329-8634
aburger@dubois.fisk.edu

Dr. Craig Burkhard
Clarkson University
International Center for Gravity, Materials Sci-
ence and Applications
Box 5814
Potsdam, NY 13699-5814
F 315-268-3833

Dr. Federico Carminati
CERN
EP/AIP, Bat. 12 1-013
CH-1221 Geneva 23, Switzerland
T 41 22 767 4959; F 41 22 767 9480
federico.carminati@cern.ch

Dr. William E. Carswell
University of Alabama in Huntsville
Mail Code SD47
Marshall Space Flight Center
MSFC, AL 35812
T 256-544-0829; F 256-544-8762
bill.carswell@msfc.nasa.gov

Dr. Adrian V. Catalina
Universities Space Research Assoc.
Mail Code SD47
Marshall Space Flight Center
MSFC, AL 35812
T 256-544-1326; F 256-544-2559
adrian.catalina@msfc.nasa.gov

Prof. Peggy Cebe
Tufts University
Department of Physics and Astronomy
Science and Technology Center, Room 208
4 Colby Street
Medford, MA 02155
T 617-627-3365; F 617-627-3744
peggy@cebe.phy.tufts.edu

Prof. Soyoung Stephen Cha
University of Illinois, Chicago
Department of Mechanical Engineering
M/C 251, 2039 ERF
842 West Taylor Street
Chicago, IL 60607-7022
T 312-996-9612; F 312-413-0447
sscha@uic.edu

Dr. Arnon Chait
NASA GRC
Mail Stop 105-1
21000 Brookpark Road
Cleveland, OH 44135
T 216-433-3558; F 216-433-5033
arnon.chait@grc.nasa.gov

Mr. Yuri Chekanov
University of Southern Mississippi
Department of Chemistry and Biochemistry
P. O. Box 5043
Hattiesburg, MS 39406-5053
F 601-266-6045

Prof. James R. Chelikowsky
University of Minnesota
Department of Chemical Engineering and Materials Science
151 Amundson Hall
421 Washington Avenue S.E.
Minneapolis, MN 55455-0132
T 612-625-4837; F 612-626-7246
jrc@msi.umn.edu

Dr. P. Y. P. Chen
University of New South Wales
School of Mechanical and Manufacturing Engineering
Sydney, NSW 2052, Australia
T 61-2-385-5162; F 61-2-633-1222

Prof. Weinong (Wayne) Chen
The University of Arizona
Department of Aerospace and Mechanical Engineering
1130 N. Mountain Avenue
Tucson, AZ 85721
T 520-621-6114; F 520-621-8191
wchen@allen.ame.arizona.edu

Prof. Alexander A. Chernov
Universities Space Research Assoc.
Mail Code SD47
Marshall Space Flight Center
MSFC, AL 35812
T 256-544-9196; F 256-544-8762
alex.chernov@msfc.nasa.gov

Prof. Michael Cima
Massachusetts Institute of Technology
Materials Processing Center
Bldg. 12-011
77 Massachusetts Avenue
Cambridge, MA 02139-4307
T 617-253-6877; F 617-258-6936
mjcima@mit.edu

Prof. Noel A. Clark
University of Colorado, Boulder
Department of Physics
Boulder, CO 80309-0390

Prof. Juan Pablo Claude
University of Alabama, Birmingham
Department of Chemistry
CHEM Building, Room 201
901 14th Street South
Birmingham, AL 35294-1240
T 205-975-2478; F 205-934-2543
jpclaude@uab.edu

Dr. M. S. Cloudsley
NASA LaRC
MS 188 B
Hampton, VA 23681
F 757-864-8094

Dr. Sharon Cobb
NASA MSFC
Mail Code SD47
Marshall Space Flight Center
MSFC, AL 35812
T 256-544-7791; F 256-544-8762
sharon.cobb@msfc.nasa.gov

Prof. Carlos Coimbra
Drexel University
Philadelphia, PA 19104

Prof. Reid F. Cooper
University of Wisconsin, Madison
Department of Materials Science and Engineering
1509 University Avenue
Madison, WI 53706-1595
T 608-262-1133; F 608-262-8353
cooper@engr.wisc.edu

Dr. Sam R. Coriell
National Institute of Standards and Technology
100 Bureau Drive, MS 8555
Gaithersburg, MD 20899-8555
T 301-975-6169; F 301-975-4553
sam.coriell@nist.gov

Prof. Thomas H. Courtney
Michigan Technological University
Department of Materials Science and Engineering
1400 Townsend Drive
Houghton, MI 49931-1295
T 906-487-2036; F 906-487-2934
thc@mtu.edu

Prof. Gregory P. Crawford
Brown University
Division of Engineering
Box D
182 Hope Street
Providence, RI 02912
T 401-863-2858; F 401-863-912
Gregory_Crawford@brown.edu

Mr. Kevin Croat
Washington University
Physics Department
Box 1105
One Brookings Drive
Saint Louis, MO 63130
T 314-935-6379; F 314-935-6219
tkc@howdy.wustl.edu

Prof. Arne Croell
TU Bergakademie Freiberg
Inst. für NE-Metallurgie und Reinstoffe
Leipziger Str. 23
D-09599 Freiberg, Germany
T 49-3731-39-2017
F 49-3731-39-2268
arne.croell@inemet.tu-freiberg.de

Mr. Daniel Crunkleton
University of Florida
Department of Chemical Engineering
P.O. Box 116005
227 CHE
Gainesville, FL 32611
T 352 392-2420; F 352 392-9513
dcrunkle@che.ufl.edu

Dr. Francis A. Cucinotta
NASA JSC
Code SN
2101 NASA Road 1
Houston, TX 77058
T 281-483-0968; F 281-483-2696
fcucinot@ems.jsc.nasa.gov

Dr. Peter A. Curreri
NASA MSFC
Mail Code SD48
Marshall Space Flight Center
MSFC, AL 35812
T 256-544-7763; F 256-544-6660
peter.curreri@msfc.nasa.gov

Prof. Jonathan Dantzig
University of Illinois, Urbana
Department of Mechanical Engineering
MC-244
1206 W. Green Street
Urbana, IL 61801
T 217-333-4107; F 217-244-6534
dantzig@uiuc.edu

Prof. Delbert E. Day
University of Missouri, Rolla
Materials Research Center
1870 Miner Circle
Rolla, MO 65409-1170
T 573-341-4354; F 573-341-2071
day@umr.edu

Dr. Henry C. de Groh III
NASA GRC
Mail Stop 105-1
21000 Brookpark Road
Cleveland, OH 44135
T 216-433-5025; F 216-433-5033
henry.c.degroh@grc.nasa.gov

Prof. Graham D. de Vahl Davis
University of New South Wales
School of Mechanical and
Manufacturing Engineering
Sydney, NSW 2052, Australia
T 61-2-385-4099; F 61-2-633-1222
g.devahldavis@unsw.edu.au

Prof. Kenneth A. Debelak
Vanderbilt University
Department of Chemical Engineering
Box 1604, Station B
Nashville, TN 37235
T 615-322-2088; F 615-343-7951
kenneth.a.debelak@vanderbilt.edu

Prof. Jeffrey J. Derby
University of Minnesota
Department of Chemical Engineering and Materi-
als Science
151 Amundson Hall
421 Washington Avenue, S.E.
Minneapolis, MN 55455-0132
T 612-625-1313; F 612-626-7246
derby@tc.umn.edu

Mr. G. Dhanaraj
State University of New York, Stony Brook
Department of Materials Science and Engineering
Stony Brook, NY 11794-2275

Prof. Alejandro R. Diaz
Michigan State University
Department of Mechanical Engineering
East Lansing, MI 48824
T 517-353-0825; F 517-353-1750
diaz@egr.msu.edu

Prof. Nikolaus Dietz
North Carolina State University
Department of Materials Science
P.O. Box 7919
Raleigh, NC 27695-7919
T 919-515-8804; F 919-515-3419
ndietz@unity.ncsu.edu

Prof. B. Discher
University of Pennsylvania
Department of Chemical Engineering
BioEngineering and Mechanical Engineering
Philadelphia, PA 19104-6315

Prof. Dennis E. Discher
University of Pennsylvania
Department of Chemical Engineering
BioEngineering and Mechanical Engineering
Philadelphia, PA 19104-6315

Dr. Peter Dold
Universitat Freiburg
Kristallographisches Institut
Hebelstrasse 25
D-79106, Freiberg 1, Germany
T 49-761-203-6449; F 49-761-203-6434
pit@sgi3.krist.uni-freiburg.de

Dr. James Patton Downey
NASA MSFC
Mail Code SD48
Marshall Space Flight Center
MSFC, AL 35812
T 256-544-6432; F 256-544-2102
james.downey@msfc.nasa.gov

Prof. Edward L. Dreizin
New Jersey Institute of Technology
Department of Mechanical Engineering
University Heights
Newark, NJ 07102-1982
T 973-596-5751; F 973-642-4282
dreizin@njit.edu

Dr. Y. Du
Michigan Technological University
Department of Materials Science and Engineering
1400 Townsend Drive
Houghton, MI 49931-1295
F 906-487-2934

Prof. Paul Ducheyne
University of Pennsylvania
Department of BioEngineering
120 Hayden Hall, 3320 Smith Walk
Philadelphia, PA 19104-6315
T 215-898-8501; F 215-573-2071
ducheyne@seas.upenn.edu

Prof. Michael Dudley
State University of New York, Stony Brook
Department of Materials Science and Engineering
Stony Brook, NY 11794-2275
T 631-632-8500; F 631-632-8052
michael.dudley@sunysb.edu

Dr. T. Duffar
Centre d'Etudes Nucléaires Grenoble
85X Avenue des Martyrs
38041 Grenoble Cedex, France
F 33-76-88-51-18

Dr. Thierry Dumont
Université Lyon I
Laboratoire d'Analyse Numérique
Batiment 101
43 bd du 11 Novembre 1918
69622 Villeurbanne Cedex, France
F 33 4 72 44 80 53

Prof. Prabir K. Dutta
Ohio State University
Department of Chemistry
120 West Eighteenth Avenue
Columbus, OH 43210
T 614-292-4532; F 614-292-1685
dutta.1@osu.edu

Dr. Walter M. B. Duval
NASA GRC
Mail Stop 105-1
21000 Brookpark Road
Cleveland, OH 44135
T 216-433-5023; F 216-433-5033
walter.m.duval@grc.nasa.gov

Prof. M. Samy El-Shall
Virginia Commonwealth University
Department of Chemistry
1001 W. Main Street
Richmond, VA 23284-2006
T 804-828-3518; F 804-828-8599
selshall@hsc.vcu.edu

Mr. Peter Engel
Wyle Laboratories Inc., Florida Operations
Bldg. K7-569, Room 1142
Wyle-32
K7-569 Saturn Causeway
P.O. Box 21072
Kennedy Space Center, FL 32815
T 321-861-5158; F 321-861-6163
peterengle@hotmail.com

Dr. Edwin Ethridge
NASA MSFC
Mail Code SD47
Marshall Space Flight Center
MSFC, AL 35812
T 256-544-7767; F 256-544-1777
edwin.ethridge@msfc.nasa.gov

Prof. James W. Evans
University of California, Berkeley
Department of Materials Science and Engineering
Berkeley, CA 94720
T 510-642-3807; F 510-642-9164
evans@socrates.berkeley.edu

Dr. Rebecca L. A. Everman
University of Wisconsin, Madison
Department of Materials Science and Engineering
1509 University Avenue
Madison, WI 53706-1595
F 608-262-8353

Prof. Alexandre Fedoseyev
University of Alabama, Huntsville
CMMR
VBRH, Research Institute D-4
Huntsville, AL 35899
T 256-824-6889; F 256-824-6944
alex@cmmr.uah.edu

Prof. Robert S. Feigelson
Stanford University
Center for Materials Research
Press Warehouse
Stanford, CA 94305-4045
T 650-723-4007; F 650-723-3752
feigel@soe.stanford.edu

Dr. A. Ferrari
INFI
Milan, Italy

Dr. Shari Feth
University of Alabama in Huntsville
Mail Code SD47
Marshall Space Flight Center
MSFC, AL 35812
T 256-544-0519; F 256-544-8762
sheri.feth@msfc.nasa.gov

Dr. Merton C. Flemings
Massachusetts Institute of Technology
Materials Processing Center
77 Massachusetts Avenue, Rm. 8-407
Cambridge, MA 02139
T 617-253-3233; F 617-258-6886
flemings@mit.edu

Mr. David T. Frate
NASA GRC
Mail Stop 500-115
21000 Brookpark Road
Cleveland, OH 44135

Dr. Donald O. Frazier
NASA MSFC
Mail Code SD40
Marshall Space Flight Center
MSFC, AL 35812
T 256-544-7825; F 256-544-2102
don.frazier@msfc.nasa.gov

Dr. J. E. Frei
Rensselaer Polytechnic Institute
CII 9113
110 8th Street
Troy, NY 12180
F 518-276 2073

Prof. Andrienne C. Friedli
Middle Tennessee State University
Department of Chemistry
Box X076 MTSU
Murfreesboro, TN 37312
T 615-898-2071; F 615-898-5182
acfriedli@mtsu.edu

Dr. Archie Fripp Jr.
125 Little John Road
Williamsburg, VA 23185
T 757-253-2822
afripp@widomaker.com

Prof. Anup K. Gangopadhyay
Washington University, St. Louis
Department of Physics
Campus Box 1105
One Brookings Drive
St. Louis, MO 63130
T 314-935-4654; F 314-935-6379
Anup@howdy.wustl.edu

Dr. H. Gao
University of Pennsylvania
Department of Mechanical Engineering and
Applied Mechanics
Philadelphia, PA 19104-6315
F 215-573-6334

Dr. N. A. Gatsonis
Worcester Polytechnic Institute
100 Institute Road
Worcester, MA 01609-2280

Dr. Yi Ge
University of Illinois, Chicago
Department of Mechanical Engineering
M/C 251, 2039 ERF
842 West Taylor Street
Chicago, IL 60607-7022
F 312-413-0447

Dr. Georgi Georgiev
Tufts University
Department of Physics and Astronomy
Science and Technology Center
4 Colby Street, Room 208
Medford, MA 02155
F 617-627-3744

Prof. Randall M. German
The Pennsylvania State University
147 Research Bldg. West
University Park, PA 16802-6809
T 814-863-8025; F 814-863-8211
rmg4@psu.edu

Dr. Donald C. Gillies
NASA MSFC
Mail Code SD47
Marshall Space Flight Center
MSFC, AL 35812
T 256-544-9302; F 256-544-8762
donald.gillies@msfc.nasa.gov

Ms. Cindie Giummarra
Rensselaer Polytechnic Institute
CII 9113
110 8th Street
Troy, NY 12180
T 518-276 6130; F 518-276 2073
giummc@rpi.edu

Prof. Matthew Glaser
University of Colorado, Boulder
Department of Physics
Condensed Matter Lab.
Boulder, CO 80309-0390
T 303-492-3029; F 303-492-2998
glaser@bly.Colorado.edu

Prof. Martin E. Glicksman
Rensselaer Polytechnic Institute
Department of Materials Science and Engineering
Materials Research Center, Room 9111
110 8th Street
Troy, NY 12180
T 518-276-6721; F 518-276-2198
glickm@rpi.edu

Prof. Arun M. Gokhale
Georgia Institute of Technology
School of Materials Science and Engineering
778 Atlantic Drive
Atlanta, GA 30332-0245
T 404-894-2887; F 404-894-9140
arun.gokhale@mse.gatech.edu

Prof. Nigel D. Goldenfeld
University of Illinois, Urbana-Champaign
Beckman Institute
Loomis Lab, MC 704
1110 W Green
Urbana, IL 61801
T 217-333-8027
nigel@uiuc.edu
nigel@guava.physics.uiuc.edu

Dr. Vladimir D. Golyshev
All-Union Science Res. Inst. of Mineral
Raw Mat. Synthesis, VNIISIMS
Institutskaya str 1
Alexandrov-City 601600
Vladimirskaya Region; Russia
T 7-095-584-5816 or 7-(09244)92693
F 7-095-584-5816
post@thermo.vladimir.su

Dr. M. Gonik
All-Union Science Res. Inst. of Mineral
Raw Mat. Synthesis, VNIISIMS
Institutskaya str 1
Alexandrov-City 601600
Vladimirskaya Region, Russia
F 7-095-584-5816

Prof. Brian Grady
University of Oklahoma
School of Chemical Engineering and Materials
Science
100 East Boyd, EC Rm. T-223
Norman, OK 73019-0628
T 405-325-4369; F 405-325-5813
bprgrad@mailhost.ecn.ou.edu

Prof. Alan R. Greenberg
University of Colorado, Boulder
Department of Mechanical Engineering
Campus Box 427
Boulder, CO 80309-0427
T 303-492-6613; F 303-492-4637
alan.greenberg@colorado.edu

Dr. Richard N. Grugel
NASA MSFC
Mail Code SD47
Marshall Space Flight Center
MSFC, AL 35812
T 256-544-9165; F 256-544-8762
richard.grugel@msfc.nasa.gov

Prof. Turgut M. Gür
Stanford University
Laboratory for Advanced Materials
McCullough Building, Room 135
476 Lomita Mall
Stanford, CA 94305-4045
T 650-723-6597; F 650-723-3044
turgut@stanford.edu

Prof. D. E. Gustafson
Vanderbilt University
Department of Chemical Engineering
P.O. Box 1604, Station B
Nashville, TN 37235

Mr. Robert J. Gustafson
Orbital Technologies Corp. (ORBITEC)
Space Center
1212 Fourier Drive
Madison, WI 53717
T 608-827-5000 Ext. 225
F 608-827-5050
gustafsonr@orbitec.com

Prof. Naomi J. Halas
Rice University
ECE Department - Mail Stop 366
6100 South Main
Houston, TX 77251
T 713-348-5611; F 713-348-5686
halas@rice.edu

Prof. Daniel A. Hammer
University of Pennsylvania
120 Hayden Hall
3320 Smith Walk
Philadelphia, PA 19104
T 215-573-6761; F 215-573-2071
hammer@seas.upenn.edu

Mr. Glen Haulenbeek
University of Alabama in Huntsville
Von Braun Research Hall, 34-M
Huntsville, AL 35899

Dr. Lawrence H. Heilbronn
Lawrence Berkeley National Laboratory
MS 74-197
One Cyclotron Road
Berkeley, CA 94720
T 510-486-4002; F 510-486-6949
LHHeilbronn@LBL.gov

Prof. John Heinbockel
Old Dominion University
Norfolk, VA 23529
jheinboc@odu.edu

Dr. J. C. Heinrich
University of Arizona
Department of Aerospace and Mechanical
Engineering
Tucson, AZ 85721
T 520-621-6118
heinrich@zeus.ame.arizona.edu

Prof. William H. Hofmeister
Vanderbilt University
Department of Chemical Engineering
P.O. Box 1604, Station B
Nashville, TN 37235
T 615-322-7053; F 615-343-3202
hof@vuse.vanderbilt.edu

Dr. Dirk Holland-Moritz
Institut für Raumsimulation
Deutsches Zentrum für Luft- und Raumfahrt
Linder Höhe
D-51170 Cologne, Germany
T 49-0-2203-601 3292
F 49-0-2203-61768
dirk.holland-moritz@dlr.de

Prof. Mark D. Hollingsworth
Kansas State University
Chemistry Department
111 Willard Hall
Manhattan, KS 66506
T 785-532-2727; F 785-532-6666
mdholl@ksu.edu

Prof. George M. Homsy
Stanford University
Department of Chemical Engineering
Sauffer Building 3, Room 113
Stanford, CA 94305
T 650-723-2419; F 650-723-9780
bud@chemeng.stanford.edu

Dr. Arlon J. Hunt
Lawrence Berkeley National Laboratory
Division of Environmental Energy Technologies
Mail Stop 70-108
One Cyclotron Road
Berkeley, CA 94720
T 510-486-5370; F 510-486-7303
ajhunt@lbl.gov

Dr. Robert W. Hyers
NASA MSFC
Mail Code SD47
Marshall Space Flight Center
MSFC, AL 358123
T 256-544-1683; F 256-544-8762
robert.hyers@msfc.nasa.gov

Dr. Ronald G. Iacocca
Pennsylvania State University
147 Research Building, West
University Park, PA 16802-6809
F 814-863-8211

Prof. Alexander F. Izmailov
Polytechnic University
Department of Chemical Engineering
Six Metrotech Center
Brooklyn, NY 11201
T 718-336-2835; F 718-336-2825
Izmailov@duke.poly.edu

Prof. Kenneth A. Jackson
University of Arizona
Arizona Materials Laboratory
Department of Materials Science and Engineering
4715 East Fort Lowell Road
Tucson, AZ 85712
T 520-322-2981; F 520-322-2993
kaj@aml.arizona.edu

Prof. Lyle Jalbert
University of Alabama, Huntsville
CMMR, Von Braun Research Hall
Huntsville, AL 35899
T 256-824-6963; F 256-824-6944
lyle.jalbert@teleionsolutions.com

Ms. Linda B. Jeter
NASA MSFC
Mail Code SD44
Marshall Space Flight Center
MSFC, AL 35812
T 256-544-7392; F 256-544-5892
linda.jeter@msfc.nasa.gov

Prof. David R. Johnson
Purdue University
School of Materials Engineering
1289 MSEE Building
West Lafayette, IN 47907-1289
T 765-494-7009; F 765-494-1204
davidjoh@ecn.purdue.edu

Dr. J. Jordan
Orbital Technologies Corp. (ORBITEC)
Space Center
1212 Fourier Drive
Madison, WI 53717
T 608-827-5000; F 608-827-5050

Dr. O. Jouravlev
Institute of Chemical Problems of Microelectronics
Vernadsky prospect 86
Moscow 117571, Russia
F 7-095-230-47-56

Dr. Frank Robert Juretzko
University of Alabama
Department of Metallurgical Engineering
Box 870202
Tuscaloosa, AL 35487-0202
T 205-348-1748; F 205-348-8574
juretzko@yahoo.com

Prof. Monica L. Kaforey
Case Western Reserve University
Department of Materials Science and Engineering
330 White Building
10900 Euclid Avenue
Cleveland, OH 44106
T 216-368-4219; F 216-368-3209
mlk14@po.cwru.edu

Ms. Natalie Kaiser
Universitat Freiburg
Kristallograph. Institute
Hebelstrasse 25
D-79104 Freiburg, Germany
T 49-761-203-6455; F 49-761-203-6434
natalie@sgi3.krist.uni-freiburg.de

Mr. Nam Hyun Kang
Pennsylvania State University
Applied Research Laboratory
150 MRI Building, Research Park
University Park, PA 16802
T 814-863-8558; F 814-863-2986
hhk105@psu.edu

Prof. David L. Kaplan
Tufts University
Department of Chemical Engineering
4 Colby Street
Medford, MA 02155
T 617-627-3251; F 617-627-3991
dkaplan1@emerald.tufts.edu

Prof. Alain S. Karma
Northeastern University
Department of Physics
111 Dana Research Center
360 Huntington Avenue
Boston, MA 02115
T 617-373-2929; F 617-373-2943
karma@neu.edu

Dr. Andrey V. Kartavykh
Institute for Chemical Problems of Microelectronics
Vernadsky prospect 86
Moscow 117571, Russia
F 7-095-230-47-56
ihpm@glas.arc.org
L22-icpm@mail.girnet.ru

Dr. Mohammad Kassemi
NTLC/NASA Glenn Research Center
Mail Stop 110-3
21000 Brookpark Road
Cleveland, OH 44135
T 216-433-5031; F 216-433-3793
mohammad.kassemi@grc.nasa.gov

Dr. Piotr Kaszynski
Middle Tennessee State University
Department of Chemistry
Box X076 MTSU
Murfreesboro, TN 37312
F 615-898-5182

Ms. Lara Keefer
Case Western Reserve University
10900 Euclid Avenue
White Building
Cleveland, OH 44106
T 216-368-0119; F 216-368-3209
lak5@po.cwru.edu

Prof. Kenneth F. Kelton
Washington University, St. Louis
Department of Physics
Campus Box 1105
One Brookings Drive
St. Louis, MO 63130
T 314-935-6228; F 314-935-6219
kfk@wuphys.wustl.edu

Prof. Tobias Kerle
University of Massachusetts
Department of Polymer Science
120 Governors Drive
Amherst, MA 01003
T 413-577-1535; F 413-577-1510
kerle@mail.pse.umass.edu

Dr. Ilyas I. Khayrullin
New Jersey Institute of Technology
Department of Electrical and Computer
Engineering
University Heights
Newark, NJ 07102-1982

Dr. M.-H. Y. Kim
College of William and Mary
P.O. Box 8795
Williamsburg, VA 23187-8795

Prof. Shinwoo Kim
Hoseo University
Department of Materials Science and Engineering
Baebang Sechul-Ri Asan Chungnam
South Korea
T 82-418-540-5474
swkim@dogsul.hoseo.ac.kr

Mr. James D. Kinnison
The Johns Hopkins Applied Physics Laboratory
11100 Johns Hopkins Road
Laurel, MD 20723-6099
T 443-778-6169; F 443-778-6696
james.kinnison@jhuapl.edu

Dr. John P. Kizito
NCMR
21000 Brookpark Road
Cleveland, OH 44135
T 216-433-2275; F 216-433-3793
jpk5@po.cwru.edu

Prof. Kenneth J. Klabunde
Kansas State University
Department of Chemistry
111 Willard Hall
Manhattan, KS 66506
T 785-532-6849; F 785-532-6666
kenjk@ksu.edu

Prof. Manoochehr M. Koochesfahani
Michigan State University
Department of Mechanical Engineering
East Lansing, MI 48824
T 517-353-5311; F 517-353-7179
koochesf@egr.msu.edu

Prof. Matthew B. Koss
Rensselaer Polytechnic Institute
Materials Science and Engineering Department
CII 4225
110 8th Street
Troy, NY 12180-3590
T 518-276-2844; F 518-276-2198
kossm@rpi.edu

Prof. Sindo Kou
University of Wisconsin, Madison
Department of Materials Science and Engineering
1103 Engineering Research Building
1500 Engineering Drive
Madison, WI 53706
T 608-262-0576; F 608-262-8648
kou@engr.wisc.edu

Prof. Matthew John M. Krane
Purdue University
School of Materials Engineering
West Lafayette, IN 47907
T 765-494-4107; F 765-494-1204
krane@ecn.purdue.edu

Prof. William Krantz
University of Cincinnati
Department of Chemical Engineering
Cincinnati, OH 43221-0171
T 513-5564021 ; F 513-556-6741

Dr. Shankar Krishnan
Containerless Research, Inc.
906 University Place
Evanston, IL 60201
T 847-467-2678; F 847-467-2679
shanky@containerless.com

Prof. Anil D. Kulkarni
St. Louis University Medical Center
3635 Vista at Grand
St. Louis, MO 63110-0250
T 314-268-5274; F 314-268-5180

Mr. Jeffrey C. LaCombe
Rensselaer Polytechnic Institute
Materials Science and Engineering Department
CII Building, Room 4219
Troy, NY 12180
T 518-276-8068; F 518-276-2198
lacomj@rpi.edu

Dr. F.-C. Lai
University of Oklahoma
School of Aerospace and Mechanical Engineering
Room 212
865 Asp Avenue
Norman, OK 73019
F 405-325-1088

Prof. Ravindra B. Lal
Alabama A&M University
Department of Physics
P.O. Box 71
Normal, AL 35762
T 256-858-8148; F 256-851-5622
lal@caos.aamu.edu

Prof. David J. Larson Jr.
SUNY-SB/NASA Headquarters
Mail Code UM
Washington, DC 20546-0001
T 202-358-2237; F 202-358-2837
dlarson@hq.nasa.gov

Prof. C.-M. Lee
University of Pennsylvania
120 Hayden Hall
3320 Smith Walk
Philadelphia, PA 19104

Dr. Sandor L. Lehoczký
NASA MSFC
Mail Code SD40
Marshall Space Flight Center
MSFC, AL 35812
T 256-544-7758; F 256-544-8762
sandor.lehoczký@msfc.nasa.gov

Dr. R. A. Lemdiasov
Worcester Polytechnic Institute
100 Institute Road
Worcester, MA 01609-2280

Mr. Eddie Leonardi
University of New South Wales
School of Mechanical and Manufacturing
Engineering
Sydney, NSW 2052, Australia
T 61-2-385-5162; F 61-2-633-1222
e.leonardi@unsw.edu.au

Dr. Fred W. Leslie
NASA MSFC
Mail Code SD47
Marshall Space Flight Center
MSFC, AL 35812
T 256-544-1633; F 256-544-6660
fred.leslie@msfc.nasa.gov

Prof. Jennifer A. Lewis
University of Illinois, Urbana-Champaign
Department of Materials Science and Engineering
Room 212A Ceramics Building
105 S. Goodwin Avenue
Urbana, IL 61801
T 217-244-4973; F 217-244-6917
jalewis@staff.uiuc.edu

Prof. Ben Q. Li
Washington State University
School of Mechanical and Materials Engineering
P.O. Box 642920
Pullman, WA 99164-2920
T 509-335-7386; F 509-335-4662
li@mme.wsu.edu

Prof. Fengcui Li
Clarkson University
International Center for Gravity, Materials
Science and Applications
Potsdam, NY 13699-5700
F 315-268-3841

Mr. Chaowalit Limmaneevichitr
University of Wisconsin, Madison
Department of Materials Science and Engineering
1103 Engineering Research Building
1500 Engineering Drive
Madison, WI 53706
F 608-262-8648
limmanee@cae.wisc.edu

Prof. X.-M. Lin
Kansas State University
Department of Physics
111 Willard Hall
Manhattan, KS 66506

Prof. Z. Lin
University of Massachusetts
Polymer Science and Engineering
Department
Amhurst, MA 01003-4530

Dr. Aleksey Lomakin
Massachusetts Institute of Technology
Room 13-2014
77 Massachusetts Avenue
Cambridge, MA 02139-4307
T 617-253-6804; F 617-225-2585
aleksey@critical.mit.edu

Dr. W. Loser
Institute of Solid State and Materials Research
Helmholtzstraße 20
D-01069 Dresden, Germany

Dr. Samuel A. Lowry
CFD Research Corporation
215 Wynn Drive
Huntsville, AL 35805-1958
T 256-726-4853; F 256-726-4806
sal@cfdr.com

Dr. S. Z. Lu
Michigan Technological University
Department of Materials Science and Engineering
College of Engineering
1400 Townsend Drive
Houghton, MI 49931-1295
F 906-487-2934

Dr. Afina Lupulescu
Rensselaer Polytechnic Institute
Materials Science and Engineering Department
Materials Research Center
110 8th Street
Troy, NY 12180
T 518-276-2023; F 518-276-2073
lupula@rpi.edu

Mr. Paul Luz
NASA MSFC
Mail Code SD40
Marshall Space Flight Center
MSFC, AL 35812

Prof. Nancy Ma
University of Missouri, Rolla
Department of Mechanical and Aerospace
Engineering and Engineering Mechanics
1870 Miner Circle
Rolla, MO 65409-0050
T 573-341-4626; F 573-341-6899
ma@umr.edu

Dr. Allen K. MacKnight
Honeywell International Inc.
2525 W. 190th Street
M/S-36-1-93140
Torrance, CA 90504
T 310-512-3307; F 310-512-2246
al.macknight@honeywell.com

Prof. Jules Magda
University of Utah
Department of Chemical and Fuels Engineering
50 S. Central Campus Drive, Rm. 3290
Salt Lake City, UT 84112
T 801-581-7536; F 801-581-8692
jj.magda@m.cc.utah.edu

Ms. Diane C. Malarik
NASA GRC
Mail Stop 500-115
21000 Brookpark Road
Cleveland, OH 44135
T 216-433-3203; F 216-433-8660
diane.malarik@grc.nasa.gov

Dr. Jason T. Manka
Middle Tennessee State University
Department of Chemistry
Box X076 MTSU
Murfreesboro, TN 37312
F 615-898-5182

Prof. Carlos Marin
University of Alabama, Huntsville
CMMR, VBRH, D-29
Huntsville, AL 35899
T 256-824-6950; F 256-824-6944
marinc@email.uah.edu

Prof. Raquel Martin
Tufts University
Department of Chemical Engineering
4 Colby Street
Medford, MA 02155

Prof. Jonathan Masere
University of Southern Mississippi
Department of Chemistry and Biochemistry
P. O. Box 5043
Hattiesburg, MS 39406-5053
T 601-266-5899; F 601-266-6045
jonathan@wave.st.usm.edu

Mr. Larry W. Mason
Lockheed Martin
Mail Stop BO560
P.O. Box 179
Denver, CO 80201-0179
T 303-971-9067; F 303-971-0829
larry.w.mason@lmco.com

Dr. Douglas Matson
Massachusetts Institute of Technology
Materials Processing Center
77 Massachusetts Avenue, Room 8-409
Cambridge, MA 02139
T 617-253-3248; F 617-258-6886
matson@mit.edu

Prof. David H. Matthiesen
Case Western Reserve University
Department of Materials Science and Engineering
420 White Bldg., 10900 Euclid Avenue
Cleveland, OH 44106-7204
T 216-368-1366; F 216-368-3209
dhm5@po.cwru.edu

Prof. Richard J. Matyi
University of Wisconsin, Madison
Department of Materials Science and Engineering
1509 University Avenue
Madison, WI 53706
T 608-263-1716; F 608-262-8353
matyi@engr.wisc.edu

Prof. Richard H. Maurer
Johns Hopkins University
Applied Physics Laboratory
11100 Johns Hopkins Road
Laurel, MD 20723-6099
T 240-228-6482; F 240-228-6099
richard.maurer@jhuapl.edu

Prof. Jimmy W. Mays
University of Alabama at Birmingham
Department of Chemistry
Room 201
Birmingham, AL 35294
T 205-934-8101; F 205-934-8158
jmays@uab.edu

Dr. Sandip Mazumder
CFD Research Corporation
215 Wynn Drive, #501
Huntsville, AL 35805
T 256-726-4856; F 256-726-4806
sm@cfdr.com

Dr. Konstantin Mazuruk
Universities Space Research Association
Mail Code SD47
Marshall Space Flight Center
MSFC, AL 35812
T 256-544-8633; F 256-544-8762
consty.mazuruk@msfc.nasa.gov

Ms. Sonya D. McCall
North Carolina State University
Materials Science and Engineering Department
Centennial Campus, Research Bldg. 1
Box 7919
Raleigh, NC 27695
T 919-515-8965; F 919-515-8967
sdmccall@unity.ncsu.edu

Dr. Geoffrey B. McFadden
National Institute of Standards and Technology
Computational and Mathematical
Sciences Division
Building 820, Room 365
100 Bureau Drive, Stop 8910
Gaithersburg, MD 20899-8910
T 301-975-2711; F 301-990-4127
mcfadden@nist.gov

Prof. John J. McGrath
Michigan State University
Department of Mechanical Engineering
A106 Research Complex - Engineering
East Lansing, MI 48824-1226
T 517-355-0299; F 517 355-7179
mcgrath@me.msu.edu

Prof. Michael McNallan
University of Illinois, Chicago
CME Department
M/C 246
842 W. Taylor Street
Chicago, IL 60607
T 312-996-2436; F 312-996-2426
mcnallan@uic.edu

Prof. Constantine Megaridis
University of Illinois, Chicago
Department of Mechanical Engineering
Mail Code 251
842 W. Taylor Street
Chicago, IL 60607-7022
T 312-996-3436; F 312-413-0447
cmm@uic.edu

Prof. Eckart Meiburg
University of California, Santa Barbara
Department Mechanical and Environmental
Engineering
Santa Barbara, CA 93106
T 805-893-5278; F 805-893-5278
meiburg@Engr.ucsb.edu

Dr. Jack Miller
Lawrence Berkeley National Laboratory
One Cyclotron Road, MS 29-100
Berkeley, CA 94720
T 510-486-7130; F 510-486-7934
J_miller@lbl.gov

Dr. H. A. Mook
Oak Ridge National Laboratory
Neutron Scattering Group
P.O. Box 2008
Oak Ridge, TN 37831-6393
T 423-574-5242; F 423-574-6268
ham@ornl.gov

Dr. Shariar Motakef
CAPE Simulations Inc.
One Bridge Street, Suite 100
Newton, MA 02458
T 617-796-8882 x 101; F 617-796-7870
motakef@capesim.com

Mr. Sundeep Mukherjee
University of Alabama
Department of Metallurgical Engineering
Box 870202
Tuscaloosa, AL 35487-0202
T 205-348-1748; F 205-348-8574
mukhe001@bama.ua.edu

Prof. William W. Mullins
Carnegie Mellon University
Department of Materials Science and Engineering
5000 Forbes Avenue
Pittsburgh, PA 15213
T 412-268-2541; F 412-268-7696
wm06@andrew.cmu.edu

Prof. Bruce T. Murray
State University of New York, Binghamton
Mechanical Engineering Department
P.O. Box 6000
Binghamton, NY 13902-6000
T 607-777-6561; F 607-777-4620
bmurray@binghamton.edu

Dr. Allan S. Myerson
Illinois Institute of Technology
10 West 33rd Street
Chicago, IL 60616
T 718-260-3223; F 718-260-3125
myerson@iit.edu

Prof. Ralph E. Napolitano
Iowa State University
Ames Laboratory
104 Wilhelm Hall
Ames, IA 50011-3020
T 515-294-9101; F 515-294-4291
napolitano@ameslab.gov

Prof. Ranga Narayanan
University of Florida
Department of Chemical Engineering
Gainesville, FL 32611
T 352-392-9103; F 352-392-9513
ranga@che.ufl.edu

Prof. Robert J. Naumann
University of Alabama, Huntsville
Von Braun Research Institute M-43
Huntsville, AL 35899
T 256-824-6846; F 256-824-6919
naumannr@email.uah.edu

Prof. V. Nikolakis
University of Massachusetts, Amherst
Department of Chemical Engineering
Goessmann Laboratory
Amherst, MA 01003

Dr. Paul C. Nordine
Containerless Research, Inc.
910 University Place
Evanston, IL 60201
T 847-467-2678; F 846-467-2679
pnordine@containerless.com

Prof. E. A. O'Rear
University of Oklahoma
School of Chemical Engineering and Materials
Science
100 East Boyd, EC Rm. T-223
Norman, OK 73019-0628
F 405-325-5813

Dr. Kinichi Ohsaka
University of Southern California
Aerospace and Mechanical Engineering
Los Angeles, CA 90089-1453
T 714 529-3544; F 714-529-3544

Dr. S. J. Oldenburg
Rice University
ECE Department and Department of Chemistry
Houston, TX 77005

Prof. Aleksandar G. Ostrogorsky
Rensselaer Polytechnic Institute
Department of Mechanical Engineering
JEC 2026
Troy, NY 12180
T 518-276-6975; F 518-276-6025
ostroa@rpi.edu

Dr. T. Peignier
University of Alabama, Huntsville
CMMR, VBRH, D-29
Huntsville, AL 35899
F 256-824-6944

Dr. Matthew R. Pekny
Intel Mask Operations
Mailstop SC2-12
3065 Bowers Avenue
Santa Clara, CA 95054-3202

Prof. John H. Perepezko
University of Wisconsin, Madison
Department of Materials Science and
Engineering
1509 University Avenue
Madison, WI 53706-1595
T 608-263-1678; F 608-262-8353
perepezk@engr.wisc.edu

Prof. M. L. Peterson
Kansas State University
Department of Chemistry
311 CHEM-BIOCHEM
Manhattan, KS 66506
T 785-532-5419
mpeterso@ksu.edu

Mr. Vladimir Pines
NASA GRC
Mail Stop 105-1
21000 Brookpark Road
Cleveland, OH 44135

Prof. Lawrence S. Pinsky
University of Houston
Physics Department-5506
4800 Calhoun Blvd.
Houston, TX 77204-5506
T 713-743-3552; F 713-743-3589
pinsky@uh.edu

Dr. Y. B. Pithawalla
Virginia Commonwealth University
Department of Chemistry
1001 W. Main Street
Richmond, VA 23284-2006
F 804-828-8599

Prof. David R. Poirier
University of Arizona
Department of Materials Science and Engineering
P.O. Box 210072
Tucson, AZ 85721-0072
T 520-621-6072; F 520-621-8059
poirierd@u.arizona.edu

Prof. John A. Pojman
University of Southern Mississippi
Department of Chemistry and Biochemistry
P.O. Box 5043
Hattiesburg, MS 39406-5043
T 601-266-5035; F 601-266-6075
john.pojman@usm.edu

Prof. Dmitri Popov
Clarkson University
International Center for Gravity, Materials
Science and Applications
Potsdam, NY 13699-5700
T 315-268-7672; F 315-268-3841
popovdi@craft.comp.clarkson.edu

Mr. Timothée Pourpoint
University of Alabama, Huntsville
CMMR
Von Braun Research Hall
Huntsville, AL 35899
T 256-824-6960; F 256-824-6944
pourpot@email.uah.edu

Dr. David L. Price
Argonne National Lab.
MSD-223
9700 S. Cass Ave
Argonne, IL 60439

Prof. Shula Radin
University of Pennsylvania
Department of BioEngineering
3320 Smith Walk
Philadelphia, PA 19104
T 215-898-5140; F 215-573-2071
radin@seas.upenn.edu

Prof. Leo Radzihovsky
University of Colorado, Boulder
Department of Physics
Condensed Matter Laboratory
Boulder, CO 80309-0390
T 303-492-5436; F 303-492-2998
radzihov@lulu.colorado.edu

Prof. Miriam H. Rafailovich
State University of New York, Stony Brook
Department of Materials Science and Engineering
322 Old Engineering Building
Stony Brook, NY 11794-2275
T 631-632-8483; F 631-632-5764
miriam.rafailovich@sunysb.edu

Mr. Balaji Raghothamachar
State University of New York, Stony Brook
Department of Materials Science and Engineering
Stony Brook, NY 11794-2275
T 631-632-8501; F 631-632-8052
braghoth@ic.sunysb.edu

Dr. Valery V. Rakov
Institute for Chemical Problems of Microelectronics
Vernadsky prospect 86
Moscow 117571, Russia
T 7-095-239-9953; F 7-095-233-8869
ihpm@glas.apc.org

Dr. N. Ramachandran
Universities Space Research Assoc.
Mail Code SD47
Marshall Space Flight Center
MSFC, AL 35812
T 256-544-8308; F 256-544-8891
narayanan.ramachandran@msfc.nasa.gov

Prof. Ram Ramanathan
Clarkson University
International Center for Gravity, Materials
Science and Applications
Potsdam, NY 13699-5700
F 315-268-3841

Dr. Roger Rangel
University of California, Irvine
Department of Mechanical and Aerospace
Engineering
Engineering Gateway 4200
Irvine, CA 92697-3975
rrangel@uci.edu

Dr. Nasser Rashidnia
NASA GRC
Mail Stop 500-102
21000 Brookpark Road
Cleveland, OH 44135
T 216-433-3622; F 216-433-3793

Mr. Thomas J. Rathz
University of Alabama, Huntsville
Mail Code SD47
Marshall Space Flight Center
MSFC, AL 35812
T 256-544-1409; F 256-544-1374
tom.rathz@msfc.nasa.gov

Prof. Chandra S. Ray
University of Missouri, Rolla
Materials Research Center
Martin E. Straumanis Hall
Rolla, MO 65409
T 573-341-6432; F 573-341-2071
csray@umr.edu

Prof. Liya L. Regel
Clarkson University
International Center for Gravity,
Materials Science and Applications
8 Clarkson Avenue
Box 5814
Potsdam, NY 13699-5700
T 315-268-7672; F 315-268-3833
regel@agent.clarkson.edu

Dr. Won-Kyu Rhim
Jet Propulsion Lab.
M/S 183-401
4800 Oak Grove Drive
Pasadena, CA 91109
T 818-354-2925; F 818-393-5039
won-kyu.rhim@jpl.nasa.gov

Dr. Eric E. Rice
Orbital Technologies Corp.
1212 Fourier Drive
Space Center
Madison, WI 53717
T 608 827-5000 x 230 F 608 827-5050
ricee@orbitec.com

Dr. Michael B. Robinson
NASA MSFC
Mail Code SD47
Marshall Space Flight Center
MSFC, AL 35812
T 256-544-7774; F 256-544-2176
mike.robinson@msfc.nasa.gov

Dr. Jan R. Rogers
NASA MSFC
Mail Code SD47
Marshall Space Flight Center
MSFC, AL 35812
T 256-544-1081; F 256-544-2102
jan.rogers@msfc.nasa.gov

Prof. Gregory S. Rohrer
Carnegie Mellon University
Department of Materials Science and Engineering
Roberts Engineering Hall
Room 143
5000 Forbes Avenue
Pittsburgh, PA 15213
T 412-268-2696; F 412-268-7596
gr20@andrew.cmu.edu

Prof. Christopher M. Roland
North Carolina State University
Department of Physics
Box 8202
Raleigh, NC 27695-8202
T 919-515-3170; F 919-515-7331
roland@gatubela.physics.ncsu.edu

Prof. Paul D. Ronney
University of Southern California
Department of Aerospace and Mechanical
Engineering; OHE 430H
Los Angeles, CA 90089-1453
T 213-740-0490; F 213-740-8071
ronney@usc.edu

Prof. David R. Roth
The Johns Hopkins University
Applied Physics Laboratory
11100 Johns Hopkins Road
Laurel, MD 20723-6099
T 240-228-4022; F 240-228-6696
david.roth@jhuapl.edu

Prof. John A. Roth
Vanderbilt University
Department of Chemical Engineering
Box 1604 B
Nashville, TN 37235
T 615-322-3517; F 615-343-7951
jar@vuse.vanderbilt.edu

Dr. M. Rushyniak
Virginia Commonwealth University
Department of Chemistry
1001 W. Main Street
Richmond, VA 23284-2006
F 804-828-8599

Prof. Thomas P. Russell
University of Massachusetts
Polymer Science and Engineering Department
Amherst, MA 01003-4530
T 413-577-1617; F 413-545-0082
russell@iskra.pse.umass.edu

Dr. Marie-Louise Sabougi
Argonne National Laboratory
MSD-223
9700 S. Cass Ave
Argonne, IL 60439

Prof. Albert Sacco, Jr.
Northeastern University
Center for Advanced Microgravity Material
Processing
342 Snell Engineering Center
360 Huntington Avenue
Boston, MA 02115
T 617-373-7910; F 617-373-2209
asacco@coe.neu.edu

Prof. Satwindar S. Sadhal
University of Southern California
Department of Aerospace and Mechanical
Engineering
Olin Hall - OHE 430
Los Angeles, CA 90089-1453
T 213-740-0492; F 213-740-8071
sadhal@usc.edu

Prof. Donald R. Sadoway
Massachusetts Institute of Technology
Department of Materials Science and Engineering
77 Massachusetts Avenue, Room 8-109
Cambridge, MA 02139-4307
T 617-253-3487; F 617-253-3487
dsadoway@mit.edu

Dr. Paola Sala
INFI
Milan, Italy

Prof. Rajiv Sampath
Cornell University
Sibley School of Mechanical and Aerospace
Engineering
188 Frank H.T. Rhodes Hall
Ithaca, NY 14853-3801
F 607-255-9410

Prof. Paul G. Sanders
Harvard University
Division of Engineering and Applied Sciences
29 Oxford Street
Cambridge, MA 02138-2901
F 617-495-9837

Dr. Robert J. Schaefer
National Institute of Standards and Technology
Metallurgy Division
Materials (223), Room B268, Stop 8550
100 Bureau Drive
Gaithersburg, MD 20899-8550
T 301-975-5961; F 301-926-4553
robert.schaefer@nist.gov

Dr. Marcus Schweizer
Universities Space Research Assoc.
Mail Code SD47
Marshall Space Flight Center
MSFC, AL 35812
T 256-544-4167; F 256-544-8762
marcus.schweizer@msfc.nasa.gov

Prof. Rose Scripa
University of Alabama, Birmingham
Department of Materials Science and Engineering
1075 13th Street S
Birmingham, AL 35294
T 205-934-8453; F 205-934-8437
rscripa@Engr.uab.edu

Prof. Robert F. Sekerka
Carnegie Mellon University
Department of Physics
6416 Wean Hall
Pittsburgh, PA 15213-3890
T 412-268-2362; F 412-681-0648
rs07@andrew.cmu.edu

Dr. Subhayu Sen
Universities Space Research Assoc.
Mail Code SD47
Marshall Space Flight Center
MSFC, AL 35812
T 256-544-8264; F 256-544-8762
s.sen@msfc.nasa.gov

Dr. D. Sengupta
CFD Research Corporation
215 Wynn Drive
Huntsville, AL 35805-1958

Miss Brenda Serrano
University of Florida
Department of Chemical Engineering
P.O. Box 116005
227 CHE
Gainesville, FL 32611
T 352-392-2420; F 352-392-9513
besr@grove.ufl.edu

Dr. C. Seybert
University of California, Berkeley
Department of Materials Science and Engineering
Berkeley, CA 94720
F 510-642-9164

Prof. Mark Shavers
Loma Linda University/JSC
SN3
NASA Johnson Space Center
Houston, TX 77058
T 281-483-5899; F 281-483-5276
mshavers@ems.jsc.nasa.gov

Mr. In-Seok Shin
University of Alabama, Huntsville
VBRH, M-40
Huntsville, AL 35899
T 256-824-6630; F 256-824-6791
shini@email.uah.edu

Dr. J. L. Shinn
NASA LaRC
MS 188 B
NASA Langley Research Center
Hampton, VA 23681
F 757-864-8094

Dr. Laurent Sibille
Universities Space Research Assoc.
Mail Code SD48
Marshall Space Flight Center
MSFC, AL 35812
T 256-544-5221; F 256-544-6660
laurent.sibille@msfc.nasa.gov

Prof. Albert Sievers
Cornell University
Laboratory of Atomic and Solid State Physics
517 Clark Hall
Ithaca, NY 14853-2501
T 607-255-6422; F 607-255-6428
sievers@ccmr.cornell.edu

Prof. Jogender Singh
Pennsylvania State University
Applied Research Laboratory
Engineering Science and Mechanics Department
P.O. Box 30
University Park, PA 16802
T 814-863-9898; F 814-863-2986
jxs46@psu.edu

Dr. N. B. Singh
Northrop Grumman Corporation
Science and Technology Center
ESSS MS-3D14, ATL
1212 Winterson Road
Linthicum, MD 21090
T 410-765-1590; F 410-765-7652
narsingh_b_singh@md.northgrum.com

Dr. Robert C. Singleterry, Jr.
NASA LaRC
Materials Division
Environmental Interactions Branch
Mail Stop 188B
Hampton, VA 23681
T 757-864-1437; F 757-864-8094
r.c.singleterry@larc.nasa.gov

Dr. James Singletery, Jr.
Jet Propulsion Laboratory
4800 Oak Grove Drive
Mail Stop 302-306
Pasadena, CA 91109-8099
T 818-354-5046; F 818-393-4540

Dr. James S. Slepick
University of Illinois, Chicago
Department of Mechanical Engineering
M/C 251, 2039 ERF
842 West Taylor Street
Chicago, IL 60607-7022
F 312-413-0447

Dr. David D. Smith
NASA MSFC
Mail Code SD48
Marshall Space Flight Center
MSFC, AL 35812
T 256-544-7778; F 256-544-2102
david.d.smith@msfc.nasa.gov

Prof. Grant D. Smith
University of Utah
Materials Science and Engineering Department
122 S Central Campus Drive, Rm. 304
Salt Lake City, UT 84112-0560
T 801-585-3381; F 801-581-4816
gsmith2@geoffrey.emro.utah.edu

708

Prof. V. A. Snyder
Northwestern University
Department of Materials Science and Engineering
2225 North Campus Drive
Evanston, IL 60208-3108
F 847-491-7820

Prof. Kwang Jin Song
Yale University
Mason Lab M15
9 Hillhouse Avenue
New Haven, CT 06520
T 203-432-4342; F 203-432-7654
kwangjin.song@yale.edu

Prof. Christopher M. Sorensen
Kansas State University
Department of Physics
Manhattan, KS 66506
T 785-532-1626
sor@phys.ksu.edu

Prof. K. R. Sridhar
University of Arizona
NASA Ames Research Center
MS 239-23
Moffett Field, CA 94035-1000
T 650-604-1649; F 650-604-1092
sridhar@ares.ame.arizona.edu

Prof. Doru M. Stefanescu
University of Alabama
Department of Metallurgy and Materials Engineering
Solidification Laboratory
Room A-129 Bevill Bldg.
P. O. Box 870202
Tuscaloosa, AL 35487-0202
T 205-348-1748; F 205-348-8574
doru@coe.Engr.ua.edu

Dr. Ingo Steinbach
ACCESS
e.V.
Intzestr. 5
52072 Aachen, Germany
T 49-241-805899; F 49-241-38578
i.steinbach@access.rwth-aachen.de

Prof. S. Stoeva
Kansas State University
Department of Chemistry
111 Willard Hall
Manhattan, KS 66506

Dr. Ching-Hua Su
NASA MSFC
Mail Code SD47
Marshall Space Flight Center
MSFC, AL 35812
T 256-544-7776; F 256-544-8762
ching.hua.su@msfc.nasa.gov

Dr. Frank R. Szofran
NASA MSFC
Mail Code SD47
Marshall Space Flight Center
MSFC, AL 35812
T 256-544-7777; F 256-544-8762
frank.szofran@msfc.nasa.gov

Prof. Daniel R. Talham
University of Florida
Department of Chemistry
P.O. Box 117200
Gainesville, FL 32611-7200
T 352-392-9016; F 352-392-3255
talham@Chemicalufl.edu

Prof. Surendra N. Tewari
Cleveland State University
Department of Chemical Engineering
S.H. 464
Cleveland, OH 44115
T 216-523-7342; F 216-687-9220
tewari@csvax.egr.csuohio.edu

Dr. Sheila Ann Thibeault
NASA LaRC
Mail Stop 188B
Hampton, VA 23681-2199
T 757 864-4250
S.A.Thibeault@larc.nasa.gov

Dr. V. Timchenko
University of New South Wales
School of Mechanical and Manufacturing
Engineering
Sydney, NSW 2052, Australia
T 61-2-385-5162; F 61-2-633-1222

Dr. Padetha Tin
NASA GRC
NCMR
21000 Brookpark Road
Cleveland, OH 44135
T 216-433-8164; F 216-433-5033
padetha.tin@grc.nasa.gov

Dr. Paul Todd
SHOT Inc.
7200 Highway 150
Greenville, IN 47124
T 812-923-9591; F 812-923-9598
ptodd@shot.com

Prof. Lawrence W. Townsend
University of Tennessee
Nuclear Engineering Department
Knoxville, TN 37996-2300
T 865-974-5048; F 865-974-0668
ltownsen@utk.edu

Dr. Ram K. Tripathi
NASA LaRC
MS 188 B
NASA Langley Research Center
Hampton, VA 23681
T 757-864-1467; F 757-864-8094
r.k.tripathi@larc.nasa.gov

Prof. Rohit Trivedi
Iowa State University
Ames Laboratory
100 Wilhelm Hall
Ames, IA 50011-3020
T 515-294-5869; F 515-294-4291
trivedi@ameslab.gov

Dr. James D. Trolinger
MetroLaser Inc.
18010 Skypark Circle, # 100
Irvine, CA 92614-6428
T 949-553-0688; F 949-553-0495
jtrolinger@metrolaserinc.com

Dr. Mirosław Trznadel
Middle Tennessee State University
Department of Chemistry
Box X076, MTSU
Murfreesboro, TN 37312
F 615-898-5182

Prof. Michael Tsapatsis
University of Massachusetts, Amherst
Department of Chemical Engineering
159 Goessmann Laboratory
Amherst, MA 01003
T 413-545-0276; F 413-545-1647
tsapatsi@ecs.umass.edu

Dr. V. Tsvetivsky
All-Union Science Research Institute of Mineral
Raw Materials Synthesis
VNIISIMS
Institutskaya str 1
Alexandrov-City 601600
Vladimirskaia Region, Russia
F 7-095-584-5816

Dr. Dennis Tucker
NASA MSFC
Mail Code SD70
Marshall Space Flight Center
MSFC, AL 35812
T 256-544-2685; F 256-544-2659
dennis.tucker@msfc.nasa.gov

Dr. V. Ufimtsev
Institute for Chemical Problems of Microelectronics
Vernadsky prospect 86
Moscow 117571, Russia
F 7-095-230-47-56

Prof. Regina Valluzzi
Tufts University
Bioengineering Center
4 Colby Street
Medford, MA 02155
T 617-627-3136; F 617-627-3991
rv@marvin.tufts.edu

Prof. Peter G. Vekilov
University of Alabama, Huntsville
CMMR, VBRH, D-29
Huntsville, AL 35899
T 256-824-6892; F 256-824-6944
peter@cmmr.uah.edu

Prof. Dionisios G. Vlachos
University of Massachusetts, Amherst
Department of Chemical Engineering
159 Goessmann Laboratory
Amherst, MA 01003
T 413-545-6143; F 413-545-1647
vlachos@snail.ecs.umass.edu

Dr. Marcus Vlasse
NASA MSFC
Mail Code SD10
Marshall Space Flight Center
MSFC, AL 35812
T 256-544-7781; F 256-544-7128
marcus.vlasse@msfc.nasa.gov

Dr. Vitaly Volpert
Université Lyon I
Laboratoire d'Analyse Numérique
Batiment 101
43 bd du 11 Novembre 1918
69622 Villeurbanne Cedex, France
T 33 4 72 44 83 17; F 33 4 72 44 80 53
VOLPERT@LAN1.UNIV-LYON1.FR

Dr. Martin P. Volz
NASA MSFC
Mail Code SD47
Marshall Space Flight Center
MSFC, AL 35812
T 256-544-5078; F 256-544-8762
martin.volz@msfc.nasa.gov

Prof. Peter W. Voorhees
Northwestern University
Department of Materials Science and Engineering
2225 North Campus Drive
Evanston, IL 60208-3108
T 847-491-7815; F 847-491-7820
p-voorhees@northwestern.edu

Dr. Ljubomir Vujisic
CAPE Simulations Inc.
One Bridge Street, Suite 100
Newton, MA 01752
T 617-796-8882 x 103
F 617-796-7870
vujisic@capecsim.com

Prof. John S. Walker
University of Illinois, Urbana
Mechanical and Industrial Engineering Department
140 Mechanical Engineering Building
1206 West Green Street
Urbana, IL 61802
T 217-333-7979; F 217-244-6534
jswalker@uiuc.edu

Dr. D. B. Wallace
Microfab Technologies
1104 Summitt Avenue
Plano, TX 75074

Dr. Y. Wang
Clarkson University
International Center for Gravity, Materials
Science and Applications
Box 5814
Potsdam, NY 13699-5814
F 315-268-3833

Prof. J. Douglas Way
Colorado School of Mines
Chemical Engineering and Petroleum Refining
Department
1500 Illinois Street
Golden, CO 80401-1887
T 303-273-3519; F 303-273-3730
dway@mines.edu

Dr. Richard Weber
Containerless Research, Inc.
906 University Place
Evanston, IL 60201-3149
T 847-467-2678; F 847-467-2679
weber@containerless.com

Prof. Francis C. Wessling
University of Alabama, Huntsville
CMDS, VBRH, M-65
301 Sparkman Drive
Huntsville, AL 35899
T 256-824-6620; F 256-824-6791
wessling@email.uah.edu

Dr. A. A. Wheeler
University of Southampton
Highfield
Southampton SO17 1BJ
United Kingdom

Prof. Joe B. Whitehead Jr.
University of Southern Mississippi
Department of Physics and Astronomy
Box 5046
Hattiesburg, MS 39406
T 601-266-4934; F 601-266-5149
Joe.Whitehead@usm.edu

Ms. Michaela E. K. Wiegel
Massachusetts Institute of Technology
77 Massachusetts Avenue
13-4150
Cambridge, MA 02139
T 617-253-2381; F 617-253-5827
wiegel@mit.edu

Prof. William R. Wilcox
Clarkson University
International. Center for Gravity, Materials
Science and Applications
Box 5814
Potsdam, NY 13699-5814
T 315-268-7672; F 315-268-3833
wilcox@clarkson.edu

Dr. Hermann Wilke
Institute for Crystal Growth
Rudower Chaussee 6
D-12489 Berlin – Adlershof
Germany

Prof. Donna Wilson
Tufts University
Department of Chemical Engineering
4 Colby Street
Medford, MA 02155

Dr. John W. Wilson
NASA LaRC
Materials Division
Mail Stop 188-B
8 West Taylor Street
Hampton, VA 23681-0001
T 757-864-1414; F 757-864-7730
john.w.wilson@larc.nasa.gov

Dr. Thomas L. Wilson
NASA JSC
Mail Code SN3
Houston, TX 77058
T 281-483-2147; F 281-483-5276
thomas.l.wilson@jsc.nasa.gov

Mr. William K. Witherow
NASA MSFC
Mail Code SD48
Marshall Space Flight Center
MSFC, AL 35812
T 256-544-7811; F 256-544-2102
bill.witherow@msfc.nasa.gov

Prof. August F. Witt
Massachusetts Institute of Technology
Department of Materials Science and Engineering
77 Massachusetts Avenue, Room 13-4138
Cambridge, MA 02139-4307
T 617-253-5303; F 617-253-5728
afwitt@mit.edu

Mr. Daniel Wolfe
Rice University
ECE Department and Department of
Chemistry
Houston, TX 77005

Prof. Y.-Y. Won
University of Minnesota
Department of Chemical Engineering and Materials Science
Amundson Hall
421 Washington Avenue S.E.
Minneapolis, MN 55455-0132

Prof. Andrew Yeckel
University of Minnesota
Chemical Engineering and Materials Science
421 Washington Avenue SE
Minneapolis, MN 55455
T 612-626-9455; F 612-626-7246
yeckel@cems.umn.edu

Prof. Nicholas J. Zabaras
Cornell University
Sibley School of Mechanical and Aerospace
Engineering
188 Frank H.T. Rhodes Hall
Ithaca, NY 14853-3801
T 607-255-9104; F 607-255-9410
zabaras@cornell.edu

Dr. J. Zaccaro
CNES
Laboratoire de Cristallographie
BP 166 38042
Grenoble cedex 09, France

Dr. Anvar A. Zakhidov
Honeywell Inc.
Honeywell Technical Center (HTC)
101 Columbia Road
Morristown, NJ 07962-1021
T 973-455-3935; F 973-455-5991
anvar.zakhidov@honeywell.com

Dr. J. Zartman
University of Colorado, Boulder
Department of Mechanical
Engineering
Campus Box 427
Boulder, CO 80309-0427
F 303-492-4637

Prof. Maria I. Zugrav
University of Alabama, Huntsville
CMD5, VBRH D-29
301 Sparkman Drive
Huntsville, AL 35899
T 256-824-6650; F 256-824-6944
zugravm@email.uah.edu

Dr. Cary Zeitlin
Lawrence Berkeley National Laboratory
One Cyclotron Road
Mail Stop 29-100
Berkeley, CA 94720
T 510-486-5518; F 510-486-6949
cjzeitlin@lbl.gov

Dr. H. Zhang
Northrop Grumman Corporation
Science and Technology Center
ESSS MS-3D14, ATL
1212 Winterson Road
Linthicum, MD 21090
F 410-765-7652

Prof. Hui Zhang
State University of New York, Stony Brook
Department of Mechanical Engineering
Stony Brook, NY 11794-2300
T 631-632-8492; F 631-632-8544
Hui.Zhang@sunysb.edu

Prof. Evgenii V. Zharikov
Russian Academy of Sciences
General Physics Institute
Laser Materials and Technology Research Center
Vavilov Street 38, Build. D
117942 Moscow, Russia
T 7-095-135-8352; F 7-095-135-0270
zharikov@Isk.gpi.ru

Dr. Shen Zhu
Universities Space Research Assoc.
Mail Code SD47
Marshall Space Flight Center
MSFC, AL 35812
T 256-544-2916; F 256-544-8762
shen.zhu@msfc.nasa.gov

REPORT DOCUMENTATION PAGE			Form Approved OMB No. 0704-0188	
Public reporting burden for this collection of information is estimated to average 1 hour per response, including the time for reviewing instructions, searching existing data sources, gathering and maintaining the data needed, and completing and reviewing the collection of information. Send comments regarding this burden estimate or any other aspect of this collection of information, including suggestions for reducing this burden, to Washington Headquarters Services, Directorate for Information Operation and Reports, 1215 Jefferson Davis Highway, Suite 1204, Arlington, VA 22202-4302, and to the Office of Management and Budget, Paperwork Reduction Project (0704-0188), Washington, DC 20503				
1. AGENCY USE ONLY (Leave Blank)		2. REPORT DATE March 2001		3. REPORT TYPE AND DATES COVERED Conference Publication
4. TITLE AND SUBTITLE Microgravity Materials Science Conference 2000			5. FUNDING NUMBERS	
6. AUTHORS N. Ramachandran,* N. Bennett,* D. McCauley,** K. Murphy,*** S. Poindexter,* Editors				
7. PERFORMING ORGANIZATION NAMES(S) AND ADDRESS(ES) George C. Marshall Space Flight Center Marshall Space Flight Center, AL 35812			8. PERFORMING ORGANIZATION REPORT NUMBER M-1003	
9. SPONSORING/MONITORING AGENCY NAME(S) AND ADDRESS(ES) National Aeronautics and Space Administration Washington, DC 20546-0001			10. SPONSORING/MONITORING AGENCY REPORT NUMBER NASA/CP-2001-210827	
11. SUPPLEMENTARY NOTES Proceedings of a conference held at Huntsville, AL, June 6-8, 2000. *Universities Space Research Association, **University of Alabama in Huntsville, ***Morgan Research Corporation (all Huntsville, AL)				
12a. DISTRIBUTION/AVAILABILITY STATEMENT Unclassified-Unlimited Subject Category 23 Standard Distribution			12b. DISTRIBUTION CODE	
13. ABSTRACT (Maximum 200 words) The 2000 Microgravity Materials Science Conference was held June 6-8 at the Von Braun Center, Huntsville, Alabama. It was organized by the Microgravity Materials Science Discipline Working Group, sponsored by the Microgravity Research Division (MRD) at NASA Headquarters, and hosted by NASA Marshall Space Flight Center and the Alliance for Microgravity Materials Science and Applications (AMMSA). It was the fourth NASA conference of this type in the microgravity materials science discipline. The microgravity science program sponsored ~200 investigators, all of whom made oral or poster presentations at this conference. In addition, posters and exhibits covering NASA microgravity facilities, advanced technology development projects sponsored by the NASA Microgravity Research Division at NASA Headquarters, and commercial interests were exhibited. The purpose of the conference was to inform the materials science community of research opportunities in reduced gravity and to highlight the Spring 2001 release of the NASA Research Announcement (NRA) to solicit proposals for future investigations. It also served to review the current research and activities in materials science, to discuss the envisioned long-term goals, and to highlight new crosscutting research areas of particular interest to MRD. The conference was aimed at materials science researchers from academia, industry, and government. A workshop on in situ resource utilization (ISRU) was held in conjunction with the conference with the goal of evaluating and prioritizing processing issues in Lunar and Martian type environments. The workshop participation included invited speakers and investigators currently funded in the material science program under the Human Exploration and Development of Space (HEDS) initiative. The conference featured a plenary session every day with an invited speaker that was followed by three parallel breakout sessions in subdisciplines. Attendance was close to 350 people. Posters were available for viewing during the conference and a dedicated poster session was held on the second day. Nanotechnology, radiation shielding materials, Space Station science opportunities, biomaterials research, and outreach and educational aspects of the program were featured in the plenary talks. This volume, the first to be released on CD-Rom for materials science, is comprised of the research reports submitted by the Principal Investigators at the conference.				
14. SUBJECT TERMS microgravity research, materials science, in situ resource utilization, new technology, biomaterials research, radiation shielding			15. NUMBER OF PAGES 719	
			16. PRICE CODE A99	
17. SECURITY CLASSIFICATION OF REPORT Unclassified	18. SECURITY CLASSIFICATION OF THIS PAGE Unclassified	19. SECURITY CLASSIFICATION OF ABSTRACT Unclassified	20. LIMITATION OF ABSTRACT Unlimited	